OPTIMIZING HEAT AND ALGAL BIOMASS AS RENEWABLE ENERGY SOURCES IN BUILDING FAÇADE SYSTEMS

BY

ADHAM M. ELMALKY

A thesis

presented to the University of Waterloo

in fulfillment of the

thesis requirement for the degree of

Doctor of Philosophy

in

Mechanical and Mechatronics Engineering

Waterloo, Ontario, Canada, 2024

© Adham M. Elmalky 2024

Examining Committee Membership

- Dr. Mohamad T. Araji (Supervisor), Department of Mechanical and Mechatronics Engineering and School of Architecture, University of Waterloo

- Dr. Michael Collins, Department of Mechanical and Mechatronics Engineering, University of Waterloo

- Dr. Roydon Fraser, Department of Mechanical and Mechatronics Engineering, University of Waterloo

- Dr. Scott Walbridge, Department of Civil and Environmental Engineering, University of Waterloo

- Dr. James Jones (External), Department of Architecture, Virginia Polytechnic Institute and State University

Author's Declaration

I hereby declare that I am the sole author of this thesis. This is a true copy of the thesis, including any required final revisions, as accepted by my examiners.

I understand that my thesis may be made electronically available to the public.

Abstract

The growing demand for sustainable design strategies in buildings has underscored the potential of microalgae photobioreactors (PBRs) as a renewable source for heat and bioenergy generation. In cold climates, PBR modules integrated in double-skin façades (DSFs) can mitigate snow deposition impact and minimize adverse effects of heat loss to low ambient temperatures. This research presented a two-part study to develop a heat transfer model of DSFs and establish optimal chemical kinetics for PBRs functionality in the system. In the first study, hourly heat transfer analysis was performed to assess PBRs in terms of energy production, panels' efficiency and tilt angle, DSF cavity width, and heat gain profiles in cellular and multistory typologies. For this purpose, shading analysis was carried out to evaluate the solar radiation received by the PBRs. The system's productivity in terms of heat and bioenergy generation was maximized using exploratory and multi-objective optimization algorithms, including graphical and Pareto search methods. In the second study, the chemical model was experimentally validated by applying non-invasive biomass prediction methods using RGB image processing and Neural Networks to predict biomass production from solar energy. The chemical model additionally evaluated the impact of variable flow rate of fresh medium and optimized PBR integration into different façade surfaces, ranging from flat to folded and free-form geometries.

In terms of heat transfer in DSFs, PBRs in direct contact with building occupied spaces significantly reduced winter heat loss, achieving an average gain of 35.7 W/m^2 compared to a loss of 82.1 W/m^2 with conventional façades. It was further noticed that multistory DSFs were advantageous by generating 20.4% more thermal energy and 79.5% more biological energy than cellular DSFs. A developed Trigonometric Model for shading prediction was comparable to Polygon Clipping and Pixel Counting techniques by achieving an average error of 5.2% while significantly reducing simulation time by over 40%. Computationally, Neural Network – Aided algorithms substantially reduced optimization time from 17.2 hours to 6.5 minutes on average. In relation to chemical analysis, variable residence time of microalgae increased biomass generation by 28.8% and CO_2 extraction by 10.8% in various façade geometries. Overall, this research established a comprehensive framework on the behavior of DSFs with integrated renewable sources that can alleviate the burden of climate change in the built environment.

Acknowledgments

I would like to express my sincere gratitude to my supervisor Dr. Mohamad T. Araji for his unwavering guidance, invaluable support, and boundless expertise throughout the journey of completing this doctoral thesis. His mentorship has been instrumental in shaping both my academic pursuits and personal growth.

I am profoundly thankful to my parents for their endless encouragement, sacrifices, and unwavering belief in my potential, which have been the cornerstone of my academic journey.

To my beloved wife, Reham Raafat, your unwavering love, patience, and understanding have been my greatest source of strength. Your unwavering support and encouragement have sustained me through the challenges and triumphs of this endeavor. I am indebted to your love and unwavering support.

Dedication

To My Mother & Father

Table of Contents

Examining Committee Membership ii
Author's Declaration iii
Abstract iv
Acknowledgments v
Dedication vi
List of Figures xi
List of Tables xvi
Nomenclature xvii
Chapter 1 : Introduction 1
1.1 Background 1
1.2 Motivation 3
1.3 State-of-the-art 7
1.4 Research Objectives and Methods 10
1.5 Thesis Layout 15
Chapter 2 : Literature 18
2.1 Microalgae Photobioreactors 18
2.1.1 Design Parameters of Flat Panel PBRs 18
2.1.2 Performance Indicators of PBRs 19
2.1.3 PBRs Challenges 21
2.2 Double Skin Façades 21
2.2.1 Design Parameters of DSFs 21
2.2.2 Performance Indicators of DSFs 23
2.2.3 DSFs Challenges 24
2.3 Shading Prediction Techniques 25
Chapter 3 : Heat Transfer Modeling for DSF Systems Integrating PBR Panels 28
3.1 Introduction 28
3.2 Method 30
3.2.1 Description of model geometry 30

3.2.2 Heat transfer model definitions, assumptions, and constraints 33
3.2.3 Rate of heat transfer through the DSF 36
3.2.4 Radiative heat transfer 39
3.2.5 Convective heat transfer 42
3.2.6 Setup of the CFD model 44
3.2.7 Parametric analysis with ANSYS-MATLAB coupling 45
3.2.8 Solar irradiation and energy generation model 48
3.3 Results and Discussions 50
3.4 Summary of Chapter 61
Chapter 4 : Optimization to Maximize Thermal and Bioenergy Generation 63
4.1 Introduction 63
4.2 Method 64
4.2.1 Description of model geometry 65
4.2.2 Rate of heat transfer through the DSF 67
4.2.3 Solar irradiation and energy generation model 69
4.2.4 Heat gain by the building façade 72
4.2.5 Multi-Objective Optimization 73
4.3 Results and Discussions 75
4.4 Summary of Chapter 85
Chapter 5 : Chemical Kinetics Modeling and Experimental Analysis for PBRs in DSFs 88
5.1 Introduction 88
5.2 Method 92
5.2.1 PBR condition 92
5.2.2 Chemical kinetics model 94
5.2.3 Experimental Setup 96
5.2.4 Biomass Monitoring 97
5.2.5 Optimization methods 102

5.2.6 Application in various Canadian cities 111
5.3 Results and Discussions 112
5.3.1 Model validation and parametric analysis 112
5.3.2 Neural networks for biomass prediction 114
5.3.3 Neural network-aided optimization 119
5.3.4 Hooke-Jeeves and Powell's Conjugate Direction Methods 123
5.3.5 Volumetric biomass production 125
5.3.6 Application in various Canadian cities 127
5.4 Summary of Chapter 128
Chapter 6 : Variable Flow Rate of Fresh Medium and Façade Geometry Impact 131
6.1 Introduction 131
6.2 Method 133
6.2.1 Variable flow rate 133
6.2.2 Shading models 136
6.2.3 Façade geometry impact 144
6.3 Results and Discussions 152
6.3.1 Variable flow rate 152
6.3.2 Façades solar availability 155
6.3.3 Chemical model equivalent efficiency 159
6.3.4 Bioenergy façades performance 159
6.3.5 Optimization methods performance 161
6.4 Summary of Chapter 166
Chapter 7 : Conclusions 169
7.1 Summary 169
7.2 Conclusions on Heat Transfer Modeling for DSF Systems Integrating PBR Panels . 171
7.3 Conclusions on Optimization to Maximize Thermal and Bioenergy Generation..... 172
7.4 Conclusions on Chemical Kinetics and Experimental Analysis for PBRs in DSFs ... 172

7.5 Conclusions on Variable Flow of Fresh Medium and Façade Geometry Impact..... 173
7.6 Contributions..... 174
7.7 Future Works 175
References.....178

List of Figures

Figure 1.1. Schematic diagram of a closed microalgae cultivation system, PBR. 2

Figure 1.2. Types of DSFs. 2

Figure 1.3. Possible integrations of PBRs into DSFs [19]. 3

Figure 1.4. Global Horizontal Irradiation map of Canada [39]. 5

Figure 1.5. Hourly mean curves showing the occupied space heat gain for DSF systems integrating PBRs [15]. 7

Figure 1.6. The BIQ building, the first algae-powered building, designed by Arup. Left: PBR modules. Middle: PBR panels installation. Right: South façade [49]. 8

Figure 1.7. Microalgae façade consists of interconnected bioreactors containing spirulina, a type of blue-green microalgae [53]. 9

Figure 1.8. Trends in the publication of research articles on DSFs [69]. 10

Figure 1.9. Research objectives and applied methods. 11

Figure 1.10. Key steps, methods, publications, and outstanding work for achieving the first objective. 12

Figure 1.11. Key steps, methods, publications, and outstanding work for achieving the second objective. 13

Figure 1.12. Key steps, methods, publications, and outstanding work for achieving the third objective. 14

Figure 1.13. Key steps, methods, publications, and outstanding work for achieving the fourth objective. 15

Figure 3.1. DSF system with the relevant optical model and the solution domain for internal ventilation cases and mixed ventilation cases. 32

Figure 3.2. DSF elements' radiative thermal resistance model (left) and convective thermal resistance model (right) 36

Figure 3.3. Top, view factors for parallel plates with parallel midlines and separated perpendicular plates (without a common edge). Bottom, view factor cases applied to the DSF elements. 38

Figure 3.4. Schematic of the cavity solution domain (left), and sequence implemented in the code (right). 47

Figure 3.5. The impact of the cavity width on the shading factor for different elements in the DSF. 49

Figure 3.6. Validation and grid independence test for the developed CFD model. y/Y and x/X represent the temperature variation with the cavity height and width, respectively. 51

Figure 3.7. Top, validation of the integral heat balance model. Bottom, regression analysis for both Andelkovic and the developed model. 52

Figure 3.8. Hourly mean curves for the solar irradiation reaching the PVs/PBRs, energy generation, useful heating, and overall efficiency for both PV and PBR panels. 54

Figure 3.9. Velocity profiles for all ventilation cases. 56

Figure 3.10. Velocity variation adjacent to the cavity top, cavity bottom, PVs/PBRs, and inner glass layer 57

Figure 3.11. Mean velocity adjacent to the cavity top, cavity bottom, PVs/PBRs, and inner glass layer 58

Figure 3.12. Temperature variation along the cavity width in both the upper and the lower halves in winter and summer for all ventilation schemes. 59

Figure 3.13. Generated energy, conversion efficiency, heat loss, and associated temperature for the PVs/PBRs in all cases. Colored bars represent ventilation schemes and whiskers extend to the maximum and minimum to express the amount of increment or decrement if the vents are closed. 60

Figure 3.14. PBRs' panels associated inside convective heat transfer coefficient, heat added to water, and required water flow rate to keep the PBRs' water within the acceptable temperature range. 61

Figure 4.1. Top, proposed façade systems integrating PBR panels. Bottom, 3D representations of cellular and multistory DSF systems. 66

Figure 4.2. Convective and radiative thermal resistance models for system 1 (left) and system 2 (right). 68

Figure 4.3. Shading factor calculation procedure for system 1. 71

Figure 4.4. Shading factor calculation procedure for system 2. 72

Figure 4.5. Left, multiple levels with different ranks. Right, Pareto front volume in relation to the reference point 75

Figure 4.6. Variation of the solar exposure percent with the cavity width, PBRs' tilt angle, and solar latitude angle for the cellular design. 76

Figure 4.7. Shaded area percentage for different combinations of PBRs' base width(W), PBRs' tilt angle (β), and offset (d). 77

Figure 4.8. Multistory design average shading factor, average incidence factor, and estimated solar gain in different locations 78

Figure 4.9. PBRs plates' temperature, thermal heat generation, and biological mass production for the cellular design 80

Figure 4.10. The multistory design performance in terms of PBRs plates' temperature, thermal energy gain, and biological energy generation. 81

Figure 4.11. Graphical optimization for cellular and multistorey DSF designs. 82

Figure 4.12. Top, search space generated by random points generation. Bottom, Pareto front generated by both SA and GA. 83

Figure 4.13. Energy savings achieved by DSFs compared to SSFs. 85

Figure 5.1. Examined parameters of the DSF system with the integrated flat PBRs. 93

Figure 5.2. a) Setup main dimensions in cm. b) 3D construction. c) Section view without one side. d) Cavity and inner layer. e) Outer layer view from inside the cavity. f) PBR. 96

Figure 5.3. Four steps of the RGB Image-Based Monitoring Technique. 98

Figure 5.4. Employed three-layered neural network. 100

Figure 5.5. Sequence followed to implement GA. 103

Figure 5.6. Top, employed procedure for implementing PSO. Bottom, position and velocity update for each particle within the swarm. 105

Figure 5.7. Left, 2D illustration of the HJ method. (a) Exploratory moves. (b) Pattern move for case 1. (c) Pattern move for case 2. (d) Pattern move for case 3. Right, Schematic of the used framework to apply the HJ algorithm. 108

Figure 5.8. a) Parallel subspace property employed by PCD method. b) Schematic of the used framework to apply PCD method. c) Adopted line search minimization method. 109

Figure 5.9. Model validation. Left, model biomass concentration compared to experimental measurements. Right, biomass production after 20 days. 113

Figure 5.10. Aerial biomass generation per year for different decision variables. 114

Figure 5.11. Correlation coefficient and computational effort of FNNs trained with different algorithms. 115

Figure 5.12. CNNs' input images derived from the structured data represented by the variables vector [τ, δ, W, β]. 116

Figure 5.13. RMSE values for both the training and validation sets of CNNs trained using the SGDM algorithm. 117

Figure 5.14. RMSE values computed for the training and validation sets of CNNs trained using the RMSP optimizer, while varying the SGDM values. 118

Figure 5.15. RMSE values calculated for the training and validation sets of CNNs trained using the Adam optimizer. 119

Figure 5.16. Variation of correlation coefficient (R) and required time for different sizes of datasets. 121

Figure 5.17. Top, variation of maximum mB and overall time with number of points. Bottom, impact of NN integration on the overall time. 123

Figure 5.18. Performance of the HJ algorithm and PCD in relation to variation of the objective function, aerial biomass harvest, and decision variables with iterations. 124

Figure 5.19. Optimal parameters for maximum volumetric productivity. 126

Figure 5.20. Sensitivity analysis and optimal decision variables for different locations across Canada 128

Figure 6.1. Schematic of the used sequence to apply GA for maximizing biomass generation over shorter intervals of time. 135

Figure 6.2. Different forms of façade typologies. 137

Figure 6.3. Typical linear and elliptical urban contexts. 138

Figure 6.4. Parameters considered for examining solar exposure of a building façade within a site context: (a) Linear site arrangement, and (b) Elliptical site arrangement. 139

Figure 6.5. Left, computational procedure followed to generate urban forms using *MATLAB*. Right, illustration showing the building's plan view and height variation in 3D. 141

Figure 6.6. Left, intersection points between the solar plane and the buildings located within the plane. Right, the solar plane for one façade element at a given solar time. 142

Figure 6.7. Schematic of the algorithm implemented to calculate α_{min} for the investigated façade points on an hourly basis. 143

Figure 6.8. Examined façades in relation to the surrounding elements. 145

Figure 6.9. (a) Modeled parameters of surrounding elements. (b) Folded façades parameters. (c) Various cases for calculating the shading factor for upper and lower panels. (d) Possible combinations of PBRs and vision panels. 147

Figure 6.10. Solar beam reflections in free-form façades. Left, no reflections at lower solar elevation angles. Right, multiple reflections received by the same panel at higher solar elevation angles. 149

Figure 6.11. Schematic of the applied GA to optimize PBRs integration into free-form façades. 151

Figure 6.12. Performance of different selection techniques in terms of variation of the objective function value (mB) with iterations. 153

Figure 6.13. Top, m_B and CO_2 extraction for both fixed and variable τ_d. Bottom, impact of the developed system on the operational carbon footprint. 154

Figure 6.14. Variation of solar irradiation with surrounding tilt, S_2/L, and building height, H/L. (a) Absolute values of solar irradiation, I_{avg}. (b) Difference between tilted and flat surroundings, ΔI_{avg}. 156

Figure 6.15. Top, impact of δ/L on surface azimuth angle (ζ), tilt angle (β), irradiation (I_{avg}), and irradiation difference (ΔI_{avg}) for free-form façades. a) δ = 0.00 L, b) δ = 0.02 L, c) δ = 0.05 L, and d) δ = 0.07 L. Bottom, variation of façade irradiation difference ($\Delta Iavg$) for different street and surroundings width. 158

Figure 6.16. Top, verification of the developed model against literature. Middle, weekly average irradiation (I) and bioenergy Generation (B). Bottom, cumulative bioenergy generation (B_c) and the corresponding Error. 159

Figure 6.17. Top, variation of maximum bioenergy generation (B_{max}) with different locations (latitude angles, φ) and façade orientations (surface azimuth angles, ζ). Bottom, comparison between optimized and unoptimized façades. 161

Figure 6.18. Folded façades optimum points, solution paths, and section views. 162

Figure 6.19. (a) Performance of GA for different façade orientations. (b) Bioenergy generation (B) evolution with iterations for south-oriented façades. (c) Façade transformation at different iterations. 164

Figure 6.20. Performance comparison between HJ and GA for optimizing folded façades at a latitude of 55°, and free-form façades oriented east/west. 166

List of Tables

Table 2.1. Summary of different studies on applied techniques for shading prediction. 27
Table 3.1. Model definitions, assumptions, and constraints. 33
Table 3.2. Radiation fluxes defined at a surface [159]. 40
Table 3.3. Temperature conditions for different cavity elements in ℃. 45
Table 4.1. Differences between cellular and multistorey DSF systems. 67
Table 5.1. Applied parameters with corresponding definitions and values [1,21]. 95
Table 6.1. Optimal solution with associated tilt angles. 160

Nomenclature

English Symbols:

A	Area, m^2
A_1	Street width, m
A_2	Surrounding width, m
B	Bioenergy, W/m^2
C_X	Biomass concentration, kg/m^3
d	Distance, m
E	Error, or generated energy, W/m
E_a	Coefficient of mass absorption, m^2/kg
E_s	Coefficient of mass scattering, m^2/kg
f	Objective function
F	View factor
G	Received solar irradiation, W/m
h	Heat transfer coefficient, $W/m^2 \cdot K$
H	Height, m
HV	Heating value, kJ/kg
I_b	Direct beam Irradiation, W/m^2
I_d	Diffuse sky irradiation, W/m^2
J	Radiosity, W/m^2
k	Kinetic energy of turbulence, or thermal conductivity, W/m·K
K	Photosynthetic half-saturation constant, μmolhv/kg·s
K_r	Inhibition constant for respiration, μmolhv/kg·s
L	Length, m
m	mass, kg
M_B	C-molar mass for microalgae biomass, Kg/C-mol
Nt	Number of iterations
P	Generation rate of k/ω
p	Population number
q	Heat transfer, W/m
Q	Total heat transfer, W/m^2
R	Thermal resistance, $m^2 \cdot K/W$

r	Biomass growth rate, $kg/m^3 \cdot s$
R	Reflected irradiation component, W/m^2
Ref	Glass reflectivity
$RMSE$	Root Mean Square Error
S	Source term of k/ω, or Surroundings height, m
SF	Shading factor
ST	Solar time
T	Temperature, ºC
U	Overall heat transfer coefficient, $W/m^2 \cdot K$
V	Velocity, m/s, or Volume, m^3
W	Width, m
X	Percentage of new points
Y	Dissipation rate of k/ω
z	Distance inside microalgae culture, m
Z_s	Surface azimuth angle, rad

Greek Symbols:

J_{NADH2}	Cofactor regeneration rate on the respiratory chain, $mol_{NADH2}/kg \cdot s$
α	Solar altitude angle, rad, or thermal diffusivity, m^2/s
β	Tilt angle or thermal expansion coefficient, K^{-1}
δ	Thickness or sunken/protruding distance, m
Δ	Step size
ε	Emissivity
ζ	View or solar azimuth angle, rad
η	Efficiency
θ	Angle of incidence, rad
ν	Kinematic viscosity, m^2/s
$\nu_{NADH-O2}$	Cofactor regeneration stoichiometric coefficient on the respiratory chain
ν_{O2-B}	Stoichiometric coefficient of oxygen evolution
ρ	Energy yield for photon conversion
ρ_{max}	Maximum energy yield for photon conversion
σ	Stefan-Boltzmann constant, $W/m^2 \cdot K^4$

τ	Transmissivity
τ_d	Residence time, days
φ	Latitude angle, rad, or mole quantum yield, mol/μmolhv
$\bar{\phi}'$	O_2 mole quantum yield, $mol_{O2}/\mu mol_{hv}$
ω	Hour angle, rad, or specific dissipation rate
Γ	Effective diffusivity of k/ω

Subscripts & Superscripts:

a	Ambient
avg	Average
b	Cavity bottom
B	Biomass
c	Cavity or cumulative
conc	Concentration
conv	Convection
f	Film
G	Global
g	Ground
gen	Generated
h	Horizontal
ig	Inner glass
in	Inlet flow
k	Floor number
l	Lower
min	Minimum
max	Maximum
og	Outer glass
opt	Optimal
pl	Plenum or panel
r	Reflected solar beam
ra	Room air
rad	Radiation
rw	Room walls

s	Sky
si	Sill
surr	Surroundings
t	Cavity top
u	Upper
v	Variable
w	Water
X	Microalgae species

Abbreviations:

AR	Area ratio
BIQ	Bio Intelligent Quotient
CS	ClimateStudio
DS	Domus
DSF	Double skin façade
E+	EnergyPlus
GA	Genetic Algorithms
HJ	Hooke-Jeeves
PBR	Photobioreactor
PCD	Powell's conjugate direction
PgC	Polygon clipping
PV	Photovoltaic
PxC	Pixel counting
SHGC	Solar heat gain coefficient
SS	Shading II plug-in for SketchUp
SSF	Single skin façade
SST	Shear-stress transport
TgM	Trigonometric model
V	Ventilation
VIS	Vision glass

Dimensionless groups:

Rayleigh number (Ra_L)	$\frac{g\beta(T_s - T_\infty)L^3}{\alpha\nu}$	Dimensionless number associated with buoyancy-driven flow
Nusselt number (Nu_L)	$\frac{hL}{k_f}$	Dimensionless temperature gradient at the surface.
Prandtl number (Pr)	$\frac{c_p\mu}{k} = \frac{\nu}{\alpha}$	Ratio of the momentum and thermal diffusivities.
Reynolds number (Re_L)	$\frac{VL}{\nu}$	Ratio of the inertia and viscous forces.

Chapter 1: Introduction

Microalgae photobioreactors (PBRs) are emerging as a valuable system that cultures organic feedstock in nutrient-rich water for biological growth. If widely integrated into building envelopes, such a system can help absorb carbon dioxide, release oxygen, provide adaptive shading, utilize a building's greywater and preserve land resources for alternative harvesting. Globally, very few experiments established a physical model for building integrated PBRs [1,2]. In cold climates, microalgae cultivation research has been focusing on standalone reactors without any consideration of the systems' potential when integrated into buildings due to the adverse effects of the ambient environment. To mitigate such an impact, this work will consider the inclusion of PBRs within the inner layer of double skin façades (DSFs) defined as a pair of glass layers separated by an air space cavity in buildings. The inner and outer layer of the DSF will be regarded as a single-glazed and double-glazed units, respectively.

This chapter is divided into five key sections: background, motivation, the state-of-the-art in building-integrated PBRs, research objectives and methodologies, and an outline of the thesis structure.

1.1 Background

Algae are living species that comprise a diverse group of aquatic organisms, which have the ability to conduct photosynthesis. Such organisms can survive and flourish in variant conditions and different environments such as terrestrial environments, freshwater, and highly saline water. Algae surpass other organisms by having chlorophyll in every single cell which thus have the potential to perform the photosynthesis process on its own. For that reason, biomass production from algae, in both open and closed systems, is very robust compared to other plants [3]. Open systems, normally ponds or lakes, are characterized by high production rates as they are relatively large and have direct contact with the atmosphere [4]. On the other hand, closed systems are more controllable and are known as PBRs, Figure 1.1.

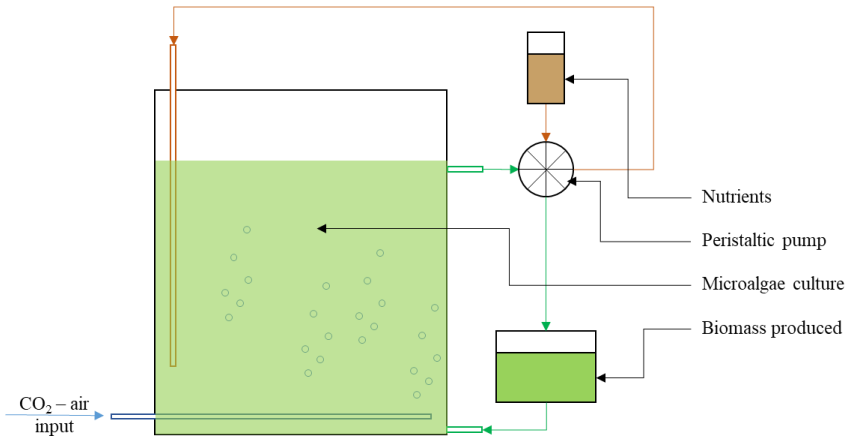


Figure 1.1. Schematic diagram of a closed microalgae cultivation system, PBR.

DSFs are receiving increased attention in recent applications aimed at efficient building envelopes. For different climatic regions, such systems reduce energy consumption, offer improved indoor air control, and restrict undesired solar irradiation and exterior airflow [5,6]. However, few studies reported higher cooling demands for DSFs due to cavity heat accumulation in summer [7]. Moreover, the higher initial and operational costs of DSFs can reduce the feasibility of such systems compared to conventional façades [8]. Therefore, applying such technology requires the proper selection of façade geometry along with suitable utilization of glass panes and shading devices in addition to opening principles and airflow modes [9,10]. As shown in Figure 1.2, DSF systems are generally divided into various types such as shaft-box with a vertically continuous cavity, corridor with a horizontally continuous cavity, multistory with a fully connected cavity in the vertical and horizontal directions, and box-window with a cavity divided by floor.

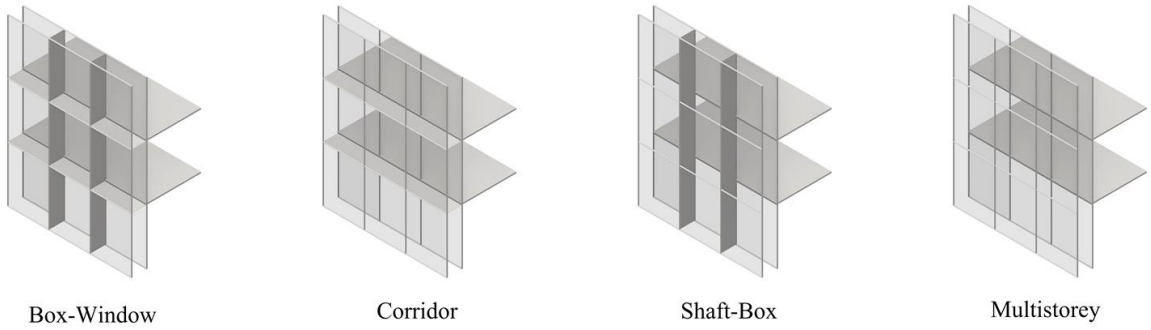


Figure 1.2. Types of DSFs.

1.2 Motivation

Buildings account for 40% of global energy use and 33% of greenhouse gas emissions [11]. Recent studies have been dedicated to integrating renewable sources with the goal of improving the performance and efficiency of buildings [12,13]. Microalgae PBRs integrated into DSFs have been examined by recent studies as a sustainable resource to mitigate the impact of the outdoor environments [14,15]. Figure 1.3 shows possible integrations of PBRs into DSFs. There have been many studies carried out on heat transfer analysis of DSF systems, but very few on building-integrated renewable energy façades and especially for extremely cold climates. Particularly, there are no studies available for heat transfer analysis of DSFs comprising PBRs. The associated optimum geometry and composition in the presence of renewable energy are still unknown. Many studies optimized the cavity width in DSFs to cool down PV panels when added to the outer skin by modes of forced [16,17] or natural convection [18]. For both modes, heat gain was reduced by 11.6% using a 2.5 m wide cavity, and by 18.7% using a 5 m/s airflow [16]. However, more research should be carried out to evaluate the reduction in received irradiation, especially for PBR panels integrated into the inner skin. In this study, the term "irradiation" is used to denote solar irradiation, defined as the power per unit area (W/m^2) received from the Sun in the form of electromagnetic radiation within the wavelength range of the measuring instrument.

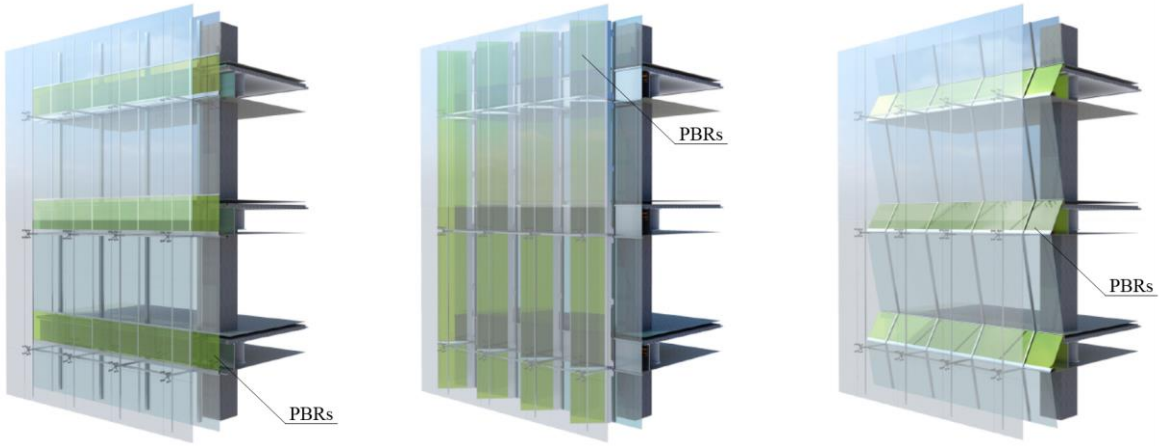


Figure 1.3. Possible integrations of PBRs into DSFs [19].

In terms of PBRs, optimal biomass generation is significantly influenced by light attenuation, nutrient limitation, fluctuating pH value and temperature, and medium contamination [20].

Numerical PBR models were efficient in many studies, including: 1) Artificial and solar light sources [21,22]; 2) Sizing and optimizing cultivation strategies [23,24]; and 3) Selection of various microalgae species [25,26]. However, the employed optimization strategies were either focused on cylindrical PBRs [23] or external light sources with constant photon flux density [24]. Moreover, the previous studies lacked the application of constrained local optimization methods which can search for the most efficient geometrical and operational parameters within their associated feasible range. The proposed research will address these gaps by applying optimization techniques for flat PBRs using solar light. The optimal performance in the literature was achieved by assigning a fixed value to the microalgae residence time which maximized biomass generation throughout the year [22]. However, no previous research proposed an unsteady residence time by employing variable speed pumps. Therefore, the research will also focus on additional analysis that examines a novel PBR with a variable flow rate of fresh medium.

Solar irradiation varies across Canada, as shown in Figure 1.4, from over 4 kWh/m²·day in the southern center to about 2 kWh/m²·day in the far north and west coast. Most urban centers, including Calgary, Regina, Winnipeg, Toronto, Ottawa, and Montreal, receive over 3.6 kWh/m²·day. In such dense cities, maximizing the performance of building-integrated PBRs is challenging due to the limited sunlight access. Tools are thus required to accurately model and correlate solar irradiation on façades while maintaining reasonable computational efficiency [27–29]. Façades, within building envelopes, offer several advantages for solar applications since they constitute a significant portion (60% to 80%) of the buildings' total surface area [30], can employ PV panels as cladding material [31–35], and resist dust accumulation and snow deposition for advanced performance due to vertical positioning [36]. Solar energy collection through such an application is exploited during winter days and through extreme hours in summer days due to lower altitude angles [1,37,38]. However, challenges arise from shading caused by the surrounding environment, especially in dense urban areas. Efficient shading prediction methods would help in assessing the solar irradiation received by building façades and optimizing solar energy utilization in urban areas.

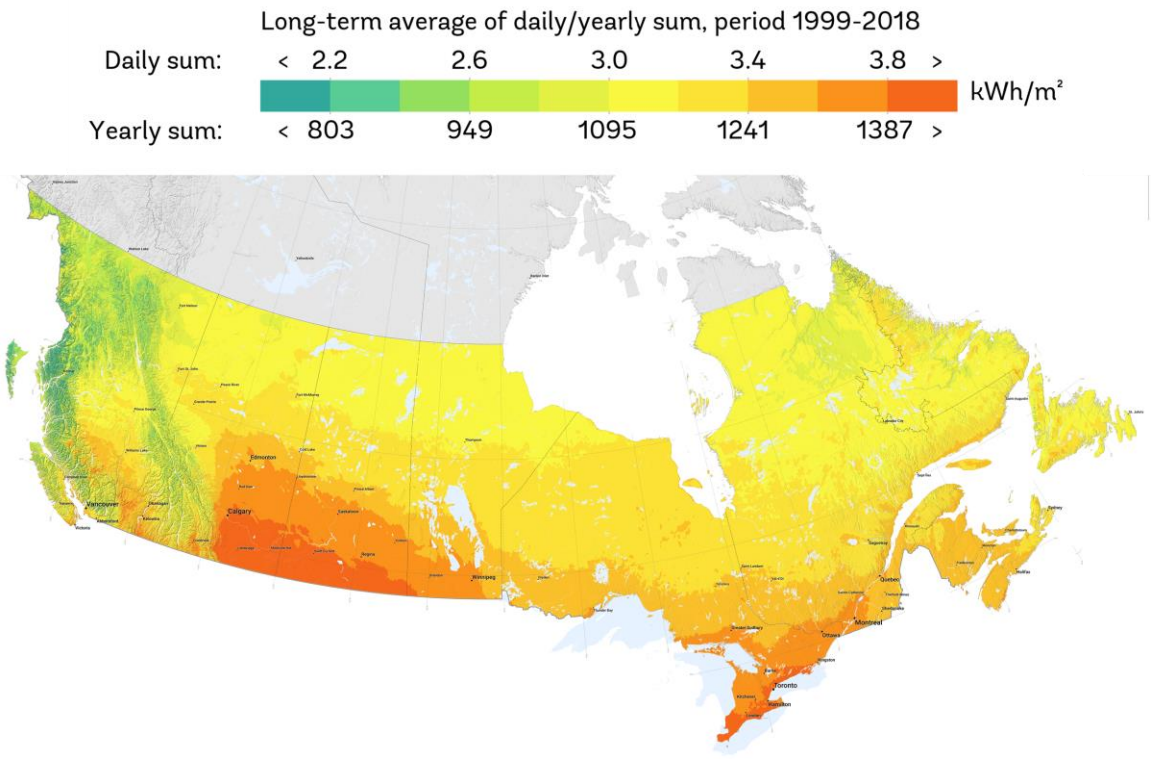


Figure 1.4. Global Horizontal Irradiation map of Canada [39].

Computational procedures of solar irradiation have been utilized for building façades analysis with different capabilities. LiDAR technology and similar tools use geographic information-based 3D models to evaluate solar irradiation in urban areas [40]. Geographic Information Systems (GIS) databases are also used to analyze solar irradiation and shading impact. Other software options like ClimateStudio (CS) [41], DIVA for Rhino [42], EnergyPlus (E+) [43–47], Daysim [47,48], and Radiance [47] offer alternatives for façade solar assessment and shadow modeling. E+ is faster but less accurate, while Daysim and Radiance provided better results [47]. However, current tools have limitations impacting accuracy and computation due to simplifications, high resource demands, and data prerequisites. The subsequent section provides an extensive background of various tools and techniques applied for the prediction of solar irradiation.

Driven by the previous challenges of optimizing the integration of PBRs into building façades, this research is aiming to:

- Design a DSF system with built-in PBRs to address challenges in cold climates. This system will assess energy production, panel efficiency, and heating gains in building

façades, considering shading and ventilation effects. This corresponds to the first objective and is detailed in Chapter 3.

- Address the shortcomings of previous studies on cavity heat accumulation in summer. Figure 1.5 illustrates the increase in heat gain in occupied spaces from June to September due to such heat accumulation in the cavity. This is achieved by formulating a multi-objective problem to minimize heating and cooling loads and maximize bioenergy generation from the PBRs. This aligns with the second objective and is thoroughly discussed in Chapter 4.
- Develop and optimize a detailed chemical kinetics model for building-integrated PBRs using constrained local optimization methods. An experimental setup will be built to monitor microalgae growth with RGB imaging, and the chemical model's accuracy will be validated against collected experimental data. This corresponds to the third objective and is detailed in Chapter 5.
- Couple the chemical model with GA to assess a novel PBR with a variable flow rate of fresh medium. The same method will be applied to optimize the integration of PBRs into different façade forms. This necessitated the development and refinement of Trigonometric Models (TgMs) to investigate the shading imposed by the surrounding buildings. This aligns with the fourth objective and is thoroughly discussed in Chapter 6.

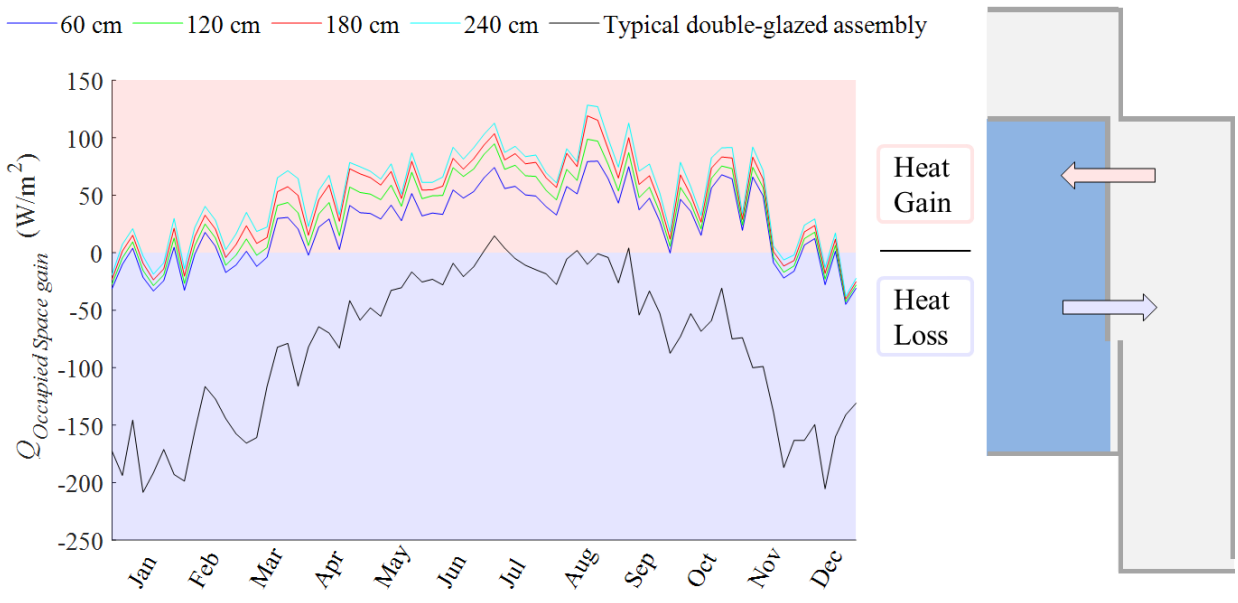


Figure 1.5. Hourly mean curves showing the occupied space heat gain for DSF systems integrating PBRs [15].

1.3 State-of-the-art

The first application of PBRs in buildings was reported in the BIQ house in Hamburg, Germany [49], where the outer skin façade incorporated sun-tracking panels able to convert solar energy to biomass and thermal heat by 8-10% and 40%, respectively [50]. As shown in Figure 1.6, these sun-tracking panels consists of 129 reactor modules (PBRs) with the dimensions of 70 cm × 270 cm × 8 cm (width × height × thickness). The PBRs are housed inside a steel frame serving as a wiring channel. Within the PBRs, water serves as the nurturing medium for cultivating microalgae. CO_2 is introduced into the culture medium from the flue gas produced by a combined heat and power unit fueled by biogas. To prevent the microalgae from sinking and to ensure they remain suspended, the culture medium undergoes continuous agitation. This is achieved by introducing compressed air into the PBRs through an airlift mechanism. Deposition of microalgae and biological contaminants is mitigated by fast-moving currents along the inner walls of the PBRs. During operation, the PBRs are linked sequentially, allowing the culture medium to circulate through each one. During daylight hours, PBRs can reach temperatures up to 35°C to act as solar thermal collectors. Microalgae medium is circulated through the building's central service hub, where biomass is centrally collected via filtration, and heat is extracted using a heat exchanger.



Figure 1.6. The BIQ building, the first algae-powered building, designed by Arup. Left: PBR modules. Middle: PBR panels installation. Right: South façade [49].

Other attempts for building integrated PBRs were constructed in central Europe at the Centre for Biotechnology in Nové Hrady, Czech Republic [51]. An experimental setup consisting of two-stage south-facing PBR was developed utilizing solar concentrators, specifically linear Fresnel lenses, to assess the impact of high irradiation on tubular microalgae concentration. Each of the two vertical façade units comprises six panels measuring 0.75 m × 2 m (width × height), totaling 9 m^2, while each of the two inclined-roof units consists of ten panels covering an area of 15 m^2 each. As per the reported measurements, approximately 25% of solar irradiation is lost by either reflection or tube wall absorption. Even when the microalgal suspension has a relatively low biomass concentration of 0.2 kg/m^3, over 60% of light gets absorbed within a few millimeters of the suspension's photic zone. If additional stress (e.g., suboptimal temperatures) were to occur, these cultures could experience significant photostress. The tubular configuration was thus more suitable for microalgae media with higher biomass concentrations.

Recent attempts have explored using rotational molding to make interlocking modular systems (Figure 1.7) for freeform photobioreactors integrated into building façades [52,53]. However, the energy performance, specifically concerning bioenergy production and thermal insulation, remains ambiguous for such systems. It is evident that these systems capture less light than flat panel PBRs and do not allow for glazing windows on the façade, a critical feature for building occupants. In addition, the system's catch basins may indicate a potential leakage risk. The ecoLogicStudio in London, England developed curtain walls with tubular PBRs to absorb 3 kg/m^2 of CO_2 per year [54]. These walls comprise around 16 bioplastic modules with the dimensions approximately 2 m × 7 (width × height). However, the tubular configuration had a lower efficiency in relation to sunlight utilization compared to flat panel PBRs [55]. The latter was integrated into façades and

allowed for sufficient daylighting due to the transparent nature of microalgae cultures [1]. On average, such a design produced 2.3 kg/m^2 of biomass and sequestrated 31.7 kg/m^2 of CO_2 per year [13]. Nonetheless, adding PBRs to outer building skins increased the adverse effect of ambient temperature on the microalgae medium, especially in cold regions. Beyond said benefits, the utility of solar energy modules can be in replacing part of the structural material in façades and providing high insulation for the building [33,34].



Figure 1.7. Microalgae façade consists of interconnected bioreactors containing spirulina, a type of blue-green microalgae [53].

Mitigating the impact of cold climates can be achieved by integrating PBRs into the inner layer of DSFs, which acquired significant popularity following their invention in 1903 [56]. A thorough search of the relevant literature didn't reveal any studies examining DSFs in relation to PBRs integration. The main focus in current DSFs integrating renewable sources revolves around PV systems. Over the past two decades, research on DSFs has accelerated significantly, as shown in Figure 1.8, with most findings highlighting its outstanding energy performance [57]. The first documented use of renewable sources in DSFs appeared in the public library in Mataro, Spain in 1998 [58]. However, the following decade saw limited adoption of this technology [59,60]. Since 2010, research on DSFs integrating renewable sources has surged due to growing concerns about climate change and government policies. Early DSF designs utilized PV panels [59] and incorporated dual airflow paths including a thermal buffering mode and an external circle [61].

Currently, multiple attempts have investigated DSFs regarding thermal comfort [62,63], energy efficiency [31,64], and daylighting availability [65]. Parameter analysis has been extensively examined for optimizing renewable sources integration into DSFs for improved energy-saving potential [66,67]. This was applied to address the extended payback period exceeding 80 years, making large-scale utilization of DSFs economically impractical [68].

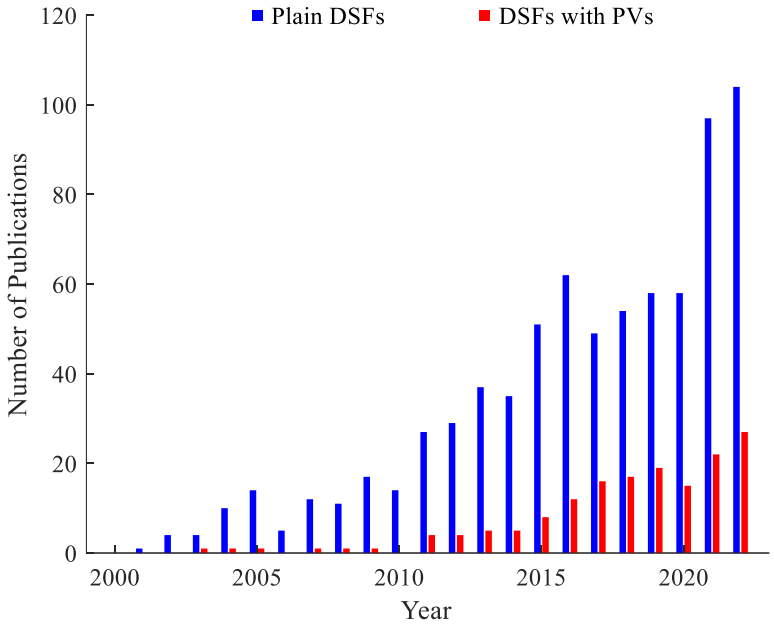


Figure 1.8. Trends in the publication of research articles on DSFs [69].

1.4 Research Objectives and Methods

The primary objective of this thesis is to optimize and assess the potential of DSF systems in cold climatic regions. The goal is to investigate the performance of PBR panels integrated into buildings regarding associated heat transfer through the multiple layers of the DSF and energy generation from the PBRs. Figure 1.9 depicts the interconnections between research objectives and applied methods. Overall, this research will use various experimental and analytical modeling techniques in addition to simulation tools to implement the following objectives:

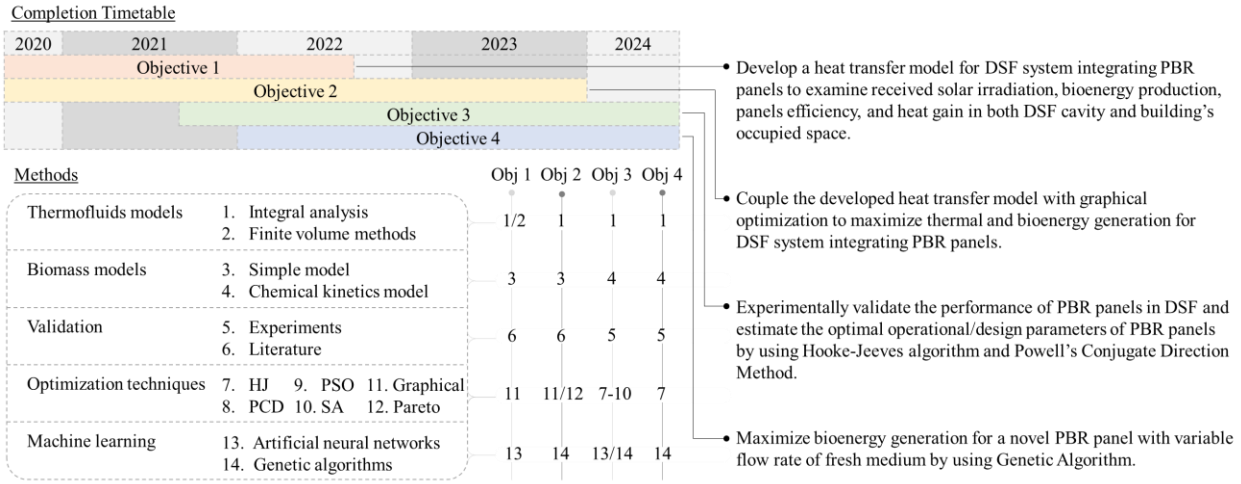


Figure 1.9. Research objectives and applied methods.

Objective 1: Develop a heat transfer model for DSF system integrating PBR panels to examine received solar irradiation, bioenergy production, panels efficiency, and heat gain in both DSF cavity and building's occupied space.

The 1st objective of this research, as shown in Figure 1.10, explores a novel DSF system with integrated PBRs for energy production in cold climates by analyzing shading for solar irradiation and using a validated numerical model to study airflow's effect on panel temperature and performance. The model geometry of the DSF is defined, and heat transfer is analyzed using thermodynamic principles. The CFD model is set up in ANSYS with appropriate boundary conditions and fluid properties, followed by a parametric analysis using ANSYS-MATLAB coupling. This objective is addressed and elaborated on in Chapter 3 and has also been published in the following articles:

J1 **Elmalky, A. M.**, & Araji, M. T. (2022). Computational fluid dynamics using finite volume method: A numerical model for Double Skin Façades with renewable energy source in cold climates. *Journal of Building Engineering*, *60*, 105231 [15].

C1 **Elmalky, A. M.**, & Araji, M. T. (2022, November). Integral Model with Machine Learning for Balancing Heat Transfer and Energy Generation in Algal Bio-reactive Façades. In *uSim Conference 2022* (Vol. 3, pp. 1-10). IBPSA-Scotland [70].

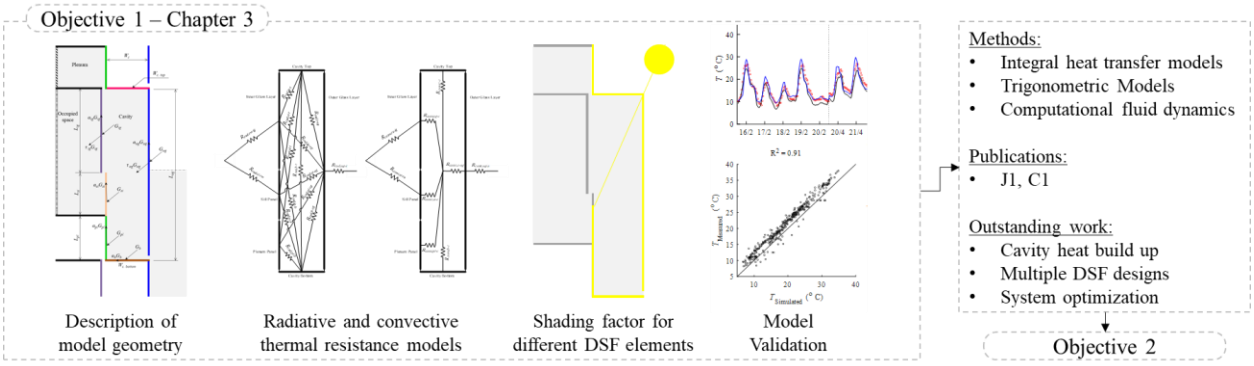


Figure 1.10. Key steps, methods, publications, and outstanding work for achieving the first objective.

Objective 2: Couple the developed heat transfer model with graphical optimization to maximize thermal and bioenergy generation for DSF system integrating PBR panels.

The 2nd objective of this research, as shown in Figure 1.11, applies the developed heat transfer model to a cellular DSF with PBRs at the floor plenum and a multistory DSF with PBRs alternating with the inner glass layer. A multi-objective problem is used to minimize heating/cooling loads while maximizing bioenergy. The optimized DSF is compared to unoptimized DSFs and single skin façades (SSFs) to assess feasibility in various climates. This objective is addressed and elaborated on in Chapter 4 and has also been published in the following articles:

J2 **Elmalky, A. M.**, & Araji, M. T. (2023). Multi-objective problem of optimizing heat transfer and energy production in algal bioreactive façades. *Energy*, *268*, 126650 [14].

C2 **Elmalky, A. M.**, & Araji, M. T. (2024, January). Pareto Optimization for Enhanced Building Energy Efficiency and Bioenergy Generation. In *2024 4th International Conference on Smart Grid and Renewable Energy (SGRE)* (pp. 1-6). IEEE [71].

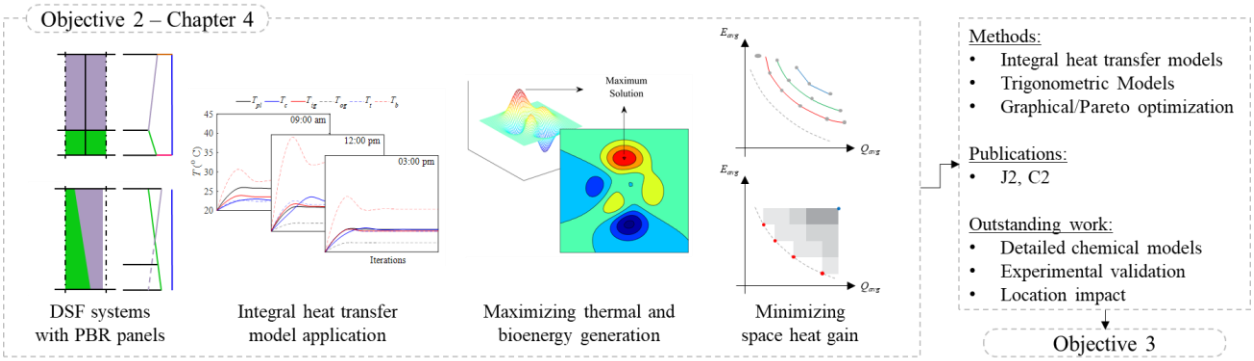


Figure 1.11. Key steps, methods, publications, and outstanding work for achieving the second objective.

Objective 3: Experimentally validate the performance of PBR panels in DSF and estimate the optimal operational/design parameters of PBR panels by using Hooke-Jeeves algorithm and Powell's Conjugate Direction Method.

The 3rd objective of this research, as shown in Figure 1.12, develops a chemical kinetics model for DSFs integrating PBRs. Two novel biomass monitoring techniques are introduced: an RGB image-based method and an ML image-based method. An experimental setup is built to monitor microalgae growth with RGB imaging, and the chemical model's accuracy was validated against collected experimental data. Optimization methods are evaluated for accuracy and efficiency. The computational time of original exhaustive methods is compared to that of methods incorporating neural networks. The optimized PBR integration is tested in various Canadian cities for climate impact assessment. This objective is addressed and elaborated on in Chapter 5 and has also been published in the following articles:

J3 **Elmalky, A. M.**, & Araji, M. T. (2024). Chemical Kinetics Model with Experimental Validation for Optimal Microalgae Generation in Double Skin Façades, *Energy* – Under Review [72].

J4 **Elmalky, A. M.**, & Araji, M. T. (2024). Efficient Conversion of Solar Energy to Algal Biomass in Buildings Using Neural Network-Aided Optimization, *Renewable Energy* – Under Review [73].

J5 **Elmalky, A. M.**, & Araji, M. T. (2024). Neural Networks for Monitoring Microalgae Biomass in Building Façades. *Technology | Architecture + Design*, *8*(1), 60–69 [74].

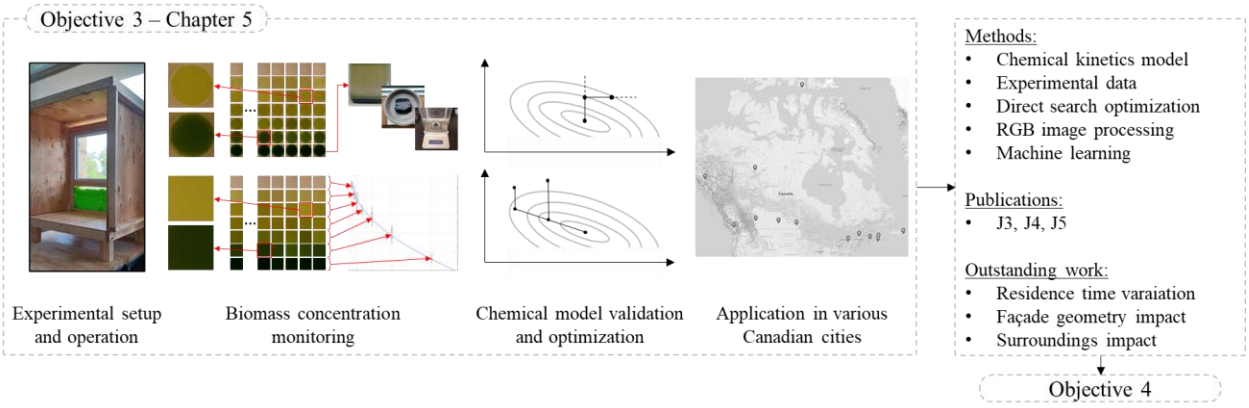


Figure 1.12. Key steps, methods, publications, and outstanding work for achieving the third objective.

Objective 4: Maximize bioenergy generation for a novel PBR panel with variable flow rate of fresh medium by using Genetic Algorithm.

The 4th objective of this research, as shown in Figure 1.13, examines a novel PBR with variable fresh medium flow using the developed chemical kinetics model. It evaluates the system's carbon footprint reduction for buildings with varying number of floors. In this objective, Trigonometric Models are developed and refined to study shading effects from surrounding buildings. This is required to examine the solar availability on buildings for optimizing PBR integration into different façade geometries. This objective is addressed and elaborated on in Chapter 6 and has also been published in the following articles:

J6 **Elmalky, A. M.**, & Araji, M. T. (2024). Optimization models for photosynthetic bioenergy generation in building façades. *Renewable Energy*, *228*, 120607 [75].

J7 **Elmalky, A. M.**, & Araji, M. T. (2023). A new trigonometric model for solar radiation and shading factor: Varying profiles of building façades and urban eccentricities. *Energy and Buildings*, *282*, 112803 [29].

J8 **Elmalky, A. M.**, & Araji, M. T. (2023). Computational procedure of solar irradiation: A new approach for high performance façades with experimental validation. *Energy and Buildings*, *298*, 113491 [76].

C3 **Elmalky, A. M.**, & Araji, M. T. (2023, April). A Novel Genetic Algorithm for Optimizing Microalgae Residence Time in Flat Panel Photobioreactors. In *2023 International Conference on Mechanical, Automotive and Mechatronics Engineering (ICMAME)* [77].

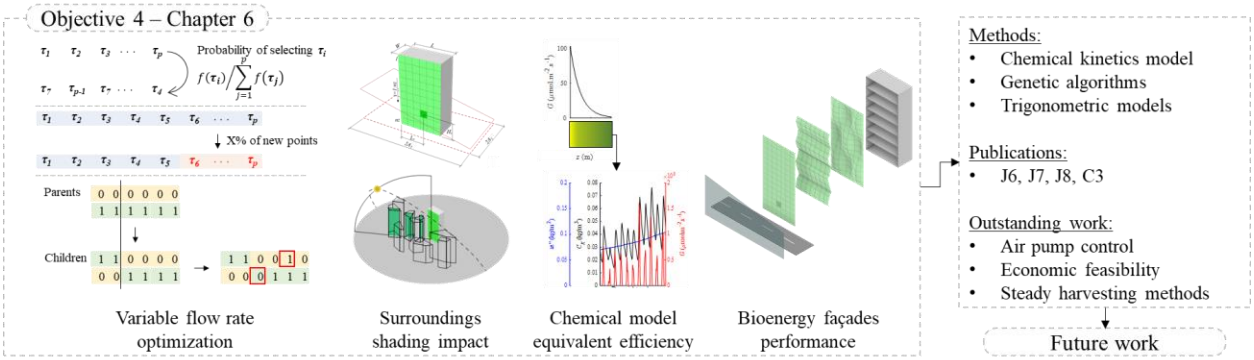


Figure 1.13. Key steps, methods, publications, and outstanding work for achieving the fourth objective.

The first objective yielded publications J1 and C1. J1 investigated a novel DSF system with integrated PBRs for energy production in cold climates by analyzing solar irradiation and using a validated numerical model to study airflow's impact on panel temperature and performance. C1 extended this work by assessing the DSFs' potential in preserving the thermal energy for PBRs in cold climates. The second objective led to publications J2 and C2. J2 applied the developed heat transfer model to a cellular DSF with PBRs at the floor plenum and a multistory DSF with PBRs alternating with the inner glass layer. C2 expanded on this by employing a multi-objective optimization problem to minimize heating and cooling loads while maximizing bioenergy production. The third objective produced publications J3, J4, and J5. J3 developed a chemical kinetics model for DSFs with PBRs, using RGB image-based biomass concentration monitoring. J4 optimized this model with neural network-aided techniques and compared their accuracy and efficiency to original methods. J5 extended the use of neural networks for monitoring microalgae biomass concentration in DSFs with PBRs. The fourth objective produced publications J6, J7, J8, and C3. J7 and J8 developed and refined TgM to study shading effects from surrounding buildings. J6 used the developed TgM coupled with GA to optimize PBR integration into various façade geometries. C3 applied the GA framework with a chemical model to examine a novel PBR with variable fresh medium flow.

1.5 Thesis Layout

In light of the previous research objectives, this dissertation is structured into seven chapters. The following section provides an overview of each chapter:

Chapter 1 introduces the concept of PBRs integrated into building envelopes and their potential benefits. It highlights the lack of research on PBRs in cold climates and DSFs. The chapter then outlines the motivation for the research, including the need to address challenges like heat transfer and shading in urban environments. Finally, it provides a brief overview of the research objectives and methodologies employed in each subsequent chapter.

Chapter 2 reviews the current research and applications of PBRs and DSFs, identifying knowledge gaps that inform design parameters, performance indicators, and challenges. It covers the design and performance of flat panel PBRs, their bioenergy generation, thermal behavior, shading impacts, and integration challenges. Additionally, it explores DSF design parameters, performance indicators, energy efficiency, and thermal behavior, with a focus on their application in cold climates and the associated challenges.

Chapter 3 achieves the 1st objective by developing a novel model of DSF systems integrating PBRs for cold climates. It evaluates heat transfer, solar irradiation, and energy production to enhance the system's energy performance. The study highlights ventilation strategies, shading impacts, and compares PBRs with PVs, demonstrating PBRs' superiority in thermal energy preservation and space heating efficiency.

Chapter 4 delves into the 2nd objective by optimizing the integration of PBRs into two DSF designs using graphical and multi-objective optimization techniques for minimizing heating and cooling loads while maximizing bioenergy generation. The analysis demonstrated significant improvements in thermal and bioenergy outputs, with the multistory DSF design showing superior performance. Results highlight optimal design parameters, energy savings, and climate adaptability, demonstrating the efficiency of PBRs integrated into DSFs for enhancing building performance.

Chapter 5 achieves the 3rd objective by developing a comprehensive chemical kinetics model for estimating biomass generation in building-integrated PBRs, incorporating factors such as light attenuation and day-night cycles. Novel biomass prediction techniques, including RGB image processing and neural networks, were developed and employed for model validation using

collected experimental data. Five optimization methods were assessed for maximizing microalgae production and enhancing computational efficiency. The developed optimization framework is applied to evaluate PBR performance across various Canadian cities. The chapter underscores the significant improvements in biomass generation and computational efficiency achieved through advanced monitoring and optimization strategies.

Chapter 6 delves into the 4th objective by exploring a dynamic PBR system with hourly variable residence times optimized using Genetic Algorithms (GA). This chapter also optimizes the integration of PBRs into different façade forms. TgMs are developed and refined to investigate the shading imposed by the surrounding buildings. The findings demonstrate that optimizing PBR residence times and façade geometries can significantly enhance biomass generation and energy efficiency in buildings.

Chapter 7 presents the dissertation conclusion. It provides a summary of the research findings and highlights publications in conferences and peer-reviewed journals that originated from this Ph.D. program. The chapter finally identifies potential directions for future research.

Chapter 2: Literature

This chapter presents the research and applications relevant to PBRs and DSFs to-date. The intent is to identify the knowledge gaps that would inform the research statement on design parameters, performance indicators, and expected challenges.

2.1 Microalgae Photobioreactors

PBRs are made of closed vessels for controlled biomass generation that use gas regulators to exchange Carbon Dioxide (CO_2) and Oxygen (O_2) with the surrounding environment. For this purpose, this system comprises a circulation pump with inlet and outlet pipes and a heat exchanger. The common two types of PBRs include tubular PBRs and flat panel PBRs [3]. The former utilizes designs that are compulsory for volatile compound production (e.g., biological hydrogen), or for microalgae strains that need to grow within a strict temperature range [78]. The latter is considered most practical for building envelope applications due to the higher surface area-to-volume ratio ($\approx$0.28 m^2/m^3) allowing for increased access to solar energy [79]. Therefore, flat PBR panels will be the scope of this study. Typical dimensions of flat PBRs are usually around 700 mm (width) × 2500 mm (height) × 80 mm (thickness) [9]. A peak thickness of 50 mm has been characterized by a higher growth rate of bioenergy equivalent to 1.67 times that of tubular reactors [78,80].

2.1.1 Design Parameters of Flat Panel PBRs

Flat panel PBRs have many design parameters that impact their general performance such as the panel thickness (light path), panel orientation, panel tilt angle, and inner structures.

2.1.1.1 Panel Thickness (Light Path) of PBRs

The thickness of flat PBR panels has a direct impact on the light intensity received by algal cells in the PBR, which in turn affect bioenergy production qualitatively and quantitatively [81]. For instance, shorter light paths expose each algal cell in the PBR to strong light for a long time. This reduces the production of unsaturated fatty acids, which are considered the healthiest type of fat [82]. On the other hand, longer light paths increase light attenuation and thus decrease both microalgae growth rate and subsequent bioenergy generation [22]. Therefore, more research should be carried out regarding this aspect to estimate the optimal PBR light path, especially for

PBR panels integrated into DSFs. Generally, the optimum light path was reported to be in the range of 0.2 to 0.4 m [20].

2.1.1.2 Orientation and Tilt Angle of PBRs

For average latitudes (≈45°N), south-oriented panels yielded 50% more bioenergy production than east/west-oriented panels [20]. For the same locations, light intercepted by vertical, horizontal, and 45° inclined PBR panels was around 1000 kWh/m^2, 1220 kWh/m^2, and 1440 kWh/m^2, respectively [1]. Therefore, the inclination angle of 45° lead to maximizing the yearly amount of light energy received by fixed PBR panels [22]. For adjustable PBR panels, vertical installation should be applied in winter to compensate for the lower solar altitude angle while horizontal installation should be applied in summer. Recent studies examined vertical installation only for PBR panels integrated into façades [1]. This was justified by the vertical inclination of almost all building façades, which was considered a major integration constraint that cannot be avoided. Nonetheless, inclined PBR panels can be integrated into buildings, especially for DSF systems.

2.1.1.3 PBRs Inner structures

Inner structures, defined as the separation baffles inside the PBR panel, can enhance the mixing conditions and thus improve the PBR performance [83,84]. Flat panel PBRs are generally divided into various types such as bubble PBR without inner components, split flat panel airlift PBR with one baffle, and central flat panel airlift PBR with two baffles [85]. The optimal design was the split airlift PBR followed by the central airlift PBR [85]. The enhanced mixing in airlift PBRs improved the overall efficiency by saving 16.3% of the operational energy in terms of lighting and pumping systems [86]. Nevertheless, such a percentage can be increased by considering other mixing variables related to air flow rates and the location of spargers.

2.1.2 Performance Indicators of PBRs

This section illustrates the investigation methods of flat panel PBRs. Besides, it highlights the key considerations regarding bioenergy generation, thermal behavior, and shading impact. The performance of PBRs was investigated by various methods such as simplified analytical models [15,19], detailed chemical models [1], Computational Fluid Dynamics (CFD) models [87], and experimentation [88]. Simplified models allowed for optimizing microalgae systems to maximize biomass production in buildings [15,19]. Chemical models facilitated the investigation of specific

parameters in standalone PBRs such as light attenuation, temperature sensitivity, and nutrient concentration. CFD models were useful in examining the flow rate and other mixing hydrodynamics in airlift PBRs [1,22]. Studies limited to simulation and theoretical approaches reinforced the basic understanding of the performance of PBRs in buildings. However, experimentation provided more reliable results that justified the relatively extra cost and time required by such methods.

2.1.2.1 Bioenergy Generation

Microalgae converts 9% of the received solar energy to biomass that is pyrolyzed to produce crude bio-oil [89]. Such a sustainable oil can replace liquid fossil fuels consumed in buildings. However, the relatively high preparation cost of this oil is a significant barrier to its mass production. Among numerous species of micro-algae, Chlorella Vulgaris and Dunaliella Tertiolecta were found to be more appropriate for building integrated PBRs [19]. Dunaliella Tertiolecta requires 160 W/m^2 of light intensity [90] and can be cultivated in hot media up to 43 °C [91]. Such species have a growth rate of 1.824 per day [92]. Chlorella Vulgaris requires 180-230 W/m^2 of light intensity [93], has a growth rate of 1.23 per day [94], and can be cultivated at a temperature up to 35 °C [94].

2.1.2.2 Thermal Behavior of PBRs

Thermal regulation of solar-illuminated PBRs is required to keep the microalgae medium within the optimal temperature range of 25 °C to 30 °C [95]. Water overheating was reported to be a major threat to PBRs in hot regions [96]. Specifically, about 90% of the incident solar energy is transformed to heat inside the cultivation medium [1]. This was resolved by applying heat-reflecting surfaces in PBRs to reduce the use of cooling water for thermal regulation [97]. In cold climates, DSFs can mitigate the negative impact of ambient temperatures and environmental deposition on PBRs by placing the panels behind the outermost layer of the façade [15].

2.1.2.3 Impact of Shading on PBRs

The inclusion of PBRs in DSF would require shading analysis, which is a critical indicator of solar energy performance. To overcome shading in PBR panels, mechanical stirring or mixing minimizes dark zones and generates homogeneous light distribution, thus leading to cells receiving different intensities in cycles [98]. For building purposes, the use of PBRs as translucent screening elements was additionally capable of regulating natural light and coping with reduced visibility

[99]. Low light intensity levels that can result from either obstacles' shadows, high cultivation depths, or cloud covers proved to reduce biomass production from 34.57 to 15.17 gm/m^2·day [100,101].

2.1.3 PBRs Challenges

Numerous technologies have been developed to enhance biomass production and energy output from microalgae cultivation [102]. However, the shift towards building integrated PBRs is ongoing and yet to be established due to the various challenges facing such systems. Optimizing these PBRs will require special consideration for the light regime, cultivation medium, and applied materials [103]. Another challenge facing PBRs is the extra energy demand imposed by spinning spargers, artificial light, liquid pumps, and gas compressors [104]. Currently, the cost of algal biofuel outweighs the remaining fossil fuels. It is thus quite challenging to encourage new buildings to utilize PBRs for fuel production. However, savings in greywater treatments and associated carbon biofixation can promote the overall feasibility of these systems.

2.2 Double Skin Façades

This section gives an overview of the associated design parameters of DSF in cold climates, including: the cavity depth, cavity height, ventilation schemes, and the properties of the inner and outer skins. The section highlights the most dominant performance aspects of DSFs such as methods of investigation, energy efficiency, and thermal behavior. Finally, the section summarizes the possible challenges facing the application of DSFs in cold climates.

2.2.1 Design Parameters of DSFs

DSFs have many parameters that impact their general performance. Such parameters are dependent on either cavity features such as depth, height, and ventilation scheme, or properties of the inner and outer skins.

2.2.1.1 Cavity Depth

Narrow cavities boost the stack effect and enhance the airflow that works on extracting the warmer air from the occupied space. Cavities larger than 1 m in width suppress the stack effect increasing heat gain to the occupied space [105,106]. Improper cavity design can lead to a higher temperature in the occupied space and thus reduce thermal comfort [107]. Cavity design purposes can be

hosting only shading devices or allowing more space for cleaning and maintenance. The cavity depth can either be as small as 10 cm or be extended to more than 2 m. Narrow cavities are used for shading device installation, middle-depth cavities are used for PVs/PBRs integration, and wide cavities are used for occupancy purposes. Cavities should be kept between 0.7 and 1.2 m to achieve the balance between heat gain and air extraction [108]. More attention should be given to the cavity width for DSFs integrating PVs/PBRs as shading becomes a crucial factor affecting energy generation in wide cavities.

2.2.1.2 Cavity Height

The cavity height is a vital factor that impacts the stack effect in DSFs [109]. Shaft-box and multi-story DSF systems surpass corridor-type and box-window DSF systems in naturally ventilated buildings [110]. The air velocity inside the cavity is directly proportional to the cavity height [111]. However, more attention should be given to the location of ventilation openings which can affect the air velocity as much as the height. The cavity height can either be in the range of 3 to 4 m for box-window and corridor types of DSFs, or be higher than 28 m in shaft-box and multistory types of DSFs.

2.2.1.3 Ventilation Schemes

DSFs are ventilated naturally or mechanically. In the mechanical ventilation scheme, the air is driven inside the cavity by electric fans. The natural ventilation scheme doesn't require any powered force and only relies on louvers, vents, and dampers. However, it offers a relatively weak thermal buffer compared to the mechanical ventilation mode, which has a higher impact on the thermal performance of DSFs [112]. Designing the ventilation openings should always avoid sharp edges of the openings to decrease the pressure drop and thus reduce the power consumption of the fans [113]. The openings width should be selected properly as it has a significant impact on the mean velocity of the airflow in the cavity. The optimum width giving the highest ACH was 23 cm in naturally ventilated box-window DSFs [114].

2.2.1.4 Inner Skin Properties

The performance of DSF systems is strongly dependent on the material selection of the DSF layers. Materials with higher thermal mass are often assigned to inner layers [110]. For inner layers combining glazed panels and concrete, the irradiation incident on the glazing panels leads to higher

temperatures [108,115]. Materials with lower thermal mass (glazed panels) in the inner layer contributed to decreasing the cooling load of the building [116]. Also, solar heat gain was decreased to one-half by substituting the inner glass layer with low e-glass. Alternatively, decreasing the transmissivity of the installed glass to 55% lead to comparable results [117]. Double-glazed panels applied to inner skins decreased thermal loads in air-conditioned buildings [118]. However, the same impact was achieved by installing such panels on the outer layer [68]. Therefore, more research should be performed to determine the most efficient location of double-glazed panels when integrated into DSFs.

2.2.1.5 Outer Skin Properties

Unlike inner skins, which add other materials to glass such as concrete, outer skins are normally fully glazed [112]. Single-glazed panels with higher transmittance were recommended for outer layers [110]. These panels increased the heat gain and enhanced the stack effect by elevating the cavity temperature. In conclusion, the optimal combination of glazing units is still being investigated to balance heat gain and stack effect, especially for naturally ventilated buildings.

2.2.2 Performance Indicators of DSFs

This section introduces a summary of the investigation methods used to analyze the performance of DSF systems. It also highlights the research areas of interest such as energy efficiency, and thermal behavior. Thermal and energy performance of DSF systems were examined using several methods such as finite volume approach [6,9], self-developed CFD codes [119], and integral models aided by Ansys [120], Simcenter STAR-CCM+ [121,122], DesignBuilder [123], TRNSYS [5], or OpenFOAM [124]. Although the analytical models provided limited insight into the detailed flow behavior [124], they required less time and relied on moderate computational tools [121]. Experimentally, wind peak pressure was investigated in porous DSFs when acting on the inner layer [125]. Other literature analyzed the performance of DSFs through empirical and validation procedures [5,124].

2.2.2.1 Energy Efficiency of DSFs

The application of DSFs offers a relatively strong thermal buffer which enhances the U-value compared to standard glazing units. Theoretically, DSFs have an overall U-Value of 1.8 $W/m^2 \cdot K$ [126]. For SSFs, the baseline U-values are 3 $W/m^2 \cdot K$, and 1.2 $W/m^2 \cdot K$ for double-glazing, and

triple-glazing units, respectively [127]. For cold climates applications, the inclusion of PBRs can promote the energy efficiency of DSFs due to the additional heat build-up caused by the panels. In warm periods, more research should be conducted to mitigate this heat build-up by proper selection of DSF typologies and ventilation schemes.

2.2.2.2 Thermal Behavior of DSFs

DSF systems reduce heating demand in cold climates by trapping the air inside the cavity, which acts as thermal insulation that preserves the building heat [15]. Proper employment of the cavity airflow can reduce cooling requirements by expelling solar heat gain and interior heat load from the building. However, it was concluded that DSFs increased the cooling load during summer in temperate climates [7]. The functionality of DSF systems decreased because of higher solar irradiation and warm temperatures throughout the year in average climatic regions [117]. However, this can be improved by utilizing glass panes and shading devices in addition to opening principles and airflow modes.

2.2.3 DSFs Challenges

One of the major challenges facing DSFs is the cavity heat accumulation in summer leading to higher cooling demands [7]. Other challenges include uncertainties related to the selection of geometric features, glazing types, shading systems, and ventilation schemes [128]. Compared to conventional façades, DSFs have higher investment value in terms of initial and operational costs [8]. DSFs also have limitations related to acoustics, moisture, and fire safety [8]. Furthermore, the use of DSFs is less experimented and investigated in cold climates where additional analysis is required. Recent applications of DSF systems considered the integration of various technologies such as regular and concentrating photovoltaics (PVs) [129], phase change material [119], and TiO_2 plates [130]. However, the challenges associated with integrating PBRs into DSFs are still unknown. Additionally, challenges arise from shading caused by the surrounding environment, especially in dense urban areas. Efficient shading prediction methods would help in assessing the solar irradiation received by building façades and optimizing solar energy utilization in urban areas.

2.3 Shading Prediction Techniques

Solar availability has been assessed using different techniques such as the PgC technique, PxC technique, and TgM. The most common methods for estimating solar irradiation on exterior surfaces in BES (Building Energy Simulation) tools are TgM and PgC techniques [131]. TgM was developed to calculate the shadow patterns on building façades by considering the geometric relationship between the sun, objects, and examined points [132]. Although the model is flexible and can handle various geometries [133], it may involve simplified assumptions that can reduce the accuracy of the results [132]. TgM is also limited to a few simple shading geometries such as overhangs and fins [134]. These limitations were addressed by the PgC technique which offers high accuracy for complex geometries and supports various polygon types [135]. However, when applied to certain geometries with multiple overlaps, it requires considerable computational power [136,137]. PgC relies on dividing the shading elements into projected polygons and analyzing their intersection with the examined surface [131]. However, it has limitations when applied to hollowed surfaces and shading elements with many overlaps, requiring significant processing resources [136,137]. Integrating the Sutherland-Hodgman method into PgC techniques improved accuracy for concave surfaces, but hollowed surfaces were still unsupported [136].

Many attempts were made to enhance the reliability of the PgC technique such as the incorporation of external shading reduction coefficients and the development of advanced algorithms to handle polygon intersections [134,137]. Other attempts recommended using the PxC technique for shading calculations by generating solar orthogonal projections on the examined surface, counting the visible pixels, and analyzing the distribution of the sun patches [138]. The PxC technique provides accurate results for non-convex zones, hollowed or concave surfaces, and non-rectangular rooms with multiple openings [131]. Average error associated with PxC techniques for building applications was 1% [139]. However, associated pixelation can impact the results' accuracy [140]. TgM addressed these limitations, offering comparable accuracy while reducing computational burden by more than 40% [29]. the PxC technique may also require a hardware-accelerated graphics card for efficient computation [140]. Despite these limitations, PxC is a user-friendly approach that offers high precision and can be integrated into simulation packages for shading calculations [131]. Table 2.1 provides a summary of various studies applying these techniques for shading prediction.

GIS tools and LiDAR technology have been emerging as accurate 3D modelers that can capture complex urban features for real-time analysis of shadow patterns. GIS tools rely on geographic data to create 3D urban models and simulate the shadow patterns at different times through tools like gvSIG [30], ArcGIS Solar Analyst [141,142], and CityGML [143]. Advantages of using GIS tools include accurate modeling in 3D urban environments, real-time analysis of shadow patterns, and visual representation that facilitates result interpretation [141]. However, the complexity of these tools requires a high level of technical expertise and significant computational resources [143]. ArcGIS alongside GPU machines and C++ language revealed a notable technical limitation in dealing with larger urban areas, leading to a 24-hour computing time [144]. Data availability may also restrict the reliability of GIS tools [143]. LiDAR technology involves capturing detailed 3D data of the environment using LiDAR sensors before creating digital surface models [145]. Such models provide high-resolution data that enables precise mapping of buildings, trees, and terrain [146]. However, LiDAR technology required specialized equipment, expertise, and considerable computing capacity [146]. Applying LiDAR technology, image processing, and cloud computing reduced the simulation time from 40 hours to 16 hours [28]. Data availability and integrability can pose additional challenges in certain regions [147]. TgM addressed these limitations by considering the geometric relationship between the sun, objects, and examined points, thus reducing the reliance on resource-intensive techniques while maintaining accuracy [29]. Although TgM is more computationally efficient, its current capabilities are limited to handling basic geometries [29]. This highlights the need for further enhancements to make it applicable to a wider range of scenarios.

Table 2.1. Summary of different studies on applied techniques for shading prediction.

Applied Technique	Employed Tool	Shadow Source	Examined Elements	Approach	Location	Building Typology	Simulation Time	Error	Study	Advantages	Disadvantages
Geographic Information Systems	gvSIG	Real buildings	Façades	Simulation	Spain	Residential	24 minutes	–	[30]	1. Accurate modeling in 3D urban environments. 2. Real-time analysis showing shadow patterns at different times. 3. Visual representation facilitating the interpretation of results.	1. Complexity imposed by requiring a high level of technical expertise. 2. Data availability can limit the reliability of the tool. 3. Significant computational requirements.
	ArcGIS Solar Analyst	Real buildings	Façades, roofs, and ground	Simulation	Switzerland	Mixed	24 hours	< 5 %	[144]		
	CityGML	Real buildings	Façades, roofs, and ground	Simulation	USA and Germany	Mixed	42 minutes	< 1 %	[143]		
LiDAR Technology	Self-developed codes	Real buildings	Façades, roofs, and ground	Simulation	Switzerland	Mixed	16 hours	7 %	[28]	1. Non-intrusive data collection technique. 2. Accurate and detailed 3D mapping of the urban form. 3. Ability to capture complex urban features, such as buildings, trees, and terrain.	1. Costly equipment and limited availability of LiDAR data in some regions. 2. Weather conditions can affect data collection. 3. Challenges in data integration with other geospatial datasets.
	LiDAR360 software	Real buildings and trees	Streets	Simulation	China	Mixed	> 4 hours	–	[146]		
	Self-developed codes	Real buildings	Roofs	Simulation & Experimental	Australia	Mixed	–	3.9 %	[147]		
Pixel Counting	OpenGL in Domus	Modeled buildings and trees	Façades	Simulation & Experimental	Brazil	Mixed	48 minutes	1.3 %	[131]	1. User-friendly implementation with minimal technical expertise. 2. Accurate modeling for non-convex zones. 3. High precision for non-rectangular rooms with multiple openings.	1. Lower-resolution images can impact the results accuracy. 2. Higher computational costs by requiring an accelerated graphics card. 3. Limited application in simulation packages.
	Shading II in SketchUp	Shading overhangs	Façades and interior space	Simulation & Experimental	France	Office	–	8 %	[138]		
	Shading II in SketchUp	Modeled buildings and trees	Façades	Simulation & Experimental	Brazil	Mixed	2.9 hours	4.5 %	[131]		
Polygon Clipping	DOE-2	Modeled blinds, and overrides	Façades	Simulation	United Kingdom	Office	–	–	[148]	1. High accuracy for complex geometries. 2. Widely integrated into building simulation software packages. 3. Ability to support various polygon types.	1. Lower accuracy when applied to hollowed surfaces. 2. Shading elements with many overlaps require significant processing resources. 3. Limited to interior angles of less than 180 degrees.
	EnergyPlus	Modeled buildings and trees	Façades	Simulation & Experimental	Brazil	Mixed	9.4 hours	9.2 %	[131]		
	TRNSYS	Modeled overhangs	Façades	Simulation	Morocco	Residential	–	–	[149]		
Trigonometric Models	Self-developed codes	Two modeled buildings	Façades	Simulation	Germany	Office	–	–	[132]	1. Accurate calculations of shadow patterns. 2. High flexibility by handling various geometries. 3. Modest computational costs and quick analysis.	1. Simplified assumptions can reduce the results accuracy. 2. Complexity imposed by requiring advanced mathematical calculations and programming skills. 3. Limited integration with simulation packages.
	Self-developed codes	Circular form of buildings	Single Point	Simulation	India	Mixed	–	–	[133]		
	Self-developed codes	Rectangular and circular buildings	Façades	Simulation	Canada	Mixed	6.1 minutes	5.2 %	[29]		

Chapter 3: Heat Transfer Modeling for DSF Systems Integrating PBR Panels[1]

This chapter fulfills the first objective of this thesis by examining a novel model of DSF systems integrated with PBRs. This addresses the limitation of previous studies by investigated building-integrated PBRs in cold climates. Hourly heat transfer analysis is conducted to evaluate the energy production, efficiency of PV and PBR modules, and the heat gain in the DSF cavity and occupied spaces. Shading analysis is performed to assess the solar irradiation received by the modules. A numerical model is developed incorporating these modules with various ventilation schemes to examine the impact of airflow on the panels' temperature and associated performance.

3.1 Introduction

Novel façade technologies have been undergoing continuous evolution for advanced building performance [5,150]. Among the notable systems, DSF systems are often considered the most critical in creating a steady buffer between outdoor and indoor environments [120,151]. The core functionality of DSF depends on the active use of its cavity that acts as an insulator for varying ambient conditions. Optimizing the entire system leads to balanced energy use and thermal behavior that can apply to various climate zones [123,125]. However, the analysis requires the proper selection of façade geometry along with suitable utilization of glass panes and shading devices in addition to opening principles and airflow modes [6,10].

Available methods for heat transfer and computational fluid dynamics (CFD) analysis in DSF vary from simulation and optimization tools [122] to experimental studies with data validation

[1]This chapter is based on the following articles:

Elmalky, A. M., & Araji, M. T. (2022). Computational fluid dynamics using finite volume method: A numerical model for Double Skin Façades with renewable energy source in cold climates. *Journal of Building Engineering*, *60*, 105231 [15].

Elmalky, A. M., & Araji, M. T. (2022, November). Integral Model with Machine Learning for Balancing Heat Transfer and Energy Generation in Algal Bio-reactive Façades. In *uSim Conference 2022* (Vol. 3, pp. 1-10). IBPSA-Scotland [70].

techniques [124] and other numerical models with finite control volume approach [6,152]. Using OpenFOAM computational toolbox, Dama et al. [124] presented a model based on a pressure loop and an integral approach to the heat transfer along the façade cavity. Both, the airflow rate and the heat removed calculated by the model had a mean error of -22% and 26% respectively. However, the previous model was limited to naturally ventilated DSFs without considering the impact of mechanical ventilation on the cavity airflow. In terms of energy assessment, the performance of DSFs was reported to be inconclusive due to uncertainties in geometric attributes and material selection, shading and ventilation strategies, wind loads, and fluctuating operational overhead [57,153]. DSF applications showed flexibility to allow the integration of different smart technologies, including Titanium dioxide (TiO_2) plates, phase change material, and compatible solar energy modules. TiO_2 plates use the photocatalytic oxidation technique under natural sunlight to decompose Benzene, Toluene, Ethylbenzene, and O-xylenes (BTEX) in the air [130].

Despite the utility of the preceding systems, the use of solar energy modules in DSF introduces power production and adaptive shading in addition to accompanying environmental advantages that involve CO_2 bio-fixation, O_2 production, utilization of a building's wastewater, and land resource preservation for alternative harvesting, as applied with PBRs [35,154]. PBRs integrated into buildings have many merits, such as biomass production, O_2 generation, CO_2 sequestration, and wastewater treatment [79]. Annually, flat panel PBRs generated 22.7 kWh/m^2 of methane and 30 kWh/m^2 of heat when added to building façades [2]. Other attempts of PBRs inclusion in buildings achieved a biomass production of 2.3 kg/m^2·year and CO_2 bio-fixation of 31.7 kg/m^2·year [13]. Nevertheless, previous attempts didn't investigate the performance of PBRs in extremely cold regions. The relatively low temperature in such climates led to very low growth rates of microalgae [155]. All attempts to integrate PBRs in buildings considered only SSFs [2,13]. However, DSFs offered the flexibility to host energy-efficient technologies [156], in addition to adjusting heat transfer through building envelopes [157,158].

In light of the above, this chapter examines a new model of DSF systems with integrated PBRs. In cold climates, such systems can provide a solution to low ambient temperatures and snow deposition for façade-integrated energy production. Hourly heat transfer analysis is performed to assess PV and PBR modules to compare their energy production, panels efficiency, and heat gain

in the DSF cavity and occupied space. For this purpose, shading analysis is carried out to evaluate the solar irradiation received by the modules. A numerical model is developed in the presence of these modules with various ventilation schemes to examine the airflow impact on the panels' temperature and associated performance.

3.2 Method

In this chapter, the model geometry was described in detail by defining the dimensions and material properties of the DSF. The rate of heat transfer through the DSF was then analyzed to understand thermal performance by utilizing principles of thermodynamics and heat transfer. The setup of the CFD model was conducted by involving the selection of appropriate boundary conditions, meshing of the model, and specification of fluid properties within ANSYS. A parametric analysis was then performed using ANSYS-MATLAB coupling. Finally, a solar irradiation and energy generation model was integrated to account for the effects of solar energy on the DSF by incorporating calculations for solar angles, incident irradiation, and potential energy gains.

3.2.1 Description of model geometry

For the examined climate zone, the DSF system was designed to comprise an inner layer of single-glazed 6 mm generic clear glass pane (with 77.1 % transmittance, 5.818 W/m^2·K U-value, and 0.818 SHGC) and an outer layer of a double-glazed insulating unit of two 6 mm generic clear glass separated by 12 mm air-gap (with 60.69 % transmittance, 2.552 W/m^2·K U-value, and 0.705 SHGC). Using the double-glazed insulating unit on the outer layer would better isolate the cavity air and prevent heat loss from the PVs/PBRs to the ambient environment. PVs/PBRs have been placed alongside the inner layer to avoid harsh environmental interactions, thus achieving optimum performance. The outermost layer further incorporated a floor-to-ceiling mullionless butt-joint glazing assembly, which allowed for uniform shading on these panels. Figure 3.1 shows the DSF system where an office space has been sought as a building typology with a south-facing orientation on a typical building floor. The floor-to-floor height has been identified as 4 m to observe the recent practice for the highest flexibility of program space in mixed-use buildings. To make the best utilization of the integrated PVs/PBRs, its upper part was brought in contact with the occupied space to counter the heat loss to the cold environment. Both the plenum panel height (L_{pl}) and the sill panel height (L_{si}) were considered 1 m. The inner glass height (L_{ig}) was set at 2

m. The cavity width (W_c) has been investigated to vary between 0.6 m and 2.4 m in different cases to analyze the impact of the ventilation scheme, cavity width, and ambient temperature. The cavity width was evaluated with values around 0.6 meters to reflect common practices found in the literature and extended up to 2.4 meters to ensure the cavity provided usable space and remained accessible to building occupants.

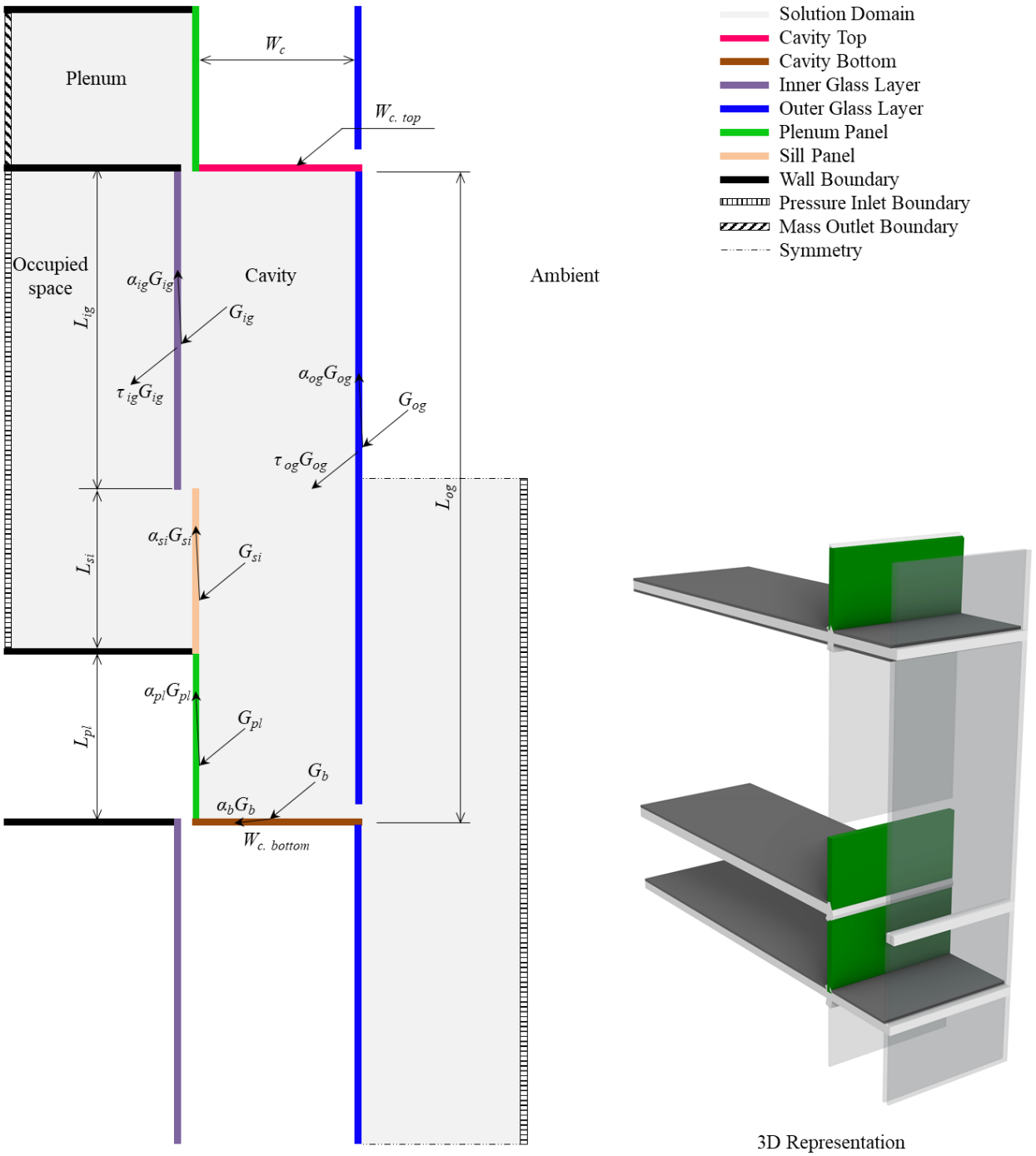


Figure 3.1. DSF system with the relevant optical model and the solution domain for internal ventilation cases and mixed ventilation cases.

Figure 3.1 also shows the fluid solution domain and vents locations planned for the airflow. The system was designed to exhaust air from the occupied space in addition to the ambient into the cavity and then to the plenum. The internal air vent was located between the inner glass layer and

the sill panel for the practicality of façade assembly and to give the air stream from the occupied space the chance to travel through most of the cavity. The external air vent was located at the bottom of the outer glass layer to allow the ambient air stream to interact with the whole cavity components. The exhaust air vent was located at the top between the inner glass layer and the plenum panel to act as a sink for both streams from the occupied space and the ambient. Although this configuration will produce a dead airspace at the cavity top, it will allow the ambient air stream to interact with the PVs/PBRs and the inner glass layer. An exhaust fan with a proper airflow rate of 0.21 $kg/m^2 \cdot s$ was installed in the plenum to create negative pressure that will withdraw warm air from the occupied space, generate inhabitable airspeed in the cavity, and avoid noise in the air vents. Accordingly, internal ventilation and mixed-mode ventilation schemes were examined. In the case of the former scheme, fresh air was admitted through the mechanical HVAC system.

3.2.2 Heat transfer model definitions, assumptions, and constraints

Actual heat flow characteristics in DSFs are quite complicated. For simplifying the analysis, the employed assumptions are shown in Table 3.1.

Table 3.1. Model definitions, assumptions, and constraints.

Model	Equation(s)	Definitions (□), Assumptions (-), and Constraints (○)	Reference(s)
View factor	Eq (3.1) to Eq (3.4)	▫ F is the radiation view factor ▫ a and b are the lengths of the two parallel plates ▫ c is the distance between the two parallel plates - DSF elements have uniform radiosity ○ $0 < F < 1$	[159]
Energy balance equations	Eq (3.5) to Eq (3.11)	▫ α is the absorptivity ▫ G is the incident solar irradiation, W/m^2 ▫ E is the energy generated from the associated PVs/PBRs, W/m^2 ▫ q_{rad} is the heat transfer by radiation, W/m^2 ▫ q_{conv} is the heat transfer by convection, W/m^2 - No internal heat source was considered inside the DSF - Steady-state energy flow was considered for all elements - The optical and thermal properties of DSF materials were kept constant - End effects were assumed negligible - Heat transfer through joints between adjacent elements was neglected. This was justified by the small area of edges compared to the total area of the DSF elements - Heat transfer in the axial direction of the DSF was neglected. This is reasonable for most cases where the total building width is sufficiently higher than each floor height - Thermal stratification in the cavity was neglected and inside air was well-mixed with a uniform temperature. This can be justified by the small temperature difference in the cavity (≈ 2 °C)	[160–164]

		- The model was a zero-dimensional model that treated each surface within the system as a point. It neglected variations in surface temperatures along each element - Interior of the building and the surrounding ambient environment maintained a consistent condition, characterized by a uniform temperature throughout each. Therefore, convective and radiative thermal resistance diagrams were modeled with a single point of origin and termination ○ $0 < \alpha < 1$	
Blackbody radiation	Eq (3.12) and Eq (3.13)	▫ E is the emissive power or the rate at which radiation is emitted from a surface, W/m^2 ▫ T_s is the absolute temperature of the surface, K ▫ σ is the Stefan–Boltzmann constant ▫ ε is the surface emissivity - A blackbody absorbs all incident radiation, regardless of wavelength and direction. - For a prescribed temperature and wavelength, no surface can emit more energy than a blackbody. ○ $0 < \varepsilon < 1$ ○ $\sigma = 5.67 \times 10^{-8}\ W/m^2 \cdot K^4$	[159]
Radiative heat transfer	Eq (3.14) to Eq (3.26)	▫ G is the rate at which radiation is incident upon a surface, W/m^2 ▫ J is the rate at which radiation leaves a surface, W/m^2 ▫ q is the net rate of radiation leaving a surface, W/m^2 ▫ α is the surface absorptivity ▫ ρ is the surface reflectivity ▫ ε is the surface emissivity ▫ A is the surface area, m^2 - The optical and thermal properties of DSF materials were kept constant - All surfaces were assumed to be grey bodies with diffuse reflection and emission properties ○ $J = E + \rho G$ ○ $0 < \rho < 1$ ○ $\alpha = 1 - \rho$ ○ $\rho = 1 - \alpha = 1 - \varepsilon$	[161]
Convective heat transfer	Eq (3.27) to Eq (3.35)	▫ T is the temperature, K ▫ h is the heat transfer coefficient, $W/m^2 \cdot K$ ▫ A is the surface area, m^2 ▫ Nu_H is the Nusselt number based on the surface height ▫ H is the surface height, m ▫ k is the fluid thermal conductivity, $W/m \cdot K$ ▫ Ra_H is the Rayleigh number based on the surface height ▫ Pr is the Prandtl number ▫ g is the gravitational acceleration constant, m/s^2 ▫ β is the fluid thermal expansion coefficient, K^{-1} ▫ ν is the fluid kinematic viscosity, m^2/s ▫ L is the characteristic length, m ▫ V is the fluid speed, m/s - Fluid velocity at the wall is zero - Transition occurs at a critical Reynolds number - The airflow has negligible viscous dissipation and body forces - Air is an incompressible fluid with constant properties	[159]

		- Two-dimensional flow ○ g = 9.81 m/s^2 ○ Pr = 0.71	
2D SST k-ω turbulence model	Eq (3.36) to Eq (3.37)	▫ k is the kinetic energy of turbulence ▫ ω is the specific dissipation rate ▫ Y is the generation and dissipation rates of ω ▫ Γ is the effective diffusivity factor ▫ S is the source term - CFD simulations was performed by taking air properties as constants or considering their variation with temperature. All fluid properties were taken as constant values except for density in the buoyancy term - Radiation and conjugate heat transfer between different surfaces have been substituted by constant values of surface temperature ○ W_c: 0.6 m/2.4 m ○ Renewable source: PVs/PBRs ○ Ambient temperature: -25 ºC/25 ºC	[165,166]
Solar irradiation model	Eq (3.38) to Eq (3.40)	▫ I_b is the direct normal irradiation, W/m^2 ▫ θ_v is the solar incidence angle on vertical surfaces, rad ▫ θ_h is the solar incidence angle on horizontal surfaces, rad ▫ W_c is the DSF cavity width, m ▫ L_{og} is the outer glass layer height, m ▫ τ_{og} is the outer glass layer transmissivity ▫ G_x is the solar irradiation incident on the DSF elements, W/m^2 ▫ L_x is the length of the associated element, m ▫ SF_x is the shading factor of the associated element - A uniformly distributed heat flux was considered over the partially irradiated elements ○ L_{og} = 4 m ○ L_{ig} = 2 m ○ L_{si} = 1 m ○ L_{pl} = 1 m ○ β = 90º ○ 0.6 m < W_c < 2.4 m ○ 0 < SF_x < 1	[159]
Energy generation	Eq (3.41)	▫ η_{si} is the sill panel efficiency ▫ η_{pl} is the plenum panel efficiency - Energy generated by PVs/PBRs was directly dependent on the received irradiation by a conversion efficiency ○ η_{PBR} = 9%	[19,167]
Efficiency variation	Eq (3.42)	▫ η is the PV panel's efficiency ▫ T is the panel's temperature - The PV panel has a uniform temperature ○ 16.6% < η < 22.2% ○ 0 ºC < T < 70 ºC	[167]

3.2.3 Rate of heat transfer through the DSF

The radiative thermal resistance model is shown in Figure 3.2. Heat is transferred by radiation from the outer glass layer to the sky at a rate of $q_{rad,og\text{-}s}$. On the occupied space side, the sill panel loses heat by radiation at a rate of $q_{rad,si\text{-}rw}$ to the walls, which in turn loses heat by radiation to the inner glass layer at a rate of $q_{rad,rw\text{-}ig}$. Within the DSF, the cavity is enclosed by six elements; the inner glass layer, the outer glass layer, the sill panel, the plenum panel, the cavity top, and the cavity bottom. Heat is transferred by radiation between any two of the preceding elements as long as they share a view factor.

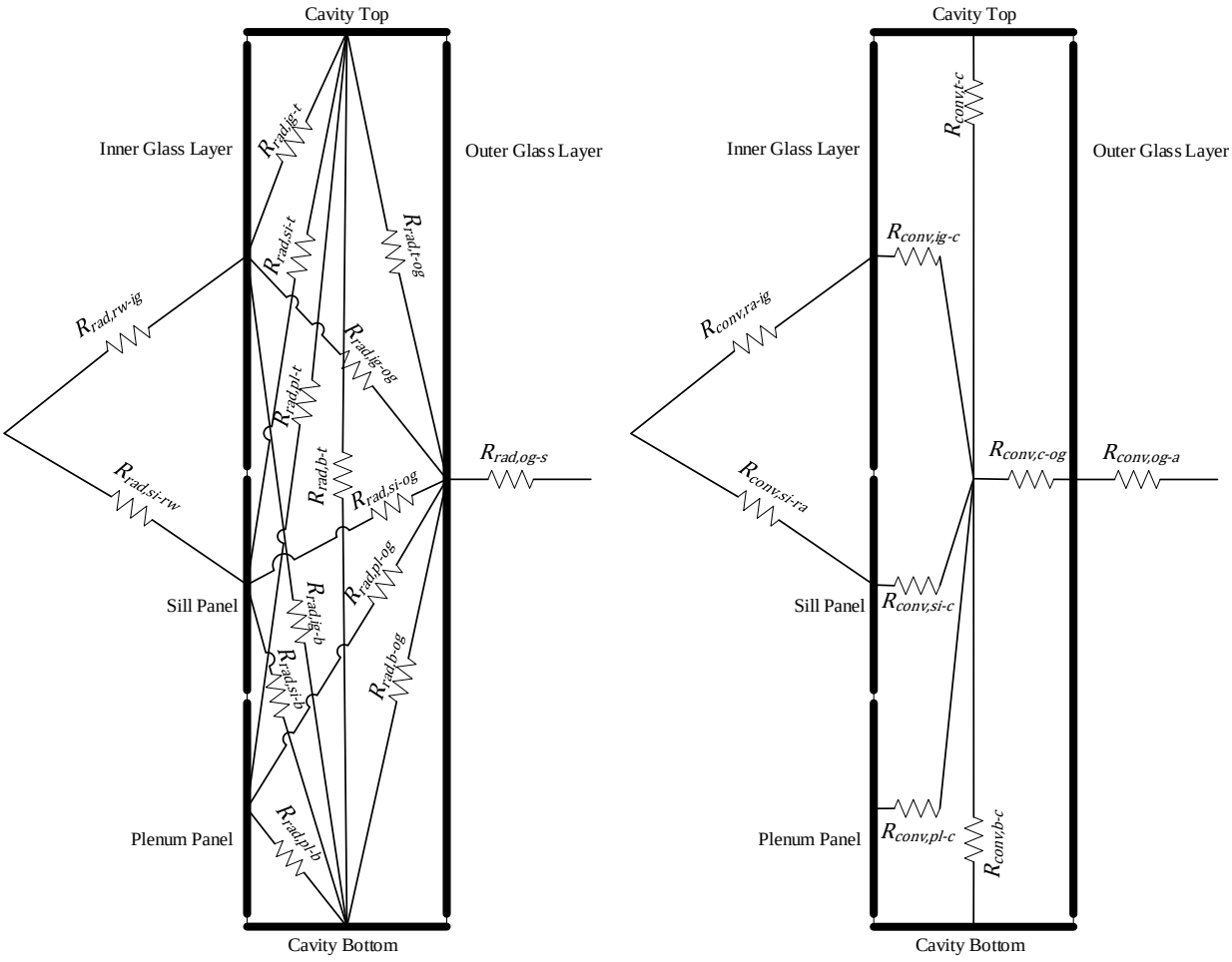


Figure 3.2. DSF elements' radiative thermal resistance model (left) and convective thermal resistance model (right).

The view factors between two parallel plates sharing a midline, Eq. (1), or two perpendicular plates sharing a common edge, Eq. (2), can be calculated as [159]:

$$F = \frac{\sqrt{(a/c + b/c)^2 + 4} - \sqrt{(a/c - b/c)^2 + 4}}{2a/c} \tag{3.1}$$

$$F = \frac{1 + b/a - \sqrt{1 + (b/a)^2}}{2} \tag{3.2}$$

where F is the radiation view factor. a and b are the lengths of the two parallel plates. c is the distance between the two parallel plates.

Using Eq. (3.1) and Eq. (3.2), a more general view factor between any two parallel or perpendicular elements applicable to the cavity in the DSF can be calculated as (Figure 3.3):

$$F_{AB} = \frac{L}{4a}\left(\sqrt{\left(\frac{a}{L} + \frac{d}{L}\right)^2 + 4} - \sqrt{\left(\frac{a}{L} - \frac{d}{L}\right)^2 + 4} - \sqrt{\left(\frac{a}{L} + \frac{c}{L}\right)^2 + 4} + \sqrt{\left(\frac{a}{L} - \frac{c}{L}\right)^2 + 4}\right) \tag{3.3}$$

$$F_{AD} = \frac{c}{2a}\left[\sqrt{1 + \left(\frac{a+b}{c}\right)^2} - \sqrt{1 + \left(\frac{b}{c}\right)^2}\right] - \frac{c+d}{2a}\left[\sqrt{1 + \left(\frac{a+b}{c+d}\right)^2} - \sqrt{1 + \left(\frac{b}{c+d}\right)^2}\right] \tag{3.4}$$

where F_{AB} is the radiation view factor between plates A and B. F_{AD} is the radiation view factor between plates A and D. The dimensions a, b, c, d, and L in addition to the plates A, B, and D can be reviewed by referring to Figure 3.3. The thermal radiative resistances (R_{rad}) shown in Figure 3.2 were employed to illustrate the radiative thermal exchange between elements. However, the integral model applied the estimated view factor as detailed in the next Subsection.

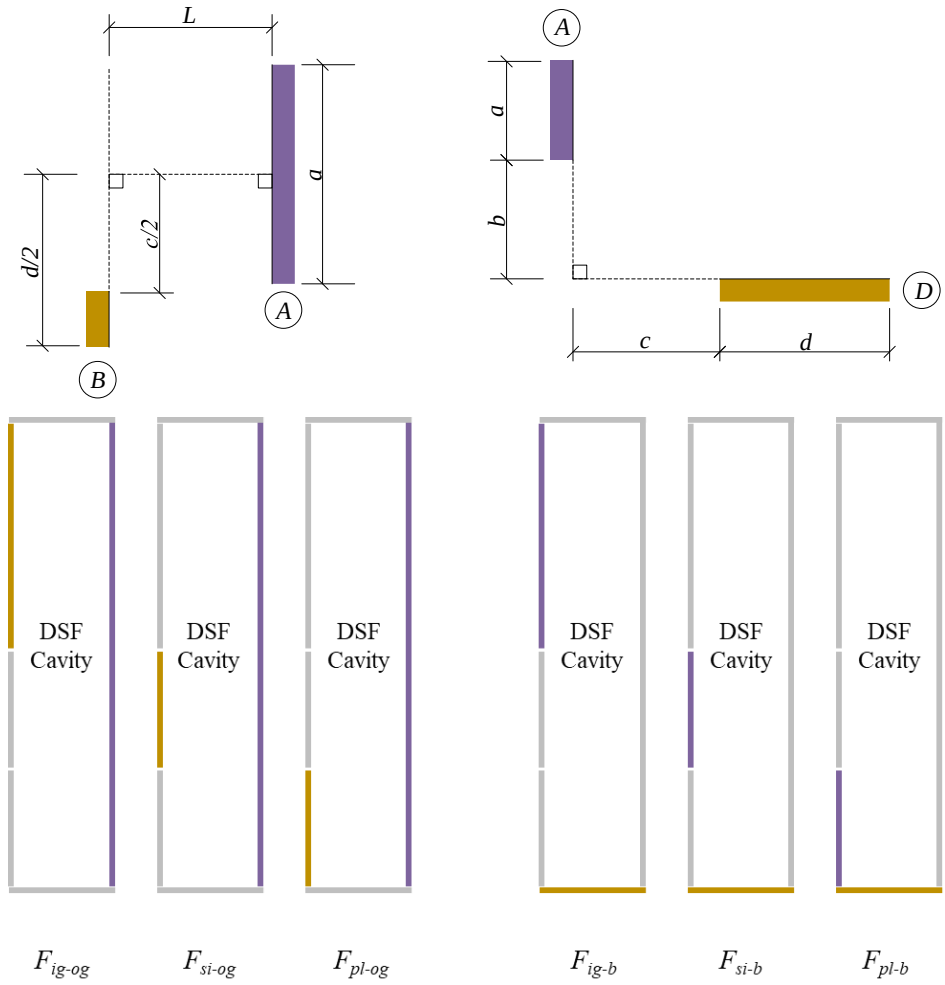


Figure 3.3. Top, view factors for parallel plates with parallel midlines and separated perpendicular plates (without a common edge). Bottom, view factor cases applied to the DSF elements.

Figure 3.2 also introduces the convective thermal resistance model. The sill panel exchanges heat by convection with the occupied space air at a rate of $q_{conv,si\text{-}ra}$. The air in the occupied space exchanges heat by convection at a rate $q_{conv,ra\text{-}ig}$ with the inner glass layer. The cavity top, inner glass layer, sill panel, plenum panel, and cavity bottom exchange heat by convection with the air in the cavity at rates of $q_{conv,t\text{-}c}$, $q_{conv,ig\text{-}c}$, $q_{conv,si\text{-}c}$, $q_{conv,pl\text{-}c}$, and $q_{conv,b\text{-}c}$, respectively. The air in the cavity exchanges heat by convection at a rate of $q_{conv,c\text{-}og}$ with the outer glass layer, which exchanges heat by convection with the ambient at a rate of $q_{conv,og\text{-}a}$.

As a result, the steady-state energy balance equations in DSF were considered such that energy is conserved at each element. Therefore,

$$\alpha_{og}G_{og} + q_{rad,ig-og} + q_{rad,si-og} + q_{rad,pl-og} + q_{rad,t-og} + q_{rad,b-og} + q_{conv,c-og} = q_{rad,og-s} + q_{conv,og-a} \quad (3.5)$$

$$q_{conv,ig-c} + q_{conv,si-c} + q_{conv,pl-c} + q_{conv,t-c} + q_{conv,b-c} = q_{conv,c-og} \quad (3.6)$$

$$\alpha_{ig}G_{ig} + q_{rad,rw-ig} + q_{conv,ra-ig} = q_{rad,ig-og} + q_{rad,ig-t} + q_{rad,ig-b} + q_{conv,ig-c} \quad (3.7)$$

$$\alpha_{si}G_{si} = q_{rad,si-og} + q_{rad,si-rw} + q_{rad,si-t} + q_{rad,si-b} + q_{conv,si-c} + q_{conv,si-ra} + E_{si} \quad (3.8)$$

$$\alpha_{pl}G_{pl} = q_{rad,pl-og} + q_{conv,pl-c} + q_{rad,pl-t} + q_{rad,pl-b} + E_{pl} \quad (3.9)$$

$$q_{rad,ig-t} + q_{rad,si-t} + q_{rad,pl-t} + q_{rad,b-t} = q_{conv,t-c} + q_{rad,t-og} \quad (3.10)$$

$$\alpha_{b}G_{b} + q_{rad,ig-b} + q_{rad,si-b} + q_{rad,pl-b} = q_{rad,b-t} + q_{conv,b-c} + q_{rad,b-og} \quad (3.11)$$

where α is the absorptivity. G is the incident solar irradiation, W/m. E is the energy generated from the associated PVs/PBRs, W/m. Eq (3.5), Eq (3.6), Eq (3.7), Eq (3.8), Eq (3.9), Eq (3.10), and Eq (3.11) represent the energy balance equations for the outer glass layer, cavity air, inner glass layer, sill panel, plenum panel, cavity top, and cavity bottom, respectively. Eq (3.5) shows that the outer glass layer receives heat by solar energy at a rate of $\alpha_{og}G_{og}$, by convection from the cavity air at a rate of $q_{conv,c-og}$, and by radiation from the inner glass layer, sill panel, plenum panel, cavity top, and cavity bottom at rates of $q_{rad,ig-og}$, $q_{rad,si-og}$, $q_{rad,pl-og}$, $q_{rad,t-og}$, and $q_{rad,b-og}$, respectively. The outer glass layer exchanges heat by radiation with the sky at a rate of $q_{rad,og-s}$, and by convection with the ambient air at a rate of $q_{conv,og-a}$. Remaining equations can be interpreted in the same sequence.

3.2.4 Radiative heat transfer

Thermal radiation refers to the energy released by matter that has a temperature above absolute zero. The radiation emitted from a surface comes from the thermal energy within the material confined by that surface. The amount of energy discharged per unit area (W/m^2) is known as the surface emissive power, E. The maximum possible emissive power is determined by the Stefan–Boltzmann law

$$E_b = \sigma T_s^4 \quad (3.12)$$

where T_s is the absolute temperature of the surface, K. σ is the Stefan–Boltzmann constant. Such a surface is called an ideal radiator or blackbody. The heat flux emitted by a real surface is less than that of a blackbody at the same temperature and is given by

$$E = \varepsilon\sigma T_s^4 \tag{3.13}$$

where ε represents a radiative characteristic of the surface known as emissivity. Ranging from 0 to 1, this property indicates how effectively a surface emits energy compared to a blackbody. Emissivity is heavily influenced by the material and texture of the surface.

Different forms of heat flux are associated with the study of radiation heat transfer. Table 3.2 lists four distinct radiation fluxes that can be defined at a surface. The emissive power, E (W/m^2), is the rate at which radiation is emitted from a surface per unit surface area, over all wavelengths and in all directions. This emissive power is related to the behavior of a blackbody through Eq (3.12).

Table 3.2. Radiation fluxes defined at a surface [159].

Flux (W/m^2)	Description	Comment
Emissive power, E	Rate at which radiation is emitted from a surface per unit area	$E = \varepsilon\sigma T_s^4$
Irradiation, G	Rate at which radiation is incident upon a surface per unit area	Irradiation can be reflected absorbed, or transmitted
Radiosity, J	Rate at which radiation leaves a surface per unit area	For an opaque surface $J = E + \rho G$
Net radiative flux, $q''_{rad} = J - G$	Net rate of radiation leaving a surface per unit area	For an opaque surface $q''_{rad} = \varepsilon\sigma T_s^4 - \alpha G$

The term q_i, which is the net rate at which radiation leaves surface i, represents the net effect of radiative interactions occurring at the surface. This value corresponds to the rate of energy that would need to be delivered to the surface by other mechanisms to keep its temperature steady. It is defined as the difference between the surface radiosity and irradiation and can be formulated as

$$q_i = A_i(J_i - G_i) \tag{3.14}$$

By applying the definition of radiosity found in Table 3.2, the net radiative energy transfer from the surface can be estimated by

$$q_i = A_i(E_i - \alpha_i G_i) \tag{3.15}$$

where use has been made of the relationship $\alpha_i = 1 - \rho_i$ for an opaque surface. Recognizing that $E_i = \varepsilon_i E_{bi}$ and noting that $\rho_i = 1 - \alpha_i = 1 - \varepsilon_i$ for an opaque, diffuse, gray surface, the radiosity can also be expressed as

$$J_i = \varepsilon_i E_{bi} + (1 - \varepsilon_i) G_i \tag{3.16}$$

By solving for G_i and substituting into Eq (3.14), it follows that

$$q_i = A_i \left(J_i - \frac{J_i - \varepsilon_i E_{bi}}{1 - \varepsilon_i} \right) \tag{3.17}$$

or

$$q_i = \frac{E_{bi} - J_i}{(1 - \varepsilon_i)/\varepsilon_i A_i} \tag{3.18}$$

To apply Eq (3.18), the surface radiosity J_i must be determined. To calculate this, it is necessary to consider the radiation exchange between all surfaces within the enclosure.

The irradiation on surface *i* can be calculated from the radiosities of all surfaces in the enclosure. Specifically, using the definition of the view factor, the total rate at which radiation arrives at surface *i* from all surfaces, including surface *i*, is given by

$$A_i G_i = \sum_{j=1}^{N} A_i F_{ij} J_j \tag{3.19}$$

By canceling out the area A_i and substituting into Eq (3.14) for G_i, it follows that

$$q_i = A_i \left(J_i - \sum_{j=1}^{N} F_{ij} J_j \right) \tag{3.20}$$

Alternatively, using the view factor summation rule, it follows that

$$q_i = A_i \left(\sum_{j=1}^{N} F_{ij} J_i - \sum_{j=1}^{N} F_{ij} J_j \right) \tag{3.21}$$

Thus,

$$q_i = \sum_{j=1}^{N} A_i F_{ij} (J_i - J_j) = \sum_{j=1}^{N} q_{ij} \tag{3.22}$$

Eq (3.22) equates the net rate of radiation transfer from surface *i*, q_i, to the sum of components q_{ij} associated to radiative exchange with the other surfaces. By combining Eq (3.18) and Eq (3.22), it follows that

$$\frac{E_{bi} - J_i}{(1-\varepsilon_i)/\varepsilon_i A_i} = \sum_{j=1}^{N} \frac{J_i - J_j}{\left(A_i F_{ij}\right)^{-1}} \tag{3.23}$$

For two surfaces that exchange radiation solely with each other, the net rate of radiation transfer rate from surface 1 (q_1) must equal the net rate of radiation transfer to surface 2 (q_2) and both must equal the net rate of radiation exchange between the two surfaces. Thus,

$$q_1 = -q_2 = q_{12} \tag{3.24}$$

The rate of radiation transfer can be found by applying Eq (3.23) to surfaces 1 and 2 and solving the resulting equations for J_1 and J_2. These values can then be used in conjunction with Eq (3.18) to calculate q_1 and q_2. Therefore, substituting from Eq (3.12), the net radiation exchange between the surfaces can be expressed as [159]

$$q_{rad,1-2} = q_{12} = q_1 = -q_2 = \frac{\sigma(T_1^4 - T_2^4)}{\frac{1-\varepsilon_1}{\varepsilon_1 A_1} + \frac{1}{A_1 F_{12}} + \frac{1-\varepsilon_2}{\varepsilon_2 A_2}} \tag{3.25}$$

where σ is the Stefan-Boltzmann constant, W/m^2·K^4. T, A, and ε are the temperature, area, and emissivity of the surfaces. When radiation is between a finite plate and a very large surface as the sky. A_2 in Eq (3.25) tends to ∞ and the view factor approaches unity. Therefore

$$q_{rad,1-2} = \sigma \varepsilon_1 A_1 (T_1^4 - T_2^4) \tag{3.26}$$

3.2.5 Convective heat transfer

According to Newton's law of cooling, the heat transfer by convection is given by [159]

$$q_{conv} = hA(T_1 - T_2) \tag{3.27}$$

where T is the temperature, K. h is the heat transfer coefficient, W/m^2·K. A is the surface area, m^2. The heat transfer coefficient is the heat transferred by convection per unit area per Kelvin. It is dependent on many parameters including surface temperature, surface geometry, surface orientation, fluid temperature, fluid type, and fluid velocity. For forced-moving fluids, heat is transferred by forced convection. For free-moving fluids, heat is transferred by free convection, which is calculated by applying the correlation developed for vertical or horizontal plates. For vertical plates, the heat transfer coefficient is calculated from [159]

$$Nu_H = \frac{hH}{k} = 0.68 + \frac{0.670 Ra_H^{1/4}}{[1 + (0.492/Pr)^{9/16}]^{4/9}} \tag{3.28}$$

where Nu_H is the Nusselt number based on the surface height. H is the surface height, m. k is the fluid thermal conductivity calculated at the film temperature, W/m·K. Ra_H is the Rayleigh number

based on the surface height. *Pr* is the Prandtl number calculated at the film temperature. The Rayleigh number is calculated from [159]

$$Ra_H = \frac{g\beta(T_1 - T_2)H^3}{\nu\alpha} \tag{3.29}$$

where *g* is the gravitational acceleration constant, m/s^2. β is the fluid thermal expansion coefficient calculated at the film temperature, K^{-1}. ν is the fluid kinematic viscosity calculated at the film temperature, m^2/s. α is the fluid thermal diffusivity calculated at the film temperature, m^2/s. The fluid properties are calculated at the film temperature, which is calculated from [159]

$$T_f = \frac{T_1 + T_2}{2} \tag{3.30}$$

In the current study, tilted plates were approximated as vertical plates. For horizontal plates, the heat transfer coefficient for the upper surface of hot plates or the lower surface of the cold plates is calculated from [159]

$$Nu_L = \frac{hL}{k} = 0.54Ra_L^{1/4} \tag{3.31}$$

where *L* is the characteristic length defined as the area to perimeter ratio, m. The previous equation is valid for Ra_L between 10^4 and 10^7. For Ra_L above 10^7, the previous equation is replaced by [159]

$$Nu_L = \frac{hL}{k} = 0.15Ra_L^{1/3} \tag{3.32}$$

The heat transfer coefficient for the lower surface of hot plates or the upper surface of cold plates is calculated from [159]

$$Nu_L = \frac{hL}{k} = 0.27Ra_L^{1/4} \tag{3.33}$$

The forced convection heat transfer coefficient is calculated by applying the correlation developed for flat plates [159]

$$Nu_L = \frac{hL}{k} = \left(0.037Re_L^{4/5} - 871\right)Pr^{1/3} \tag{3.34}$$

where Nu_L and Re_L are Nusselt and Reynolds numbers based on the distance parallel to the fluid travel direction. The Reynolds number is calculated from [159]

$$Re_L = \frac{VL}{\nu} \tag{3.35}$$

where *V* is the fluid speed, m/s.

3.2.6 Setup of the CFD model

For this study, ANSYS Fluent CFD code was applied to carry out the numerical simulations, using the finite volume method and implementing the Reynolds-averaged Navier–Stokes equations (RANS) and energy conservation equations governing non-isothermal, turbulent flow [168].

The shear stress transport (SST) *k-ω* model, developed by Menter [169], shows good behavior in both near-wall and free-stream domains. This model is also reliable in modeling separating flows and adverse pressure gradients [170]. Therefore, the present work utilized the SST *k-ω* turbulence model for both the validation and subsequent computations. At steady state conditions, the 2D SST *k-ω* turbulence model was applied by employing the transport equations [171]

$$\frac{\partial}{\partial x_i}(\rho k u_i) = \frac{\partial}{\partial x_j}\left(\Gamma_k \frac{\partial k}{\partial x_j}\right) + G_k - Y_k + S_k \tag{3.36}$$

$$\frac{\partial}{\partial x_i}(\rho \omega u_i) = \frac{\partial}{\partial x_j}\left(\Gamma_\omega \frac{\partial \omega}{\partial x_j}\right) + G_\omega - Y_\omega + S_\omega \tag{3.37}$$

where k is the kinetic energy of turbulence. ω is the specific dissipation rate. G and Y are the generation and dissipation rates of k or ω, respectively. Γ and S are the effective diffusivity and the source term, respectively. Detailed equations of these variables can be viewed by referring to [171].

The CFD model subdivided the domain boundaries where uniform temperature conditions have been imposed at all surfaces, including inner and outer glass layers, cavity top and bottom, and PVs/PBRs. CFD simulations can be performed by taking air properties as constants or considering their variation with temperature. Pasut et al. [165] proved that the maximum variation for air thermal conductivity and specific heat in DSFs were 0.00105 W/m·K and 1 J/kg·K, respectively. These variations were 2.6% and 0.1% of the corresponding values at 293.15 K. It was thus concluded that considering air properties as polynomial functions of temperature was not reasonable, and it further increased the computation time without significant impact on the CFD results [165]. Therefore, all fluid properties in the present study were taken as constant values except for density in the buoyancy term.

In an optimal scenario, the radiation and convection models should be integrated with CFD analysis to accurately capture the impact of heat transfer interactions involving radiation, convection, solar heat gain, and wind speed. However, for the present study, radiation and convection models were decoupled from the CFD analysis in accordance with the methodology outlined in Ref [166]. Alternatively, radiation and conjugate heat transfer between different surfaces have been substituted by constant values of surface temperature (Table 3.3). In terms of airflow, external to internal vent area ratio (AR) metric was applied to investigate the effect of vent sizing. All vents were chosen to be 10 cm in height to implement the mean value available in the market. Applied AR values were 0.5 and 2, respectively. For air noise, the airflow velocity was kept in the range of 2.2 to 3.8 m/s to avoid the aerodynamic noise, as recommended by ASHRAE [172]. The occupied space temperature was fixed at 23 ℃.

Table 3.3. Temperature conditions for different cavity elements in ℃.

Building Element	Ambient (-25 ºC)				Ambient (25 ºC)			
	PV		PBR		PV		PBR	
	0.6 m	2.4 m	0.6 m	2.4 m	0.6 m	2.4 m	0.6 m	2.4 m
Inner glass layer	14	16	14	16	26	30	26	30
Sill panel	26	28	29	30	31	32	32	32
Plenum panel	30	33	34	37	42	45	43	46
Outer glass layer	-8	-7	-7	-6	25	28	25	28
Cavity bottom	15	17	18	19	50	55	51	55
Cavity top	7	11	8	12	30	39	30	39

3.2.7 Parametric analysis with ANSYS-MATLAB coupling

It was anticipated that the warm stream from the occupied space will always offer a thermal shield to the inner glass layer in the cavity upper half, where the thermal behavior has no significant impact on any key variable. In the lower half of the cavity, the thermal behavior can affect the solar energy modules' temperature. In [167], for each 10 ℃ increase in temperature, solar cell efficiency is decreased by 0.8 %. As a result, the current study focused on representing the lower half of the cavity, which can be identified through Figure 1.2 as the domain bounded by the two lines intersecting the x-axis (lx and ux) and the two lines intersecting the y-axis (ly and uy). This domain was divided into identical nx×ny rectangles. A code, written in MATLAB, was developed to import the ANSYS results and calculate one mean temperature value using only the values at

the nodes enclosed inside each rectangle. The code generates a ny×nx matrix where the rows can be averaged to give 1×nx matrix, which was considered as the temperature variation along the cavity. The figure shows a schematic that represents the cavity solution domain and the sequence implemented in the code.

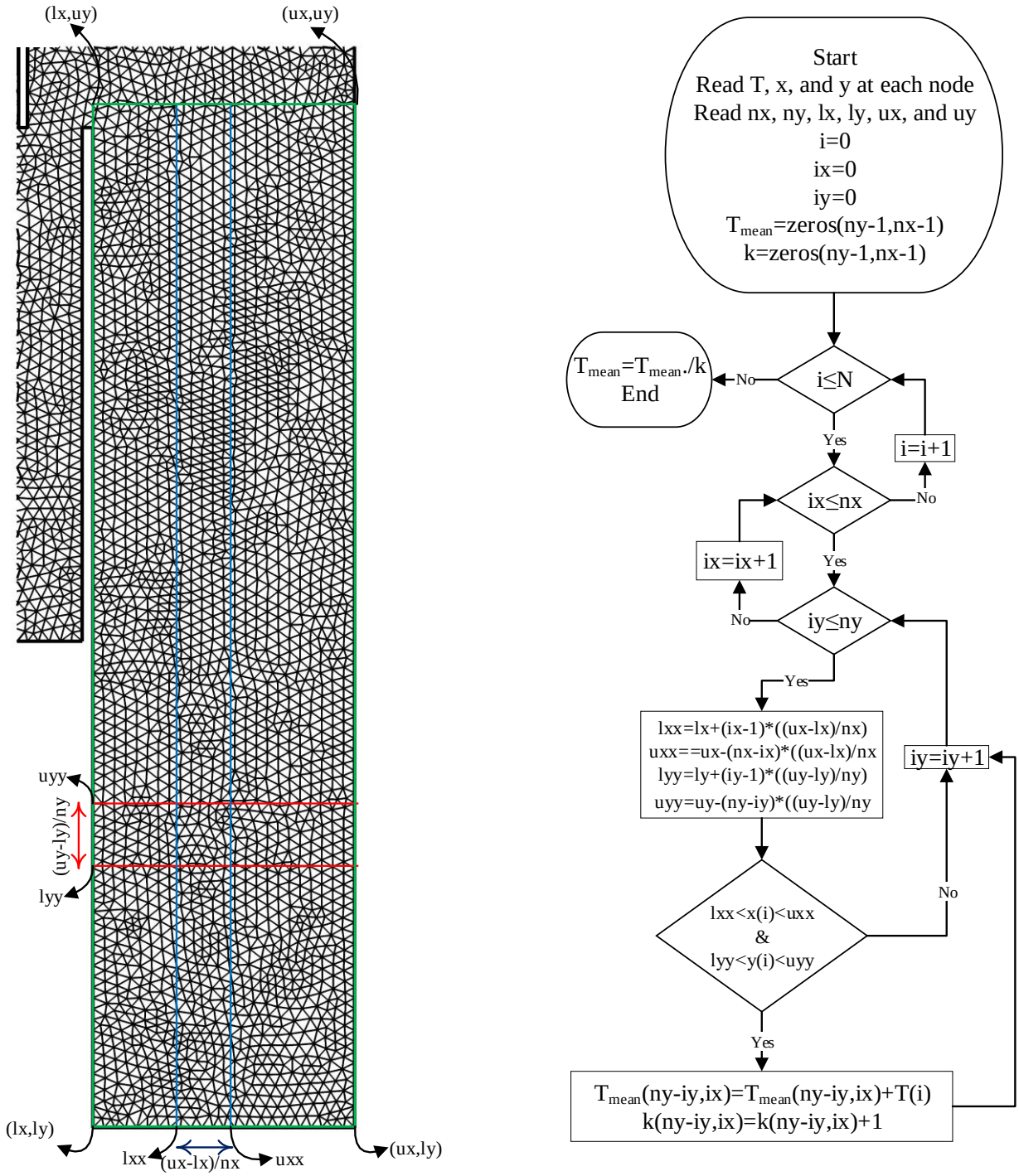


Figure 3.4. Schematic of the cavity solution domain (left), and sequence implemented in the code (right).

3.2.8 Solar irradiation and energy generation model

Solar irradiation is incident on the right side of the outer glass layer at a rate of G_{og}.

$$G_{og} = (I_b \times \cos\theta_v) \times L_{og} \tag{3.38}$$

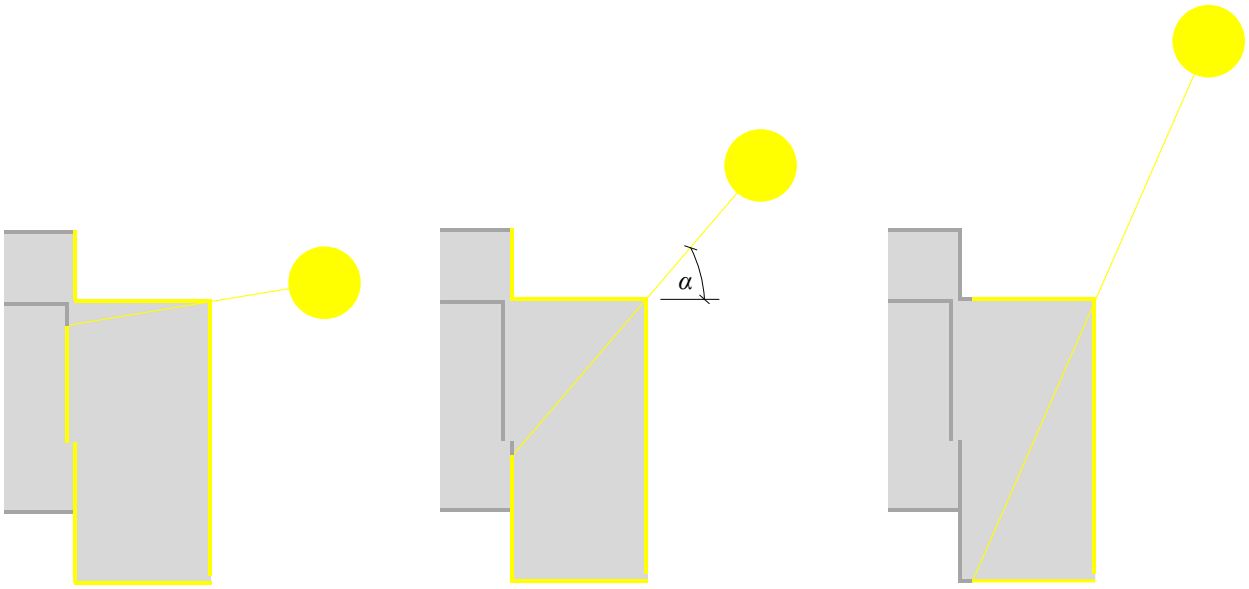
where I_b is the direct normal irradiation, W/m^2. θ_v is the solar incidence angle on vertical surfaces, rad. L_{og} is the outer glass layer height, m. G_{ig}, $G_{si,}$ and G_{pl} are the rates by which solar irradiation is incident on the inner glass layer, the sill panel, and the plenum panel, respectively.

$$G_x = \tau_{og} G_{og} \times L_x / L_{og} \times SF_x \tag{3.39}$$

τ_{og} is the outer glass layer transmissivity. G_x is the solar irradiation incident on the inner glass layer, the sill panel, or the plenum panel, W/m. L_x is the length of the associated element, m. SF_x is the shading factor of the associated element due to uniform shading. It is worthy to note that non-uniform shading due to irregular obstacles, such as mullions or spaceframe rods holding the outer glass layer, can reduce solar efficiency of the shaded panel by 70% [173]. Figure 3.5 clarifies the impact of the cavity width on the shading factor for different elements in the DSF. Solar irradiation incident on the cavity bottom is calculated from:

$$G_b = I_b \times \cos\theta_h \times \tau_{og} \times W_c \times SF_b \tag{3.40}$$

where G_b is the rate by which solar irradiation is incident on the cavity bottom. θ_h is the solar incidence angle on horizontal surfaces, rad. W_c is the DSF cavity width, m. SF_b is the shading factor of the cavity bottom.



Winter Spring/Fall Summer

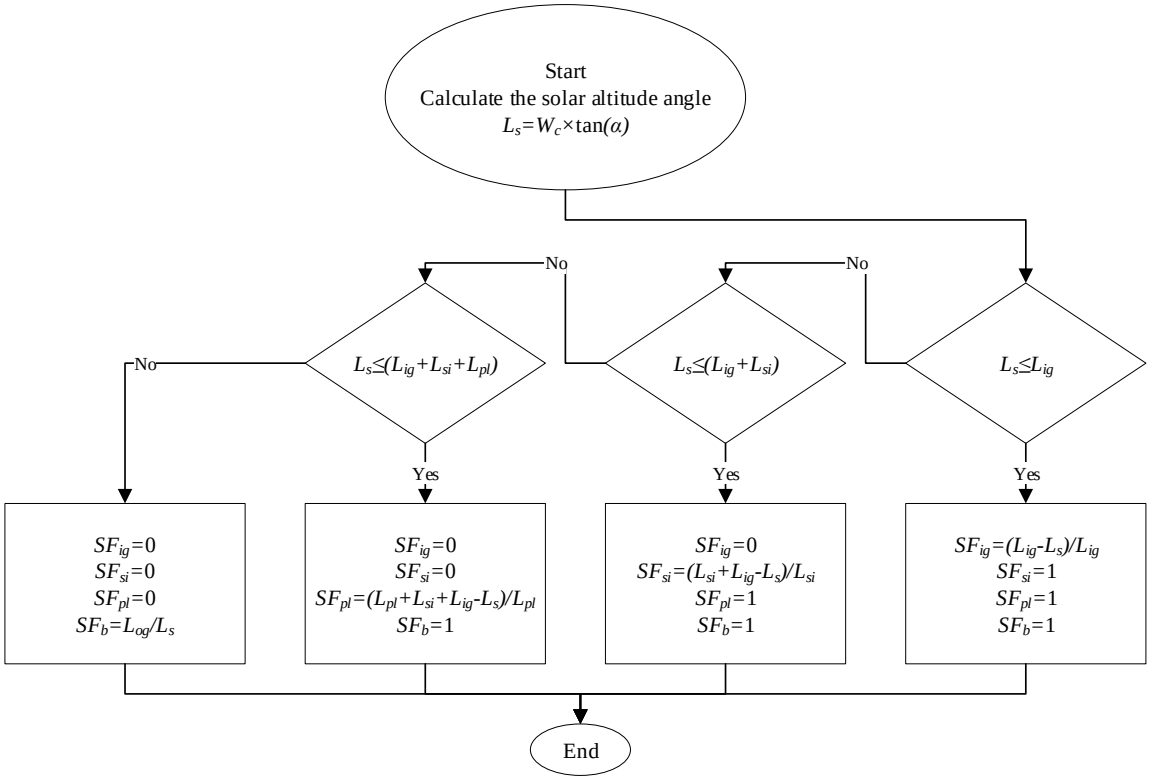


Figure 3.5. The impact of the cavity width on the shading factor for different elements in the DSF.

In conclusion, the energy generated from the panels can be calculated from:

$$E = \eta_{si} \times G_{si} + \eta_{pl} \times G_{pl} \tag{3.41}$$

where E is the generated energy, W/m. η_{si} is the sill panel efficiency. η_{pl} is the plenum panel efficiency. For PBRs, the efficiency was temperature-independent with a constant value of 0.09 [19]. However, the PVs' efficiency changes with the temperature (T) according to [167]:

$$\eta = 0.223 - 8.1429 \times 10^{-4} \times (T - 273) \tag{3.42}$$

3.3 Results and Discussions

The developed CFD model was first validated against the experimental results. The temperature variation along the DSF cavity height was measured by Dama et al. in four different cases [124]. The new model was applied to two cases representing different boundary conditions. In the first case, the temperature for the ambient, outer glass layer, and inner glass layer were 14.6 °C, 28.6 °C, and 29.5 °C, respectively. These values were 15.1 °C, 18.9 °C, and 21.2 °C in the second case. The wind had a magnitude of 4.3 m/s and 9.2 m/s with a direction of 107° and 287° (0° Nord) for both cases. The results were compared to Dama's model and experimental data (Figure 3.6). The developed model showed an average error of 1.9 °C. The grid independence test for the temperature in the cavity upper half with AR=0.5 (0.6 m) is presented in Figure 3.6. The last two mesh sizes were closely matched, and the maximum estimated relative error for the temperature distribution was 0.07%, which was significantly small. By considering computation time and results' accuracy, the grid number of 96,654 was selected and the same mesh was applied to all simulated cases. This resolution corresponded to a grid size of 2 cm.

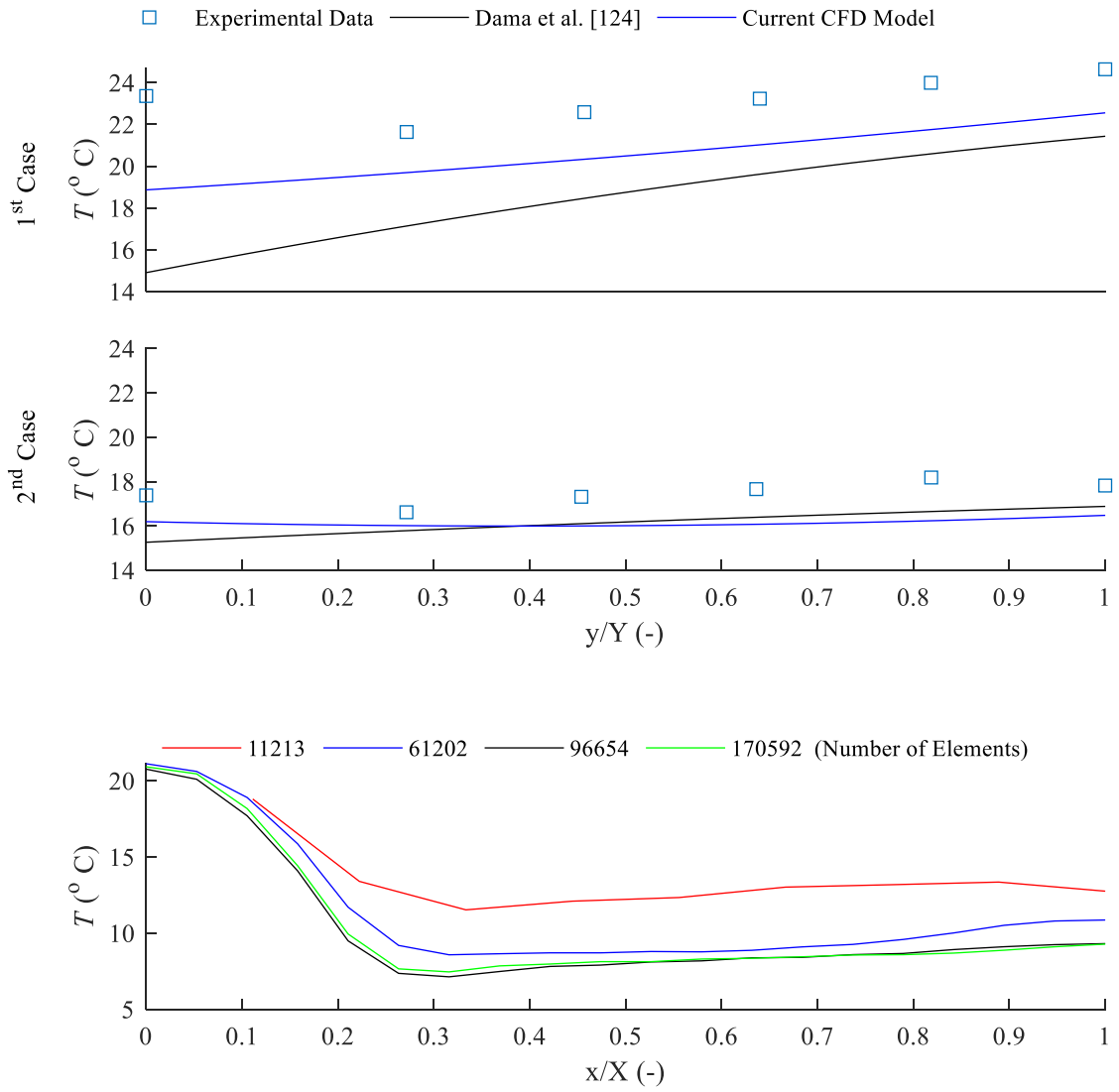


Figure 3.6. Validation and grid independence test for the developed CFD model. y/Y and x/X represent the temperature variation with the cavity height and width, respectively.

The developed integral model has been validated against experimental measurements. Andelkovic et al. [174] measured the air temperature inside the DSF cavity for five consecutive days in each February, April, and July. These months were selected as representatives of the winter, transitional, and summer seasons, respectively. The same study applied *EnergyPlus*™ coupled with *DesignBuilder*® to calculate the air temperature analytically. The boundary conditions of the examined location in terms of irradiation and ambient temperature have been applied to validate the current integral model. Figure 3.7 shows the results of both models compared to experimental measurements. The integral model showed a local average error of 1.7 °C, 1.9 °C, and 3.5 °C for

winter, transitional, and summer seasons. These values were 2.0 °C, 2.2 °C, and 2.5 °C for the Andelkovic simulation model. Overall, the global average error was 2.2 °C and 2.4 °C for both models, respectively. However, this study showed a close correlation with an *R*-value of 0.96 compared to 0.95.

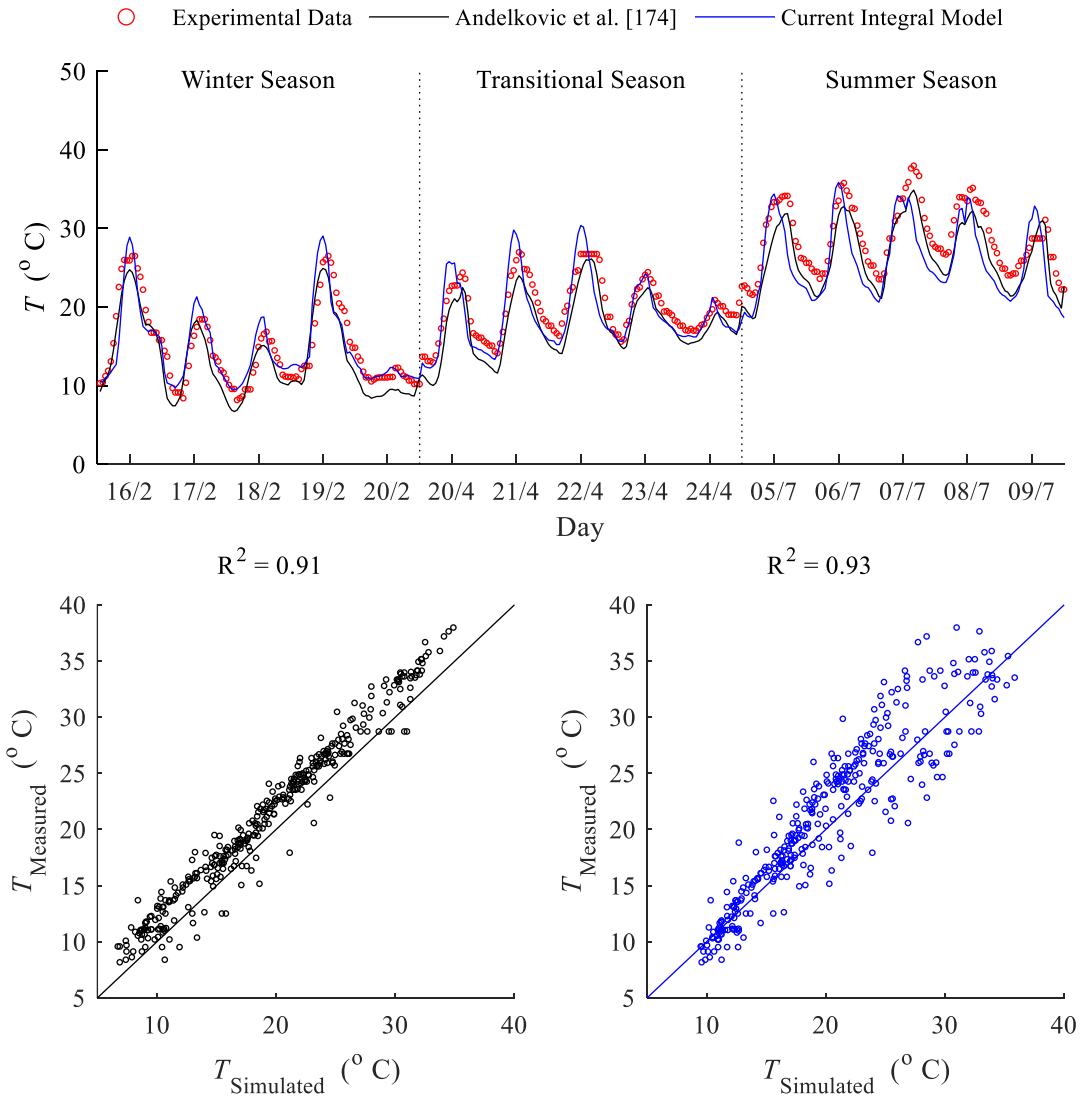


Figure 3.7. Top, validation of the integral heat balance model. Bottom, regression analysis for both Andelkovic and the developed model.

The DSF's thermal performance, energy generation, and useful heating for cavity and occupied space were first analyzed on an hourly basis throughout the year. Figure 3.8 presents the DSF with alternative integration of PV and PBR panels. Solar irradiation reaching the panels was affected by the incidence angle and shading factor. The minimum W_c value that provided full solar exposure

for panels, annually, was around a width of 1 m. Due to the vertical orientation of panels, the incidence angle decreased irradiation from 409.5 W/m^2 in winter (-25 ℃) to 123.07 W/m^2 in summer (25 ℃) with W_c = 0.6 m. Moreover, for W_c of 1.2, 1.8, and 2.4 m, the shading effect diminished irradiation by 0.74, 44.8, and 104.7 W/m^2 in summer. The relatively low altitude angle in the winter guaranteed full solar exposure to the PVs/PBRs for all cavity widths. For energy generation, the PV electrical output with W_c = 0.6 m was increased from 23.1 W/m^2 in summer to 73.3 W/m^2 in winter. In the case of W_c = 2.4 m, the summer output had a lower value of 9.6 W/m^2. With PBRs, the biological energy generation went up from 11.9 W/m^2 in summer to 36.9 W/m^2 in winter with W_c = 0.6 m. With wide cavities, the summer output was near 4.7 W/m^2 for W_c = 2.4 m. Compared to PVs, the heating potential of PBRs was higher by up to 8.1%. The highest useful heating gained in winter was for W_c = 2.4 m, with 91.7 W/m^2 from PBRs and 84.8 W/m^2 from PVs. The PVs' higher energy generation, due to their higher conversion efficiency, outweighed their lower heating contributions, hence the PVs' overall efficiency is higher. On average, this efficiency ranged from 23.7% in summer to 21.2% in winter for PVs. Such a value was comparable to the 22% efficiency for the PV-Thermal air collector examined by [175]. PBRs had the average overall efficiency ranging between 18.6% and 15.5% in summer and winter, respectively. Solar energy trapped inside the cavity was directed to both the occupied space and the ambient, whose share was higher in winter and lower in summer. Lastly, the rate of convective and radiative heat transfer was documented against a typical façade with a double-glazed assembly. It was noted that heat loss from this façade had an annual average of 82.1 W/m^2 which was countered by 35.7 W/m^2 heat gain with the proposed DSF.

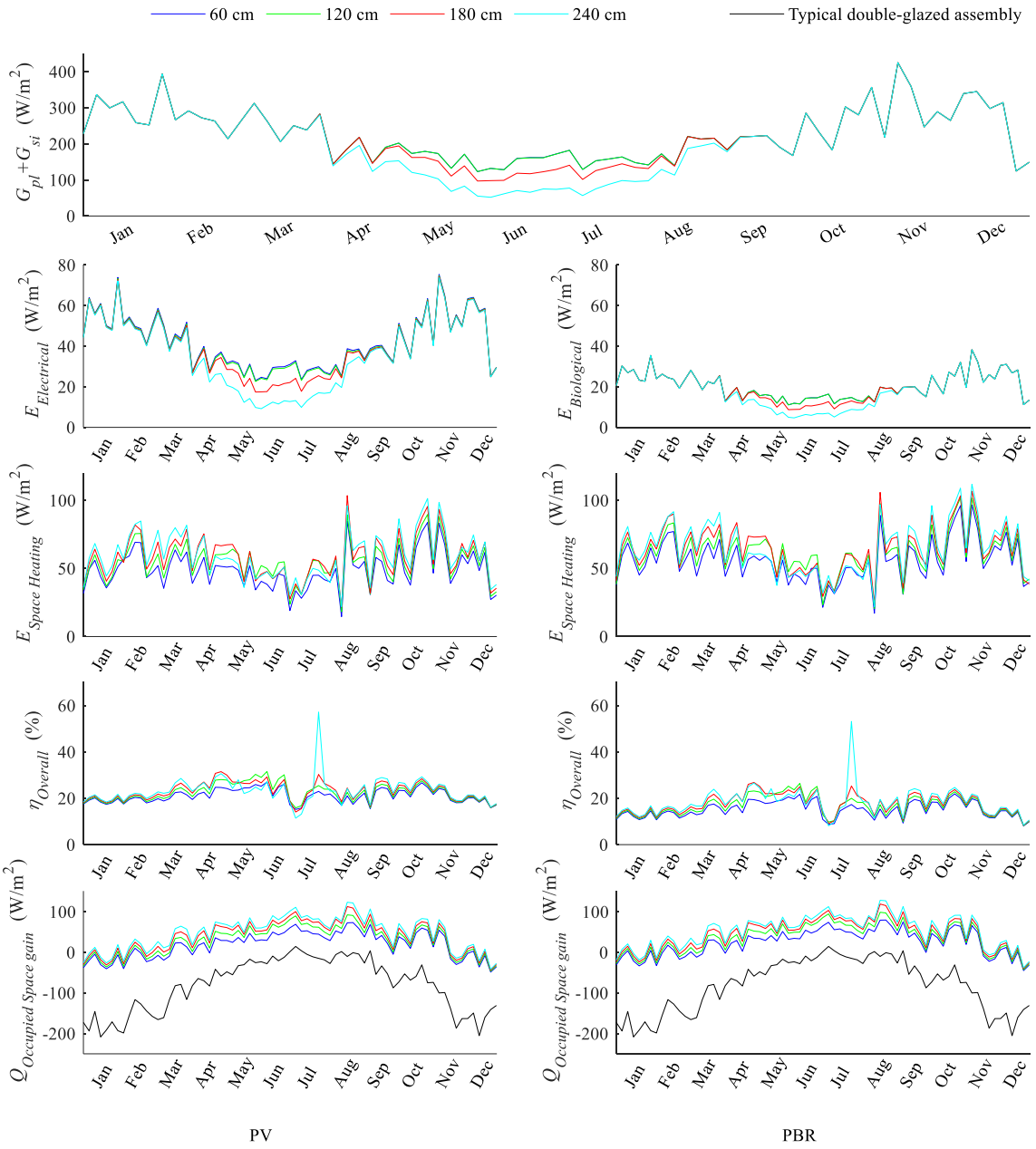


Figure 3.8. Hourly mean curves for the solar irradiation reaching the PVs/PBRs, energy generation, useful heating, and overall efficiency for both PV and PBR panels.

The second part of the study investigated the airflow patterns in the DSF system (Figure 3.9). All internal ventilation ($V_{Internal}$) schemes had the occupied space as the only source that compensates for the plenum's suction flow. As the occupied space temperature was constant regardless of the ambient conditions, the velocity profiles were very similar in the $V_{Internal}$ cases. The key difference was the adjacent flow to the outer glass layer in narrow cavities due to their limited width.

However, for all $V_{Internal}$ cases, the high-velocity contours (2.5 m/s) were 2 m above the cavity floor. Two W_c scenarios were examined, including W_c = 0.6 m and W_c = 2.4 m. The airflow in W_c = 2.4 m was far from the outer glass layer allowing backflow to recirculate in the cavity. As a result, the thermal effect of the airstream was more significant as compared to that of W_c = 0.6 m. At -25 ℃, the cavity lower half of W_c = 2.4 m benefited more from the relatively hot stream of the occupied space and was warmer than that of W_c = 0.6 m by 3.3 ℃. At 25 ℃, the wider cavity was also advantageous due to the cold stream of the conditioned occupied space. However, the convective heating from the cavity ground facing the sun made the wide cavity hotter than narrow cavities by 3.4 ℃. With the mixed ventilation (V_{Mixed}) schemes, the mass flux from the occupied space was lower than that of the $V_{Internal}$ (percent reduction can reach 61.7% for AR=2.0), and the mass flux from the ambient flowed adjacent to the inner layer, which led to suppressing the occupied space flow pattern. At 25 ˚C, the relatively lower density of the ambient stream allowed more dispersion in the cavity compared to the same cases in cold conditions. This dispersed airflow moved in the cavity at about 0.7 m/s with AR = 0.5 and AR = 2.0. In the cases of AR = 2.0, higher mass flux of ambient air was directly introduced into the cavity and reduced the effect of the cavity width on temperature profiles. Both wide and narrow cavities were at -11.7 ℃ and 26.4 ℃ when the ambient was at -25 ℃ and 25 ℃, respectively. For all cases, the air velocity was below 3 m/s.

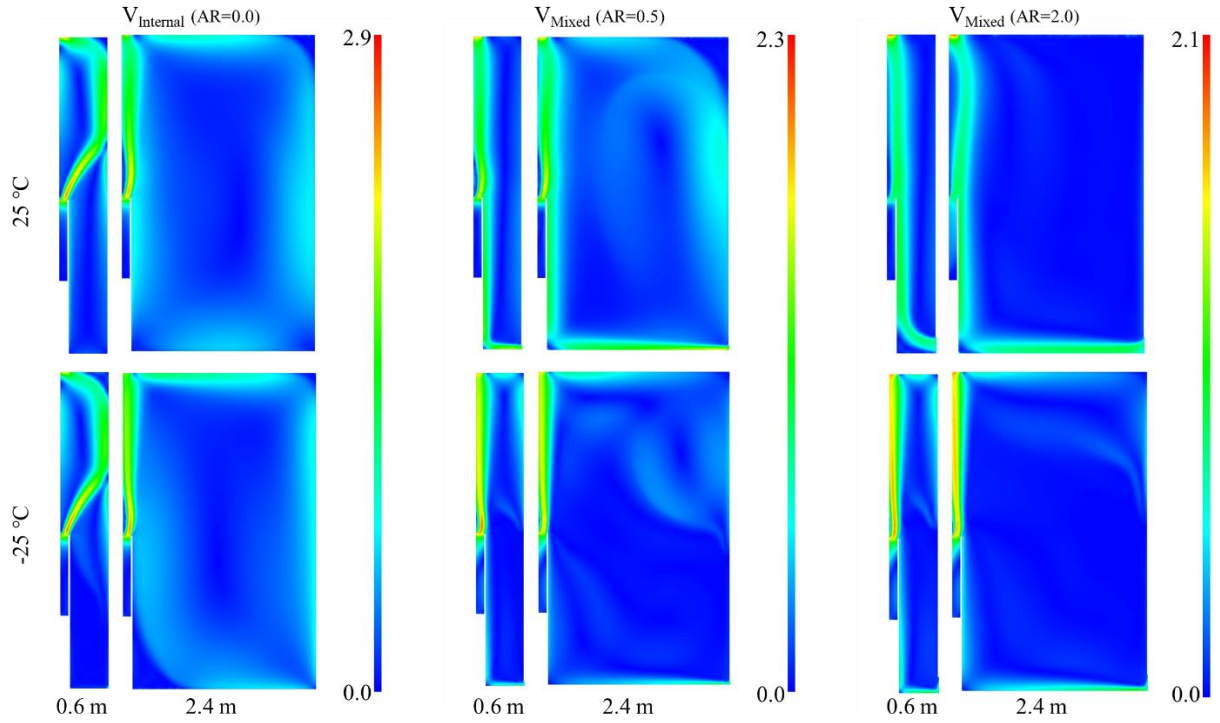


Figure 3.9. Velocity profiles for all ventilation cases.

Figure 3.10 shows the velocity variation adjacent to L_{si}+L_{pl}, L_{ig}, $W_{c.top}$, and $W_{c.bottom}$. Above the cavity bottom and in front of PVs/PBRs, the velocity trends were always higher for 25 °C, except for $W_{c.bottom}$ in the case of AR=2.0 (for W_c = 0.6 m), in which the mass flux from the ambient entered the cavity without any contact with the bottom (velocity was at 0.08 m/s). Narrowing the external vent by applying AR = 0.5 helped in forcing the ambient mass flux to be attached to the cavity bottom, setting a velocity increase to 0.7 m/s in summer and to 0.4 m/s in winter. Air moved naturally without any driving force over the bottom of the $V_{Internal}$ cases. Therefore, the flow velocity for $V_{Internal}$ above $W_{c.bottom}$ was around 0.1 m/s for W_c = 0.6 m and 0.2 m/s for W_c = 2.4 m, respectively. $V_{Internal}$ (0.6 m) had the highest flow velocity (up to 1.2 m/s) below the cavity top among all cases. In cold conditions, the denser ambient air increased the share of the mass flux from the occupied space. As a result, V_{Mixed} at lower ambient temperatures had high flow velocity over the L_{ig} layer (up to 1.7 m/s). The ambient temperature had a negligible effect, on the flow velocity adjacent to L_{ig} in $V_{Internal}$ (0.6 m) due to the flow guidance provided by the small cavity size. Specifically, the velocity adjacent to L_{ig} ranged between 0.1 and 0.7 m/s. The significant amount of denser cold air with the low-temperature case led to suppressing the occupied space stream flowing over L_{ig} with $V_{Internal}$ (2.4 m), hence the velocity there went up to 1.7 m/s.

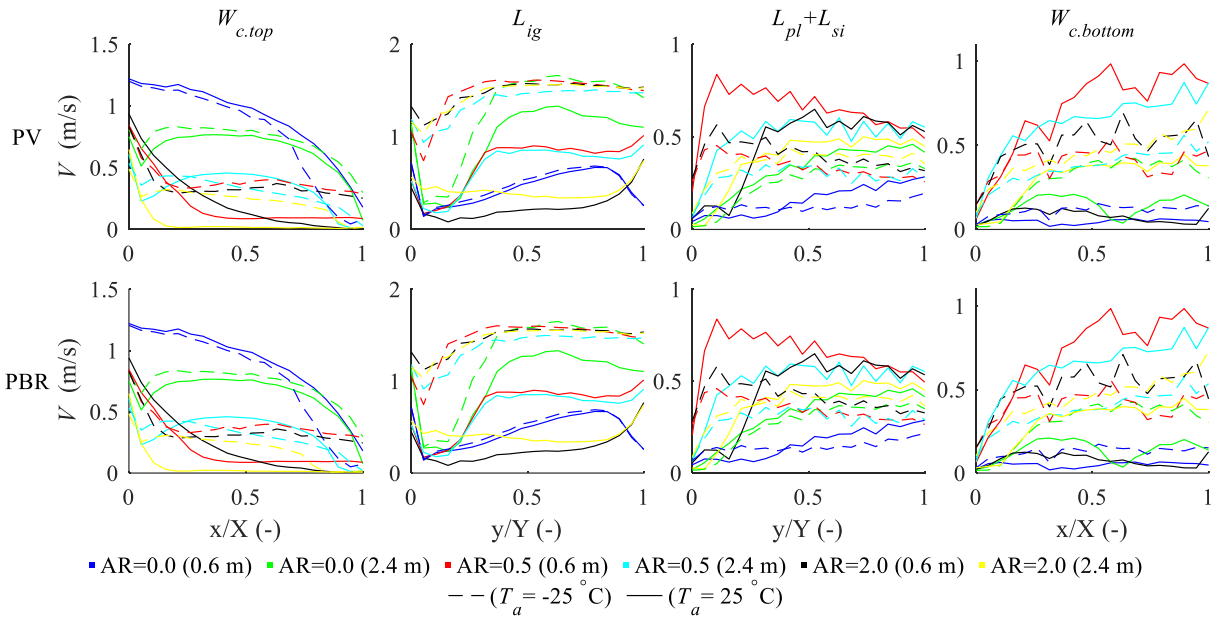


Figure 3.10. Velocity variation adjacent to the cavity top, cavity bottom, PVs/PBRs, and inner glass layer.

It was noticed that the trend of curves in Figure 3.10 varied with the airflow and ventilation scheme. For $V_{Internal}$ (0.6 m) at $W_{c.top}$, the curve convexity demonstrated the occupied space's stream circulating over the outer glass layer and then the cavity top in only these cases. Other curves had concave form as with AR = 2.0 for the predominance of the stream flowing over the inner layer without much contact with $W_{c.top}$. There was a curve spike over L_{ig} as in $V_{Internal}$ (2.4 m) due to the flow rejoining the inner glass layer after traveling around 0.5 m in the cavity space.

In Figure 3.11, the shift in heat transfer by convection from free convection to forced convection was analyzed by contrasting the mean velocities in the cavity. The airflow over L_{ig} acted as a heat source for the occupied space in winter and as a heat sink in summer. $V_{Internal}$ (0.6 m) offered the weakest thermal shield with a mean velocity of 0.48 m/s. Moreover, the convective heat exchange depended strongly on the mean velocity over the glass, which was around 1.5 m/s for all V_{Mixed} schemes with colder ambient temperature. This made the flow over L_{ig} a perfect thermal shield in this case. $V_{Internal}$ (2.4 m) offered a comparable thermal shield with a mean velocity of 1.3 m/s. In summer, the flow over the inner glass layer acted as a coolant for the glass gaining heat by radiation. The faster the flow the better the cooling effect was. The best cooling effect was provided by $V_{Internal}$ (2.4 m) where the flow velocity registered 1 m/s. The minimum cooling effect was

offered by AR=2.0 (0.6 m) where the mean velocity was 0.27 m/s. Similarly, cooling was essential for PVs/PBRs in summer, especially with PVs. The best cooling impact for the panels was achieved by AR=0.5 (0.6 m) when the adjacent velocity was 0.64 m/s. The heat transfer coefficient corresponding to this velocity was 8.1 W/m^2·K as depicted by [124]. In summer, $V_{Internal}$ (0.6 m) offered the lowest cooling effect when the airflow over the panels was at 0.16 m/s. Lastly, the mean velocity over the cavity bottom varied from 0.08 m/s in AR=2.0 (0.6 m) to 0.7 m/s for AR = 0.5 (0.6 m). The latter case had the highest mean value as the narrow external vent directed the air to contact $W_{c.bottom}$.

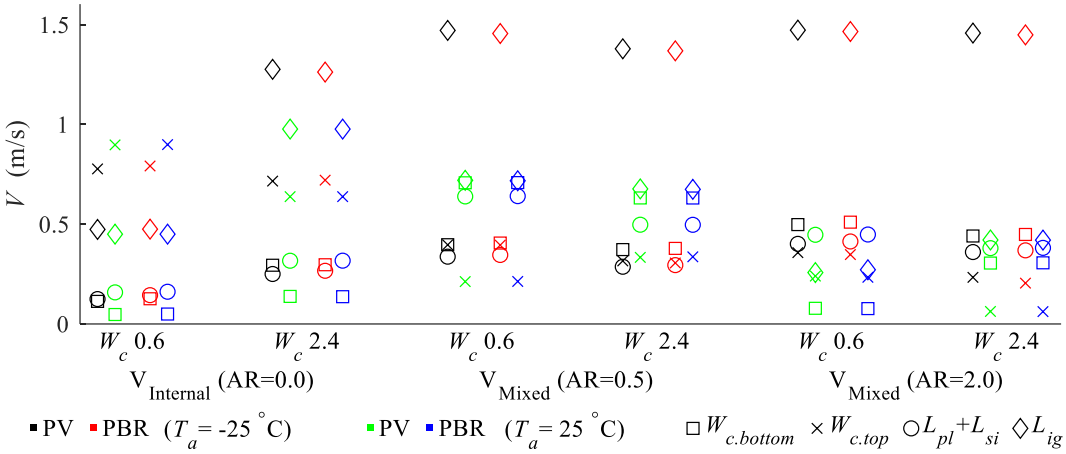


Figure 3.11. Mean velocity adjacent to the cavity top, cavity bottom, PVs/PBRs, and inner glass layer.

Figure 3.12 presents the temperature variation along the cavity width in the upper and the lower halves. At -25 °C, the cavity temperature in the lower half ranged from -14.7 °C to 16.8 °C and in the upper half from 2.0 °C to 21.2 °C. For the lower half, V_{Mixed} decreased the average air temperature from 16.3 °C to -6.8 °C and to -11.1 °C for AR=0.5 (2.4 m) and AR=2.0 (2.4 m). For narrow cavities (0.6 m), the temperature drop was from 13.3 °C to -10.8 °C and to -12.2 °C for AR=0.5 and AR=2.0, respectively. At 25 °C, the cavity temperature ranged from 24.7 °C to 29.8 °C for both halves. Deductively, the impact of the ambient temperature was more dominant in winter in the lower half for all ventilation schemes and cavity sizes. In summer, the temperature of the lower half was always slightly higher than the upper half by around 1.2 °C, except for AR=2.0 (2.4 m), where the large external vent size introduced more cold air and the wide cavity size enhanced the flow dispersion. $V_{Internal}$ (0.6 m) had the maximum difference of 2.3 °C because the heat buildup by the panels was not opposed by either the relatively cold ambient stream or the

backflow from the cold occupied space stream. In winter, the temperature difference between the two halves of the internally ventilated cavities was around 7.1 °C for W_c = 0.6 m. However, this difference almost vanished for W_c = 2.4 m due to the backflow from the upper half to the lower half. Such backflow with V_{Mixed} decreased the temperature difference between the upper and the lower halves from 20.0 °C in W_c = 0.6 m to 15.0 °C in W_c = 2.4 m. In winter, the cavity's lower half in the case of W_c = 2.4 m was warmer than that of W_c = 0.6 m by around 2.9 °C. This resulted in saving heating energy by 3.3, 4.2, and 1.2 kJ/kg for $V_{Internal}$, AR = 0.5, and AR = 2.0, respectively.

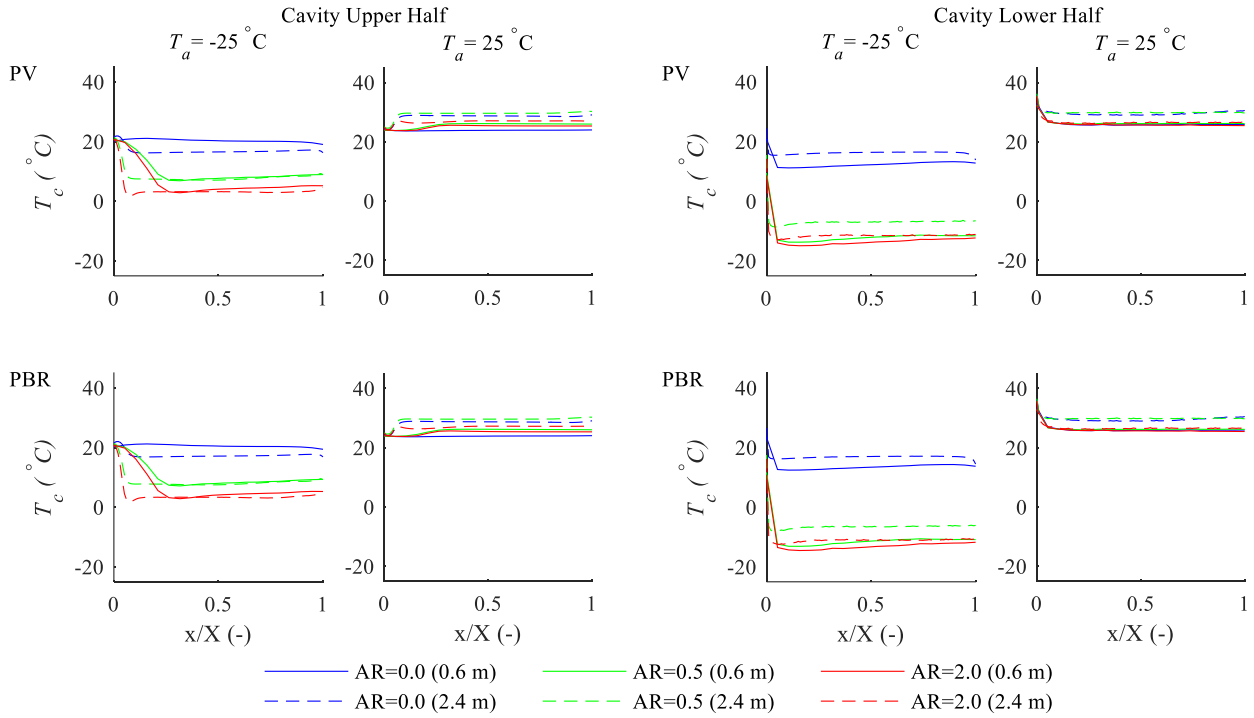


Figure 3.12. Temperature variation along the cavity width in both the upper and the lower halves in winter and summer for all ventilation schemes.

To investigate the impact of cavity width and ventilation scheme on PVs/PBRs performance, all ventilation schemes were examined by fixing the ambient temperature and the solar irradiation. Figure 3.13 exhibits the generated energy, conversion efficiency, heat loss, and associated temperature for the PV and PBR panels. The panels contribution was maximum in winter due to the low incidence angle, which offered full solar exposure even in wide cavities. Such a contribution ranged from 52.9 W/m^2 by $V_{Internal}$ (2.4 m) to 57.2 W/m^2 by AR=2.0 (0.6 m). The cooling effect imposed on the PVs increased their efficiency. For AR = 0.5 (0.6 m), the PV panels'

temperature was lowered by 17.5 °C, hence the solar cell efficiency increased from 19.9% to 21.4%. This increase corresponds to generating 3.9 W/m^2 of the building's energy use. For an average of six sunny hours per day, this value corresponded to around 8.5 kWh/m^2 per year (3.9 W/m^2 × 6 hours/day × 365 days/year). A similar trend was achieved with AR = 2.0 (0.6 m). In summer, the high incidence angle and the shading effect in wide cavities weakened the panels' energy generation. The PV panels produced around 20.3 W/m^2 with W_c = 0.6 m and 7.1 W/m^2 with W_c = 2.4 m. Similarly, PBRs produced around 9.3 W/m^2 and 3.3 W/m^2 with the same cavity sizes, not accounting for the thermal energy conversion of these panels. The lower conversion efficiency of PBRs led to higher heat loss. This loss was 14.5% higher than that of PVs (229 W/m^2 compared to 200 W/m^2).

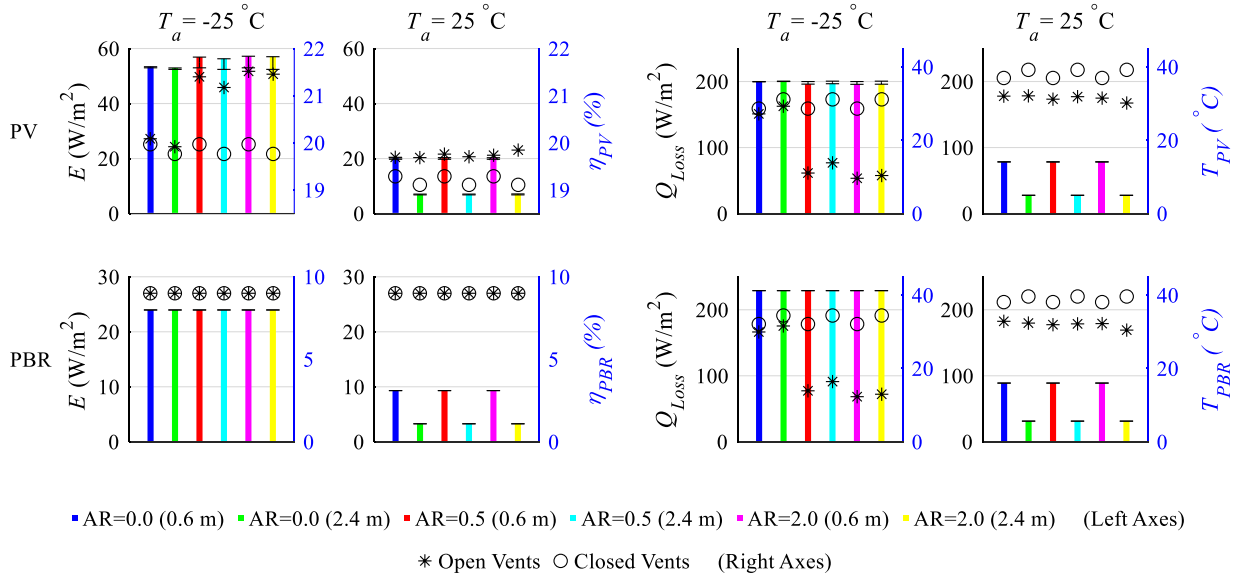


Figure 3.13. Generated energy, conversion efficiency, heat loss, and associated temperature for the PVs/PBRs in all cases. Colored bars represent ventilation schemes and whiskers extend to the maximum and minimum to express the amount of increment or decrement if the vents are closed.

For microalgae performance, the allowable and optimal temperature ranges for cultivation have been found to be 15–35 °C and 25–30 °C, respectively [95]. When the temperature of the PBRs' panels (T_{PBR}) increased, heat was transferred to the inside water by free convection with a mean heat transfer coefficient (h) of 314.1, 300.1, and 280.8 W/m^2·K when T_w was at 25, 30, and 35 °C, respectively. The convective heat transfer to the PBRs' water (q) was in the range of 2.2-24.5 kW/m^2 depending on T_w and T_{PBR}. To encounter q, cold water was introduced to keep T_w within

the acceptable limit. The amount of such cold water ($\dot{m}_{water}$) was dependent on the available water temperature ($T_{w,in}$) and q. The colder the available water, the less the required flow rate. For T_{PBR} of 40 ℃ and 60 ℃, $\dot{m}_{water}$ varied form 0.02 kg/s to 0.39 kg/s and from 0.16 kg/s to 1.18 kg/s with an overall average value of 0.26 kg/s. 10 ℃ reduction in $T_{w,in}$ cut down the required $\dot{m}_{water}$ by 81.6% (from 0.76 kg/s to 0.14 kg/s). The maximum T_{PBR} here was 39.6 ℃ (≈ 40 ℃), as shown in Figure 3.13. For an average $T_{w,in}$ of 15 ℃, the required mass flow rates were 0.12 kg/s, 0.08 kg/s, and 0.06 kg/s for T_w of 25 ℃, 30 ℃, and 35 ℃, respectively. Figure 3.14 demonstrates the impact of T_w, $T_{w,in}$, and T_{PBR} on h, q, and $\dot{m}_{water}$.

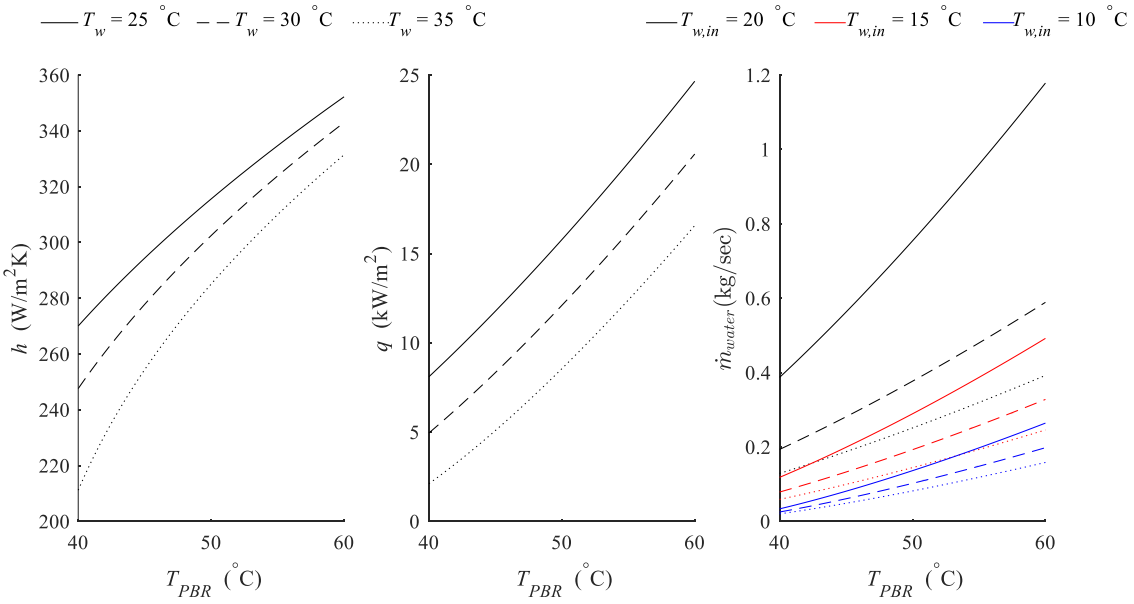


Figure 3.14. PBRs' panels associated inside convective heat transfer coefficient, heat added to water, and required water flow rate to keep the PBRs' water within the acceptable temperature range.

3.4 Summary of Chapter

The purpose of this chapter was to examine DSF systems with integrated PVs/PBRs in cold climates. Hourly heat transfer analysis was performed on annual basis to study the solar energy conversion for different cavity widths. Assessment of PVs and PBRs involved modeling of solar irradiation, energy production, panels efficiency, and heat gain in DSF cavity and occupied space. The developed model has been experimentally validated with an average error of 1.9 °C. The findings highlight:

- **Internal Ventilation:** For internal ventilation, the model provided better heat insulation and relatively warm temperature, especially for wide cavities in cold conditions.

- **Mixed Ventilation:** In the case of mixed ventilation mode, better heat insulation was offered by forcing the warm air stream to flow over the inner glass layer.
- **Seasonal Insulation:** In winter, the weakest and perfect thermal shields were achieved by internally ventilated narrow cavities and mixed ventilated cavities while in summer, the airflow over the inner glass acted as a coolant for the occupied space.
- **Efficiency in Summer:** The efficiency drop was likely to occur in summer for PVs only due to hot ambient. On contrary, the high temperature impact on PBRs was negligible as the fluid temperature kept below that of the assembly because of the water steady flow into the panels.
- **Performance Comparison:** In terms of shading, the drop in efficiency would lead to low PV performance due to two reasons: 1) Ineffective shaded area on solar cells, and 2) Electrical loads of solar cells acting in reverse bias as hot-spot creators that increased the temperature of PV panels. Overall, PBRs outweighed PVs by 8.1% for space heating purposes (91.7 W/m^2 compared to 84.8 W/m^2).
- **Thermal Energy Preservation:** Moreover, PVs/PBRs managed to preserve the occupied space thermal energy. Heat loss from common façades in winter had an annual average of 82.1 W/m^2. This was countered by 35.7 W/m^2 heat gain with the proposed DSF.
- **Ventilation Recommendations:** For maximum benefit, a mixed ventilation scheme should be adopted in DSF throughout the year with adjustable external air vents. In wide cavities, these adjustable vents should be regulated depending on the ambient temperature and the personal occupancy level in the cavity. In narrow cavities, the cavity size is already hindering inhabitation, but the adjustable vents should be fully opened as long as the ambient temperature is lower than that of the solar panels.

These findings underscore the importance of ventilation schemes and proper cavity design in enhancing thermal insulation and energy preservation, making them viable solutions for sustainable building practices in harsh weather conditions. However, further research is needed to examine and optimize various DSF system designs incorporating PBRs, with a particular focus on developing a multi-objective optimization framework to address heat buildup in the cavity during hot periods, which is the scope of the next chapter.

Chapter 4: Optimization to Maximize Thermal and Bioenergy Generation[1]

The previous chapter highlighted the need to examine and optimize various DSF system designs incorporating PBRs, particularly focusing on developing a multi-objective optimization framework to address heat buildup in the cavity during hot periods. While the primary focus of the thesis is on reducing heating requirements in cold climates, it is also necessary to improve the system's overall efficiency by mitigating heat accumulation in the cavity during warmer periods. This chapter addresses this requirement and fulfills the second objective by developing a heat transfer model for PBRs integrated into the inner layer of both cellular and multistory DSFs. It employs graphical optimization to identify the optimal design parameters for such systems. Graphical optimization was selected due to its simplicity and accuracy in addressing two-variable optimization problems. Additionally, the chapter formulates a multi-objective problem to minimize heating and cooling loads while maximizing bioenergy generation from the PBRs. It compares the optimized DSF system with both unoptimized DSF systems and common SSFs to assess the feasibility of the developed framework in different climate zones.

4.1 Introduction

Various methods have been explored to address the challenges posed by multi-objective optimization problems in the context of building façades and renewable energy integration [14,176–178]. However, a thorough search of the relevant literature didn’t reveal any studies examining bio-reactive DSFs in relation to maximizing heat and biomass output using graphical optimization. Pareto curve optimization of building cogeneration systems resulted in a significant 45.2% reduction in CO_2 emissions with a modest 7.3% increase in total annual cost by employing

[1]This chapter is based on the following articles:

Elmalky, A. M., & Araji, M. T. (2023). Multi-objective problem of optimizing heat transfer and energy production in algal bioreactive façades. *Energy*, *268*, 126650 [14].

Elmalky, A. M., & Araji, M. T. (2024, January). Pareto Optimization for Enhanced Building Energy Efficiency and Bioenergy Generation. In *2024 4th International Conference on Smart Grid and Renewable Energy (SGRE)* (pp. 1-6). IEEE [71].

mixed integer linear programming techniques [179]. Evolutionary algorithms for high-quality Pareto fronts increased energy savings by 11% when considering energy conservation and occupants' comfort as conflicting objectives [180]. Nevertheless, the employed multilevel hierarchical control systems had limited adaptability to dynamic situations such as environmental conditions or occupant preferences. Pareto front coupled with Design Builder had an error of 2.7% to optimize envelope parameters for a 10.6% reduction in energy consumption and a 32.2% improvement in thermal comfort [181]. However, the employed non-dominated sorting Genetics Algorithm (GA) involved a significant computational burden, particularly when dealing with large-scale optimization problems. The greedy algorithm reduced the computational load by over 48.5% by obtaining near-optimal solutions aligned with the Pareto front population (PFP) [182]. Nonetheless, such an algorithm tended to be trapped in local extrema, and its performance was highly influenced by the choice of initial points.

In this chapter, the developed heat transfer model for integrating PBRs in the inner layer of the DSF was applied to two façade systems. Such systems include: 1) A cellular DSF with PBRs integrated at the floor plenum, and 2) A multistory DSF with PBRs alternating with the inner glass layer of the façade. Table 4.1 shows additional comparison between both systems. Graphical optimization was carried out to identify the optimal design parameters for such systems. A multi-objective problem was then formulated to minimize heating and cooling loads and maximize bioenergy generation from the PBRs. Two optimization methods were employed to solve this problem using the Pareto front. The first method utilized a pattern Search Algorithm (SA) to iteratively search for nondominated points while satisfying all bounds and linear constraints at each iteration. The second method utilized a controlled elitist GA to maintain population diversity and converge toward an optimal Pareto front. Finally, the optimized DSF system was compared to both unoptimized DSF systems and common SSFs to assess the feasibility of the developed framework in different climate zones.

4.2 Method

In this chapter, the design variables of the examined systems were defined and shading analysis was performed to estimate the amount of solar irradiation received by the elements in the DSF inner layer. Hourly thermal simulations were carried out to calculate the temperature values of all

DSF elements. This was required to calculate the thermal and bioenergy output from the integrated PBRs in addition to the heat gain/loss by the occupied space. Graphical optimization was performed to determine the optimal design parameters of the two DSF systems that maximized thermal and bioenergy from the PBRs. A multiple-objective problem aiming to minimize heating and cooling loads while maximizing bioenergy from PBRs was formulated using both a pattern search algorithm and a controlled elitist GA.

4.2.1 Description of model geometry

Flat plate PBRs were integrated to the inner layer in both systems, to preserve the heat gained from being lost to the cold surroundings, hence keeping the temperature of the PBRs' media within acceptable limits with minimum heating requirements. Figure 4.1 shows the proposed two systems with both façades oriented due south. In both systems, the 4 m floor to floor height was divided to 3 m for the occupied space and 1 m for the plenum. Flat plate PBRs only covered the plenum in system 1, while the occupied space was covered by the inner glass layer. In system 2, the PBRs and the inner glass layer covered both the occupied space and the plenum alternately in the vertical and the horizontal directions. For system 1, the cavity width (W_c) varied between 0.6 m and 2.4 m, and the PBRs' tilt angle (β) varied between 30º and 90º. For system 2, the PBRs panels' base width (W_{pl}) varied between 0.5 m and 2 m, the PBRs' tilt angle (β) varied between 30º and 90º, and the PBRs' top offset (d) varied between 0 m and 0.2 m. The aim was to monitor the impact of these variations on the PBRs' temperature, heat generation, and biological mass production in winter and summer for both systems.

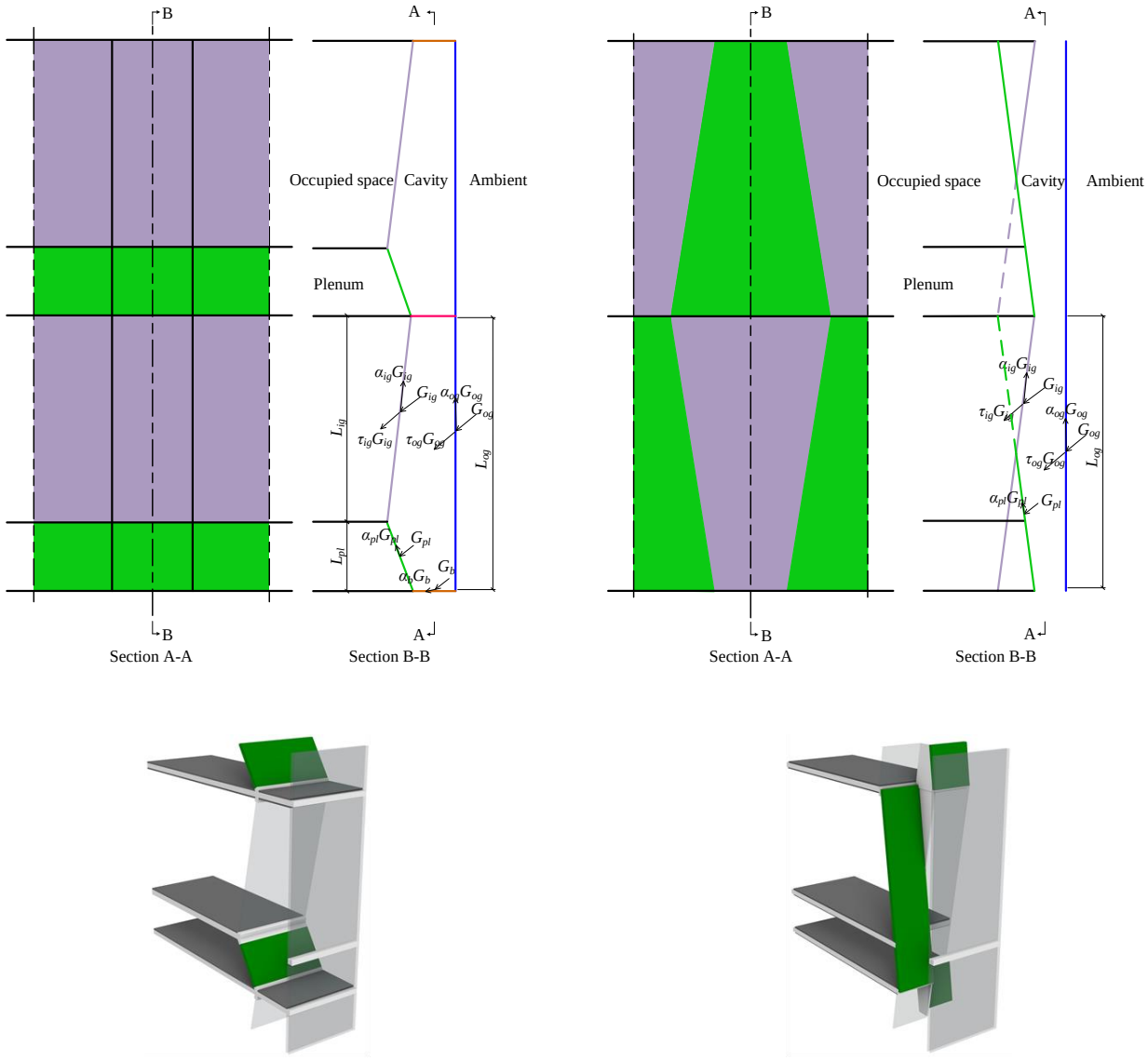


Figure 4.1. Top, proposed façade systems integrating PBR panels. Bottom, 3D representations of cellular and multistory DSF systems.

Table 4.1. Differences between cellular and multistorey DSF systems.

	Cellular DSF	Multistorey DSF
Cavity Geometry	Separated by individual floors	Connected across multiple floors
Cavity Accessibility	Accessible to building occupants	Inaccessible to building occupants
Privacy	Reduced privacy in occupied areas due to accessible cavity	Enhanced privacy in occupied areas due to closed cavity
Solar Access	Limited solar penetration due to segmented cavities	Greater solar penetration due to connected cavity
Insulation (Heat, Fire, Sound)	Superior insulation due to segmented cavities	Weak insulation due to continuous cavity
Natural Ventilation	Restricted ventilation due to limited cavity height	Improved ventilation due to extended cavity height
PBR Coverage	PBR projects over 25% of the façade surface	PBR projects over 50% of the façade surface
PBR Structural Support	Requires less structural support due to lighter PBR load	Demands more structural support due to heavier PBR load
Water Pressure Inside PBR	Equivalent to 1 m of water pressure	Equivalent to 4 m of water pressure
Optimized Variables	PBR tilt angle and cavity width	PBR tilt angle and panel width

4.2.2 Rate of heat transfer through the DSF

Both the radiative and the convective thermal resistance models for the two systems are shown in Figure 4.2. System 1 has five elements enclosing the cavity. Heat transfers by radiation between any pair of these elements as long as they have a view factor. Also, heat transfers by radiation between the occupied space walls and the inner glass layer at a rate of $q_{rad,rw\text{-}ig}$, and between the outer glass layer and the sky at a rate of $q_{rad,og\text{-}s}$. Convective heat transfer in the same system allows heat to move between the occupied space air and the inner glass layer at a rate of $q_{conv,ra\text{-}ig}$. Besides, the cavity top, bottom, inner glass, and plenum panel exchange heat by convection with the cavity air at a rate of $q_{conv,t\text{-}c}$, $q_{conv,b\text{-}c}$, $q_{conv,ig\text{-}c}$, and $q_{conv,pl\text{-}c}$, respectively. The air in the cavity exchanges heat by convection at a rate of $q_{conv,c\text{-}og}$ with the outer glass layer, which in turn exchanges heat by the same mode of heat transfer with the ambient air at a rate of $q_{conv,og\text{-}a}$. System 2 has the same heat interaction between the occupied space and the inner glass, and between the outer glass and

the surrounding. System 2's structure allows the panel to contact some building occupied space. Therefore, heat is exchanged between the panels and the occupied space by both radiation and convection at a rate of $q_{rad,pl\text{-}rw,}$ and $q_{conv,pl\text{-}ra}$, respectively. Moreover, the cavity in system 2 interacts only with 3 elements; the inner glass, the outer glass, and the panels. Heat transfers by radiation between the panels and both the inner glass and the outer glass at a rate of $q_{rad,pl\text{-}ig}$, and $q_{rad,pl\text{-}og}$, respectively. The inner glass exchanges heat by radiation with the outer glass at a rate of $q_{rad,rw\text{-}ig}$. The cavity exchanges heat by convection with the outer glass at a rate of $q_{conv,c\text{-}og}$, and exchanges heat by convection with the inner glass and the panels at a rate of $q_{conv,ig\text{-}c}$, and $q_{conv,pl\text{-}c}$, respectively.

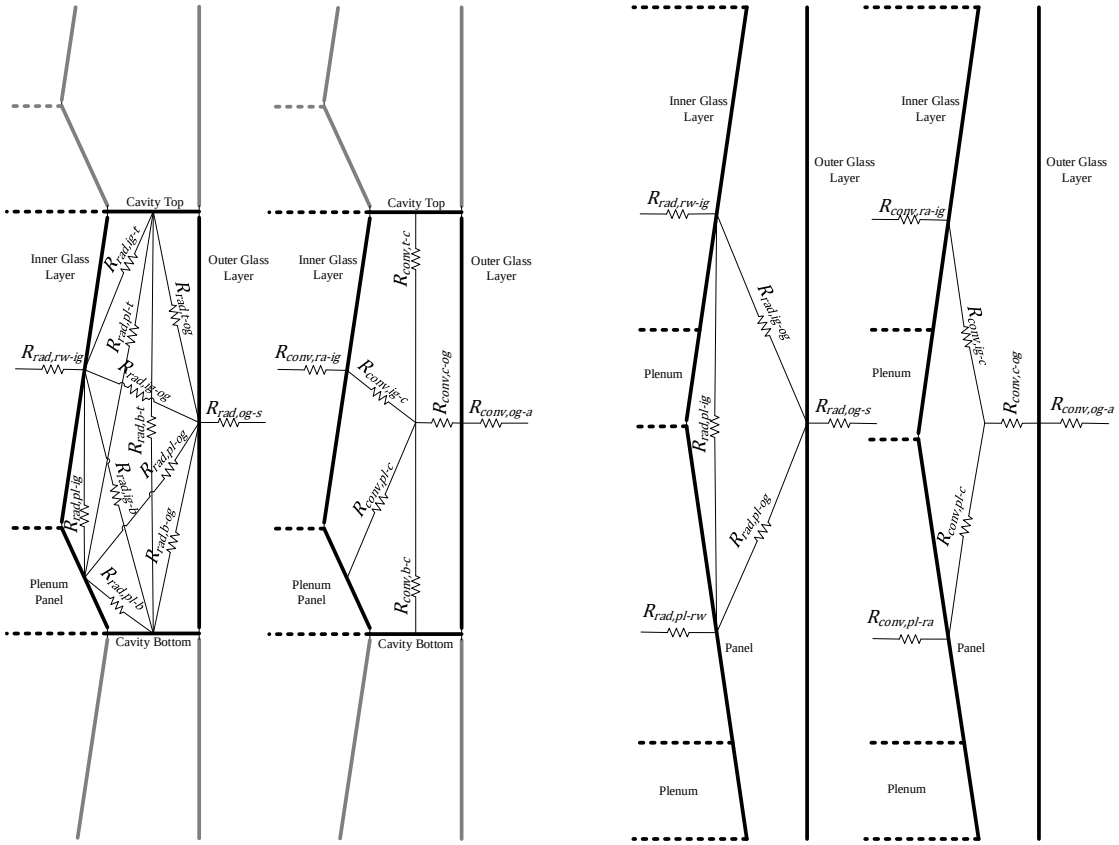


Figure 4.2. Convective and radiative thermal resistance models for system 1 (left) and system 2 (right).

Considering the solar heat gain to the DSF elements, the conversion of energy to biological mass, and the convection between the panels walls and the inside water, the energy balance equations for system 1 are as follows,

$$\alpha_{og}G_{og} + q_{rad,ig-og} + q_{rad,pl-og} + q_{rad,t-og} + q_{rad,b-og} + q_{conv,c-og} = q_{rad,og-s} + q_{conv,og-a} \quad (4.1)$$

$$q_{conv,ig-c} + q_{conv,pl-c} + q_{conv,t-c} + q_{conv,b-c} = q_{conv,c-og} \quad (4.2)$$

$$\alpha_{ig}G_{ig} + q_{rad,rw-ig} + q_{rad,pl-ig} + q_{conv,ra-ig} = q_{rad,ig-og} + q_{rad,ig-t} + q_{rad,ig-b} + q_{conv,ig-c} \quad (4.3)$$

$$\alpha_{pl}G_{pl} = q_{rad,pl-og} + q_{rad,pl-ig} + q_{conv,pl-c} + q_{rad,pl-t} + q_{rad,pl-b} + B + q_{conv,pl-w} \quad (4.4)$$

$$q_{rad,ig-t} + q_{rad,pl-t} + q_{rad,b-t} = q_{conv,t-c} + q_{rad,t-og} \quad (4.5)$$

$$\alpha_b G_b + q_{rad,ig-b} + q_{rad,pl-b} = q_{rad,b-t} + q_{conv,b-c} + q_{rad,b-og} \quad (4.6)$$

Similarly, system 2 energy balance equations are as follows,

$$\alpha_{og}G_{og} + q_{rad,ig-og} + q_{rad,pl-og} + q_{conv,c-og} = q_{rad,og-s} + q_{conv,og-a} \quad (4.7)$$

$$q_{conv,ig-c} + q_{conv,pl-c} = q_{conv,c-og} \quad (4.8)$$

$$\alpha_{ig}G_{ig} + q_{rad,rw-ig} + q_{rad,pl-ig} + q_{conv,ra-ig} = q_{rad,ig-og} + q_{conv,ig-c} \quad (4.9)$$

$$\alpha_{pl}G_{pl} = q_{rad,pl-og} + q_{rad,pl-ig} + q_{rad,pl-rw} + q_{conv,pl-ra} + q_{conv,pl-c} + B + q_{conv,pl-w} \quad (4.10)$$

where α_{og}, α_{ig}, α_{pl}, and α_b are the absorbitivity of the outer glass layer, inner glass layer, PBR panel, and cavity bottom, respectively. G_{og}, G_{ig}, G_{pl}, and G_b are the solar irradiation incident on the previous elements with the same order, W/m^2. B is the generated biological energy, W/m^2. Convective and radiative heat transfer were calculated following the same procedure and assumptions outlined in the previous chapter.

4.2.3 Solar irradiation and energy generation model

With south-oriented façades, outer glass layers receive solar irradiation at a rate of

$$G_{og} = (I_b \times \cos\theta_v) \times L_{og} \quad (4.11)$$

where I_b is the direct normal irradiation, W/m^2. θ_v is the solar incidence angle on vertical surfaces, rad. L_{og} is the outer glass layer height, m. Solar irradiation incident on other elements behind the outer glass layer follows the relation

$$G_x = \tau_{og} \times I_b \times \cos\theta_x \times L_x \times SF_x \quad (4.12)$$

where τ_{og} is the outer glass layer transmissivity. G_x is the solar irradiation incident on any element behind the outer glass layer, W/m. θ_x, L_x, and SF_x are the solar incidence angle, length (m), and shading factor corresponding to this element, respectively. The shading factor for system 1 was evaluated by comparing the solar altitude angle (α) to the angles enclosed by the line joining the cavity upper tip and both the inner glass layer bottom (α_{ig}) and the PBRs panels bottom (α_{pl}). Figure 4.3 shows the sequence followed to evaluate the shading factor for system 1. A uniformly distributed heat flux was considered over the partially irradiated elements.

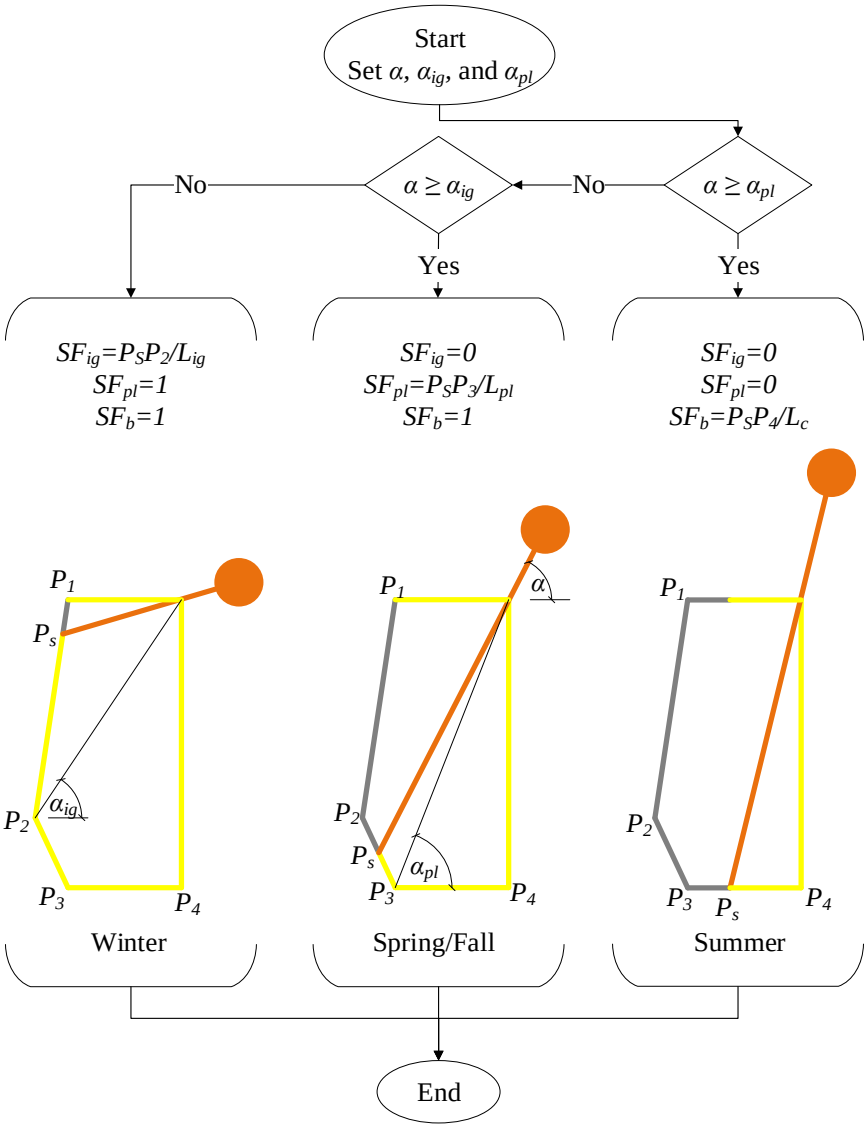


Figure 4.3. Shading factor calculation procedure for system 1.

Figure 4.4 shows the methodology implemented to evaluate the shading factor for the PBRs panels in system 2. First of all, the solar ray was expressed using the hour angle (ω) and the solar altitude angle (α) in the 3D coordinates. The parallel form of this line that intersects with both lines L_1 and L_2 was solved with the PBRs' surface equation in the same coordinates to get P_1. Also, the parallel form of the solar ray that passes through P_5 was solved with the PBRs' surface equation in the same coordinates to get P_4. Therefore, the shaded area was enclosed by the points P_1, P_2, P_3, and P_4. However, in the early morning, the points P_1 and P_4 could lie outside the PBRs plane borders. In this case, P'_1 and P'_4 were obtained by intersecting both P_1 P_2 and P_3 P_4 with L_3. Consequently, points P'_1, P_2, P_3, and P'_4 enclosed the new shaded area. When the solar altitude angle (α) was

higher than the PBRs plates' tilt angle (β), a uniform shaded zone started to creep downstream the panels similarly to system 1. This area was added to the area estimated previously.

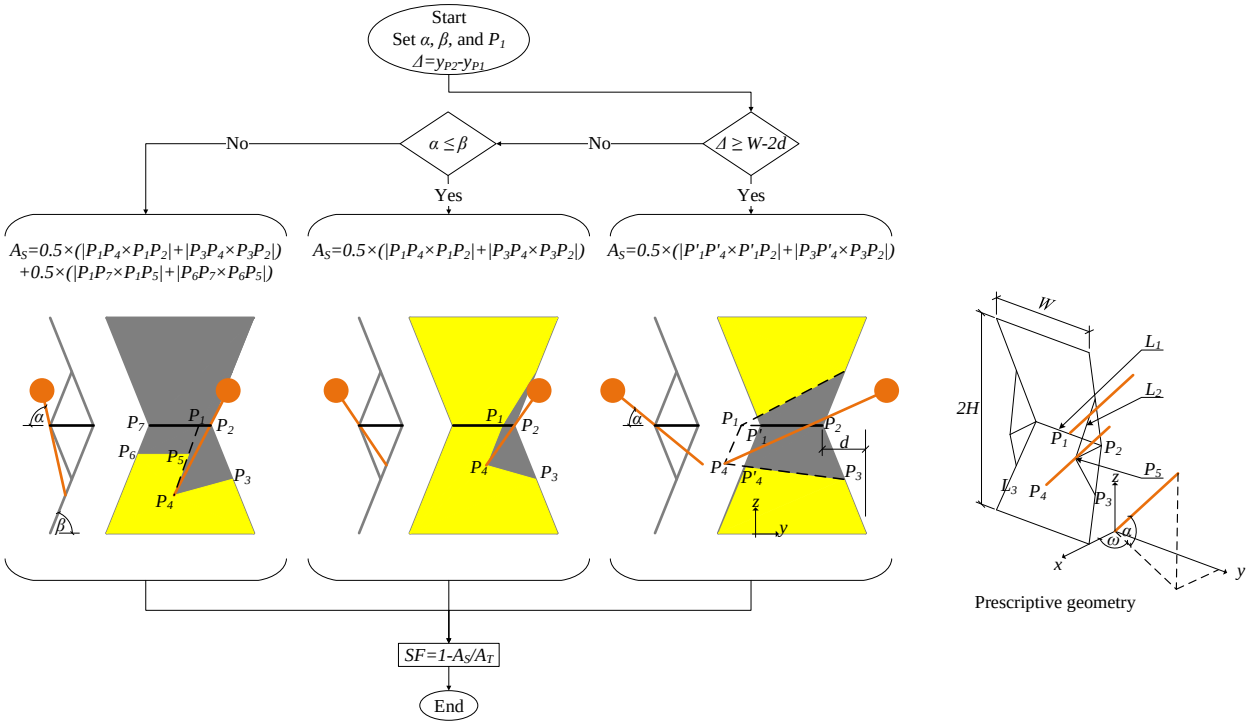


Figure 4.4. Shading factor calculation procedure for system 2.

Finally, the biological energy generated from the PBRs panels can be calculated from

$$B = \eta \times \tau_{og} \times I_b \times \cos\theta_{pl} \times A_{pl} \times SF_{pl} \tag{4.13}$$

where η is the conversion efficiency from solar irradiation to biological energy. θ_{pl} is the PBRs panels' solar incidence angle. A_{pl} is the area of the panels, m^2. SF_{pl} is the panels' shading factor. This work optimized the design variables of DSF systems to maximize both the biological energy output (B), shown in equation 25, and the thermal energy output ($q_{conv,pl\text{-}w}$) shown in equations 4 and 10. In mathematical terms, the multi-objective optimization problem can be formulated as

$$\max_{x=\begin{bmatrix} W_c \\ \beta \end{bmatrix},\ or\ \begin{bmatrix} W \\ \beta \end{bmatrix}} \left(B(x), q_{conv,pl-w}(x) \right) \tag{4.14}$$

4.2.4 Heat gain by the building façade

The hourly heat gain by the building façade was calculated by

$$Q_f = I_f + q_{rad,s-f} + q_{con,a-f} \quad (4.15)$$

where Q_f is the hourly heat gain by the building envelope, W/m^2. I_f is the solar irradiation gained through the façade, W/m^2. $q_{rad,s-f}$ is the heat gain by radiation from the sky, W/m^2. $q_{con,a-f}$ is the heat gain by convection from the ambient air, W/m^2. The absolute annual average heat gain was thus represented by

$$Q_{avg} = \frac{1}{N}\sum_{n=1}^{N}|Q_f| \quad (4.16)$$

where n is the number of hours within a year. The energy savings in comparison to SSFs were estimated by

$$E_s = Q_{avg,SSF} - Q_{avg,DSF} \quad (4.17)$$

Hourly biological energy harvest (B) was expressed by

$$B = \eta \times \tau_{og} \times I_b \times \cos\theta \times (1 - SF) \quad (4.18)$$

where τ_{og} is the outer glass transmissivity. I_b is the direct solar irradiation, W/m^2. θ is the incidence angle on the PBRs', rad. SF is the shading factor quantifying the proportion of the PBRs' area that is shaded from solar irradiation. SF was calculated using the framework developed in [14,15]. η is the efficiency by which solar energy is converted into bioenergy within the PBRs. η was reported to be varying between 4.5% and 6.5% annually [77], while another study reported η as 9% [19]. η was thus influenced by factors such as location, PBR design, and operational variables. For simplifying the analysis, η was assumed to be 9%, a value consistent with previous models assessing PBR performance [14,15]. The annual average bioenergy generation was calculated as

$$E_{avg} = \frac{1}{N}\sum_{n=1}^{N} B \quad (4.19)$$

4.2.5 Multi-Objective Optimization

Pareto SA was employed to optimize objectives E_{avg} and Q_{avg} using inputs W and β. The algorithm determined the optimal front by iteratively assessing the rank, volume, distance, and spread of points in the solution space. Initially, candidate points were assigned ranks based on their dominance relationships. Nondominated points were solutions in the multi-objective optimization problem that were not dominated by any other solution in the population. These nondominated points lay on the Pareto front. The volume of this front was calculated by examining point distribution in the objective function space. The algorithm measured the distance between points

of the same rank to promote diversity. Finally, the spread was computed as an indicator of the Pareto front's movement between iterations [183–185].

The rank of a point had an iterative definition whereas nondominated points had rank = 1. For any integer $k > 1$, a point had rank k when the only points that dominate it have rank strictly less than k. Figure 4.5 illustrates the rank of multiple points.

Distance was the measure of the closeness of an individual to its nearest neighbors. The Pareto SA measured distance among individuals of the same rank within the objective function space. This was achieved by adding up the distances between each individual and its closest neighbors in all dimensions. For an individual i, the distance was calculated by

$$d(i) = E_{avg,i+1} - E_{avg,i-1} + Q_{avg,i+1} - Q_{avg,i-1} \tag{4.20}$$

where d is the distance measure. The algorithm sorted each dimension separately, so the term neighbors meant neighbors in each dimension. Individuals of the same rank with a higher distance had a higher chance of selection.

Spread was the measure of movement of the Pareto set. To calculate the spread, the Pareto SA evaluated the standard deviation of the distance for the Pareto front points (σ). The algorithm then calculated the sum of differences between the current and previous minimum-value Pareto points for the two objective function indices (μ). The spread was thus calculated by

$$S = \frac{\mu + \sigma}{\mu + Z\bar{d}} \tag{4.21}$$

where S is the spread measure. Z is the number of points. $\bar{d}$ is the average distance among these points. The algorithm converged to the Pareto front at lower values of the spread measure. This was achieved when the extreme objective function values did not change much between iterations (for small μ) and when the points on the Pareto front were spread evenly (for small σ).

The Pareto SA procedure was enhanced by incorporating a controlled, elitist GA, which is a modified version of NSGA-II [186]. The elitist GA prioritized individuals with higher fitness values (rank), ensuring that good solutions are preserved. The main iteration of the algorithm involved several steps. First, parents for the next generation were selected using a selection function, which was done through the binary tournament. Then, children were created from the

selected parents by applying mutation and crossover techniques. The objective function values and feasibility of the children were calculated and used to score them.

The current population and the children were combined into one matrix, referred to as the extended population. The rank and distance for all individuals in the extended population were computed. Finally, the extended population was trimmed to have the desired number of individuals (population size) by keeping the appropriate number of individuals of each rank. This process helped in creating a diverse and optimal population for the next iteration.

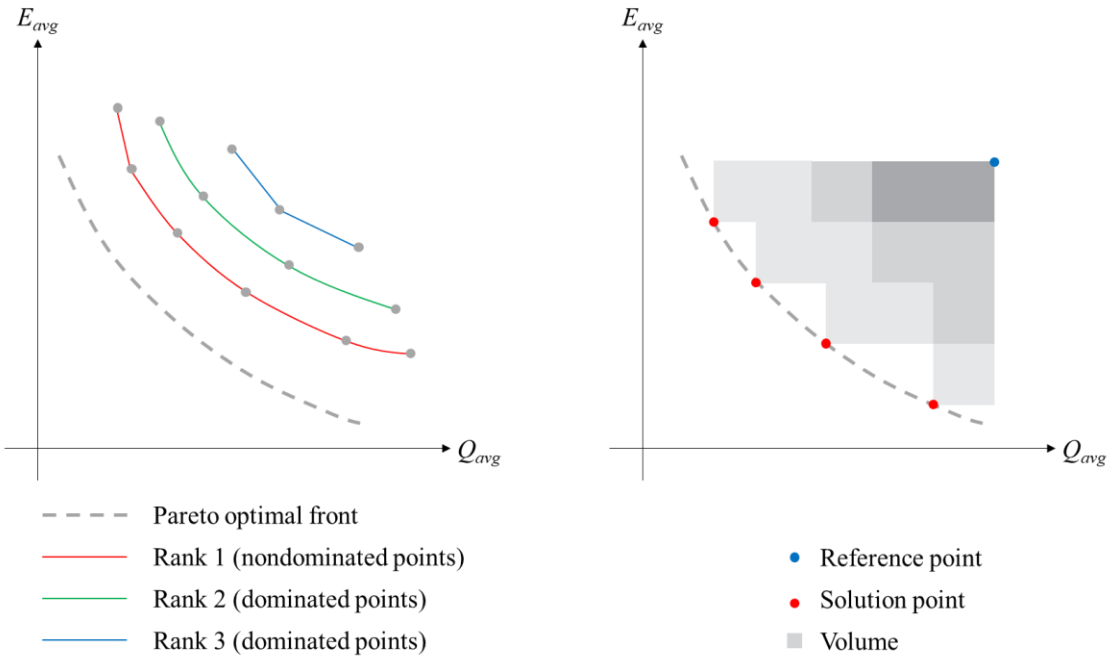


Figure 4.5. Left, multiple levels with different ranks. Right, Pareto front volume in relation to the reference point.

4.3 Results and Discussions

Elements in the cellular design received solar irradiation by different ratios depending on the cavity size (W_c), PBRs' tilt angle (β), and solar latitude angle (α) which was time dependent. Figure 4.6 shows the impact of the mentioned parameters on the solar exposure percentage. For W_c=2.4 m, the inner glass layer highest solar exposure percent at α=30º ranged from 42.6% to 52.9% as β ranged from 45º to 90º. Moreover, this percent went down as α increased such that the inner glass layer was totally shaded when α was greater than 41.5º, 45.2º, 48.3º, and 51.6º for β=45º, 60º, 75º

and 90º, respectively. The solar exposure percent was affected only when W_c was higher than 1.46 m for the cavity bottom, which had the lowest percentage (at α=70º) of 60.7% and 80.9% when W_c was 2.4 and 1.8 m, respectively. Regarding PBRs, W_c had higher impact on reducing the solar exposure percent for lower β. For β=45º, PBRs receive 62.7% of the solar irradiation when W_c=0.6 m in worst case (α=70º), while PBRs combined with W_c=2.4 m received no solar irradiation for α higher than 59.1º. Increasing β to 90º, PBRs experienced full solar exposure for W_c lower than 1.09 m at all time. However, vertical PBRs combined with W_c=2.4 m were also totally shaded for α greater than 59.1º.

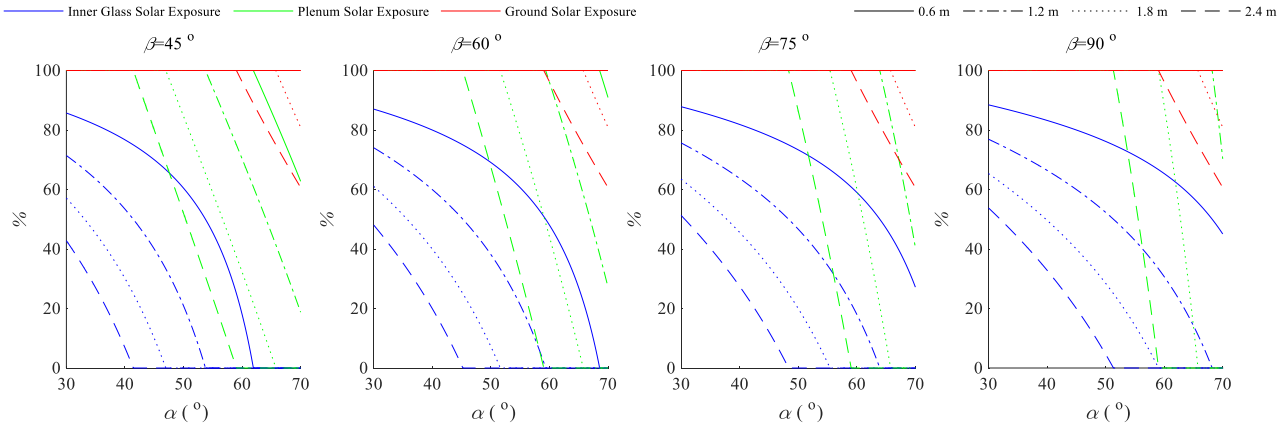


Figure 4.6. Variation of the solar exposure percent with the cavity width, PBRs' tilt angle, and solar latitude angle for the cellular design.

Figure 4.7 shows the impact of W, β, and d on the shaded area percentage in June 20th and December 21st. Both days were selected as representatives for summer and winter, respectively. The shaded area was always higher in summer because of higher α. This difference between the two seasons reached a maximum value of 25.2% for β=45º. The shaded area major trend comprised two trends before noon and identical two trends after noon. In the first trend, the shade crossed the panels' upper part totally from side to side, while the shade ended somewhere in the panels without reaching the far side in the second trend. In the first trend, the shaded area percentage decreased with time in winter at a rate of 2.1, 3.8, and 7.5% per hour when β was 45º, 60º, and 75º. The same trend in summer increased for β=45º at a rate of 2.1% per hour, was almost constant for β=60º, and decreased for β=75º at a rate of 3.5% per hour. The shaded area decreased in the second trend to approach zero percent at noon in all cases except for β=45º in summer, because α>β. Each extra

cm of *d* decreased the shaded area percentage by 0.61, 0.26, and 0.16% for *W* of 0.5, 1.0, and 1.5 m, respectively. Combining *W*=1.5 m, *d*=0.0 m, and β=75º proved to provide maximum solar exposure where the highest shaded area percentage was 26.2, and 23.4% in summer, and winter, respectively.

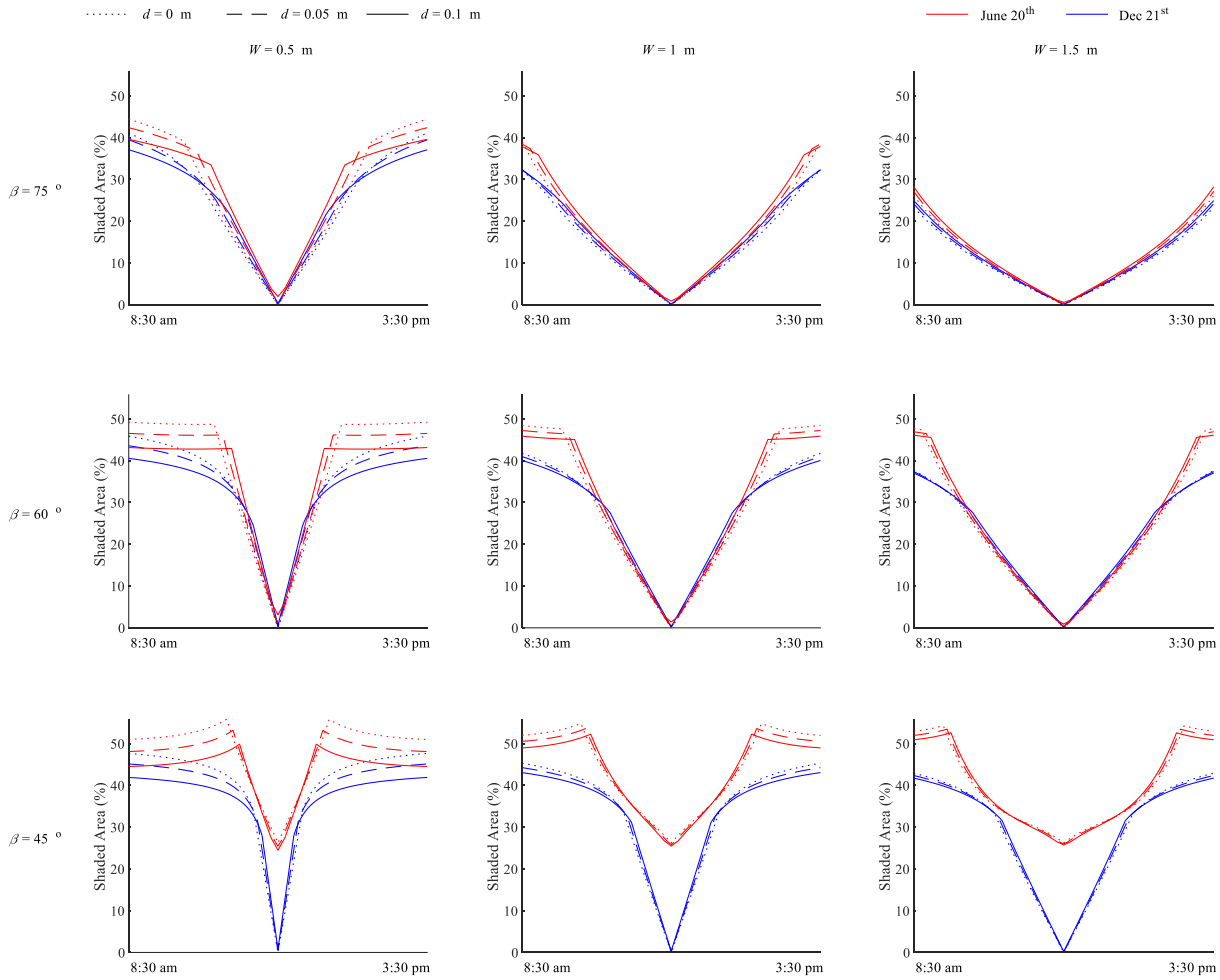


Figure 4.7. Shaded area percentage for different combinations of PBRs' base width(*W*), PBRs' tilt angle (β), and offset (*d*).

Figure 4.7 shows the shaded area percentage for the multistory design with φ=51.3°. By taking the complement to unity, averaging the results, and considering different locations with φ ranging from 25° to 65°, Figure 4.8 shows the mean shading factor, the mean incidence factor, and the predicted beam irradiation received by the multistory design in different locations. The average shading factor due to the side extrusions of the multistory design was independent on φ as long as

$\beta>\alpha$. Consequently, the shading factor increased with each 10º increase in φ at a rate of 6.8% and 11.4% in summer and winter, respectively. Tilting PBRs send their upper tips deeper into the inner layer, hence it was harder for solar irradiation to reach most of PBRs. Specifically, each 10º increase in β increased the shading factor at a mean rate of 9.2% and 5.3% in summer and winter, respectively. Generally, increasing φ by 10º had the same positive impact on the shading factor as increasing β by 7.4º and 21.5º in summer and winter, respectively. On average for all tilt angles, the incidence factor in summer increased at a rate of 9.8% per each 10º increase in φ. The incidence factor, per each 10º increase in φ, in winter increased for β=75° at an average rate of 3.3%, decreased for β=60° and β=45° at an average rate of 0.5% and 4.3%, respectively. In winter, β of 75° offered optimal performance by gaining the highest solar irradiation for all values of φ with 284.2 W/m² and 124.7 W/m² for φ=25° and 65°, respectively. The optimum β in summer was 60° which gained solar irradiation of 130.5 W/m² and 120.1 W/m² for φ=25 and 65, respectively.

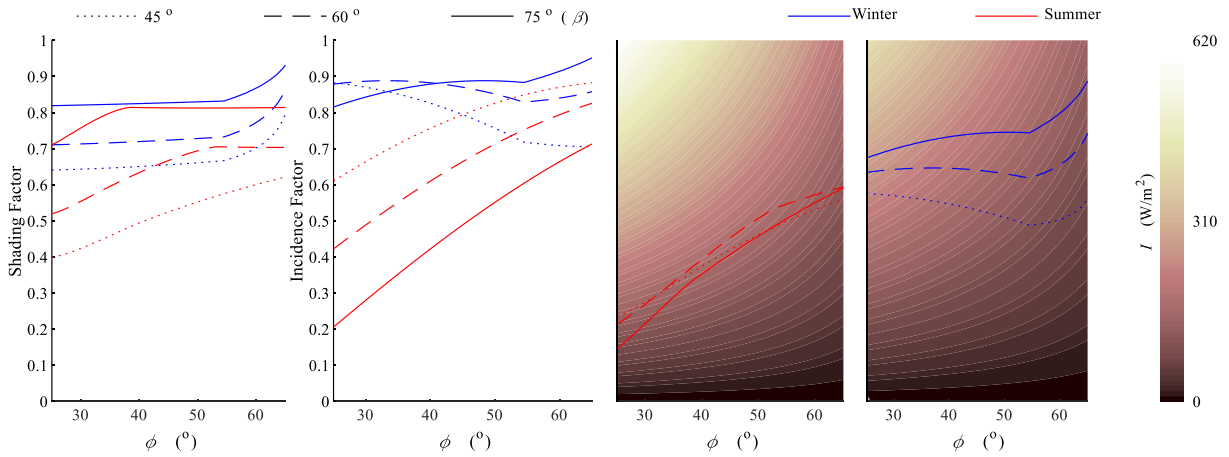


Figure 4.8. Multistory design average shading factor, average incidence factor, and estimated solar gain in different locations.

To harvest the highest available biological energy (B), PBRs' water was kept at 25 ℃ by removing thermal loads (+q) when the plates enclosing water were hotter than 25 ℃, or by imposing thermal loads (-q) when the plates were colder than 25 ℃. Figure 4.9 shows the impact of different combinations of W_c and β on T_{pl}, q, and B. T_{pl}, which was almost independent on β and slightly dependent on W_c, was higher in summer than winter by 0.6 ℃. As T_{pl} was always higher than 25 ℃ in summer, q was harvested throughout the day at a mean value of 59.7 and 31.8 W per m² of the façade for β of 45º and 90º, respectively. Lower β in narrow cavities increased the area

receiving solar irradiation without any shading. For instance, as β decreased from 90º to 45º, q went up from 54.1 to 111 W/m^2 and from 63.6 to 119.4 W/m^2 for W_c of 0.6 and 1.2 m, respectively. W_c of 2.4 m had almost constant peak of 83.2 W/m^2 for all βs, as the increase in area resulted from decreasing β was opposed by an increase in shade. The variations between qs harvested or demanded by the PBRs' water was due to the variations of T_{pl}. On the other side, B was dependent only on solar irradiation with no dependence on T_{pl}. As a result, B curves were identical in winter and in summer except for the time intervals affected by shading. As β decreased from 90º to 45º, mean B increased from 2.5 to 5.9 W/m^2 and from 3.1 to 4.3 W/m^2 in summer and winter, respectively. In summer, decreasing W_c from 2.4 to 1.8 m increased B from 4.3 W/m^2 to 8.5, 8.3, 6.9, and 5.1 W/m^2 for β=45º, 60º, 75º, and 90º, respectively.

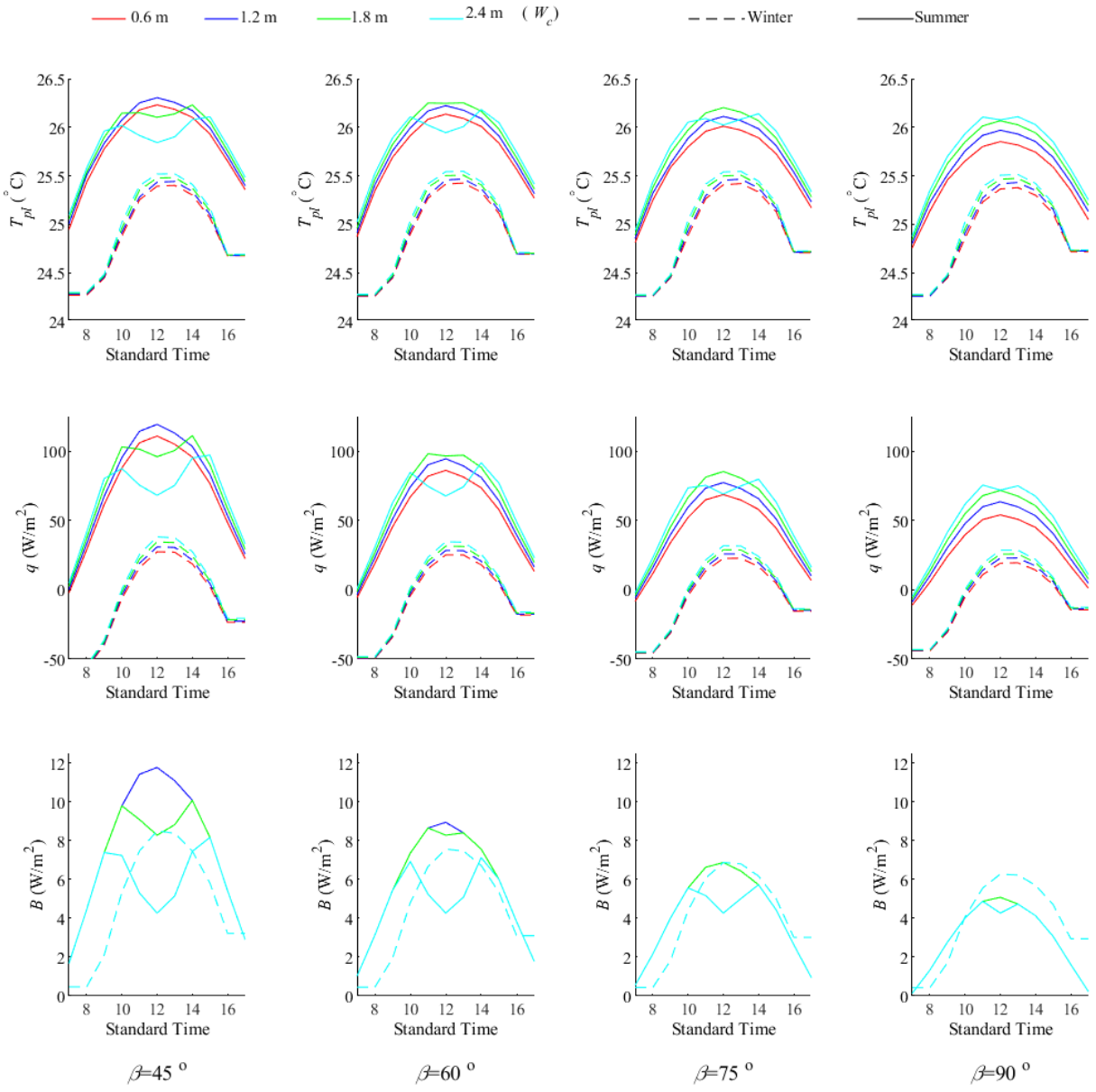


Figure 4.9. PBRs plates' temperature, thermal heat generation, and biological mass production for the cellular design.

The impact of the variables *d*, *W*, and β were investigated for the multistory design. *d* was excluded from the analysis due to its small range and insignificant impact. Figure 4.10 shows the impact of W_{pl} and β on the multistory design thermal performance. Similarly, for the cellular design, the multistory design had the panels' temperature higher than 25 ℃ in summer throughout the day, lower than 25 ℃ in early morning and late afternoon in winter, and generally higher in summer by 0.6 ℃ than winter. Compared to the cellular design, the multistory design generates on average

more q by 14.4% (53.9 W/m^2 compared to 47.1 W/m^2) and 38.0% (22.9 W/m^2 compared to 16.6 W/m^2) and more B by 65.9% (6.8 W/m^2 compared to 4.1 W/m^2) and 100.0% (7.2 W/m^2 compared to 3.6 W/m^2) in summer and winter, respectively.

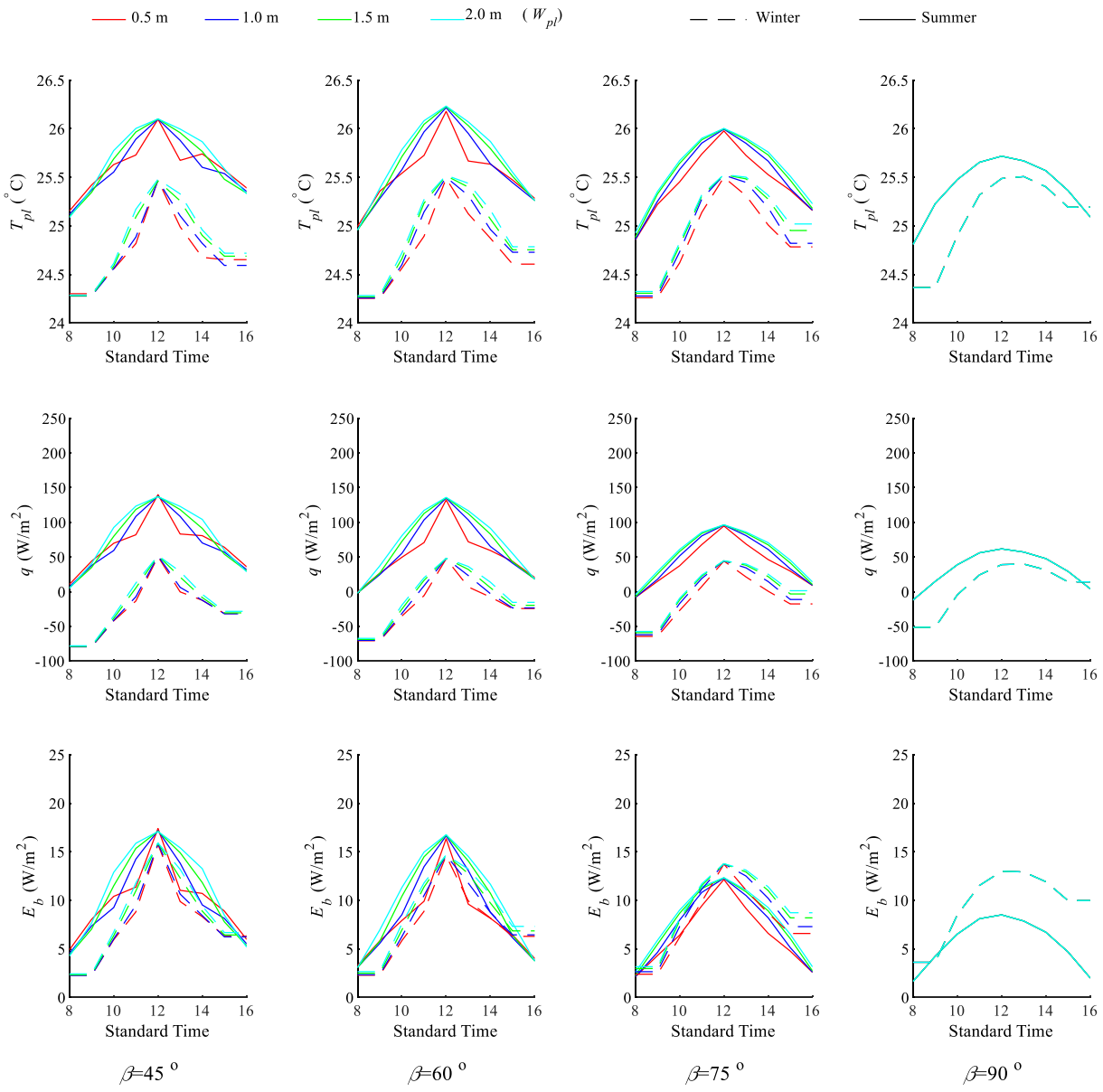


Figure 4.10. The multistory design performance in terms of PBRs plates' temperature, thermal energy gain, and biological energy generation.

The scatter plot, in Figure 4.11, showed a positive correlation between the two objectives B and $q_{conv,pl\text{-}w}$. This implied that both objectives can be maximized by tracking only one of them.

Therefore, B was maximized by optimizing the two DSF systems graphically where hourly simulation was performed for different pairs of the decision variables. The optimization decision variables were the pairs (W_c, β) and (W, β) for the cellular and multistory designs, respectively. B/B_{max} represented the normalized average of the annual energy harvest for both systems. Figure 4.11 shows the surface and 2D contour plots of B/B_{max} for different combinations of the decision variables. The optimum solution was thus achieved in the regions where B/B_{max} approached unity. B/B_{max}=1 when the decision variables for the cellular and multistorey designs were (W_c=0.6 m, β=47.4 °) and (W=2.0 m, β=34.1 °), respectively. However, The impact of W_c in the range 0.6-1.3 m was barely noticed in the cellular design. Compared to the cellular design, the optimum design variables, in the multistorey system, generated a higher annual average B of 8.3 W/m^2.

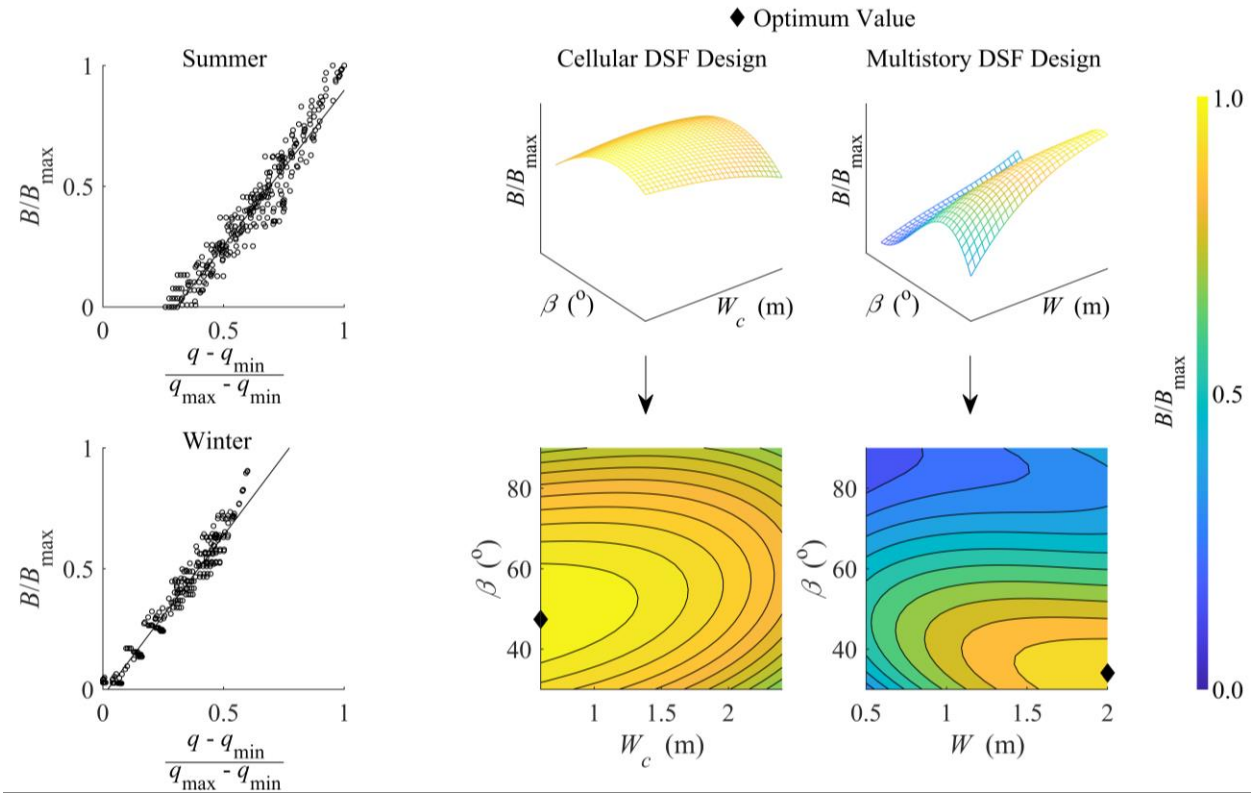


Figure 4.11. Graphical optimization for cellular and multistorey DSF designs.

The initial step involved generating a search space for assessing the reliability of both optimization methods. It was anticipated that the points selected by the PFP-SA or PFP-GA would reside along the boundaries of the search space. Figure 4.12 presents the search space alongside the Pareto front created by SA and GA. Both optimization techniques successfully yielded the PFP. However, PFP-

GA demonstrated superior accuracy in capturing additional details along the front, which were not fully captured by PFP-SA. The best DSF design was determined based on achieving the highest E_{avg} and the lowest Q_{avg}. In hot regions, the optimal DSF design was characterized by (W = 0.66 m, β = 30.1°), which resulted in Q_{avg} of 37.9 W/m² and E_{avg} of 23.2 W/m². In cold climates, the ideal DSF design was achieved with parameters (W = 0.79 m, β = 30.1°), resulting in Q_{avg} of 19.6 W/m² and E_{avg} of 12.4 W/m². This optimal bioenergy generation was comparable to the 13.1 W/m² reported for a similar cellular DSF design in [70].

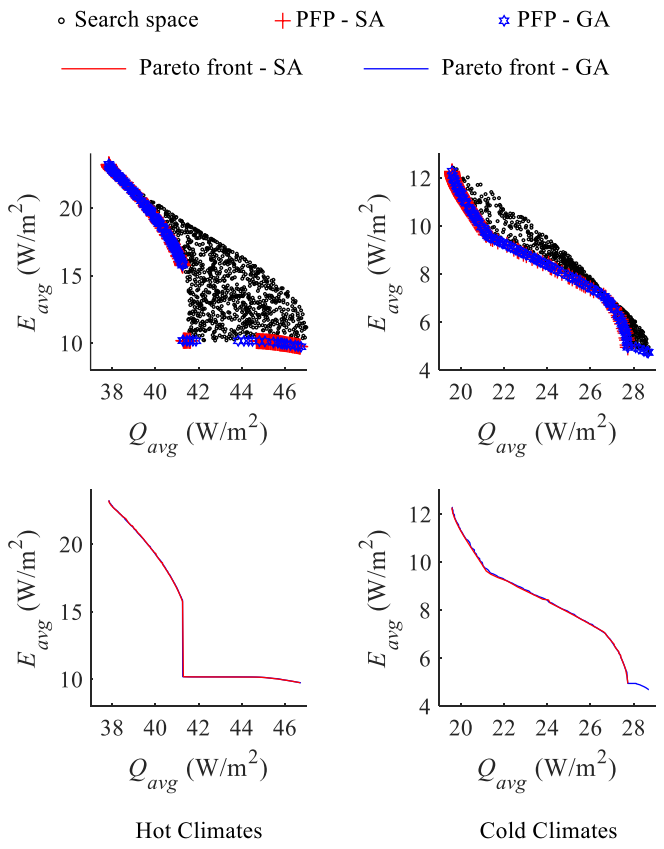


Figure 4.12. Top, search space generated by random points generation. Bottom, Pareto front generated by both SA and GA.

DSFs were assessed by considering the optimal and the least efficient (worst or suboptimal) designs. This was achieved to examine the feasibility of the diverse range of DSF systems compared to SSFs. In hot climates, the suboptimal DSF design was characterized by W = 2.4 m and β = 83.7°, resulting in Q_{avg} of 46.9 W/m², 23.7% more than the optimal design. In cold regions, the suboptimal DSF design was distinguished by W = 2.4 m and β = 88.4°, leading to Q_{avg} of 28.7

W/m², 46.4% more than the optimal design. Figure 4.13 illustrates the energy savings accomplished by DSFs in comparison to SSFs for both optimal and suboptimal DSF designs. Here, E_s denoted the energy savings achieved by DSFs compared to SSFs, quantified as $Q_{avg,SSF} - Q_{avg,DSF}$. Positive values indicated the superiority of DSFs, while negative values suggested the superiority of SSFs. On average, optimal DSFs exhibited higher efficiency in both hot and cold regions, resulting in energy savings of 10.1 W/m² and 40.2 W/m², respectively. Interestingly, even the suboptimal DSF design achieved energy savings of 31.1 W/m² in cold climates. In hot regions, it was surprisingly noticed that the suboptimal DSF remained more efficient compared to SSFs, with average energy savings of only 1.1 W/m². This can be justified by the DSF's role in blocking a significant portion of solar irradiation from entering the occupied space, coupled with its capacity to act as a thermal buffer that reduces heat loss during brief cold periods. These results promoted the adoption of DSFs over SSFs not only in cold climatic regions, as previously suggested in [15], but also in hot climates. However, the substantial reduction in heat load was predominantly observed in cold climates.

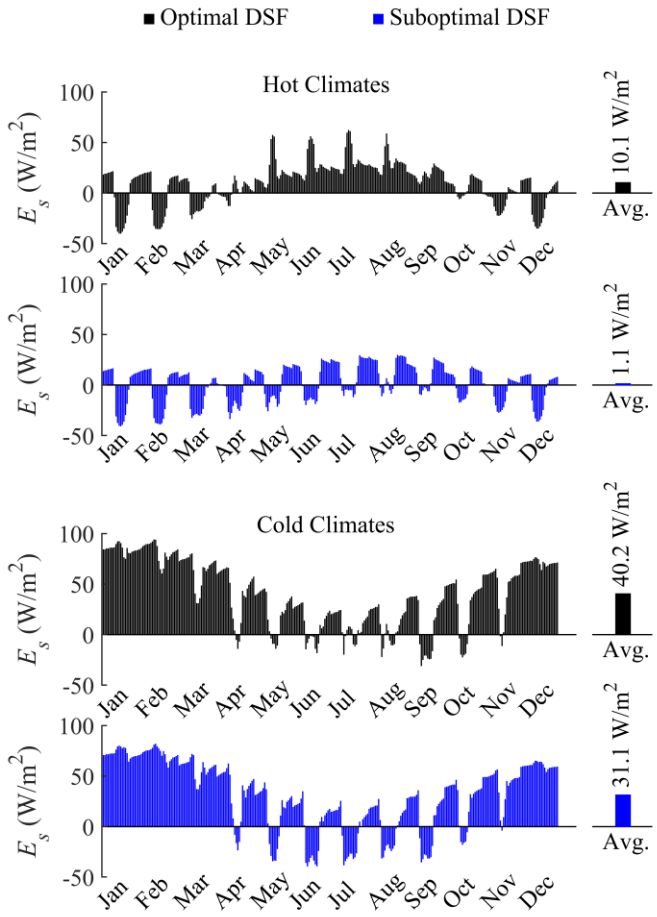


Figure 4.13. Energy savings achieved by DSFs compared to SSFs.

4.4 Summary of Chapter

Integrating PBRs into DSFs boosted the efficient performance of buildings beside enhancing the aesthetic standing. Two designs were investigated thermally, where the potential of generating both heat and biological energy was evaluated. Shading analysis was performed extensively for both designs to predict the gross solar irradiation reaching the plates. To consider the occupied space heat gain, which significantly impacts achieving the optimal energy performance, this chapter formulated a multi-objective problem with the aim of minimizing both heating and cooling loads while simultaneously maximizing bioenergy generation from the integrated PBRs. An integral model was developed to evaluate the energy performance of DSFs, and its reliability was assessed by experimental validation. The model demonstrated a reliable performance with an average error of 2.2 °C. The findings highlight:

- **Optimal Tilting:** PBRs in the cellular design had no shade all time when the tilt angle was 90º and the cavity width was below 1.1 m. In the multistory design, 1.5 m wide PBRs tilted at 75º offered the highest possible solar exposure percent where the shaded area percent was always below 26.2, and 23.4% in summer, and winter, respectively.
- **Shading Impact:** The optimum parameters, like the cavity width, plates' width, and plates' tilt angle, couldn't have been selected based on the best solar exposure percent only. However, the shading model was integrated to the thermal model and optimum parameters were selected based on the best overall performance, because those parameters receiving higher solar exposure percent weren't necessarily those generating higher energy. For instance, vertical plates in 0.6 m wide cavities in the cellular design avoided most of the shading. However, 45° tilted plates in 1.2 m wide cavities provided the highest benefit in terms of thermal and biological energy generation at the rates 119.4 and 11.8 W/m^2, respectively.
- **Performance Comparison:** On average, the cellular design generated 31.9 W/m^2 thermal energy and 3.9 W/m^2 biological energy. However, the multistory design thermal and biological energy generation was higher by 20.4% (38.4 W/m^2) and 79.5% (7.0 W/m^2), respectively.
- **Graphical Optimization:** In this chapter, the two objectives B and $q_{conv,pl\text{-}w}$ had a positive correlation. As a result, both objectives were maximized by tracking only one of them graphically. The multistory design, 2 m wide plates tilted at 34.1º generated the highest average thermal energy of 47.3 W/m^2 and the highest annual average biological energy of 8.3 W/m^2.
- **Pareto Optimization:** Pareto front population generated through Pareto Search Algorithm and Genetics Algorithm demonstrated the effectiveness of DSFs in achieving high bioenergy generation while minimizing heat transfer through the building envelope.
- **Climate Adaptation:** Optimal DSFs in hot and cold regions yielded energy savings of 10.1 W/m² and 40.2 W/m², respectively, compared to SSFs. Surprisingly, even suboptimal DSFs designs proved to be energy-efficient, achieving energy savings of 31.1 W/m² in cold regions and maintaining a slight advantage over SSFs in hot climates with energy savings of 1.1 W/m². This was attributed to the ability of DSFs to block solar irradiation and act as thermal buffers during brief cold periods.

These findings highlight the significance of optimal tilting and cavity widths for DSFs with PBRs to maximize both thermal and biological energy generation. Pareto optimizations have confirmed the effectiveness of DSFs in cold and hot climates. However, further examination of additional cold locations within the Canadian climate is required to assess system feasibility across Canada. It is also critical to integrate a detailed chemical kinetics model and validate it using experimental data to quantify biomass generation from the proposed system, which is the focus of the next chapter.

Chapter 5: Chemical Kinetics Modeling and Experimental Analysis for PBRs in DSFs[1]

The previous chapter emphasized the need to assess the system feasibility across Canada's cold locations, integrate a chemical model, and validate it with experimental data to quantify biomass generation from the proposed system. This chapter addresses these needs and fulfills the third objective by developing a detailed chemical kinetics model for building-integrated PBRs. It includes an experimental setup, monitors microalgae growth using RGB imaging, and validates the model's accuracy with experimental data. Additionally, the chapter compares optimization methods for efficiency and accuracy and evaluates the optimized PBR integration across diverse Canadian cities. Given the multiple variables addressed in this chapter, graphical optimization was excluded because it is limited to solving optimization problems involving a maximum of two variables. Instead, metaheuristic optimization algorithms were utilized due to their gradient-free nature, which was more suitable for the functions developed subsequently.

5.1 Introduction

Chemical kinetics models have been used to optimize PBRs' geometrical parameters [23,24], select microalgae species [25,26], analyze different light sources with varying intensities [22,93], and assess nutrient content, lipid production, and CO_2 fixation [90,187–189]. Micro-algae species such as *C. vulgaris* and *D. tertiolecta* were more suitable for building integrated PBRs, with higher volumetric productivity for *C. vulgaris* by 34.5% [19]. Light intensity requirements for both *C. vulgaris* and *D. tertiolecta* were 205 W/m^2 and 160 W/m^2, respectively [90,93]. Daily lipid production was higher for *C. vulgaris* by 1.1 g/m^2 when compared to other species such as *N.*

[1]This chapter is based on the following articles:

Elmalky, A. M., & Araji, M. T. (2024). Chemical Kinetics Model with Experimental Validation for Optimal Microalgae Generation in Double Skin Façades. *Energy*, Under Review [72].

Elmalky, A. M., & Araji, M. T. (2024). Efficient Conversion of Solar Energy to Algal Biomass in Buildings Using Neural Network-Aided Optimization. *Renewable Energy*, Under Review [73].

Elmalky, A. M., & Araji, M. T. (2024). Neural Networks for Monitoring Microalgae Biomass in Building Façades. *Technology | Architecture + Design*, *8*(1), 60–69 [74].

oleoabundans [26]. However, the employed optimization strategies in previous research were either focused on cylindrical PBRs [23] or external light sources with constant photon flux density [24]. Numerous studies employed statistical response surface methods to optimize biomass generation and CO_2 absorption rates [187–189]. However, these methods approximated the optimal response by applying a second-degree polynomial model with a reported root mean square error of 9.0% [190]. Higher accuracies were often achieved by employing direct optimization methods that search for the most efficient geometrical and operational parameters within their associated feasible range [191]. A thorough search of the relevant literature did not reveal any studies applying constrained local optimization methods to building integrated PBRs. In addition, developing and validating diverse monitoring techniques is critical for accurate assessment and optimization of microalgae growth.

Optimizing the performance of PBRs and ensuring maximum productivity required accurate and timely prediction of biomass accumulation [14]. Conventional approaches for biomass prediction are usually based on gravimetric measurements or microscopic analysis [192]. Both approaches were reported to be time-consuming and labor-intensive [192]. Gravimetric measurements of biomass cultures with high water content had an error margin of up to 30% [193]. The same approach was also unsuitable for small-scale experiments or continuous biomass production processes due to sacrificing a portion of the biomass for measurement [194]. Biomass prediction using microscopic analysis imposed higher costs in relation to special equipment and expert personnel [195]. This method was subjected to sampling bias due to the lack of representing the entire sample [196]. A root means square error of 49.25% was reported for this method because of the uncertainty associated with cell counting or cell size measurement [195]. Previous methods did not provide real-time feedback on biomass growth which in turn limited the ability for optimizing the PBR conditions [194]. Therefore, the development of machine learning (ML) models and image-based techniques for biomass prediction in microalgae PBRs has the potential to overcome these challenges and enable more efficient and sustainable production [197].

The demand for optimization methods that improve search efficiency and reduce computational time is increasing due to the exhaustive hourly bioenergy simulations required for PBRs. Several methods including Genetic Algorithms (GA) [198], Particle Swarm Optimization (PSO) [199],

and Simulated Annealing (SA) [200] have been applied for the optimal performance of PVs when integrated into buildings. Distributed parallel GA framework addressed the time-consuming challenges of stochastic algorithms in complex building energy optimization, significantly reducing computational requirements through global search capabilities [201]. However, this approach was exclusively suitable for optimizing building energy performance with single-objective problems. The significant reliability of such algorithms has promoted their utilization in additional fields such as data processing, algorithm learning, and discrete optimization [202–206]. The GA offspring is updated for the search outcomes and direction through five distinctive phases. This includes initial population, objective function, selection, crossover, and mutation [207]. However, inefficient selection methods decreased the solution convergence and increased the elapsed time [208].

Another metaheuristic method, PSO, was coupled with E+ and led to a 1.6–11.3% reduction in total annual building electricity consumption by optimizing orientation, window size, glazing, and wall specifications [209]. However, previous analyses primarily focused on a single-room model, offering limited assessment of complex building systems. Peak loads and customer costs were reduced by 49% and 11% using PSO, but further analysis was required for storage capacities and day categorization with price and demand variations [210]. SA found better solutions when compared to gradient descent and total state space search for energy management in buildings integrating PVs [211]. However, the high computational costs, reaching up to 942,900 iterations, required the modification of original SA methods to reduce computational requirements. Neural Networks (NN) have emerged as powerful tools in various domains, including energy technology optimization and renewable resource forecasting. The performance of NN combined with SA is still unknown, unlike NN coupled with GA and PSO for performance enhancement. NN-GA optimization addressed the lack of the optimization setup in TRNSYS, resulting in an increase in energy generation from the integrated hybrid renewable energy system to 88% [198]. NN and PSO were combined to optimize NN input data, leading to a 35% reduction in energy consumption and a 73.21% reduction in CO_2 emissions [212]. However, both studies overlooked the impact of incorporating NN on computational time for either NN-GA or NN-PSO when compared to the original methods.

Other direct search methods are unconstrained techniques that do not rely on function derivatives in the optimization process [213]. The Hooke-Jeeves (HJ) algorithm is a heuristic direct optimization method with proven reliability in multiple fields [191,214–217]. The HJ method had an extremely small error with an average accuracy of 98.9% [191]. However, original HJ algorithms were limited only to unconstrained optimization problems [216]. In order to handle constrained problems, the HJ method had to be modified by integrating additional methods such as the parabolic penalty method [12]. Although the HJ method was not used for optimizing PBRs integrated into buildings, it was reported to be the most popular method for enhancing building energy performance [218]. Alternative methods that utilize conjugate directions also had the potential to mitigate computational requirements by the efficient search for optimal solutions [213]. Powell's conjugate direction (PCD) method is another free gradient method that depends on the parallel subspace property by employing conjugate directions [213]. Similar to the HJ method, PCD method was not applied in previous literature for optimizing PBR integration into building façades, despite its numerous benefits. PCD surpassed Nelder-Mead, quasi-Newton, and stochastic methods, with a lower mean square error by 58.1% and 82.5% compared to quasi-Newton and scaled stochastic approximation [219]. However, optimal solutions obtained by either PCD or HJ methods were strongly dependent on initial points with high possibilities of trapping the algorithm in a local extremum (i.e., maximum, or minimum) [213].

In light of the above, this chapter developed a detailed chemical kinetics model for building integrated PBRs, considering light attenuation, oxygen production, and day-night cycles on microalgae growth. Two novel biomass prediction approaches were introduced: one using RGB image processing and another using neural networks (FNNs and CNNs). An experimental setup was built to monitor microalgae growth with RGB imaging, and the chemical model's accuracy was validated against collected experimental data. Optimization methods (GA, PSO, SA, HJ, and PCD) were assessed for accuracy and computational efficiency. The computational time of original exhaustive methods was compared to those incorporating neural networks. The optimized PBR integration was evaluated across various Canadian cities to assess performance in different climates.

5.2 Method

The modeled system was comprehensively defined by specifying all boundary conditions, fixed parameters, and decision variables in relation to geometric and operational variables. A detailed chemical kinetics model was then developed to estimate biomass generation from incident solar irradiation. An experimental setup was built with precisely crafted PBR frames, integrated glass panels, sealed with liquid rubber, and adjustable cavity widths. Two monitoring techniques were then developed based on image processing and ML. The developed chemical model was then validated by comparing the simulation results to the collected experimental data. The chemical kinetics model generated structured data for training FNNs. These were transformed into labeled training data (input images and target labels) to train CNNs. Input images provided raw data, while target labels indicated annual biomass harvest. ML techniques were evaluated and compared to identify the most accurate training algorithms and optimizers for FNNs and CNNs.

Five distinct optimization methods were employed in this chapter to cover a wide range of meta-heuristic optimization techniques. SA represents a single solution-based search, while GA and PSO are population-based searches classified as evolutionary and swarm intelligence algorithms, respectively. HJ algorithm and PCD method are also heuristic free-gradient direct optimization methods. The original forms of the optimization methods were initially applied to maximize microalgae generation from the algal façade, with computational time estimates. The computationally exhaustive algorithms were then aided with NN, trained using different dataset sizes. Multiple data sets were used to train NN before integrating them into the optimization methods. Subsequently, regression analysis was employed to select the data set with the smallest size and the highest correlation coefficient. The NN-aided algorithms were then utilized to maximize biomass generation, and the computational time was compared with that of the original methods. Finally, the exact optimal solution was estimated for different cities located across all Canadian provinces.

5.2.1 PBR condition

The design and operational variables of PBRs have been carefully selected based on prevailing ranges observed in similar systems as established in previous literature. Optimized decision variables for the building-integrated PBRs were as follows:

1- PBRs thickness (δ): δ had lower and upper constraints of 0.01 m and 0.2 m. This range was chosen to cover the values of 0.01 m, 0.03 m, 0.05 m, 0.08 m, and 0.15 m, as employed in prior studies [220–225].
2- PBRs tilt angle (β): β was a critical variable that was investigated over the range 10° to 90°. That's because higher tilt angles ($\beta \approx 90°$) compensated for lower solar altitude angle (α) in winter while lower angles ($\beta \approx 0°$) were more effective in summer.
3- DSF cavity width (W_c): W_c was examined over the range of 0.6 m to 2.4 m as applied in [15].
4- Microalgae residence time (τ_d): τ_d was represented by the reciprocal of the fresh medium flow rate. τ_d was varied between 0.1 days and 2 days to cover the values examined by [1,22,226,227].

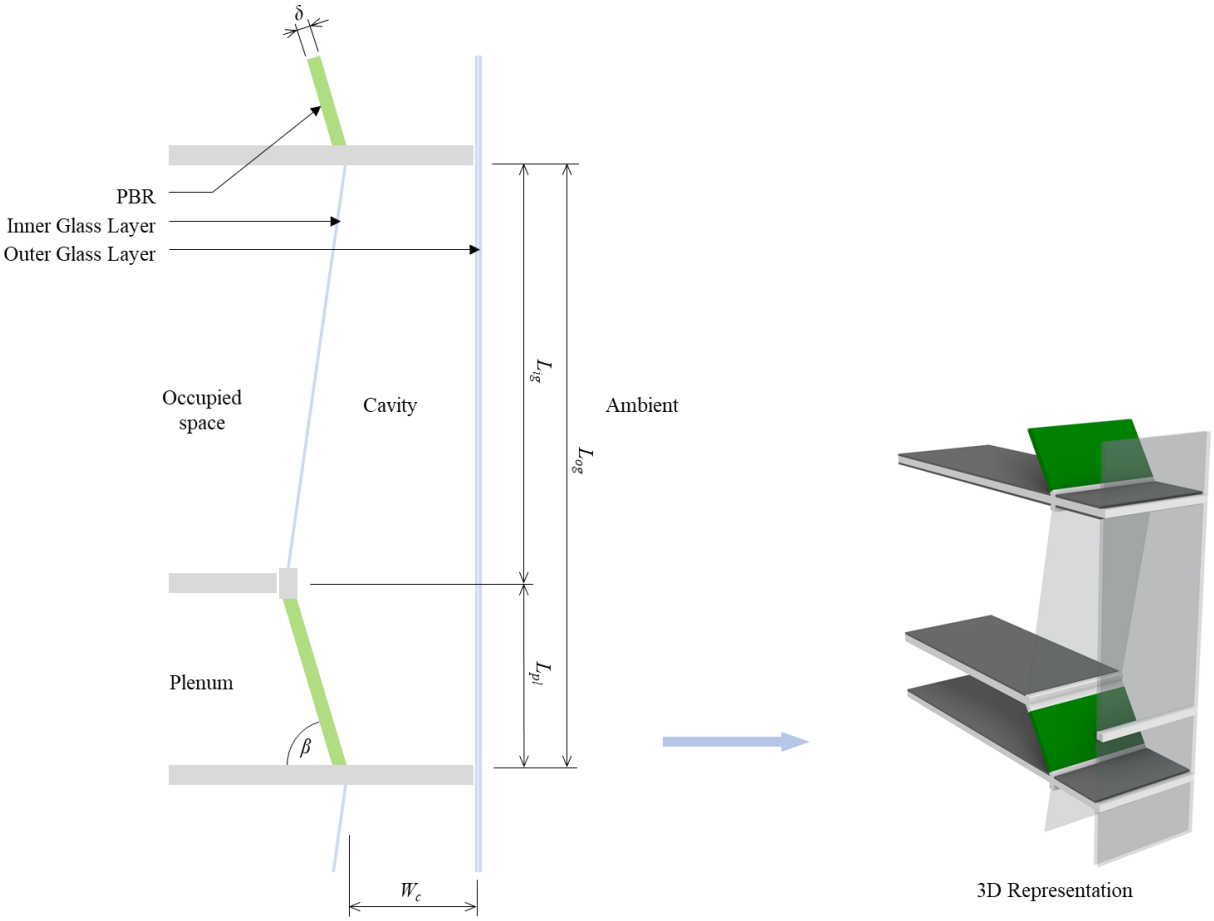


Figure 5.1. Examined parameters of the DSF system with the integrated flat PBRs.

Fixed parameters of the examined system, shown in Figure 5.1, were selected according to [14,15]. The DSF system had an inner layer of single-glazed 6 mm clear glass with transmittance, U-value, and SHGC of 77.1%, 5.818 W/m^2·K, and 0.818, respectively. The DSF outer layer was a double-glazed unit with a 12 mm air gap enclosed between two 6 mm clear glass panes. The outer layer had transmittance, U-value, and SHGC of 60.69%, 2.552 W/m^2·K, and 0.705, respectively. Floor-to-floor height (L_{og}) was set to 4 m to follow the common practice of most program spaces in multipurpose buildings. The inner glass height (L_{ig}) was set to 3 m.

5.2.2 Chemical kinetics model

Generated biomass was estimated by employing a detailed CKM that applied the governing kinetics of the photosynthesis process. This was achieved by considering the oxygen evolution rate and light attenuation inside the PBRs in addition to transient response to day-night cycles. In this model, biomass flow rate leaving the PBR was expressed by

$$\dot{m}_{out} = \frac{dm_{out}}{dt} = \dot{V} C_X = \frac{V}{\tau_d} C_X \tag{5.1}$$

where $\dot{V}$ is the volume flow rate of fresh medium entering the panel, m^3/sec. V is the PBR-occupied volume, m^3. C_X is the biomass concentration, kg/m^3. τ_d is the culture residence time inside the panel, s. Therefore, the biomass harvest over a time duration t was calculated by

$$m_{out} = \int_0^t \frac{V}{\tau_d} C_X dt = \frac{V}{\tau_d} \int_0^t C_X dt = \frac{A \times \delta}{\tau_d} \int_0^t C_X dt \tag{5.2}$$

where A is the PBR illuminated surface, m^2. δ is the thickness of the panel, m. The aerial productivity was expressed by

$$\frac{m_{out}}{A} = \frac{\delta}{\tau_d} \int_0^t C_X dt \tag{5.3}$$

Finally, the objective function f in terms of annual biomass generation was calculated by accumulating the harvest over the shorter time intervals t. For t=1 hour, the annual aerial productivity was calculated by

$$f = m'' = \frac{m_{annual}}{A} = \sum_{n=1}^{8760} \frac{m_{out}}{A} = \frac{\delta}{\tau_d} \sum_{n=1}^{8760} \int_0^t C_X dt \tag{5.4}$$

Assuming that C_X=0 in the fresh medium entering the PBR, the biomass rate of change inside the panel was expressed by

$$\frac{dm}{dt} = \dot{m}_{gen} - \dot{m}_{out} \tag{5.5}$$

where m is the inside biomass at a given time t, kg. $\dot{m}_{gen}$ is the rate of biomass generation inside the panel, kg/sec. The previous equation was reformed to

$$\frac{dC_X}{dt} = \langle r_X \rangle - \frac{C_X}{\tau_d} \tag{5.6}$$

where $\langle r_X \rangle$ is the average biomass growth rate, kg/m^3·s.

$$\langle r_X \rangle = \frac{1}{\delta} \int_{z=0}^{z=\delta} r_X \, dz \tag{5.7}$$

where r_X is the local biomass growth rate at a distance z, kg/m^3·s, which was calculated by [1]

$$r_X = \frac{J_{O_2} C_X M_B}{\upsilon_{O_2-X}} \tag{5.8}$$

$$J_{O_2} = \left[\rho_{max} \times \frac{K}{K + G(z)} \times \bar{\phi}' E_a G(z) - \frac{J_{NADH_2}}{\upsilon_{NADH_2-O_2}} \times \frac{K_r}{K_r + G(z)} \right] \tag{5.9}$$

where J_{O_2} is the production rate of local oxygen by photosynthesis, mol$_{O_2}$/kg·s. G is the locally received irradiation at a distance z in the culture, μmol/m^2·s. Values and definitions of all applied parameters are shown in Table 5.1.

Table 5.1. Applied parameters with corresponding definitions and values [1,21].

Symbol	Definition	Value	Unit
E_a	Coefficient of mass absorption	200	m^2/kg
E_s	Coefficient of mass scattering	2870	m^2/kg
J_{NADH_2}	Cofactor regeneration rate on the respiratory chain of O_2 consumption by $v_{NADH\text{-}O_2}$	0.0018	mol$_{NADH_2}$/kg·s
K	Photosynthetic half-saturation constant	30,000	µmol$_{hv}$/kg·s
K_r	Inhibition constant for respiration	150	µmol$_{hv}$/kg·s
M_B	C-molar mass for microalgae biomass	0.024	kg/C-mol
$v_{NADH\text{-}O_2}$	Cofactor regeneration stoichiometric coefficient on the respiratory chain	2	-
$v_{O_2\text{-}B}$	Stoichiometric coefficient of oxygen evolution	1.13	-
ρ_{max}	Maximum energy yield for photon conversion	0.8	-
$\bar{\phi}'$	O_2 mole quantum yield	1.1×10^{-7}	mol$_{O_2}$/µmol$_{hv}$

Light variation inside the PBRs was expressed as [228]

$$G(z) = G_0 \times \frac{4\alpha}{(1+\alpha)^2 \times e^{\delta \times C_X \times z} - (1-\alpha)^2 \times e^{-\delta \times C_X \times z}} \times SF \tag{5.10}$$

where SF is the shading factor. α and δ were calculated by [228]

$$\alpha = \sqrt{\frac{E_a}{E_a + E_s}} \tag{5.11}$$

$$\delta = \sqrt{E_a \times (E_a + E_s)} \tag{5.12}$$

where G_0 is the solar irradiation incident on the PBRs surface, μmol/m^2·s. E_s is the coefficient of mass scattering, kg/m^2. *SF* is the shading factor representing the fraction of solar irradiation intercepted by the PBRs.

5.2.3 Experimental Setup

The experimental setup was strategically placed in room 3021 on the third floor of the Architecture School in Cambridge. This location was chosen due to its south-facing window, maximizing solar exposure for the PBR (Figure 5.2 – e). The setup mimicked the structure of a DSF assembly by comprising five major components, the two sides, roof, floor, and inner façade layer consisting of glazing and the PBR.



Figure 5.2. a) Setup main dimensions in cm. b) 3D construction. c) Section view without one side. d) Cavity and inner layer. e) Outer layer view from inside the cavity. f) PBR.

The walls were robust and stable by using Framing Lumber Finger Jointed (2" x 4" x 8') for framing and load support, with 3/8" x 4' x 8' Standard Spruce Plywood as the primary wall material. The roof and sides, bearing less load, were crafted mainly from framing and sheet materials (Figure 5.2 – b). To bear the weight of the inner layer, glazing window, PBR panels, and water, additional beams were integrated into the floor for added reinforcement.

The inner layer, comprising the glazing window and PBR panels, was designed to move closer to or farther away from the outer façade layer, allowing for flexible cavity widths (Figure 5.2 – c, and d). Manufacturing the PBR panels involved processing Framing Lumber Finger Jointed (2" x 4" x 8') on a Jointer to straighten and flatten the stock, followed by rip cuts on a Table Saw to create grooves for holding the glass panels. 10 mm thick glass panels were then integrated into the grooves before applying liquid rubber to coat the wood surface and fill the gaps at the glass/wood junctions (Figure 5.2 – f). The microalgae strain used was *Chlorella vulgaris* (strain number: CPCC 90), imported from the Canadian Phycological Culture Centre at the University of Waterloo. Deposition of microalgae and biological contaminants was mitigated by fast-moving currents along the inner walls of the PBRs [49]. Such continuous agitation of the culture medium was also essential to prevent the microalgae from sinking and to ensure they remain suspended. This was achieved by introducing compressed air into the PBRs using a 1030-gallon per hour air pump.

5.2.4 Biomass Monitoring

5.2.4.1 RGB Image-Based Monitoring Technique

This technique originated from the observation that the cultivated microalgae progressively turned greener over time within the developed PBR. It involves four key steps: 1) Data collection from original and diluted cultures; 2) Determination of original and diluted concentrations; 3) Image processing and analysis; and 4) Correlating concentration to green color intensity. The four steps are detailed in Figure 5.3. This technique was subsequently used for real-time monitoring within the PBR.

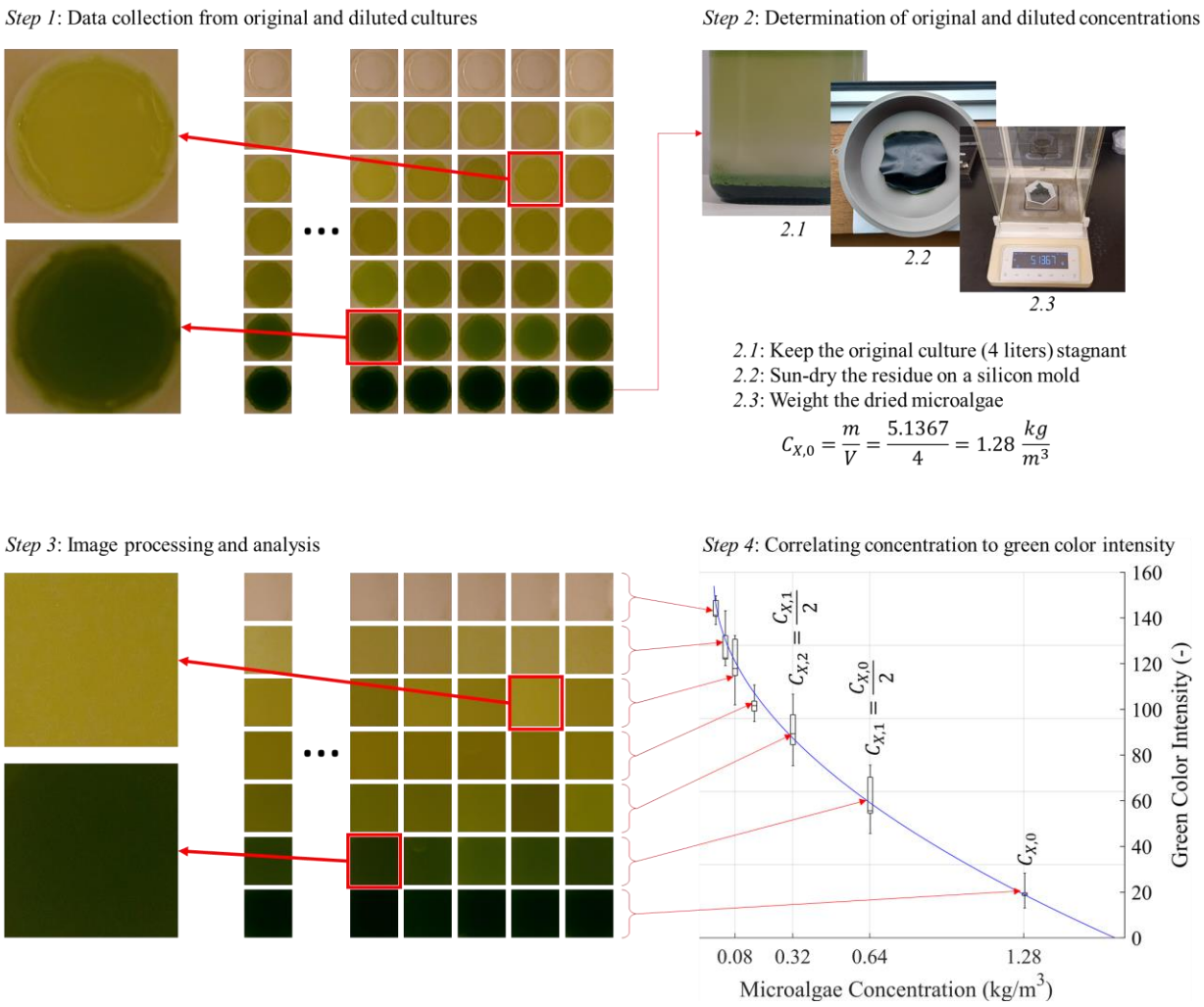


Figure 5.3. Four steps of the RGB Image-Based Monitoring Technique.

Step 1: Data collection from original and diluted cultures:

- Utilization of the most saturated microalgae culture (original culture), characterized by its intense green color, as the starting point.
- Extraction of a fixed volume (6.5 ml) from the original culture, corresponding to the volume of the subsequent imaging lid.
- Placement of the lid within a semi-closed box with controlled lighting, allowing for RGB image capture.
- Dilution of the original culture to achieve desired concentrations for subsequent imaging.
- Generation of multiple data points (RGB images) to facilitate the development of the correlation model.

Step 2: Determination of original and diluted concentrations:

- Analysis of a separate 4-liter sample of the saturated microalgae culture (original culture).
- Stagnant condition maintenance without agitation until solid microalgae precipitation.
- Removal of the supernatant, leaving behind a dense microalgae residue.
- Spreading of the residue on a silicon mold and sun-drying until complete evaporation.
- Weighing of the dried microalgae using a four-digit scale and normalization against the initial 4-liter volume to estimate the original and diluted concentrations.

Step 3: Image processing and analysis:

- The image size of the imaging lid was approximately 750 pixels x 750 pixels.
- Using MATLAB, an analysis window of 400 pixels x 400 pixels was applied to isolate and assess the green color intensity specific to the microalgae culture.
- Conversion of all images into structured data of green color intensities for all concentrations and samples.

Step 4: Correlating concentration to green color intensity:

- Combination of green color intensity values from the images obtained at different concentrations.
- Plotting the green color intensity values against the corresponding concentrations to create a calibration curve.
- Application of a suitable curve-fitting method (e.g., linear regression or polynomial fitting) to model the relationship between the green color intensity and the microalgae concentration.
- Utilization of the established correlation model for real-time concentration estimation in the PBR by continuously monitoring the green color intensity of captured images.

This technique offered a non-invasive and scalable method for monitoring microalgae culture dynamics, enabling real-time assessment, chemical model validation, and variables optimization within PBR systems.

5.2.4.2 ML Image-Based Monitoring Technique

This chapter employed a three-layer NN as shown in Figure 5.4. The network comprised an input layer, hidden layer, and output layer. The network included 4 inputs, l0 neurons in the hidden layer, and a single output. Inputs were denoted as x_1, x_2, x_3, and x_4, and the hidden layer received inputs, v_j, calculated using Equation (6).

$$v_j = \sum_{i=1}^{4} w_{ji}^h x_i \tag{5.13}$$

where w_{ji}^h are the connection weights from the input layer to the hidden layer. The hidden layer outputs, z_j, were calculated by Equation (7).

$$z_j = f_j^h(v_j) \tag{5.14}$$

where f_j^h is the activation function for the hidden layer. The overall output was calculated by Equations (8) and (9).

$$y = f^o\left(\sum_{j=1}^{10} w_j^o z_j\right) \tag{5.15}$$

$$y_s = f^o\left(\sum_{j=1}^{10} w_j^o f_j^h\left(\sum_{i=1}^{4} w_{ji}^h x_i\right)\right) \tag{5.16}$$

where w_j^o are the connection weights from the hidden layer to the output layer.

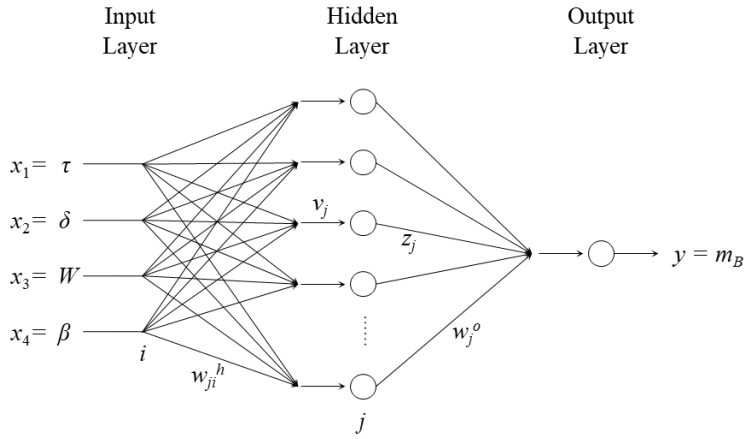


Figure 5.4. Employed three-layered neural network.

The objective was to determine the weights w_{ji}^{h} and w_{j}^{o}. The goal was to minimize the objective function specified in Equation (10).

$$\text{Minimize } E(w) = \frac{1}{2}\sum_{s=1}^{m}\left(y_{T,s} - y_s\right)^2 \tag{5.17}$$

where m is the total number of training points. y, given earlier, is the predicted output. y_T is the target output.

Addressing this unconstrained optimization problem was achieved by employing the Levenberg-Marquardt (LM) algorithm, Bayesian Regularization (BR), and Scaled Conjugate Gradient (SCG) algorithm.

In the convolution operation, CNNs employed convolutional layers to extract features from the input image. The convolution operation was represented by

$$S_{i,j} = (K * I)_{i,j} = \sum_{m}\sum_{n} K_{m,n} I_{i-m,j-n} \tag{5.18}$$

where $S_{i,j}$ is the output feature map at position (i,j). K is the convolutional kernel/filter. I is the input image. * represents the convolution operation. The kernel slides over the input image, and the dot product of the kernel weights and the input pixel values was computed at each location. This resulted in a feature map that represents the presence of certain features in the input image. An activation function was applied element-wise to the output of the convolution operation to introduce non-linearity into the network. This was achieved by using the Rectified Linear Unit (ReLU) defined by

$$f(x) = \max(0, x) \tag{5.19}$$

where x is the input. In the pooling operation, pooling layers were used to reduce the spatial size of the feature maps and make the CNNs more robust to variations in the input. Max pooling operation was applied by selecting the maximum value from rectangular regions of the feature map. The pooling operation was thus expressed by

$$M_{i,j} = \max_{m,n} S_{i+m,j+n} \tag{5.20}$$

where $M_{i,j}$ is the output of the pooling operation. S is the input feature map. The output of the last convolutional layer was then flattened into a 1D vector and passed through one or more fully connected layers. This was done to perform a linear transformation of the input followed by an

activation function. The output of the last fully connected layer represented the predicted class probabilities. Different algorithms were employed to train the CNNs for improving the convergence speed and overall performance. This included Stochastic gradient descent with momentum (SGDM), Root Mean Square Propagation (RMSP), and Adaptive Moment Estimation (Adam) optimizer.

5.2.5 Optimization methods

5.2.5.1 Genetic Algorithms

GA is a stochastic, population-based search method which begins with an initial population (P_0) having N points. Figure 5.5 illustrates the sequence followed to implement GA. The fitness value for each point was assessed based on the objective function value. Selection involved forming a mating pool of N individuals, chosen randomly from the current population, with fitter individuals having a higher probability of selection. Reproduction, involving operations like cross-over and mutation, generated offspring for the current population, maintaining a size of N. The fitness of the new population was assessed, and the algorithm terminated if the stopping criterion was met. Otherwise, the algorithm returned to the selection step. The representation of decision variables involved expressing any feasible decimal value as a binary string. Combining these binary strings formed a chromosome, which served as a representation of a point within the feasible region. The fixed-length chromosome facilitated the evaluation of the fitness value for each point. This fitness value reflected the quality of the candidate point. Higher fitness values indicated more favorable solutions in the context of maximization problems.

The survival principle of the fittest was applied in the selection phase, where individuals with higher fitness values had a greater chance of survival. The mating pool, comprising N chromosomes, was formed by selecting members from the current population. The probability of a chromosome entering the mating pool was determined by its fitness value relative to the sum of fitness values in the population. An alternative approach, the tournament scheme, involved randomly selecting pairs of chromosomes, comparing their fitness values, and selecting the fitter one for the mating pool. These steps were repeated until N chromosomes were collected in the mating pool. In the evolution phase, the cross-over and mutation operations were applied to current chromosomes to generate offspring for the GA population. Pairs of parents were randomly selected

from the mating pool, and the cross-over operation was employed to exchange bits between chromosomes with a predefined probability. The remaining chromosomes were copied to the next generation without cross-over. The mutation operation was then applied to a small percentage of chromosomes to introduce new decision variables. This process resulted in a new population of chromosomes for the subsequent iteration of the GA.

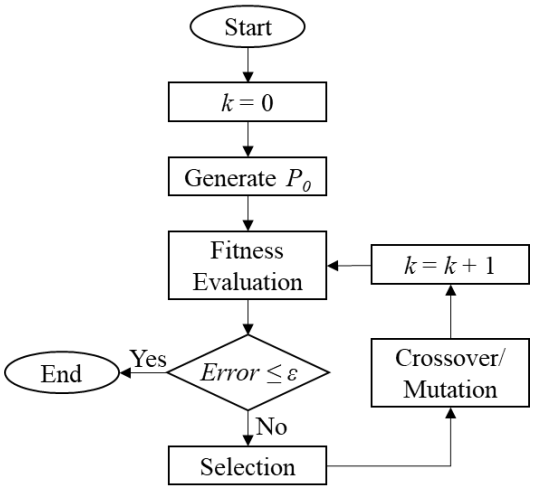


Figure 5.5. Sequence followed to implement GA.

5.2.5.2 Particle Swarm Optimization

PSO is categorized as a randomized search method characterized by the simultaneous update of a given set instead of focusing on a single point $x^{(k)}$. This set, referred to as a population or swarm, consisting of *d* particles, with each particle representing a candidate solution. The swarm navigated in an *n*-dimensional space in a search for better solutions while maintaining individual positions and velocities. Each particle had the ability to memorize its previous positions, exchange information with others, and utilize available information for decision-making. Particle movement was influenced by two factors: the best position it has visited (referred to as personal best) and the best position observed by the entire swarm (referred to as global best). Each particle velocity was defined based on its personal best and the swarm's global best by incorporating specific values for velocities toward personal and global best.

The algorithm started by initializing parameters at k = 0. It then generated initial points and velocities to update the positions and velocities for each particle. Afterward, position and velocity of particles were updated by Equations (1) and (2).

$$x_i^{(k+1)} = x_i^{(k)} + v_i^{(k+1)} \tag{5.21}$$

$$v_i^{(k+1)} = wv_i^{(k)} + c_1 r_i^{(k)} * \left(p_i^{(k)} - x_i^{(k)}\right) + c_2 s_i^{(k)} * \left(g_i^{(k)} - x_i^{(k)}\right) \tag{5.22}$$

where v_i is the velocity of the particle i. p_i is the personal best point visited by particle i. g is the global best point visited by the swarm. $r_i^{(k)}$ and $s_i^{(k)}$ are random n-vectors with their components uniformly distributed in (0,1). $*$ is the operator that multiplies corresponding elements of two matrices with identical dimensions and produce a new matrix of the same size. Personal and global best points were then determined by calculating the objective function for each point. Figure 5.6 shows the utilized process for implementing PSO. PSO incorporated random vectors and constants such as w (inertial constant), c_1 (cognitive constant), and c_2 (social constant). w was selected to be slightly less than 1, while both c_1 and c_2 were selected around 2. The algorithm continued to iterate until a stopping criterion was met.

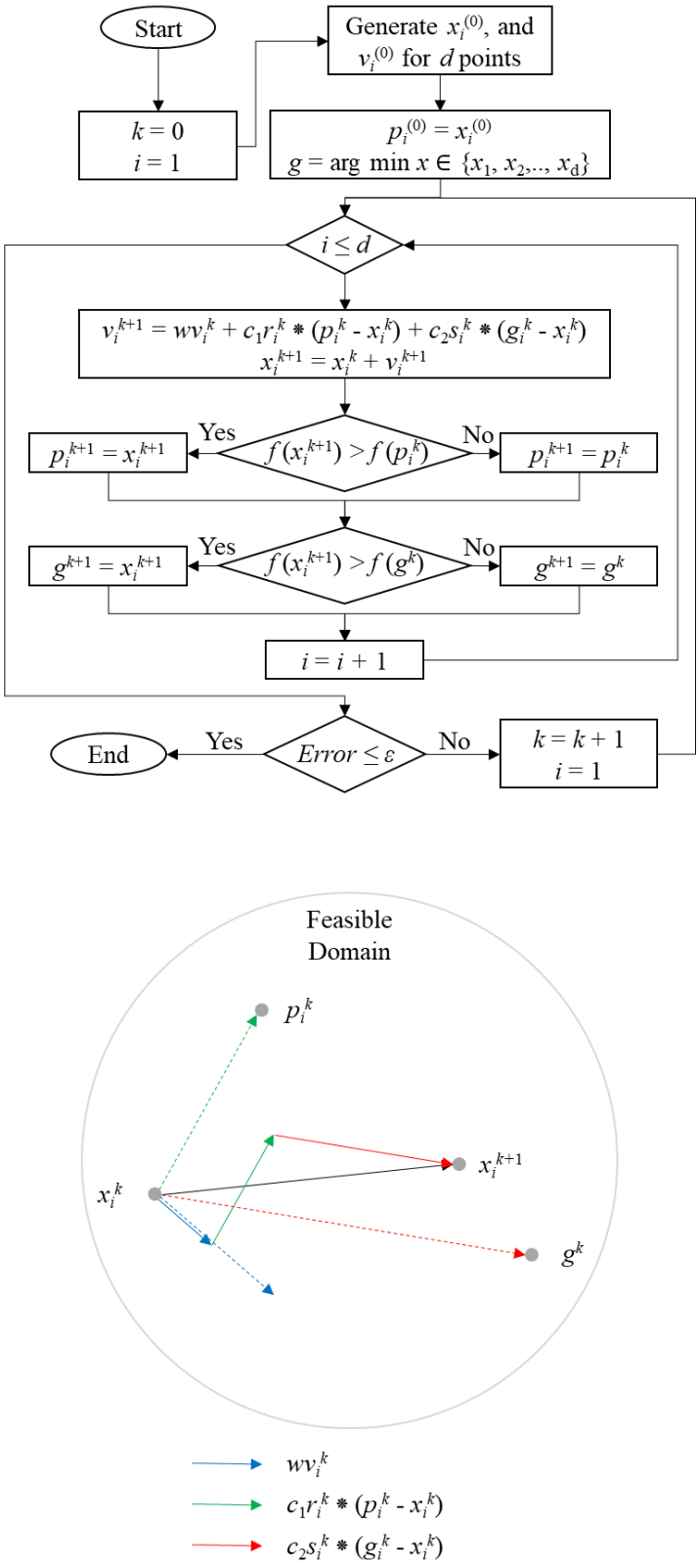


Figure 5.6. Top, employed procedure for implementing PSO. Bottom, position and velocity update for each particle within the swarm.

5.2.5.3 Simulated Annealing

Randomized search, also known as probabilistic search, starts by selecting an initial point and subsequently generating random points from the defined domain. If a generated point proves to be an improvement, the process moves to that location. Otherwise, it remains at the current point. This process is iteratively repeated until a sufficient number of random points within the defined domain have been evaluated. The initial point, $x^{(0)}$, is randomly chosen from the domain, and the subsequent points are typically generated in proximity to $x^{(0)}$. $N(x)$ represents the neighborhood of x, defining a set of points close to x. The generation of the next random point in $N(x)$ often follows a statistical distribution by employing the uniform or normal distribution. This sequence can be represented by Equation (3).

$$x^{(k+1)} = x^{(k)} + d^{(k)} \tag{5.23}$$

If the neighborhood size is too small, the algorithm may be trapped in a local minimum. Addressing this issue by increasing the neighborhood size can resolve the problem at the cost of an extended search time.

SA, as a form of randomized search method, includes a mechanism for escaping local regions. The algorithm was initiated with setting k = 0 and selecting an initial point $x^{(0)}$ from the solution domain. Subsequently, a new point $z^{(k)}$ was randomly chosen from the neighborhood $N(x^{(k)})$. According to a specific probability p, $x^{(k+1)}$ was set to $z^{(k)}$ or remained as x(k). When the new point was an improvement, p was set to 1. Even if the new point was worth, there was a non-zero probability of its selection. The selection probability was updated such that, as the new point became worse, its probability of selection decreased. This probability of accepting the new point was calculated using Equation (4).

$$p\left(k, f\left(z^{(k)}\right), f\left(x^{(k)}\right)\right) = \min\left(1, e^{\left[f\left(x^{(k)}\right) - f\left(z^{(k)}\right)\right]/T_k}\right) \tag{5.24}$$

The positive sequence T_k, known as the temperature schedule or cooling schedule, followed a monotonically decreasing trend toward 0 with increasing iteration number k. A larger T_k corresponded to a higher probability of accepting a worse point, while a smaller T_k reduced this probability. This probability formed the basis for the SA algorithm. T_k was estimated using Equation (5).

$$T_k = \frac{\gamma}{\log(k+2)} \tag{5.25}$$

where $\gamma > 0$ is a problem-specific constant. γ was sufficiently large to enable the algorithm to escape from regions surrounding local minima. The algorithm retained the best point and its corresponding function value throughout the process. If the stopping criterion was met, the algorithm concluded with the best point. The iteration continued with an increment in *k* until the stopping criterion was met.

5.2.5.4 Hooke-Jeeves Algorithm

HJ method is a heuristic, free gradient, and direct search method [229]. *Exploratory moves* were first applied to determine a suitable direction before using *pattern moves*. The optimized variables were combined in the vector *x*, where

$$x = \begin{bmatrix} \tau_d \\ \delta \\ W_c \\ \beta \end{bmatrix} \tag{5.26}$$

In *exploratory moves*, the method started with an initial point called the *base point*, $x^{(0)}$, in the 4-dimensional space because the model targets only 4 variables. Afterward, the initial *search point* $x^{(1)}$ was set to $x^{(0)}$ ($x^{(1)} = x^{(0)}$), as shown in Figure 5.7.a. The objective function value was evaluated at a $\pm\Delta$ amount in each direction of the 4 orthogonal unit vectors. Consequently, point $x^{(5)}$ was calculated after 4 searches. In *pattern moves*, three cases may occur.

Case 1 occurred when the function value at $x^{(5)}$ was less than the function value at the *base point*, $x^{(0)}$. In this case, a new *search point* was formed. This new *search point* was calculated from

$$x^{(1)} = x^{(5)} + \left[x^{(5)} - z^{(0)}\right] \tag{5.27}$$

In this case, $x^{(5)}$ was considered as the new *base point*, $x^{(0)}$, as shown in Figure 5.7.b.

Case 2 occurred when the function value at $x^{(5)}$ was greater than the function value at the *base point*, $x^{(0)}$, and the *base point* was different from the *search point*. In this case, $x^{(1)}$ was assigned to $x^{(0)}$ and the algorithm started over from *exploratory moves* ($x^{(1)} = x^{(0)}$), as shown in Figure 5.7.c.

Case 3 occurred when the function value at $x^{(4)}$ was greater than the function value at the *base point*, $x^{(0)}$, and the *base point* was the same as the *search point* in relation to coordinates and function value ($x^{(1)} \equiv x^{(0)}$). In this case, the step Δ was reduced by a given reduction factor as shown in Figure 5.7.d.

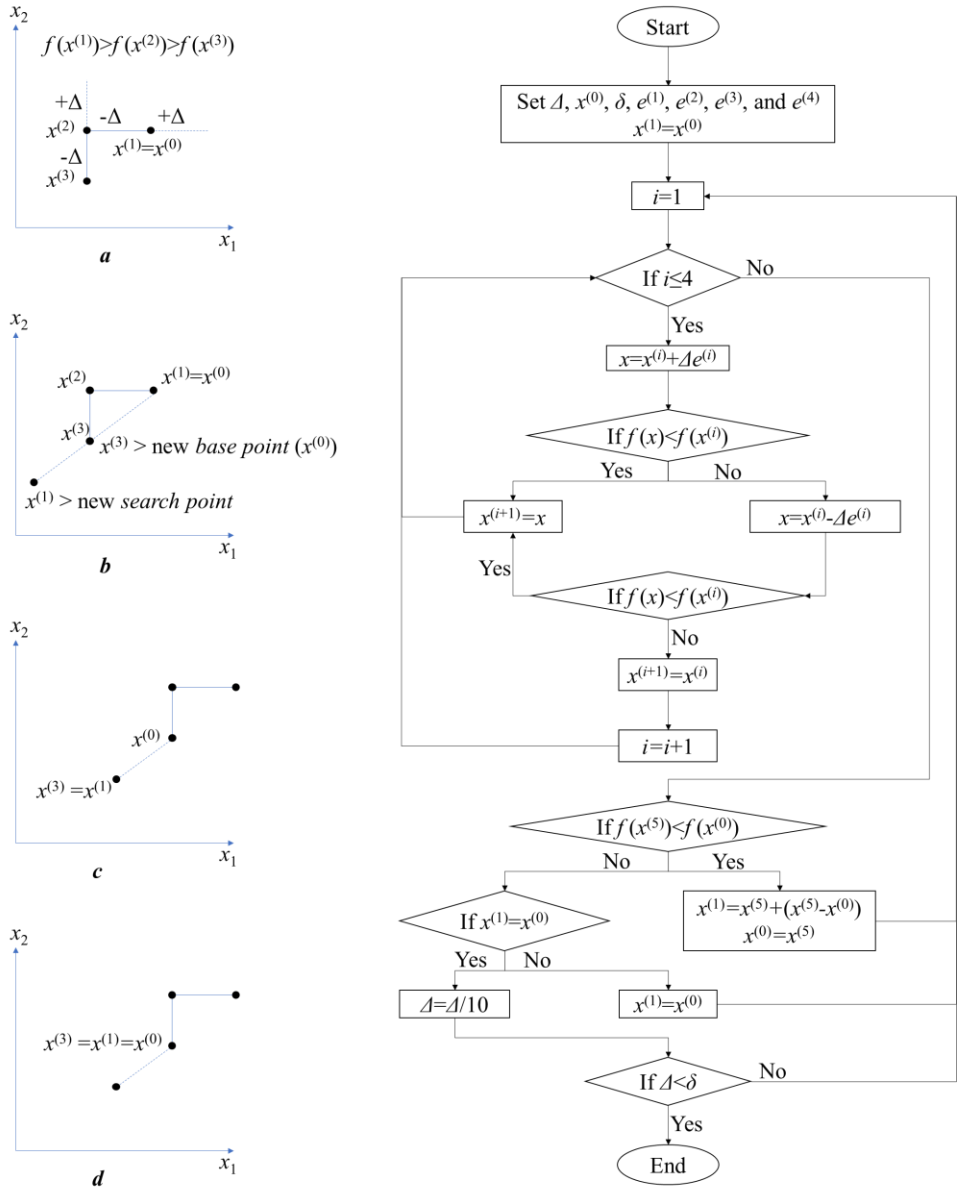


Figure 5.7. Left, 2D illustration of the HJ method. (a) Exploratory moves. (b) Pattern move for case 1. (c) Pattern move for case 2. (d) Pattern move for case 3. Right, Schematic of the used framework to apply the HJ algorithm.

5.2.5.5 Powell's Conjugate Direction Method

In PCD method, the parallel subspace property was employed by applying conjugate directions. This was achieved before estimating the minimum function value along the searched directions by performing line search methods [230]. In the 2D space, the contour levels shown in Figure 5.8.a represent the value of the quadratic function

$$f(\boldsymbol{x}) = \frac{1}{2}\boldsymbol{x}^T\boldsymbol{H}\boldsymbol{x} = \frac{1}{2}[x_1 \quad x_2]\boldsymbol{H}\begin{bmatrix}x_1\\x_2\end{bmatrix} \tag{5.28}$$

where $\boldsymbol{H}$ is the Hessian matrix. $\boldsymbol{x}$ is the vector comprising the optimized variables x_1 and x_2. The PCD method started with the random points ($\boldsymbol{u}^1$ and $\boldsymbol{u}^2$) and searched along the direction $\boldsymbol{s}^1$. The local minimum points along such a direction were $\boldsymbol{z}^1$ and $\boldsymbol{z}^2$, respectively. Based on the parallel subspace property, the updated direction ($\boldsymbol{s}^2 = \boldsymbol{z}^2 - \boldsymbol{z}^1$) will be $\boldsymbol{H}$-conjugate to $\boldsymbol{s}^1$. Further line search in the $\boldsymbol{s}^2$ direction will eventually reach the quadratic function's global minimum.

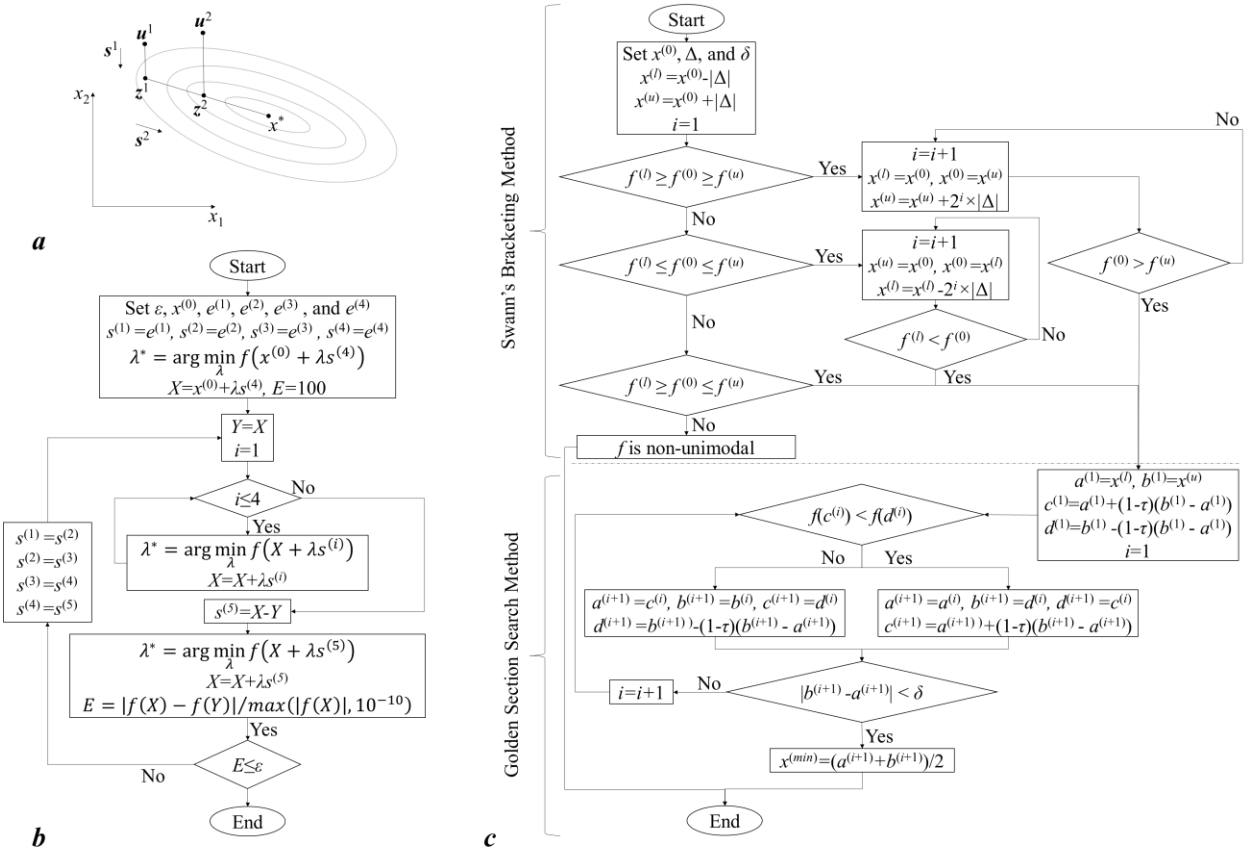


Figure 5.8. a) Parallel subspace property employed by PCD method. b) Schematic of the used framework to apply PCD method. c) Adopted line search minimization method.

The PCD method was applied to maximize biomass generation and find the corresponding decision variables. The objective function was in $\mathbb{R}^4$ and the 4 coordinate unit vectors were assigned to the initial 4 search directions ($\boldsymbol{s}_1$, $\boldsymbol{s}_2$, $\boldsymbol{s}_3$, and $\boldsymbol{s}_4$). In mathematical terms, the previous search directions were expressed by

$$\boldsymbol{s}_1 = \begin{bmatrix}1\\0\\0\\0\end{bmatrix}, \boldsymbol{s}_2 = \begin{bmatrix}0\\1\\0\\0\end{bmatrix}, \boldsymbol{s}_3 = \begin{bmatrix}0\\0\\1\\0\end{bmatrix}, \boldsymbol{s}_4 = \begin{bmatrix}0\\0\\0\\1\end{bmatrix} \tag{5.29}$$

Initial line search minimization was applied along the direction $\boldsymbol{s}_4$ using the point $\boldsymbol{x}^0$. Obtained local minimum ($\boldsymbol{X}$) was assigned to the variable $\boldsymbol{Y}$. Four successive line searches were then performed starting from the point $\boldsymbol{X}$. Obtained result after these consecutive minimizations was also assigned to the variable $\boldsymbol{X}$. Final line search was applied using the direction $\boldsymbol{s}_5$ where

$$\boldsymbol{s}_5 = \boldsymbol{X} - \boldsymbol{Y} \tag{5.30}$$

Final outcome was assigned to $\boldsymbol{X}$ and the convergence criteria were applied to the objective function values of $f(\boldsymbol{X})$ and $f(\boldsymbol{Y})$. Figure 5.8 presents the framework employed to apply the PCD method in addition to the applied line search method. This method relied on the golden section search algorithm after applying Swann's bracketing.

5.2.5.6 Constrained optimization

Decision variables of the objective function were subjected to upper and lower constraints. The PBR's thickness, tilt angle, cavity width, and residence time had lower-upper bounds of 0.01-0.2 m, 10-90°, 0.6-2.4 m, and 0.01-2 days, respectively. In mathematical terms, the previous constraints were expressed by

$$0.01 \leq \tau_d \leq 2 \tag{5.31}$$

$$0.01 \leq \delta \leq 0.2 \tag{5.32}$$

$$0.6 \leq W_c \leq 2.4 \tag{5.33}$$

$$10 \leq \beta \leq 90 \tag{5.34}$$

The parabolic penalty method was applied to transform the optimization problem from a constrained problem to an unconstrained one. This was achieved by expressing the previous constraints as

$$q_1(\tau_d, \delta, W_c, \beta) = \tau_d - 2 \leq 0 \tag{5.35}$$

$$q_2(\tau_d, \delta, W_c, \beta) = 0.01 - \tau_d \leq 0 \tag{5.36}$$

$$q_3(\tau_d, \delta, W_c, \beta) = \delta - 0.2 \leq 0 \quad (5.37)$$

$$q_4(\tau_d, \delta, W_c, \beta) = 0.01 - \delta \leq 0 \quad (5.38)$$

$$q_5(\delta, \beta, W_c, \tau_d) = W_c - 2.4 \leq 0 \quad (5.39)$$

$$q_6(\delta, \beta, W_c, \tau_d) = 0.6 - W_c \leq 0 \quad (5.40)$$

$$q_7(\tau_d, \delta, W_c, \beta) = \beta - 90 \leq 0 \quad (5.41)$$

$$q_8(\tau_d, \delta, W_c, \beta) = 10 - \beta \leq 0 \quad (5.42)$$

The minimized objective function was then expressed by

$$\min_{\tau_d, \delta, W_c, \beta} f' = -m'' + \sum_{i=1}^{8} G_i [q_i(\tau_d, \delta, W_c, \beta)]^2 h(q_i) \quad (5.43)$$

where G_i is a positive number. $h(q_i)$ is a unit step function calculated from

$$h(q_i) = \begin{cases} 0 & q_i(\tau_d, \delta, W_c, \beta) \leq 0 \\ 1 & q_i(\tau_d, \delta, W_c, \beta) > 0 \end{cases} \quad (5.44)$$

5.2.6 Application in various Canadian cities

In order to apply the developed model, the authors primarily considered Toronto, Canada, as a cold climate city. The examined location has a latitude and longitude of 43.67° North, and 79.63° West with a daily average temperature varying between -15.5 °C in winter to 26.7 °C in summer. Global irradiation has maximum and minimum daily average values of 580 W/m^2 and 9.3 W/m^2 in May and December, respectively. Throughout the year, the wind has an average velocity of 4.2 m/s.

A total of 13 additional Canadian cities were then analyzed to optimize the proposed model within various climatic conditions on annual basis. These cities included Calgary, AB; Charlottetown, PEI; Fredericton, NB; Ottawa, ON; Quebec, QC; Regina, SK; Resolute, NU; St. Johns, NL; Truro, NS; Vancouver, BC; Whitehorse, YT; Winnipeg, MB; and Yellowknife, NT. The weather file of each city was imported from E+ weather database and was processed using Climate Consultant and MATLAB, to extract the temperature, beam irradiation, diffuse irradiation, and wind velocity on an hourly basis.

5.3 Results and Discussions

5.3.1 Model validation and parametric analysis

The integration of PBRs into DSF systems should be optimized through the application and verification the the kinetics and shading models. The model's accuracy and reliability were assessed by comparing the simulation results to experimental measurements collected over two consecutive runs with varying cavity widths. The initial run was conducted with a cavity width of 20 cm over a period of 20 days from April 12th to May 2nd, followed by a second run with a cavity width of 40 cm from May 22nd to June 11th. Figure 5.9 illustrates the day-night cycles of available irradiation and their corresponding impact on microalgae concentration cycles. The RMSE for the 20 cm cavity width was 0.0279 kg/m^3, while the RMSE for the 40 cm cavity width was 8.13 x 10^{-4} kg/m^3. The overall RMSE for concentration prediction was 0.0144 kg/m^3. During periods without solar irradiation, microalgae experienced a decay rate of up to 24.87 gm/m³ per hour, which was compensated by a growth rate of 59.18 gm/m³ per hour during peak solar irradiation of 3644.15 μmol/m²·s. To further validate the model, the production output from the PBR was estimated and compared to experimental results after 20 days for both cavity widths. The model predicted a production of 11.9 gm and 4.6 gm for the 20 cm and 40 cm cavity widths, respectively, while experimental measurements showed productions of 15.6 gm and 5.0 gm. This comparison resulted in a mean deviation of 2.0 gm for microalgae production.

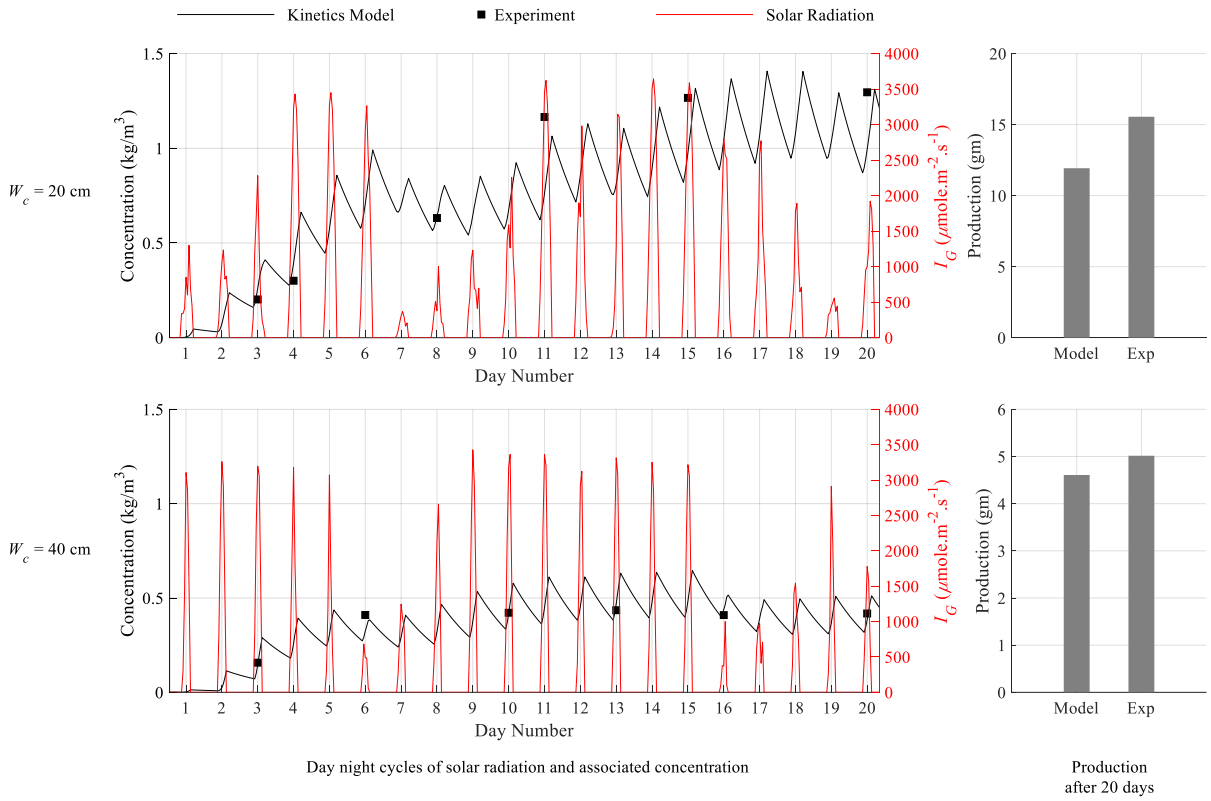


Figure 5.9. Model validation. Left, model biomass concentration compared to experimental measurements. Right, biomass production after 20 days.

Microalgae concentration was multiplied by the volume flow rate leaving the PBRs to calculate the instantaneous biomass production. This production was accumulated on an annual basis to estimate the aerial biomass harvest or m''. Figure 5.10 presents m'' for different combinations of δ, β, W_c, and τ_d. Maximum m'' of 2.2 kg/m^2 was achieved by τ_d = 1.0 days, 35° ≤ β ≤ 60°, 0.6 m ≤ W_c ≤ 1.8 m, and 5 cm ≤ δ ≤ 20 cm. Changing τ_d to either 0.5 days or 2.0 days reduced m'' to 1.5 kg/m^2 (31.8%) and 1.9 kg/m^2 (13.6%), respectively. Shifting β to 10° or 85° also decreased m'' by 13.6%. Therefore, τ_d was the most significant variable with an impact of 31.8%. For τ_d = 1.0 days, m'' was independent on both δ, throughout its whole range, and W_c, for cavities less than 1.8 m. However, m'' increased from 1.9 kg/m^2 to 2.0 kg/m^2 by increasing δ from 15 cm to 20 cm at β = 60°, τ_d = 1.5 days, and W_c = 2.4 m. Biomass generation was slightly dependent on δ and should be considered as a decision variable in subsequent optimization. The parametric analysis, shown in Figure 5.10, indicated that the optimal τ_d was around 1.0 days, optimal W_c was less than 1.8 m, and optimal β was between 35° and 60°. Such a range included the PBR's optimal tilt angles of 45° and 47° that

were concluded by [14,22]. However, the optimal δ concluded from the parametric analysis below was still unknown. This necessitated employing direct search methods to estimate all optimal variables simultaneously.

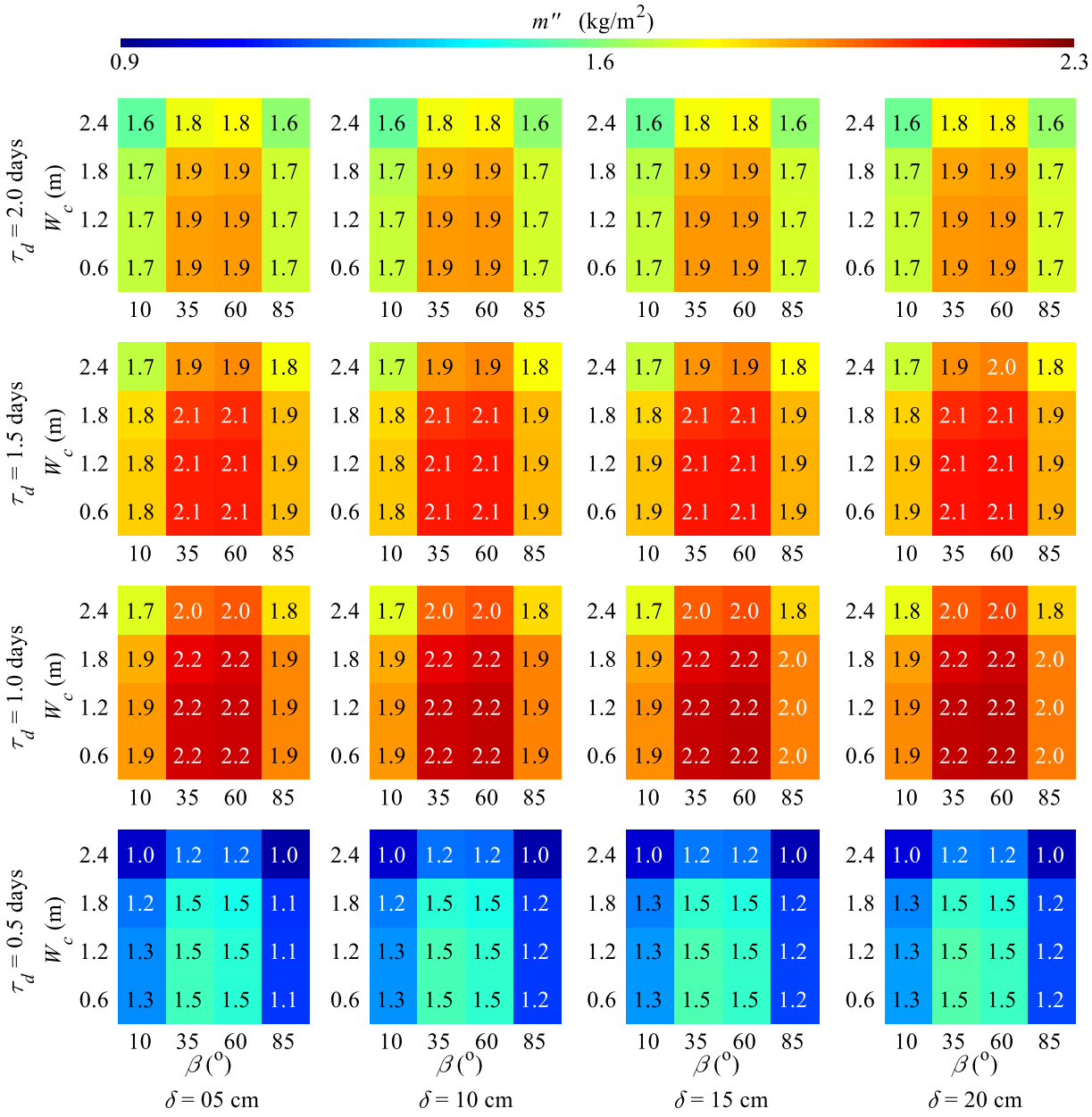


Figure 5.10. Aerial biomass generation per year for different decision variables.

5.3.2 Neural networks for biomass prediction

Supervised learning for classification and regression tasks utilized FNNs trained by multiple algorithms. Such algorithms included Levenberg-Marquardt (LM), Bayesian Regularization (BR),

and Scaled Conjugate Gradient (SCG). Strength and direction of the linear relationship between m_{True} and $m_{Predicted}$ were measured by applying the correlation coefficient or Pearson's correlation coefficient (R value). Figure 5.11 illustrates the R value and required iterations for FNNs trained with LM, BR, and SCG. All algorithms exhibited a positive linear relationship, with R values > 0. When considering the number of neurons in the hidden layer, using 1, 2, and 3 neurons resulted in average R values of 0.58, 0.72, and 0.97 across all algorithms, respectively. Increasing the number of neurons beyond 3 had a minimal impact, raising the R value from 0.99 to 1.00 for LM, from 0.98 to 0.99 for BR, and from 0.92 to 0.97 for SCG. Notably, the BR algorithm demonstrated a tendency to demand substantial computational power, which increased exponentially as the number of hidden layer neurons grew. In contrast, the LM algorithm consistently required an average of 301 iterations for 3 or more neurons in the hidden layer. On the other hand, SCG achieved comparable results with just an average of 52 iterations across the entire range of hidden layer neurons, sacrificing only 2.3% of the R value compared to LM and BR algorithms.

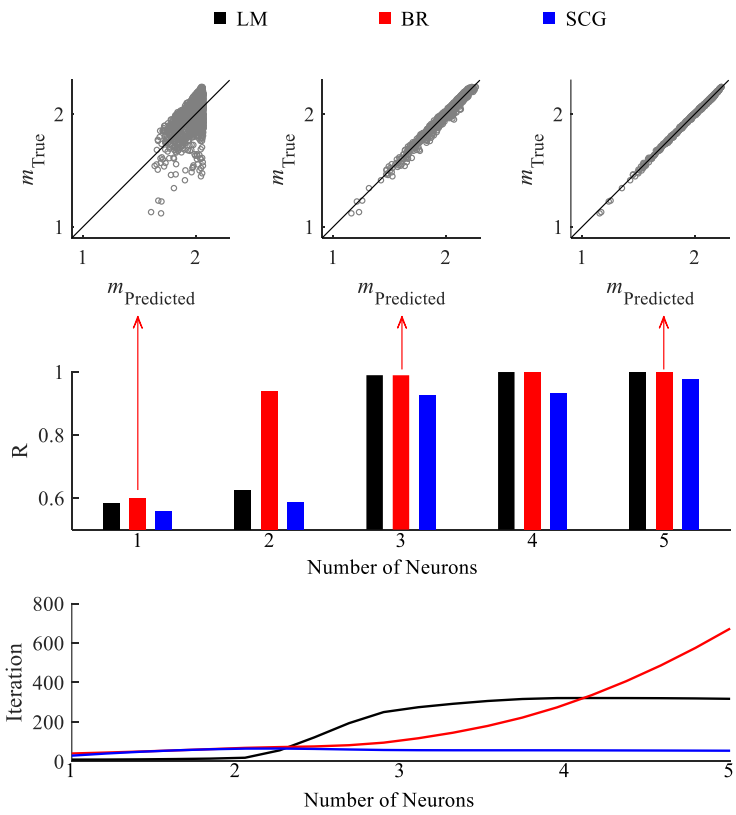


Figure 5.11. Correlation coefficient and computational effort of FNNs trained with different algorithms.

Three optimizers, namely Stochastic Gradient Descent with Momentum (SGDM), Root Mean Square Propagation (RMSP), and Adaptive Moment Estimation (Adam), were utilized to train the CNNs. The structured data were transformed to create labeled data, consisting of input images and their corresponding target labels, to train the CNNs. In this process, the structured data, represented by a vector of four variables [τ, δ, W, β], were transformed into black and white images, as shown in Figure 5.12, to facilitate the training. The input images served as the raw data for the CNNs to learn from, while the target labels provided information about the annual biomass harvest associated with each input image. To encode the structured data into images, several features were visually illustrated. τ represented the reciprocal of the fresh medium flow rate and was depicted as white disks in the generated images. Higher τ values corresponded to lower flow rates, resulting in smaller white disks in the images which indicated smaller pumps. Conversely, larger white disks indicated lower τ values and higher flow rates. δ was conveyed through the thickness of the PBR in the generated images. Higher δ values corresponded to thicker PBRs, which were visually represented in the images. Similarly, W and β were also noticeable in the generated images. The cavity width and the tilt angle of the lower panels in the images provided information about these variables.

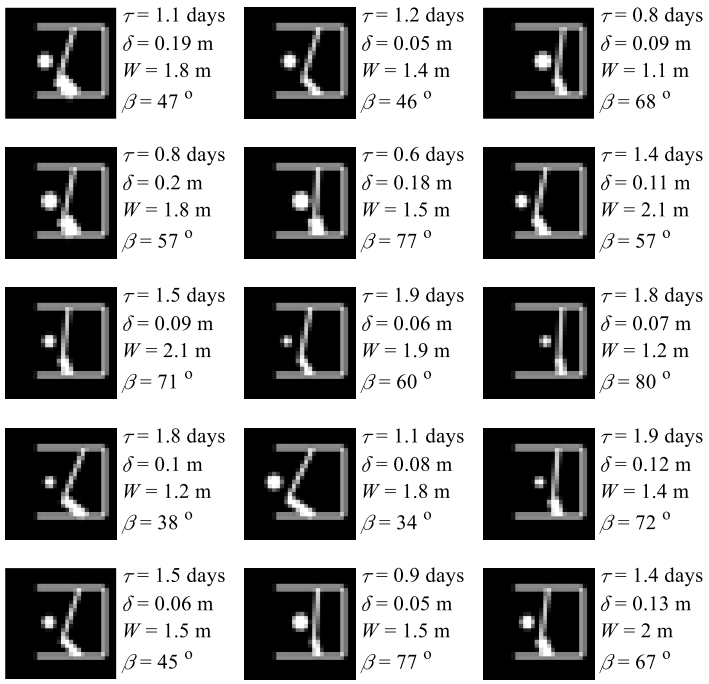


Figure 5.12. CNNs' input images derived from the structured data represented by the variables vector [τ, δ, W, β].

To assess the performance of various algorithms used to train the Convolutional Neural Network (CNN), the root mean square error (RMSE) was monitored for both the training and validation sets (Figure 5.13). Initially, when the SGDM algorithm was applied to train the CNN, the training RMSE was observed to be 0.76. However, as the training progressed, the RMSE values exhibited a decreasing trend, reaching 0.35, 0.14, and 0.13 after 3 Epochs, 30 Epochs, and 50 Epochs, respectively. Each Epoch corresponded to a specific number of iterations, with 130 iterations, 1885 iterations, and 3185 iterations completed for the above-mentioned Epochs, respectively. The validation RMSE values for the same Epochs were determined to be 0.18, 0.09, and 0.08, respectively. These decreasing RMSE values indicate an improvement in the performance of the trained CNN over time. As the training progresses, the model becomes more proficient at predicting the target variable, resulting in reduced errors between the true and predicted values. For the examined Epochs, the R values were found to be 0.50, 0.86, and 0.87, respectively. These R values suggest a positive and moderate-to-strong linear relationship between the true and predicted values.

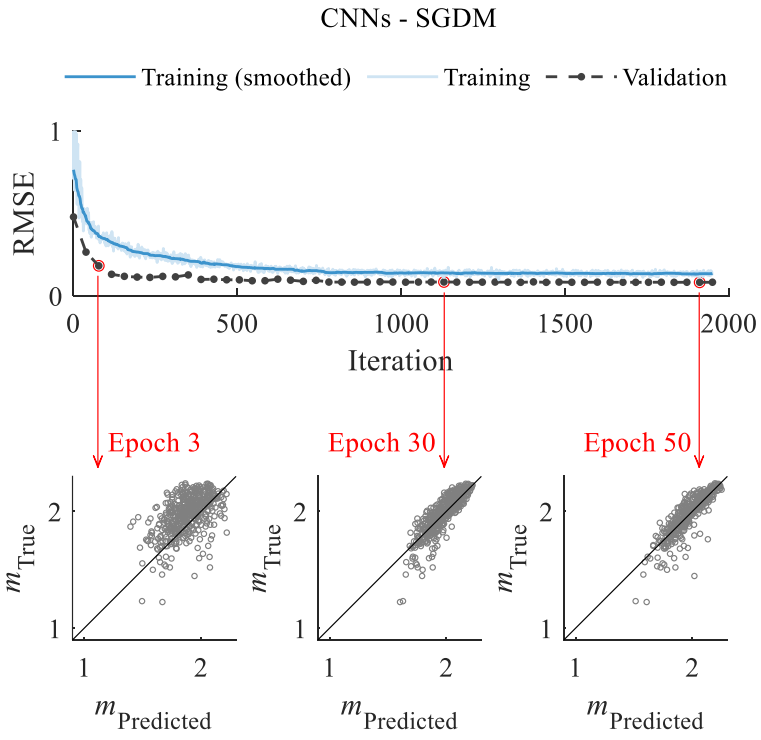


Figure 5.13. RMSE values for both the training and validation sets of CNNs trained using the SGDM algorithm.

During the training of the CNNs, different values of SGDF (Stochastic Gradient Descent Factor) were employed with the RMSP algorithm. As shown in Figure 5.14, the validation RMSE values after 50 Epochs were found to be 0.04, 0.03, and 0.09 for SGDF values of 0.8, 0.9, and 1.0, respectively. The corresponding R values for the mentioned SGDF were 0.97, 0.98, and 0.84, respectively. On average, the RMSP algorithm demonstrated a higher efficiency with an R value of 0.93, compared to the SGDM algorithm, which yielded an R value of 0.87. These R values indicated a strong linear relationship between $m_{Predicted}$ and m_{True}, suggesting the accuracy of the trained CNNs in capturing the underlying patterns in the data. However, significant fluctuations were observed in the RMSE values throughout the training process. The RMSP algorithm with an SGDF value of 0.9 exhibited the highest RMSE fluctuation of 15%. This indicated that the performance of the model varied significantly during the training process when using this specific SGDF value. In contrast, the RMSE fluctuation was only 6% for an SGDF value of 1.0 and was nearly negligible for an SGDF value of 0.8.

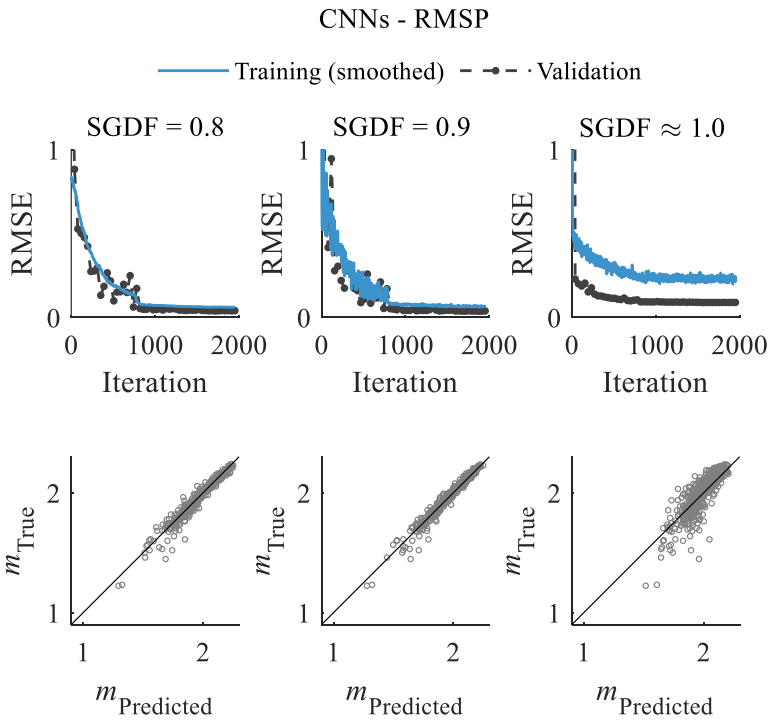


Figure 5.14. RMSE values computed for the training and validation sets of CNNs trained using the RMSP optimizer, while varying the SGDM values.

Various values of SGDF were utilized in conjunction with the Adam algorithm for training the CNNs. As shown in Figure 5.15, the validation RMSE values were observed to be 0.04, 0.03, and 0.06 for SGDF values of 0.8, 0.9, and 1.0 after 50 Epochs. To assess the correlation between the predicted and true values, the R values were computed. The corresponding R values for the above-mentioned SGDF values were 0.97, 0.98, and 0.94, respectively. On average, the RMSP algorithm exhibited higher efficiency with an R value of 0.96, in comparison to the SGDM algorithm with an R value of 0.87 and the SGDF algorithm with an R value of 0.93. However, it was worth noting that the R value of 0.98 achieved by the Adam algorithm employing SGDF of 0.9 was still lower than the R value of 1 achieved by FNNs trained using the LM and BR algorithms.

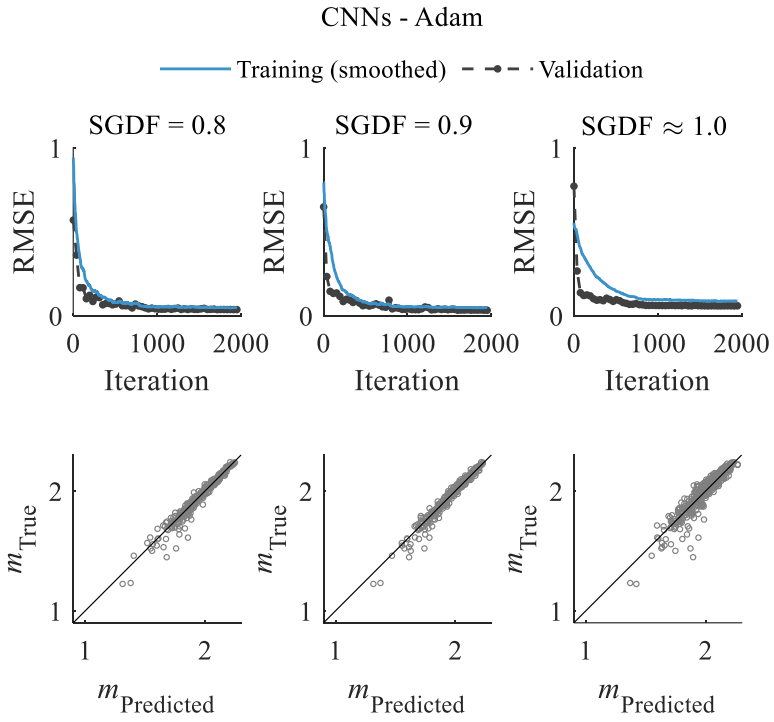


Figure 5.15. RMSE values calculated for the training and validation sets of CNNs trained using the Adam optimizer.

5.3.3 Neural network-aided optimization

The initial framework applied original meta-heuristic methods to the detailed chemical kinetics model. The original GA and PSO each took 12 minutes per iteration, while the original SA took 8 minutes per iteration. The optimization framework was then updated by incorporating NN for all algorithms. To reduce the overall time, the training dataset size for the network should be minimized. NNs were trained with datasets of different sizes to balance prediction accuracy and

data generation time. Figure 5.16 shows the prediction accuracy and time elapsed for datasets ranging from 10 to 1000 points. Data generation and training time increased linearly with 10 points-NN taking 35 seconds and 1000 points-NN taking 58.9 minutes. The time rate was 3.5 seconds per added point. Datasets below 100 points showed lower prediction accuracy with 10 points-NN having an R value of 0.661 and 50 points-NN having an R value of 0.599. This performance can be enhanced by using two hidden layers instead of one layer to achieve an R value of 0.98 for datasets with less than 64 points, as concluded by [231]. Above 100 points, accuracy significantly improved where 100 points-NN and 150 points-NN had R values of 0.996 and 0.999, respectively. Datasets with sizes exceeding 150 points achieved a perfect linear relationship with an R value of 1.

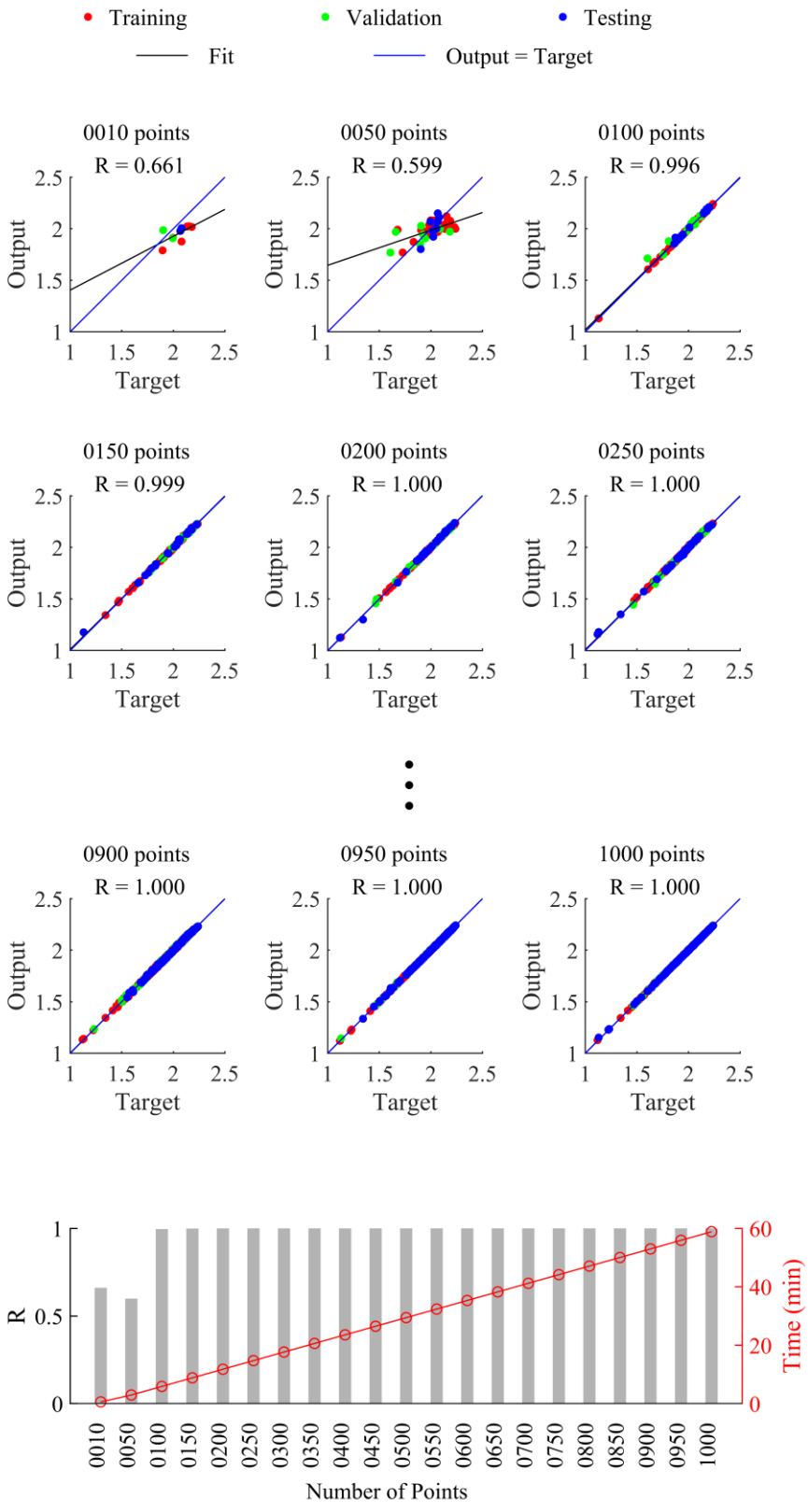


Figure 5.16. Variation of correlation coefficient (R) and required time for different sizes of datasets.

Evaluating the optimization overall time required the summation of data generation time and the time dedicated to each algorithm's execution for m_B optimization. Figure 5.17 shows the variation of optimal m_B and optimization overall time with number of points For datasets involving 10 points, an average m_B of 1.38 kg/m^2 was achieved within a computational timeframe of 1.1 minutes. As the dataset size expanded to 50 points, m_B increased to 1.57 kg/m^2, accompanied by an extended computational time of 3.4 minutes. Increasing the dataset to 100 points achieved the maximum m_B of 2.25 kg/m^2 at a computational time of 6.5 minutes. Beyond this dataset size, there was negligible impact on optimal m_B and a substantial escalation in computational time was observed. This led to adopting a dataset comprising 100 points for the assessment of NN – Aided algorithms in optimizing the proposed system. This selection aimed to achieve a balance between achieving the maximum m_B and maintaining a computationally feasible optimization process. NN – Aided algorithms showed a substantial reduction in computational time, compared to the original algorithms. Original GA demanded an extensive 24.4 hours for the system optimization, whereas NN – Aided GA accomplished the same task within only 6.0 minutes. Original PSO required 7.4 hours, while NN-Aided PSO showed higher efficiency by demanding only 5.9 minutes. SA also had a significant reduction in computational time, with the original algorithm taking 19.9 hours, while NN – Aided SA achieved optimization in only 7.6 minutes. This highlighted the advantage of reducing computational time and addressing the absence of optimization setup in simulation software by generating datasets in one engine and optimizing in another using NN, as noted in [198].

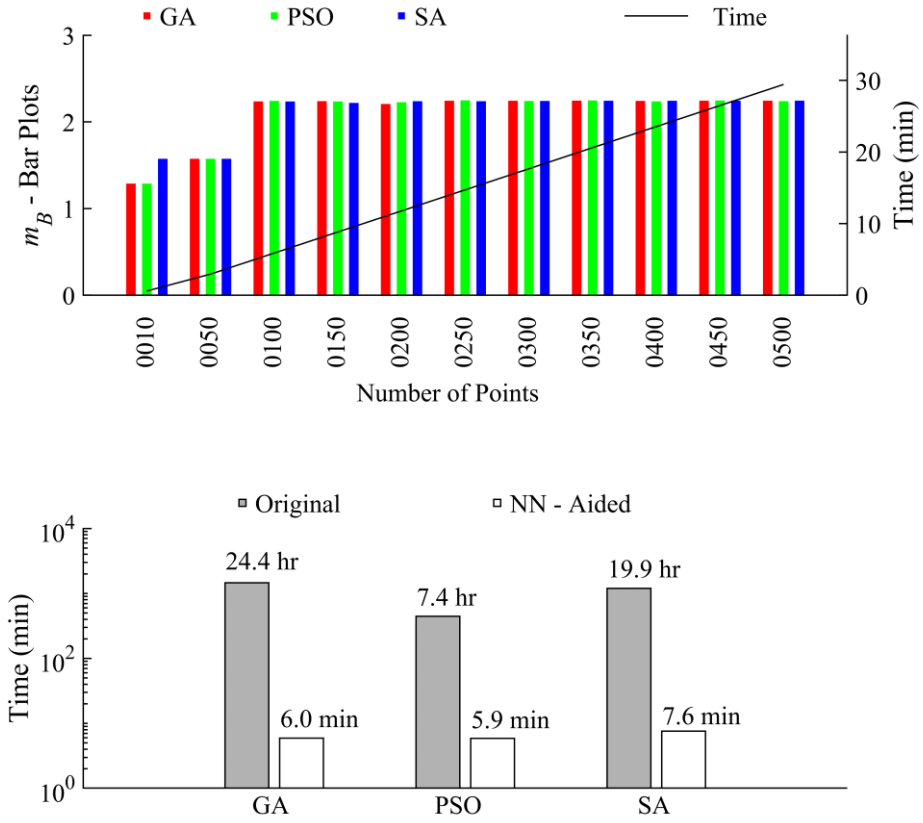


Figure 5.17. Top, variation of maximum mB and overall time with number of points. Bottom, impact of NN integration on the overall time.

5.3.4 Hooke-Jeeves and Powell's Conjugate Direction Methods

HJ algorithm and PCD method were both applied to the proposed system for estimating the optimal variables. Multiple initial points were used to ensure the accuracy and reliability of the optimization process. Figure 5.18 shows 6 pairs of plots representing the performance of both methods. The first pair at the top shows the objective function (f' or Eq. 38) to be minimized while the second pair presents the annual biomass harvest (m'' or Eq. 4) to be maximized. The remaining 4 pairs show the variation of τ_d, δ, W_c, and β with iterations. For the initial point x_0 = [0; 0; 0.6; 0], HJ and PCD methods estimated the maximum solution to be m'' = 2.3 kg/m^2 after 43 and 72 function evaluations, respectively. This biomass harvest was 4.5% higher than the value concluded by the parametric analysis in Figure 5.10. When x_0 = [2; 0.2; 2.4; 90], both methods estimated the optimal solution after 37 and 49 function evaluations, respectively. Such a performance was quite efficient compared to similar optimization methods that achieved a solution convergence after 168 function evaluations [12]. The optimal decision variables $[\tau_d; \delta; W_c; \beta]_{opt}$ for HJ and PCD methods

were [1.05; 0.2; 1.14; 50] and [1.043; 0.199; 1.24; 48.6], respectively. The HJ algorithm was more efficient compared to the PCD method which required a higher number of function evaluations. However, the line searches performed by the PCD method allowed for better accuracy compared to the fixed step Δ employed by the HJ algorithm.

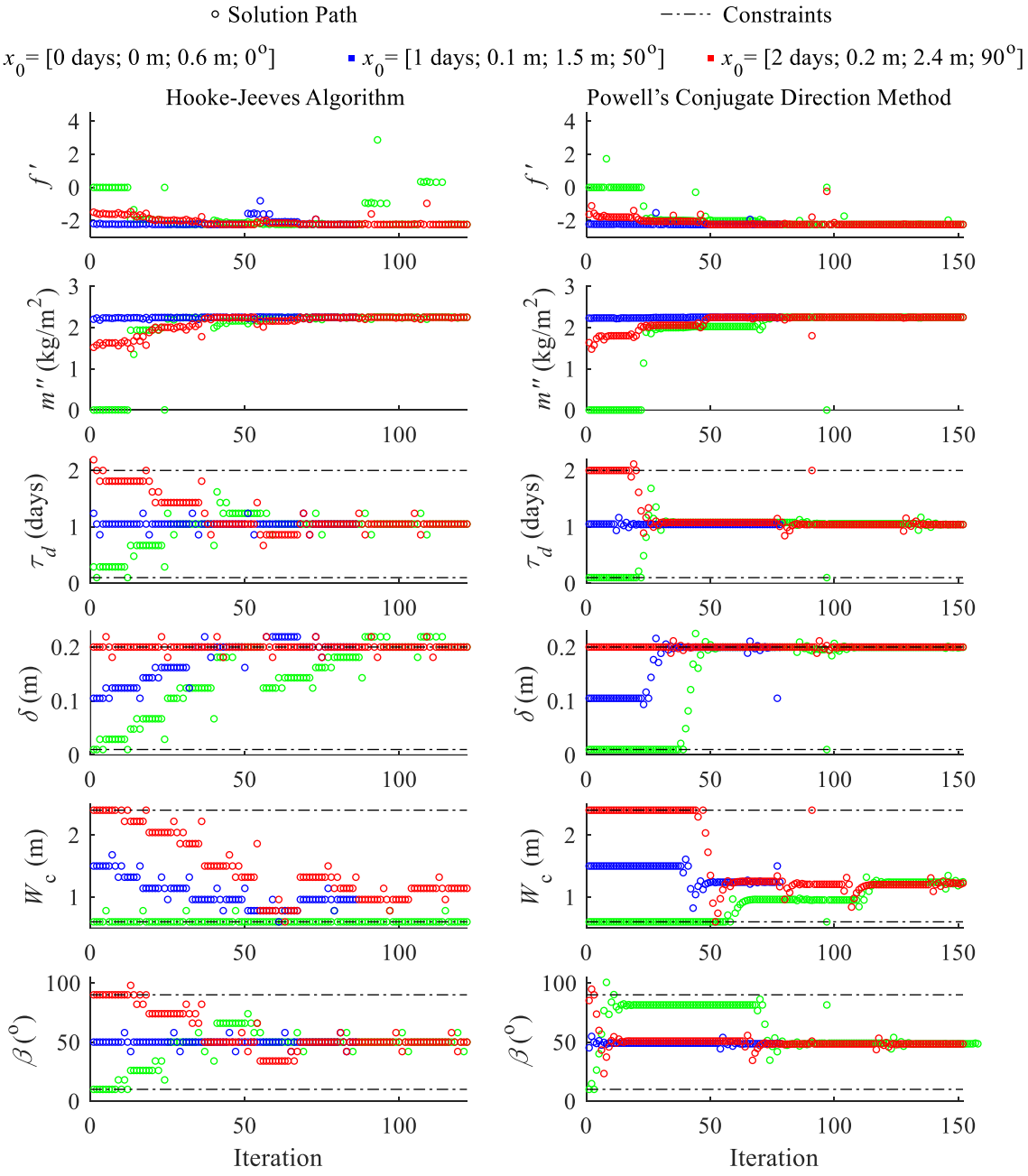


Figure 5.18. Performance of the HJ algorithm and PCD in relation to variation of the objective function, aerial biomass harvest, and decision variables with iterations.

5.3.5 Volumetric biomass production

The optimization shown in Figure 5.18 was based on biomass aerial productivity (m''). Associated optimal variables that achieved maximum m'' were

$$x_{\text{opt}} = \begin{bmatrix} \tau_d \\ \delta \\ W_c \\ \beta \end{bmatrix} = \begin{bmatrix} 1.04 & \text{days} \\ 19.9 & \text{cm} \\ 1.24 & \text{m} \\ 48.6 & ^\circ \end{bmatrix} \tag{5.45}$$

However, Figure 5.18 shows that δ was always approaching the maximum constraint. This was interpreted by the high potential of thicker PBRs to absorb greater shares of solar irradiation. However, the dark volumes behind the front surface of the PBRs had low productivity. Their corresponding biomass production was not spotted due to excluding the variable (δ) from m''. This was mitigated by including δ into m'' through optimizing the volumetric productivity ($m''' = m_{annual}/V = m_{annual}/[A \times \delta]$). The optimization process was repeated by updating the objective function to be

$$f = m''' = \frac{m_{annual}}{V} = \frac{m_{annual}}{A \times \delta} = \sum_{n=1}^{8760} \frac{m_{out}}{A \times \delta} = \frac{1}{\tau_p} \sum_{n=1}^{8760} \int_0^t C_X dt \tag{5.46}$$

Figure 5.19 presents the optimal parameters for achieving maximum volumetric productivity. Maximum m''' was 221.6 kg/m^3. The associated optimal tilt angle and residence time were the same as the optimization outcomes from aerial production ($\tau_{d\text{-opt}} = 1.043$ days and $\beta_{\text{opt}} = 48.6°$).

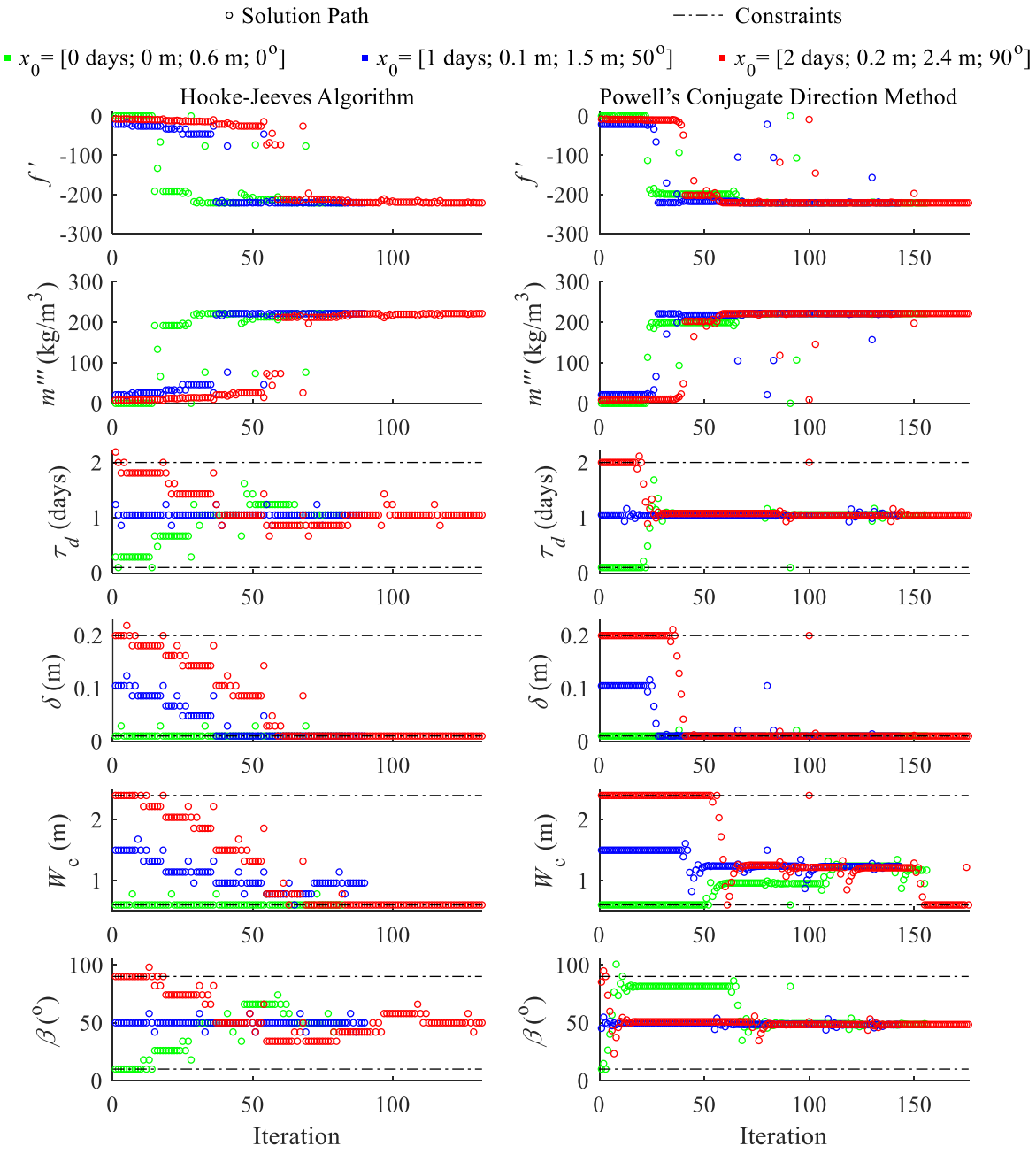


Figure 5.19. Optimal parameters for maximum volumetric productivity.

5.3.6 Application in various Canadian cities

The proposed system was optimized for 13 cities representing all Canadian provinces. A sensitivity analysis was conducted to evaluate the impact of microalgae optical parameters on areal biomass generation. The mass absorption coefficient (E_a) and mass scattering coefficient (E_s) varied in the ranges 130 to 200 and 850 to 2870 to include different microalgae strains like *Chlorella vulgaris* and *Chlamydomonas reinhardtii* [1,21]. Figure 5.20 shows the impact of mass absorption coefficient (E_a) and mass scattering coefficient (E_s) on m''. The same figure illustrates the optimized decision variables in addition to the biomass productivity for the examined locations with variation at each location showing the impact of optical parameters at each location. It was evident that the location was more impactful than the microalgae strain. Overall, m'' varied within 56.7% from 3.0 kg/m^2·year to 1.3 kg/m^2·year based on the location. On the other hand, the maximum impact on m'' because of the optimal parameters was in Resolute as m'' changed within 5.7% from 1.3 kg/m^2·year to 1.2 kg/m^2·year. $\tau_{d\text{-opt}}$ varied between 0.73 days in Vancouver to 1.26 days in Resolute. Resolute was chosen as a representative of severe environmental conditions characterized by its polar climate, featuring extended cold winters and brief cool summers. Smaller residence times corresponded to higher flow rates of the fresh medium. Such higher rates were more suitable for the excess solar energy in Vancouver compared to Resolute. δ_{opt} was 20 cm for all cities since the objective function was based on areal productivity. For volumetric productivity, δ_{opt} would approach the lower constraint of 1 cm as illustrated previously. $W_{c\text{-opt}}$ was lower for cities with less latitude angle (φ) to compensate for the higher solar elevation angle. $W_{c\text{-opt}}$ was 0.6 m and 2.15 m at φ = 45.4° and φ = 74.7° for Ottawa and Resolute, respectively. β_{opt} followed the same trend as $W_{c\text{-opt}}$ by varying from 41.8° to 56.5° for Ottawa and Resolute. Average biomass generation was 2.2 kg/m^2·year for all examined locations. Calgary and Vancouver had the maximum generation of 3.0 kg/m^2·year. In addition to PBRs, Vancouver was also the most suitable location in Canada for building integrated PVs as reported by [12]. The minimum biomass generation was 1.3 kg/m^2·year for Resolute due to the limited solar irradiation in the city compared to the remaining locations.

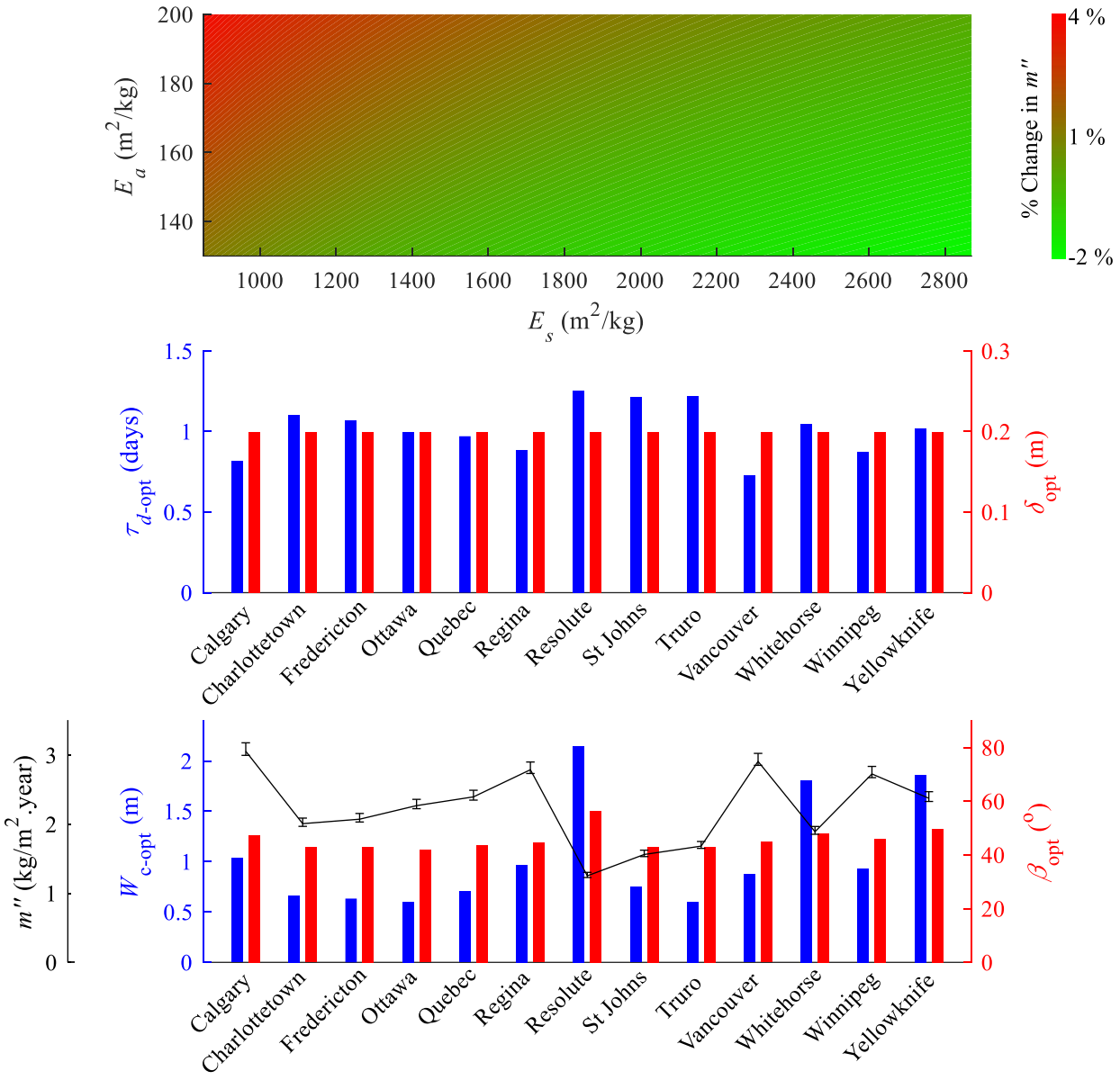


Figure 5.20. Sensitivity analysis and optimal decision variables for different locations across Canada.

5.4 Summary of Chapter

In this chapter, a chemical kinetics model was developed to estimate biomass generation from solar irradiation. An experimental setup was fabricated by comprising custom crafted PBR frames, integrated glass panels, and movable walls that allowed for adjustable cavity widths. RGB image-based monitoring technique was developed to monitor the microalgae growth in the PBRs. Collected experimental data was employed to validate the chemical kinetics model. The chemical kinetics model provided structured data for training an ML image-based monitoring technique.

Various ML algorithms were compared to find optimal training methods. Five optimization methods, including SA, GA, PSO, HJ, and PCD, were employed to maximize microalgae generation. NN-aided algorithms were then used to enhance computational efficiency. The optimal solution was estimated for different Canadian cities. The findings highlight:

- **Model Accuracy:** The RMSE values for the 20 cm and 40 cm wide cavities were 0.0279 kg/m^3 and 8.13 x 10^{-4} kg/m^3, respectively. The overall RMSE for concentration prediction was 0.0144 kg/m^3.
- **ML Image-Based Techniques:** The Adam algorithm with SGDF = 0.9 achieved the highest R values of 0.98 among all CNN algorithms. However, it did not reach the perfect linear relationship (R = 1) achieved by FNNs.
- **Direct Search Algorithms:** The HJ algorithm required less computational time compared to the PCD method. On average, the HJ algorithm reached the optimal solution in 65.6% of the function evaluations required by the PCD method. However, the line searches associated with the PCD method increased the results accuracy compared to the fixed step size utilized by the HJ algorithm.
- **NN Datasets:** Neural Networks prediction accuracy increased for datasets exceeding 100 points, with R values reaching 0.996 for 100 points and 0.999 for 150 points. Datasets exceeding 150 points achieved a perfect linear relationship with an R value of 1.
- **NN – Aided algorithms:** NN – Aided algorithms achieved a substantial reduction in computational time, compared to the original algorithms. For instance, Neural Network – Aided GA accomplished system optimization in just 6.0 minutes, a significant improvement over the 24.4 hours required by the original algorithm. Efficiency improved with Neural Network – Aided Particle Swarm Optimization, which took 5.9 minutes compared to 7.4 hours for the original method. Similarly, Neural Network – Aided Simulated Annealing took 7.6 minutes compared to the original's 19.9 hours. This highlighted the advantage of using Neural Networks to reduce computational time and addresses the optimization setup limitations in simulation software.
- **Parametric Analysis:** Present outcomes showed that using optimization methods enhanced the overall performance by around 5% compared to parametric studies.
- **Optimal Variables:** The objective function considered the decision variables to be the microalgae residence time (τ_d), PBR's thickness (δ), DSF cavity width (W_c), and PBR's tilt

angle (β). The optimal decision variables [τ_d; δ; W_c; β]$_{opt}$ were [1.043 days; 0.199 m; 1.24 m; 48.6°] that achieved an aerial biomass generation of 2.3 kg/m^2.

- **PBR Thickness:** δ approached both lower and upper constraints of 1 cm and 20 cm when the objective function was based on volumetric and aerial production, respectively. However, lower δ corresponded to a more efficient design in relation to decreasing structural and environmental impacts imposed by the higher weight and excessive materials for thicker PBRs.
- **Location Impact:** The proposed system was optimized in different provinces across Canada. The maximum biomass generation was 3.0 kg/m^2 for both Calgary and Vancouver.

These findings indicate high model accuracy in predicting microalgae concentration, with neural network-based techniques significantly improving computational efficiency compared to traditional algorithms. Optimization methods have highlighted significant biomass generation potential across diverse Canadian locations. However, further analysis is needed to examine the impact of variable residence time on biomass generation. Additionally, the impact of façade geometry under shading from surrounding buildings remain unexplored. These topics will be the primary focus of the upcoming chapter.

Chapter 6: Variable Flow Rate of Fresh Medium and Façade Geometry Impact[1]

The previous chapter highlighted the importance of examining the impact of variable residence time and façade geometry on biomass generation, particularly under shading from surrounding buildings. This chapter addresses these topics and fulfills the fourth objective by employing the developed chemical model to examine a novel PBR with variable flow rates of fresh medium. The chapter also focuses on optimizing PBR integration into various façade designs by developing and refining TgMs to consider shading effects from surrounding buildings. Multiple building orientations are considered to determine optimal façade azimuth angles across different locations, using the HJ algorithm for folded façades and the GA for free-form designs due to their respective advantages in handling variable complexity and achieving convergence.

6.1 Introduction

Numerical PBR models considered residence time, light attenuation, nutrient limits, pH value, and temperature in addition to both artificial and solar light sources [21,22]. However, the optimal performance in the literature was achieved by assigning a fixed value to the microalgae residence time which maximized biomass generation throughout the year [22]. A fixed residence time of 1.4 days increased microalgae concentration by three times with a pulsed LED light regime [227]. This value was reduced by 29% (from 1.4 days to 1 day) to increase the protein content to up to

[1]This chapter is based on the following articles:

Elmalky, A. M., & Araji, M. T. (2024). Optimization models for photosynthetic bioenergy generation in building façades. *Renewable Energy*, *228*, 120607 [75].

Elmalky, A. M., & Araji, M. T. (2023). Computational procedure of solar irradiation: A new approach for high performance façades with experimental validation. *Energy and Buildings*, *298*, 113491 [76].

Elmalky, A. M., & Araji, M. T. (2023). A new trigonometric model for solar radiation and shading factor: Varying profiles of building façades and urban eccentricities. *Energy and Buildings*, *282*, 112803 [29].

Elmalky, A. M., & Araji, M. T. (2023, April). A Novel Genetic Algorithm for Optimizing Microalgae Residence Time in Flat Panel Photobioreactors. In *2023 International Conference on Mechanical, Automotive and Mechatronics Engineering (ICMAME)* [77].

68% for cyanobacteria [232]. The biomass production rate decreased by 77% when the residence time increased from 0.4 days to 1.8 days [226]. For building integrated PBRs, biomass concentration was adjusted by employing a residence time of 1.3 days to control the light attenuation in the microalgae medium [1]. However, no previous work has examined the impact of applying a variable residence time on shorter time intervals by employing a variable speed pump. Typical pumps with flow rates between 3 liter/hr to 5 liter/hr are quite sufficient for microalgae cultivation in flat panel PBRs [2]. In this system, PBRs with an unsteady residence time on an hourly basis will generate a multivariate optimization problem of 24 variables. For such a wide multidimensional domain, GA allows for a fast convergence with a reasonable computing power [233]. GA is considered one of the most applied technologies in Artificial Intelligence Computing with an observed accuracy of 98.73% [234]. That's mainly due to its efficient global search performance without considerable algorithm complexity [207].

Façade geometry has a significant impact on buildings' energy efficiency [235], yet there is limited research on the assessment of solar irradiation for free-form façades with multiple sinks and protrusions. Optimal façades integrating PVs/PBRs are usually controlled by numerous parameters, including building surroundings, panel positions on the façade, ambient conditions, and façade geometry [1,15]. Configurations of the façade geometry often include flat or baseline façades [236], folded façades [237,238], and curved or free-form façades [29]. Shading devices or PVs/PBRs are usually installed on high irradiation spots to make the most benefit from the incident solar energy [15]. Therefore, it is critical to incorporate an optimization phase during the building design stage to find the optimal location for integrating PVs/PBRs, while considering the impact of the surrounding environment with façade geometry, building orientation, material selection, window-wall ratios, and especially in the presence of shading imposed by adjacent elements [239].

In light of the above, this chapter applied the detailed chemical kinetics model for assessing a novel PBR with a variable flow rate of fresh medium. The performance of the developed system was assessed in relation to reducing the carbon footprint for buildings with different numbers of floors. This chapter also optimized the integration of PBRs into different façade forms. The conversion efficiency from solar energy to bioenergy was estimated based on the detailed chemical kinetics model. TgMs were developed and refined to investigate the shading imposed by the surrounding

buildings. Solar angles variation, including tilt and azimuth angles, was estimated to quantify their impact on received irradiation and consequent bioenergy harvest. Multiple building orientations were considered to find the optimal façade azimuth angle at different locations. The HJ algorithm was selected for folded façades due to fewer variables. For free-form façades, the GA was chosen for its accuracy and convergence with multiple variables.

6.2 Method

For a dynamic PBR system with unsteady hourly residence times, a 24-variable multivariate optimization problem was created and optimized using GA for quick convergence with moderate computing power. Different selection techniques for the employed GA were examined and compared. Optimal façade integration considered baseline façades, folded façades, and free-form façades. TgMs were developed and refined to analyze shading impact from the surrounding elements to estimate the irradiation reduction imposed on façades integrating PBRs. The developed chemical kinetics model was applied to determine the conversion efficiency from solar irradiation to bioenergy. Folded and free-form façades were modeled to calculate the corresponding solar angles, reflections between glass panels, and self-shading factors. Finally, both façades were then optimized using HJ and GA for folded and free-form façades, respectively.

6.2.1 Variable flow rate

To develop a dynamic PBR system with variable flow rates, this chapter considered an array of residence times. This array was optimized using GA to maximize biomass generation over shorter intervals of time by processing hourly weather data. Figure 6.1 shows the followed procedure to optimize an array of n time intervals by generating a population of size p points. Each point included an array of residence times distributed on an hourly basis. The function value was then evaluated for each point. Afterward, the selection process was performed to select and mutate a new pool of points. This study applied three different selection techniques. Each technique considered a different combination of three sub-processes. These processes were the mating pool, random outsiders, and evolution. In the mating pool (tournament scheme), each point in the old pool was given a probability based on its associated function value. This probability was calculated by

$$\rho_i = f(\boldsymbol{\tau_i}) \Big/ \sum_{j}^{p} f(\boldsymbol{\tau_j}) \tag{6.1}$$

where ρ_i is the probability of selecting the i^{th} point. Afterward, the new pool was formed by choosing points from the old pool based on the corresponding probability. The process of random outsiders replaced an *X*% of the old pool with new random points. In the evolution process (pairing and cross-over), each pair of points in the new pool was formed by selecting two points randomly from the old pool. These points were then recombined to generate new offspring.

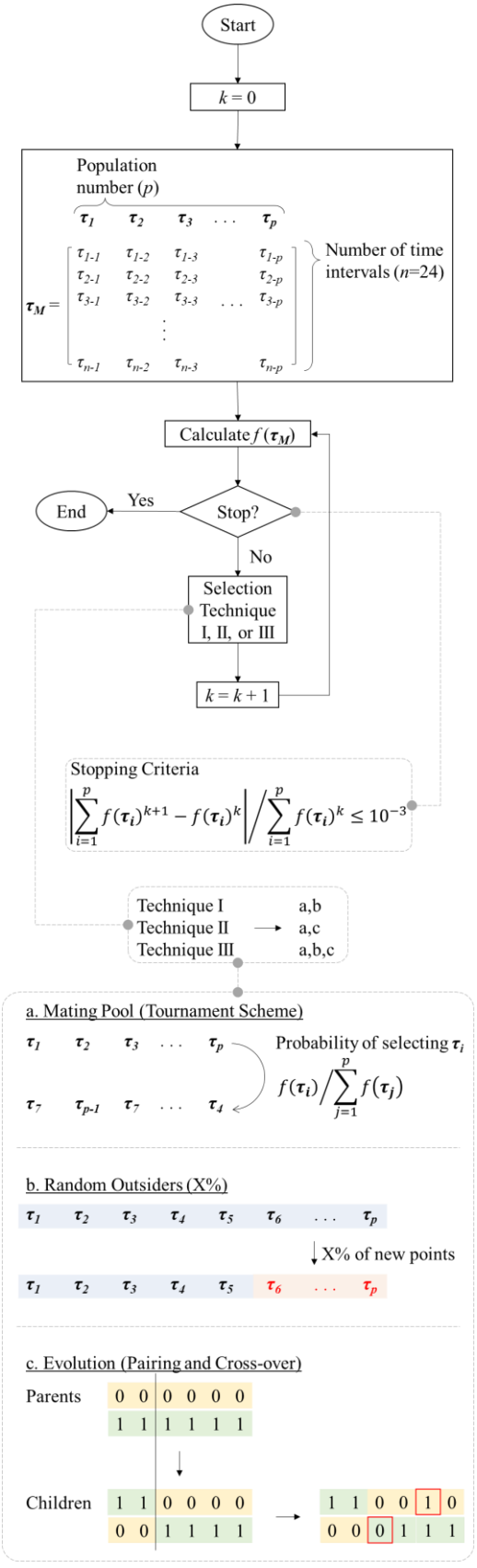


Figure 6.1. Schematic of the used sequence to apply GA for maximizing biomass generation over shorter intervals of time.

In addition to biomass production, microalgae PBRs extract CO_2 which in turn reduces the operational carbon footprint of buildings. In this study, such a reduction was correlated to various design parameters such as the number of floors, type of programs, and PBRs coverage ratio. For a given building integrating PBRs, the façade area to roof area ratio (γ) was expressed as

$$\gamma = \frac{A_F}{A_R} = \frac{n_f \times H_f \times (L + 2 \times W)}{L \times W} \tag{6.2}$$

where A_F is the total façade area, m^2. A_R is the roof area, m^2. n_f is the number of floors. H_f is the height per floor, m. L is the building length in the east-west direction, m. W is the building width in the north-south direction, m. The total carbon reduction was expressed as

$$C_R = A_F \times \delta \times I_R \tag{6.3}$$

C_R is the total carbon reduction, kg/year. I_R is the carbon reduction intensity calculated from equation 4, kg/m^2. δ is the ratio between the PBRs area and the total façade area. The building's total carbon generation was calculated from

$$C_G = n_f \times A_R \times I_G \tag{6.4}$$

C_G is the total carbon generation, kg/year. I_G is the carbon generation intensity assumed for an energy use intensity of 40 $kW/m^2 \cdot$year [19], kg/m^2. Therefore, the building's net carbon generation was calculated from

$$C_{net} = C_G - C_R = n_f \times A_R \times I_G - A_F \times \delta \times I_R \tag{6.5}$$

Or

$$C_{net}/A_R = n_f \times I_R - \gamma \times \delta \times I_G \tag{6.6}$$

6.2.2 Shading models

6.2.2.1 TgM – Version 1

In terms of buildings, façades can take infinite forms ranging from baseline to free-form surfaces. Accordingly, the TgM – Version 1 examined eight façade typologies, including: 1) baseline or flat façade, F_b; 2) Horizontally-convexed façade, F_{hx}; 3) Vertically-convexed façade, F_{vx}; 4) Horizontally-concaved façade, F_{hv}; 5) Vertically-concaved façade, F_{vv}; 6) Horizontally-bicurved

façade, F_{hbc}; 7) Vertically-bicurved façade, F_{vbc}; and 8) Free-form façade, F_f (Figure 6.2). The orientation for all examined façades was assumed due south.

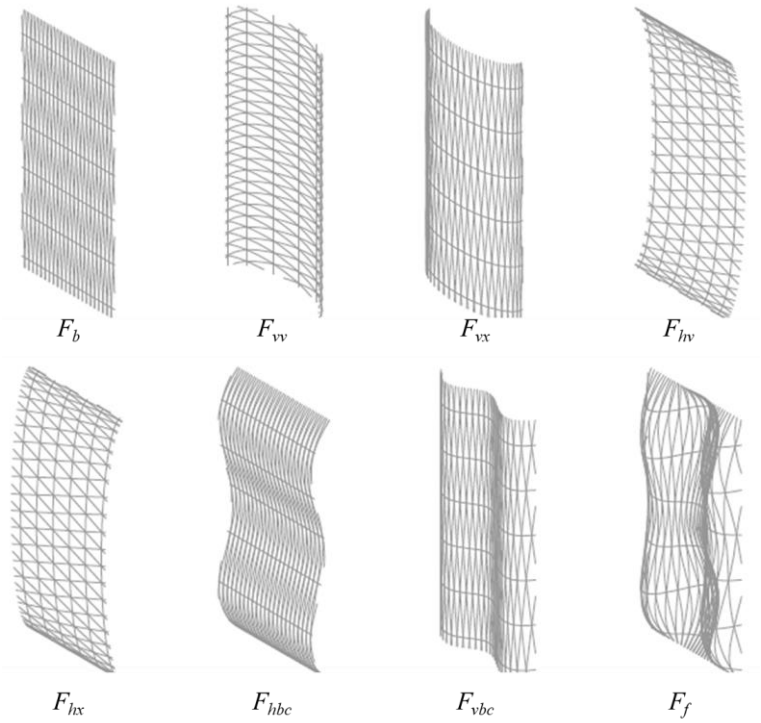


Figure 6.2. Different forms of façade typologies.

Typical cities are designed with either straight to curvilinear urban forms. The site configuration for both forms, in relation to buildings' arrangement, can be divided into orthogonal or curved streets. For this purpose, the TgM – Version 1 considered both linear and elliptical surroundings. The latter has an eccentricity of less than 1; this includes the special case of a circular form, with eccentricity equal to 0. Figure 6.3 shows both the orthogonal grid and circular plans of 12 typical cities around the world.

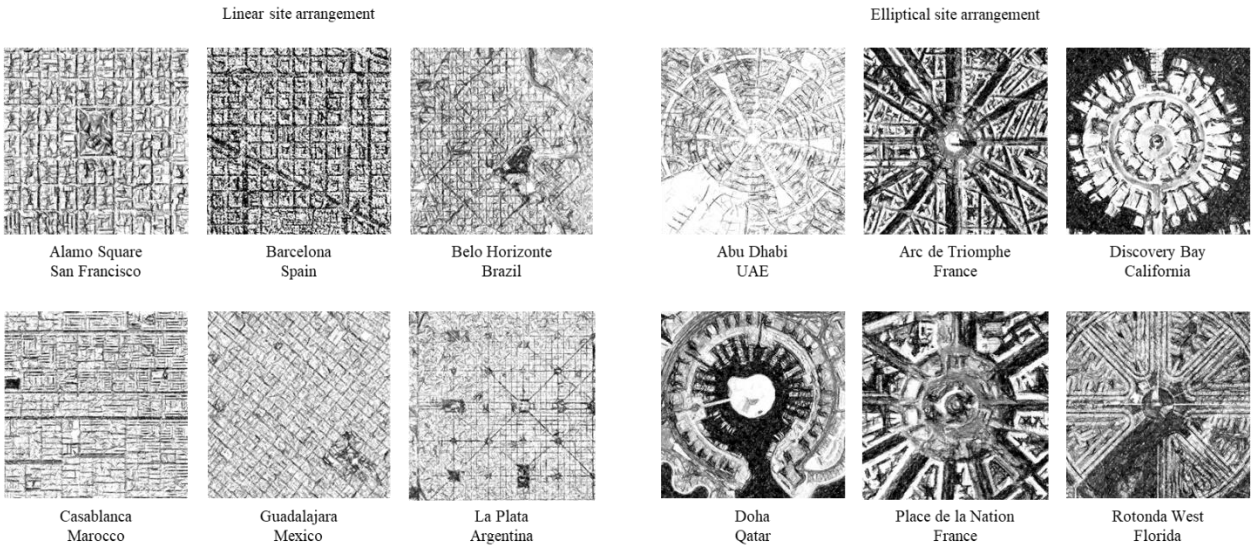


Figure 6.3. Typical linear and elliptical urban contexts.

The building height in relation to site configuration is a significant parameter in determining the shading impact on performance. Factors influencing the shadow include differences in terrain elevation between the examined building and its surrounding environment, time of year, and duration of shading in a day to loss of sunlight. The preliminary model used to predict the shadow on the façade utilized a building height H with a varying height S for surrounding buildings where $S_1 > S > S_2$. S_1, S, S_2 is the surroundings' maximum, local, and minimum height, respectively. Consequently, for the special case $S_2 = S_1$, the surroundings were uniform with a constant height. The inclination of the surroundings was normalized as $\Delta S/S_1$ or $S_1 - S_2/S_1$. Again, $\Delta S/S_1 = 0$ expressed a uniform surroundings height. As $\Delta S/S_1$ increased, more height was deducted from the original height and S_2 decreased.

A mesh of $nz \times ny$ identical elements was generated to examine the solar irradiation on each point on the façade (Figure 6.4). An element of order (i,j) was assumed to have full solar exposure if a view angle (α_{min}) between two given lines was lower than the solar latitude angle α. Figure 6.4 illustrates α_{min}, which is the angle between the line joining the element center and the tip of the surrounding buildings in the plane parallel to the solar rays and the horizontal projection of this line. Hence, this angle can be defined as the minimum solar altitude angle that offers solar exposure to the (i,j) element. Therefore,

$$\tan \alpha_{min} = (S - H_v)/d \tag{6.7}$$

where H_v is the vertical distance from the ground to the center of the *(i,j)* element, m. *d* is the horizontal distance between the center of the *(i,j)* element and the surrounding buildings in the plane parallel to the solar rays, m. For an *(i,j)* element, H_v can be expressed as

$$H_v = H - (i - 0.5) \times (H/nz) \tag{6.8}$$

i is the row order of the *(i,j)* element given that the top row is the first one. In the same sequence, the horizontal distance from the west side of the façade to the center of the *(i,j)* element (L_v) can be expressed as

$$L_v = (j - 0.5) \times (L/ny) \tag{6.9}$$

j is the column order of the *(i,j)* element given that the west column is the first one.

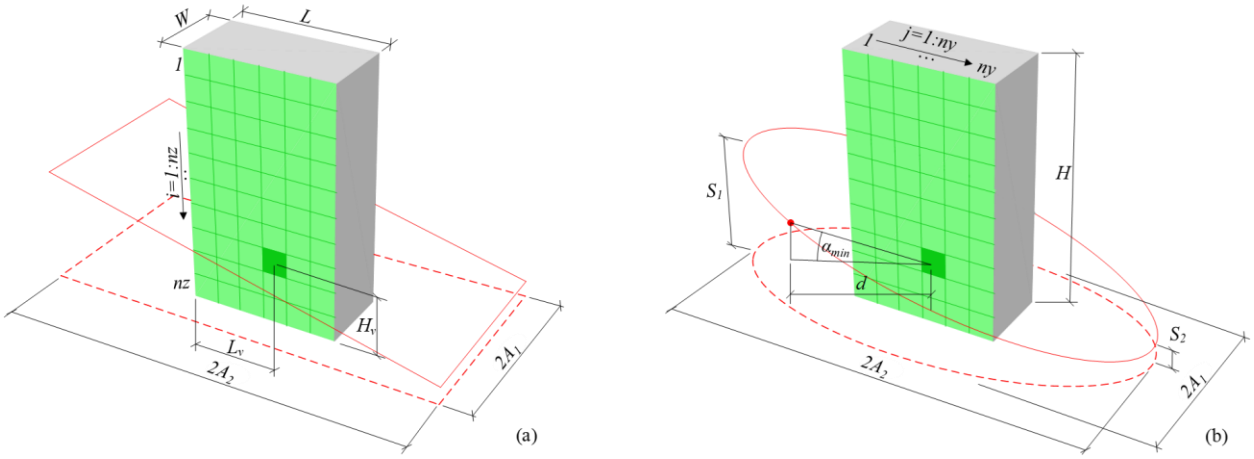


Figure 6.4. Parameters considered for examining solar exposure of a building façade within a site context: (a) Linear site arrangement, and (b) Elliptical site arrangement.

TgM – Version 1 was validated against experimental results from the literature. Rocha et al. [131] performed a detailed comparison between polygon clipping (PgC) and pixel counting (PxC) techniques and estimated their deviation from experimental data. PgC technique was applied by using E+ while PxC technique was applied by using both DS and SS [131]. Although TgM – Version 1 had an average error of 5.2%, the computational time was reduced by more than 40%. More details related to TgM – Version 1 can be viewed by referring to [29].

6.2.2.2 TgM – Version 2

In the TgM updated version, the urban form is generated by considering various façade orientations from east to west. The minimum solar altitude angle (α_{min}) is then calculated through 3D hourly analysis of the façade divided into $n_x \times n_z$ elements. Next, solar irradiation contours are generated based on annual analysis using weather data. Weather data was imported from E+, before post-processing in *MATLAB*®. Beam, diffuse, and reflected components were then computed for various urban forms.

To prepare urban forms for solar analysis, an essential step involved creating visual representations of the generated urban forms. The patch function in *MATLAB* was used to create filled polygons in the 3D space by using predefined vertices. The *x-axis* represented the south-north direction, while the *y-axis* was east-west. The streets' widths along the *x-axis* and the *y-axis* were denoted as W_1 and W_2, respectively, as shown in Figure 6.5. The cartesian coordinates of a specific building located in the i_1 row and i_2 column were then (c_5, c_3) where

$$c_3 = (W_1 + W_B) \times (i_1 - 1) \tag{6.10}$$

and

$$c_5 = (W_2 + W_B) \times i_2 \tag{6.11}$$

where W_B is the building width, m. N_1 and N_2 represented the number of buildings along the *y-axis* and the *x-axis*, respectively. The algorithm started by defining bottom vertices of buildings in the matrix M_1. Each building was represented by a row in M_1. Such a row comprised 12 elements representing four sets of three coordinates for each vertex of the building footprint. c_1, c_2, and c_4 were employed to arrange the rows inside matrix M_1. Matrix M_2 represented the coordinates of the roof vertices of the surrounding buildings. By the proper selection of the footprint vertices from M_1 and the roof vertices from M_2, both the façades and roof of each building were patched to generate the urban form, as illustrated in Figure 6.5.

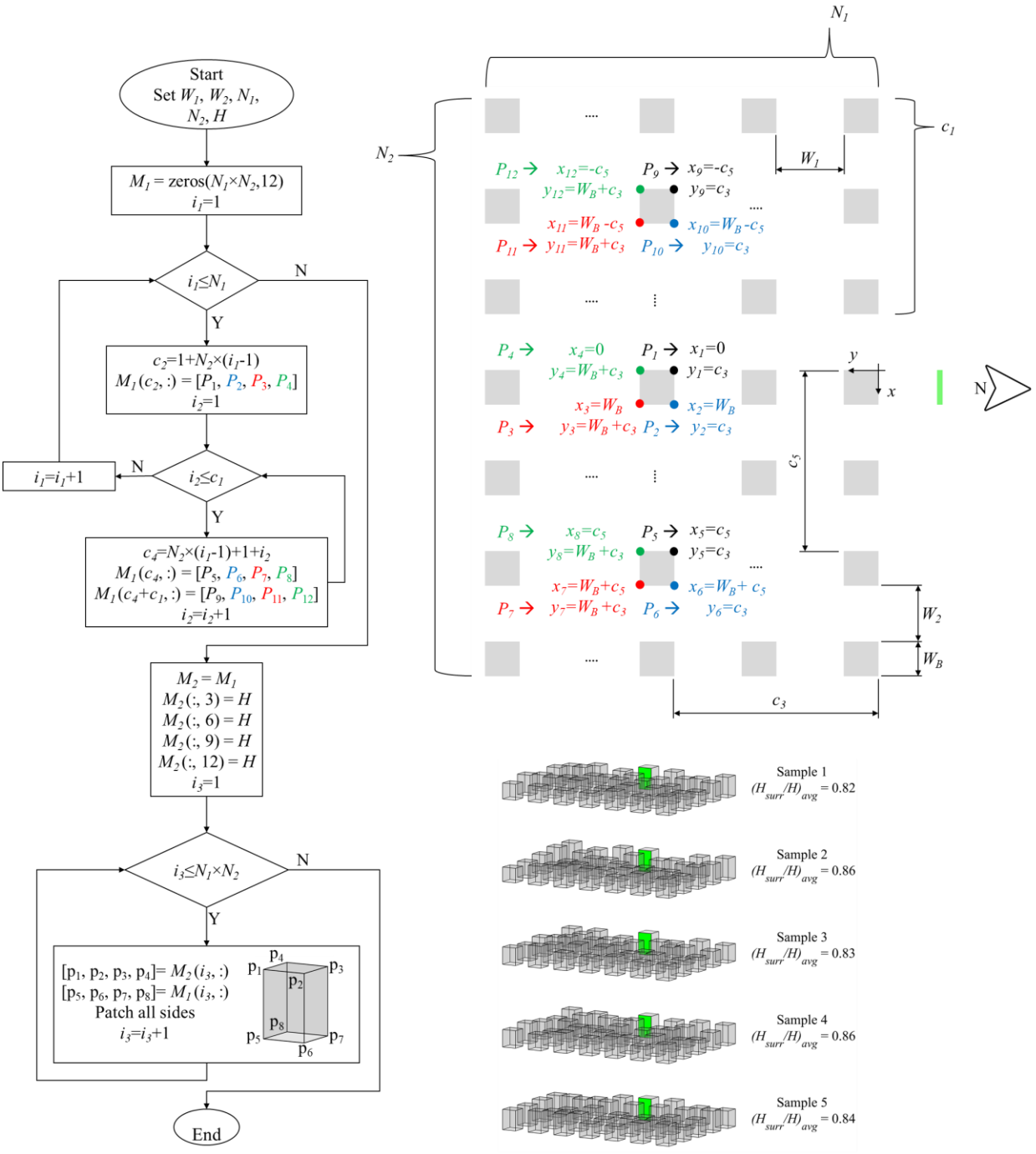


Figure 6.5. Left, computational procedure followed to generate urban forms using *MATLAB*. Right, illustration showing the building's plan view and height variation in 3D.

Solar irradiation on the building's façade was analyzed by dividing the façade into n_x×n_z elements. n_x and n_z represented the number of elements along the façade width and height, respectively. Figure 6.6 shows the façade grid with the solar plane and the surrounding buildings. In this figure,

α_{min} represents the minimum angle of solar altitude that enables solar irradiation to reach the highlighted element. Such an element was shaded for $\alpha_{min} = \alpha_1$ and unshaded for $\alpha_{min} = \alpha_2$.

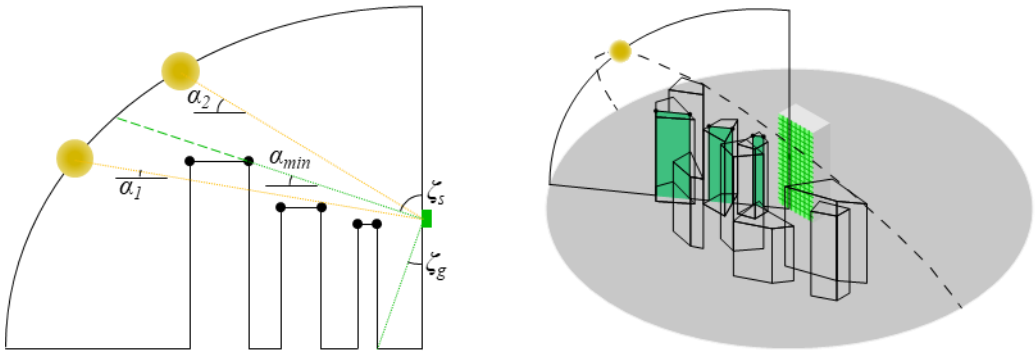


Figure 6.6. Left, intersection points between the solar plane and the buildings located within the plane. Right, the solar plane for one façade element at a given solar time.

The algorithm started by covering the daytime duration to calculate α_{min} on an hourly basis. At a standard time *ST*, the hour angle was expressed as [240]

$$\omega = 15 \times (ST - 12) \times \pi/180 \tag{6.12}$$

For a specific element with order i_x and i_z along the façade width and height, the element's distance from the façade side was expressed as

$$L_v = (W_B/n_x) \times (i_x - 0.5) \tag{6.13}$$

The element's distance from the ground was expressed as

$$H_v = (H/n_z) \times (i_z - 0.5) \tag{6.14}$$

Therefore, the coordinates of a given element were expressed as

$$\mathrm{p_d} = [L_v \quad 0 \quad H_v] \tag{6.15}$$

In the 3D coordinate geometry, the solar plane equation (P_s) was defined as the equation of the vertical plane holding both the sun and the investigated element. This equation was expressed as

$$y = \tan(\pi/2 - \omega) \times (x - L_v) \tag{6.16}$$

The $N_1 \times N_2$ buildings were examined for potential solar obstruction. The intersection point (p_n) was obtained by solving the straight-line equation of each roof edge ($p_a p_b$) with the solar plane equation (P_s). If p_n fell within the straight line $p_a p_b$, it indicated that the building obstructed the solar path of the investigated façade point and α_{min} was calculated as

$$\alpha_{min} = \tan^{-1}([\mathrm{p_n}(3) - H_v]/\|\mathrm{p_n} - \mathrm{p_d}\|) \tag{6.17}$$

Otherwise, the examined edge of the building was bypassed to the next edge, and no need to calculate α_{min}. If α_{min} exceeded the stored value, the stored value was updated by the new α_{min}. In

this case, the new edge hindering the solar path was higher than the previously examined edges. If α_{min} was lower than the stored value, the investigated edge was lower than the previous edges and the stored value of α_{min} wasn't updated. Figure 6.7 gives a detailed overview of the developed algorithm. Equations 6.10, 6.11, and 6.13 – 6.17 were obtained through the application of analytical algebra in 3D coordinate geometry.

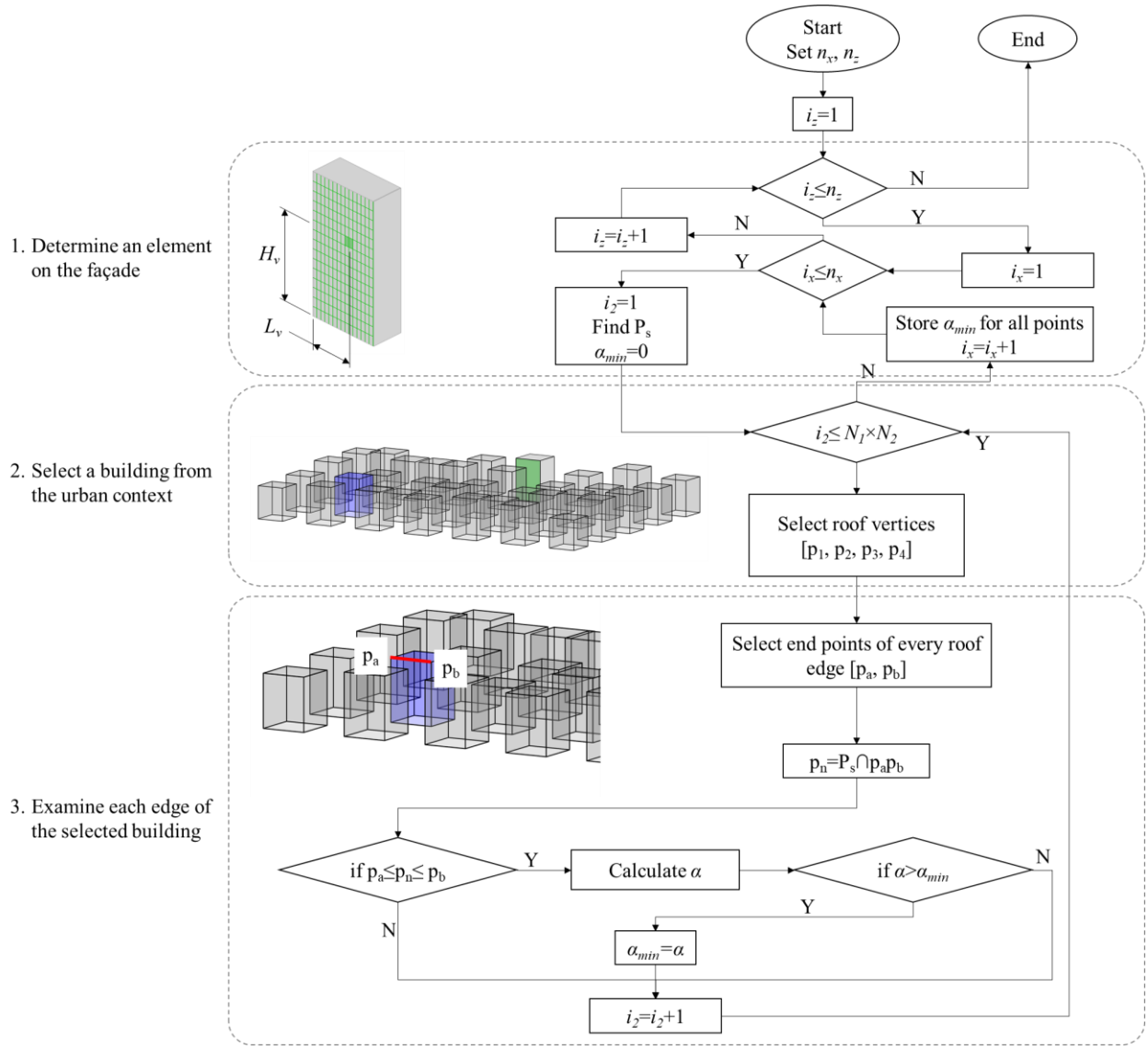


Figure 6.7. Schematic of the algorithm implemented to calculate α_{min} for the investigated façade points on an hourly basis.

TgM – Version 1 had a computational time of 6.1 minutes for analyzing a single façade. In contrast, TgM – Version 2 has significantly reduced the computation time to just 0.8 seconds per façade. This represents a remarkable improvement in computational efficiency, allowing for much faster

analysis and calculation of solar irradiation for individual façades. More details related to TgM – Version 2 can be viewed by referring to [76].

6.2.3 Façade geometry impact

In Figure 6.8, folded and free-form façades were defined by the parameter δ, which represented the sunken or protruding distance from the façade base. δ was optimized for both façades to increase the solar harvest received by the integrated PBRs throughout the year. Examined façades displayed varying orientations and dimensions, with a length denoted as L and a height as H. Impact of the surroundings tilt was examined by varying S_2/L between 0 and 1 while maintaining S_1/L=1. For this, S_2/L=1 represented flat surroundings while S_2/L=0 represented completely tilted surroundings. H/L or the aspect ratio varied between 0.5 and 8 to cover the whole range of buildings' aspect ratios [241]. For the surrounding elements, the normalized parameters A_1/L and A_2/L varied between 0.5 and 0.9 as applied in [29].

6.2.3.1 Boundary conditions

Surrounding elements were assumed to have a linear site profile. Such a profile was tilted with maximum and minimum heights of S_1 and S_2, respectively. The façade was divided into identical elements of regular size. Figure 6.8 shows the generated mesh for different façade types. Each element on the façade, denoted by P_f, was examined on an hourly basis to calculate the view angle, α_{min}. This angle represented the minimum solar elevation angle that allowed solar irradiation to reach the examined element. Based on the developed TgM, the view angle was calculated by

$$\alpha_m = \tan^{-1}\left(\frac{S - H_v}{d}\right) \tag{6.18}$$

where S is the local height of the surroundings, m. H_v is the vertical height of the examined element, m. d is the horizontal distance between the element and the surroundings in the solar plan, m. As shown in Figure 6.9-a, d was calculated by

$$d = A_1\sqrt{1 + \tan^2(\omega)} \tag{6.19}$$

where A_1 is the street width, m. ω is the hour angle, rad. The local height of the surroundings was calculated from

$$S = S_1 - \frac{(x + A_2)(S_1 - S_2)}{2A_2} \tag{6.20}$$

where A_2 is half of the surroundings width, m. When the solar elevation angle (α) was less than α_{min}, the examined element was shaded by the surroundings. Otherwise, the element was exposed to solar irradiation.

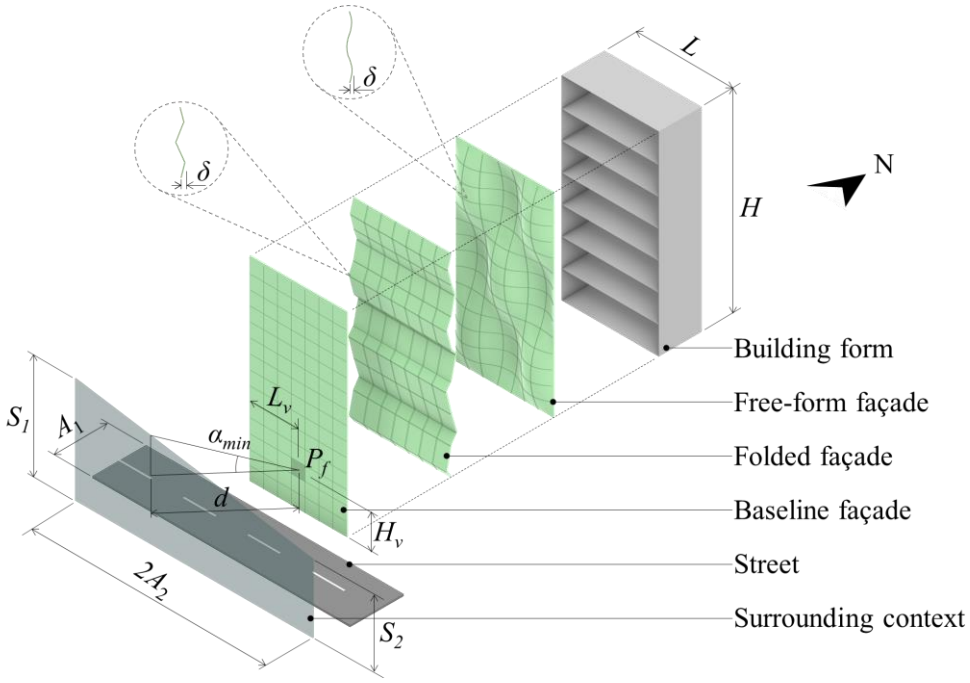


Figure 6.8. Examined façades in relation to the surrounding elements.

6.2.3.2 Façade geometry

Folded façades generally comprised multiple flat panels with different tilts as shown in Figure 6.8. In recent applications of mixed-use buildings, folded façades had two panels per storey with a floor-to-floor height of 4 m [238]. Figure 6.9-b shows the examined storey with both panels in relation to interior and exterior environment. The upper panel joined the ceiling at P_1 while the lower panel joined the floor at P_3. Both panels were connected at the adjustable point $P_2 = (x, y)$. Different locations of P_2 allowed for a wide range of solar irradiation over both panels. The goal was to replace high irradiation panels with PBRs while adding Vision Glass (VIS) elsewhere. Figure 6.9-c shows various combinations of VIS and PBRs. In all cases, shading assessment was performed to quantify the irradiation incident on both panels for various locations of P_2. Incident solar irradiation was thus calculated by

$$I = I_b \times A \times SF \times \cos\theta + I_b \times A \times SF \times Ref \times \cos\theta_r \quad (6.21)$$

where the first term accounts for direct solar irradiation, while the second term represents reflected irradiation from adjacent panels as shown in Figure 6.9-c. I is the irradiation received by the panels, W. I_b is the beam irradiation (W/m^2) imported from E+ for the city of Toronto, Canada, with a latitude and longitude of 43.67° North, and 79.63° West. A is the area, m^2. SF is the shading factor. θ is the solar incidence angle, rad. Ref is the clear glass reflectivity of 10% [242]. θ_r is the solar incidence angle of the reflected solar beam as shown in Figure 6.9-c, rad. The solar incidence angle (θ) on tilted plates was calculated by [240]

$$\begin{aligned}\sin\theta = {} & \sin\delta\sin\varphi\cos\beta - \sin\delta\cos\varphi\sin\beta + \cos\delta\cos\varphi\cos\omega\cos\beta \\ & + \cos\delta\sin\varphi\cos\omega\sin\beta\end{aligned} \tag{6.22}$$

where δ is the declination angle, rad. φ is the latitude angle, rad. β is the tilt angle, rad. ω is the hour angle, rad. β for the upper panel was calculated by

$$\beta_u = \begin{cases} \pi - \tan^{-1}\left(\dfrac{y-4}{x}\right) & x < 0 \\ \tan^{-1}\left(\dfrac{4-y}{x}\right) & x > 0 \end{cases} \tag{6.23}$$

For the lower panel, β was calculated by

$$\beta_l = \begin{cases} \tan^{-1}\left(\dfrac{-y}{x}\right) & x < 0 \\ \pi - \tan^{-1}\left(\dfrac{y}{x}\right) & x > 0 \end{cases} \tag{6.24}$$

For $x < 0$ and π-$\beta_u < \alpha$, the upper panel was fully shaded, receiving no direct or reflected solar beams. Likewise, when $x > 0$ and π-$\beta_l < \alpha$, the lower panel was fully shaded with no direct or reflected beams reaching it. Otherwise, both direct and reflected solar beams contributed to the total received irradiation.

For $x < 0$, $SF_u = SF_l = 1$ when π-$\beta_u > \alpha$. Otherwise, $SF_u = 0$, and SF_l was calculated by

$$SF_l = \frac{\overline{P_5P_3}}{\overline{P_2P_3}} \tag{6.25}$$

where P_5 is the point of intersection between the lower panel and the solar ray passing through P_1. For $x > 0$, $SF_u = SF_l = 1$ when π-$\beta_l > \alpha$. Otherwise, $SF_l = 0$, and SF_u was calculated by

$$SF_u = \frac{\overline{P_4P_2}}{\overline{P_1P_2}} \tag{6.26}$$

where P_4 is the point of intersection between the upper panel and the solar ray passing through P_2. Figure 6.9-d shows the four cases for calculating SF_u and SF_l.

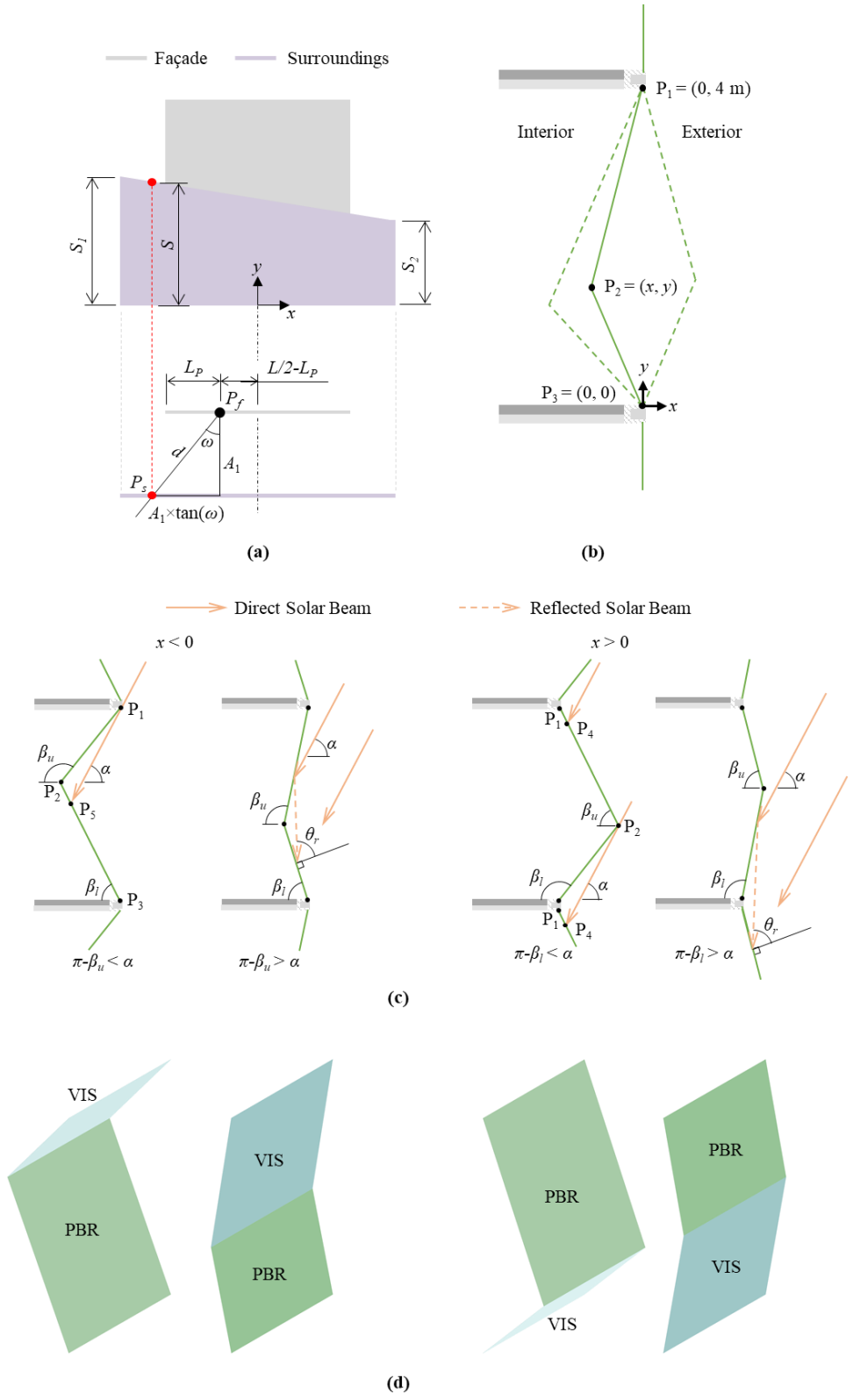


Figure 6.9. (a) Modeled parameters of surrounding elements. (b) Folded façades parameters. (c) Various cases for calculating the shading factor for upper and lower panels. (d) Possible combinations of PBRs and vision panels.

F_f was modeled by the continuous 2D polynomial function, Q. The function value, which represented the sunken/protruding distance from the façade base, was dependent on the variables H_v and L_v. As shown in Figure 6.8, H_v is the elevation of the examined point (P_f) above the ground while L_v is the offset of P_f from the façade west edge. Unlike F_d which had constant surface azimuth angles (ζ), both ζ and β were variables for free-form façades. These variables were estimated using the algorithm below

Algorithm: Free-form façades design angles

Input: Q (L_v, H_v), L_v, and H_v

Output: ζ and β

If $\partial Q/\partial L_v < 0$

  $\zeta = -\tan^{-1}(-\partial Q/\partial L_v)$

  else $\zeta = \tan^{-1}(\partial Q/\partial L_v)$

end

If $\partial Q/\partial H_v < 0$

  $\beta = \pi/2 - \tan^{-1}(-\partial Q/\partial H_v)$

  else $\beta = \pi/2 + \tan^{-1}(\partial Q/\partial H_v)$

end

The polynomial function in this study was represented by the 2D wave equation

$$Q = \delta \times \sin\left(\frac{L_v}{L} \times 3\pi\right) \times \sin\left(\frac{H_v}{H} \times 3\pi\right) \tag{6.27}$$

where Q is the sunken/protruding distance from the façade base. For a general façade form, the surface can be represented by a matrix in which every element expressed the sunken/protruding distance. These points were then fitted to a 2D surface equation. To capture most of the details in the façade, the *cftool* in MATLAB® was used to estimate the highest available fit with a 5th-order polynomial curve. The solar irradiation flux received at P_f was calculated by

$$I = I_b \times \cos\theta + \sum_{i=1}^{n} u_i \times I_b \times Ref \times \cos\theta_{r,i} \tag{6.28}$$

where u_i is a unity function that equals 1 when the i^{th} panel reflects solar irradiation toward the examined panel. If the reflected ray from the i^{th} panel isn't received by the examined panel, u_i

equals 0. θ_r is the solar incidence angle of the reflected solar beam as shown in Figure 6.9-c, rad. θ is the solar incidence angle calculated from [240]

$$\sin\theta = \sin\delta\sin\varphi\cos\beta + \sin\delta\cos\varphi\sin\beta\cos\zeta + \cos\delta\cos\varphi\cos\omega\cos\beta - \cos\delta\sin\varphi\cos\omega\sin\beta\cos\zeta - \cos\delta\sin\omega\sin\beta\sin\zeta \quad (6.29)$$

In contrast to folded façades, where the reflected beam originated only from adjacent panels, free-form façades may have multiple panels reflecting toward the examined panel. The second term in Equation 21 accounted for all potential reflections from the free-form façade panels. Figure 6.10 illustrates one possible scenario where a single panel can receive multiple reflections.

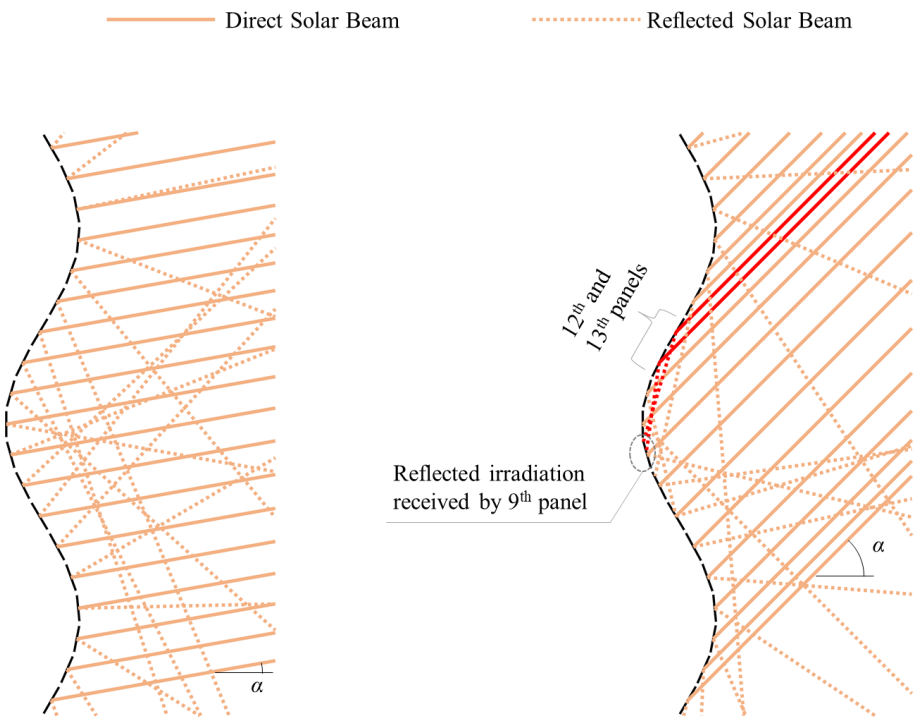


Figure 6.10. Solar beam reflections in free-form façades. Left, no reflections at lower solar elevation angles. Right, multiple reflections received by the same panel at higher solar elevation angles.

6.2.3.3 Optimization techniques

HJ algorithm was applied as a direct search method to optimize the design of F_d. This was achieved by finding the optimal x and y that maximized energy generation. The minimized objective function (F) was expressed as

$$F = -B = -\eta \times I/A \quad (6.30)$$

where B is the bioenergy generation to be maximized, W/m^2. I is the irradiation calculated from Eq. 5, W. A is the PBRs areas, m^2. The HJ algorithm was previously developed in Subsection 5.2.5.4.

In the case of free-form façades, the panels' distribution over the k^{th} floor was represented by

$$\boldsymbol{\rho}_k = [\rho_{k-1} \quad \rho_{k-2} \quad \rho_{k-3} \quad \rho_{k-4} \quad \cdots \quad \rho_{k-n}] \tag{6.31}$$

where n is the total number of panels per floor. PBR and VIS panels were represented by $\rho_{k-j} = 1$ and $\rho_{k-j} = 0$, respectively. An initial pool of p elements was first generated by the algorithm. Each element included a similar array to the one shown in Eq. 17. The bioenergy generation (B) per floor was calculated by averaging M_1 such that

$$M_1 = \boldsymbol{\rho}_k \times I_M \times \eta \tag{6.32}$$

where I_M is the array of solar irradiation calculated for each façade panel using Eq. 11. η is the conversion efficiency from solar irradiation to biological energy. The new pool was formed by $p/2$ pairs that were determined by selection and crossover. Each pair was selected at a time by comparing the function values of two random pairs. Crossover was then performed by recombining each selected pair (parents) to generate new offspring (children). Finally, the new pool was updated by adding an X% of new random points and the maximum point from the previous pool. The GA algorithm was applied for Nt iterations for each floor. Figure 6.11 shows the framework applied to optimize the integration of PBRs into free-form façades.

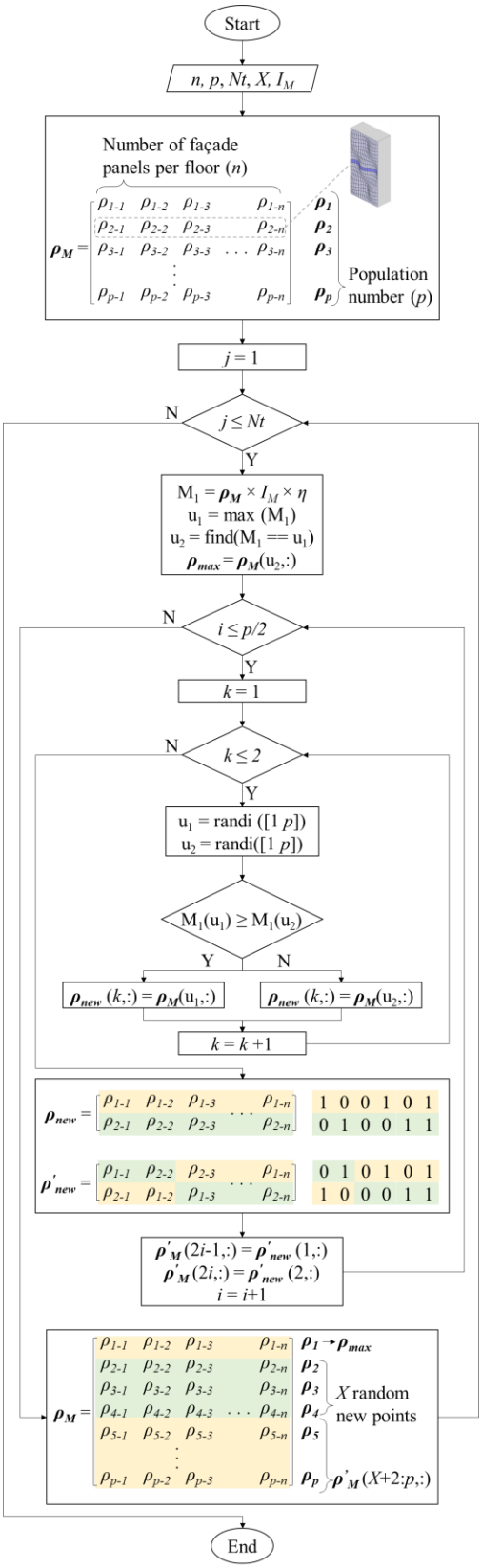


Figure 6.11. Schematic of the applied GA to optimize PBRs integration into free-form façades.

6.3 Results and Discussions

6.3.1 Variable flow rate

The present chapter examined the impact of different selection techniques on the evolution rate of the final function value (m_B). Figure 6.12 compares the performance of the applied techniques in relation to increasing m_B with iterations. New random points were added for Technique I at percentages of X=1%, 10%, 20%, and 40%. The solution had a decent evolution rate for percentages lower than 20%. Technique I with X=40% barely achieved any improvement in m_B with an average evolution rate of 0.08 mg/m^2·day per iteration. This rate increased to 0.32, 0.33, and 0.35 mg/m^2·day per iteration for 1%, 10%, and 20%, respectively. Technique II applied pairing and cross-over after the tournament scheme. The corresponding evolution rate for such a technique was 0.13 mg/m^2·day per iteration. The objective function value for Technique II was constant after the 41st iteration. Employing only pairing and cross-over was thus unrecommended as a selection method. For this purpose, Technique III combined the previous selection techniques by considering the tournament scheme, addition of new points, and evolution. This technique was the most efficient with an evolution rate of 1.2 mg/m^2·day per iteration. Technique III was thus applied and the optimized hourly residence times varied between 0.91 days and 1.97 days with an average value of 1.05 days.

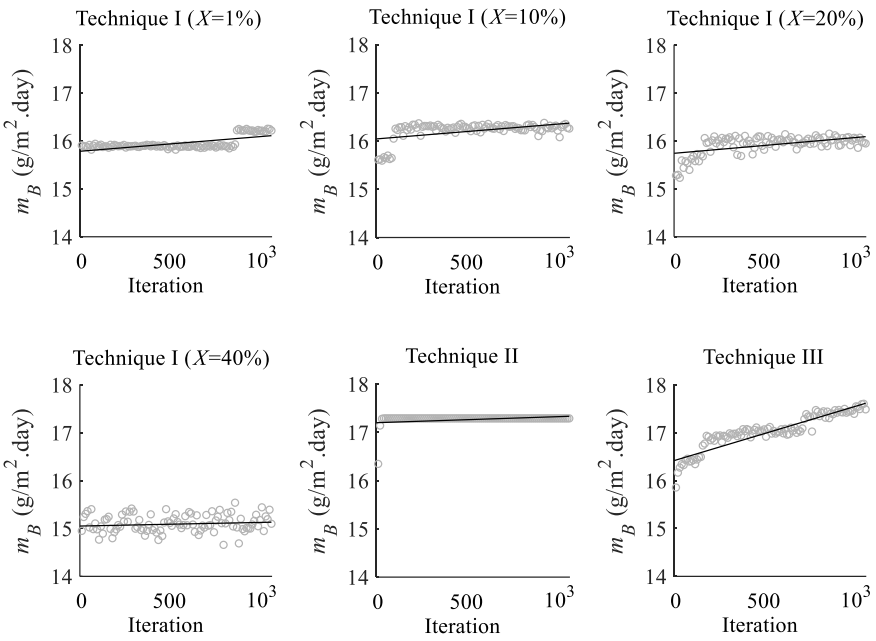


Figure 6.12. Performance of different selection techniques in terms of variation of the objective function value (mB) with iterations.

The chemical model was applied with the fixed residence times of 1.2 days [22], 1.3 days [1], 1.4 days [227], and 2 days [226]. Figure 6.13 shows the microalgae harvest and the associated CO_2 absorption for such fixed values. The average daily biomass generation and CO_2 extraction were 13.9 g/m^2 and 31.4 g/m^2, respectively. Varying the residence time on an hourly basis increased both biomass generation by 28.8% (from 13.9 g/m^2 to 17.9 g/m^2) and CO_2 extraction by 10.8% (from 31.4 g/m^2 to 34.8 g/m^2). The impact of the optimized PBRs on reducing the operational carbon footprint is also shown in Figure 6.13. In low-rise buildings (n_f=2), the annual carbon footprint reduction was only 0.01 tonCO_2/m^2. This value increased to 0.05 tonCO_2/m^2 and 0.14 tonCO_2/m^2 for mid-rise (n_f=9) and high-rise (n_f=25) buildings.

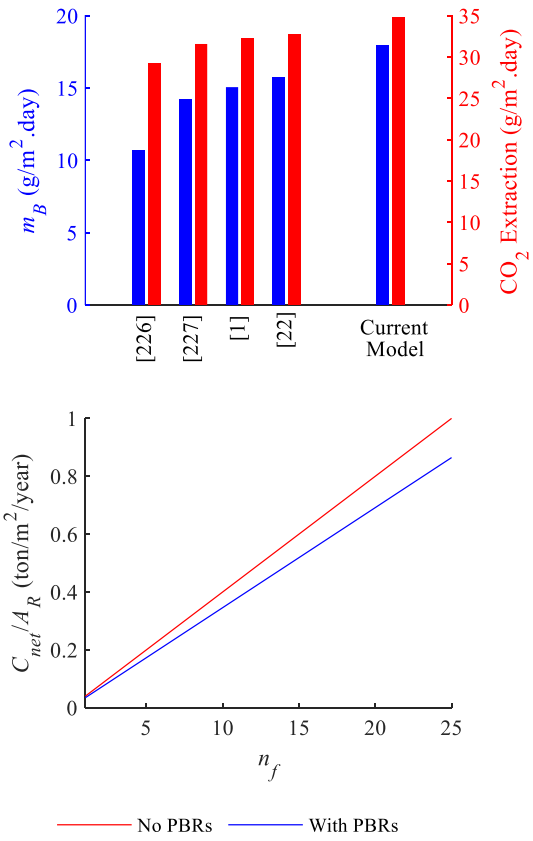


Figure 6.13. Top, m_B and CO_2 extraction for both fixed and variable τ_d. Bottom, impact of the developed system on the operational carbon footprint.

6.3.2 Façades solar availability

Different forms of surrounding environment were examined to estimate their impact on the annual average solar irradiation received by façades (I_{avg}). All variables were normalized with respect to the building width (L) to generalize the results. Normalized variables were the street width, A_1/L, surrounding width, A_2/L, surrounding tilt, S_2/L, and building height, H/L. Figure 6.14 shows the variation of irradiation with both surrounding tilt and building height for street and surrounding widths of 0.7. Minimum irradiation over the whole façade was 70.6 W/m^2 when surrounding tilt and building height were 1.0, and 0.5, respectively. Irradiation increased to 119.2 W/m^2 by decreasing surrounding tilt to 0. This additional 48.6 W/m^2 was equivalent to a percentage increase of 68.8%. Increasing building height from 0.5 to 2.0 at a surrounding tilt of 1.0 also increased irradiation by 76.3%, from 70.6 W/m^2 to 124.5 W/m^2. This highlighted the higher impact of building height compared to surrounding tilt. Such an increase in beam irradiation, 51.3 W/m^2 on average, elevated the potential of façades for PBRs integration. This included generating an additional 10.8 W/m^2 of electricity or 4.6 W/m^2 of bioenergy as depicted by [167], and [15], respectively. It was obvious from Figure 6.14 that the west façade had lower solar access compared to the east façade. This is attributed to the tilt direction that was due east as shown in Figure 6.8. For building heights greater than 2.0, the façade higher portion wasn't affected by the surroundings.

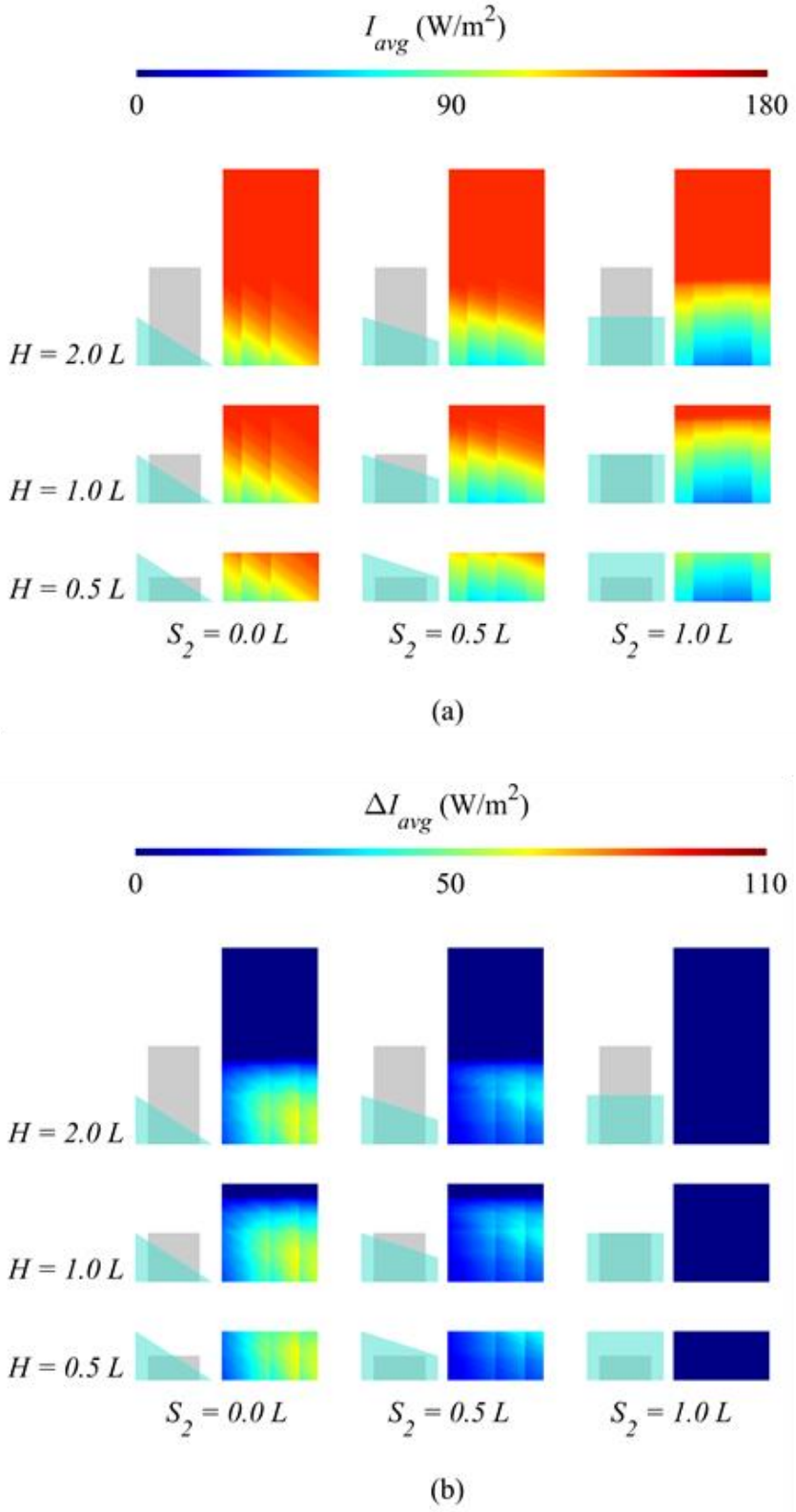


Figure 6.14. Variation of solar irradiation with surrounding tilt, S_2/L, and building height, H/L. (a) Absolute values of solar irradiation, I_{avg}. (b) Difference between tilted and flat surroundings, ΔI_{avg}.

Free-form façades were defined by the normalized sunken or protruding distance from the façade base, δ/L. The top 3 contour plots in Figure 6.15 show the impact of δ/L on the surface azimuth angle (ζ), tilt angle (β), and irradiation (I_{avg}). Irradiation difference (ΔI_{avg}) represented the local change in irradiation for free-form façades compared to baseline façades. Surfaces with $\delta/L = 0.0$, formed by baseline façades, received the maximum solar irradiation. As δ/L increased to 0.07, façade irradiation difference ($\overline{\Delta I_{avg}}$) decreased from 0 to -8.72 W/m^2. However, free-form façades had some spots on the façade where the local irradiation was higher compared to the same spots on baseline façades. This can be interpreted by the wide range of solar angles due to the curved geometry of free-form façades. The associated surface azimuth and tilt angles varied in the ranges -35° to 35° and 50° to 130° over the examined span of δ/L. These ranges were comparable to the ranges -45° to 45° and 40° to 140° concluded by [29]. The 10° deviation could be justified by the extreme case that was considered by the previous study. The same deviation could also be reduced by extending δ/L over 0.07. In terms of site impact, façade irradiation difference varied with both street and surrounding widths. Such variation was more noticeable at greater values of δ/L. For $\delta/L = 0.07$, façade irradiation difference decreased with street width at an average rate of 10.6 W/m^2. Stretching the surrounding width from 0.5 to 0.9 increased façade irradiation difference at an average rate of 4.8 W/m^2.

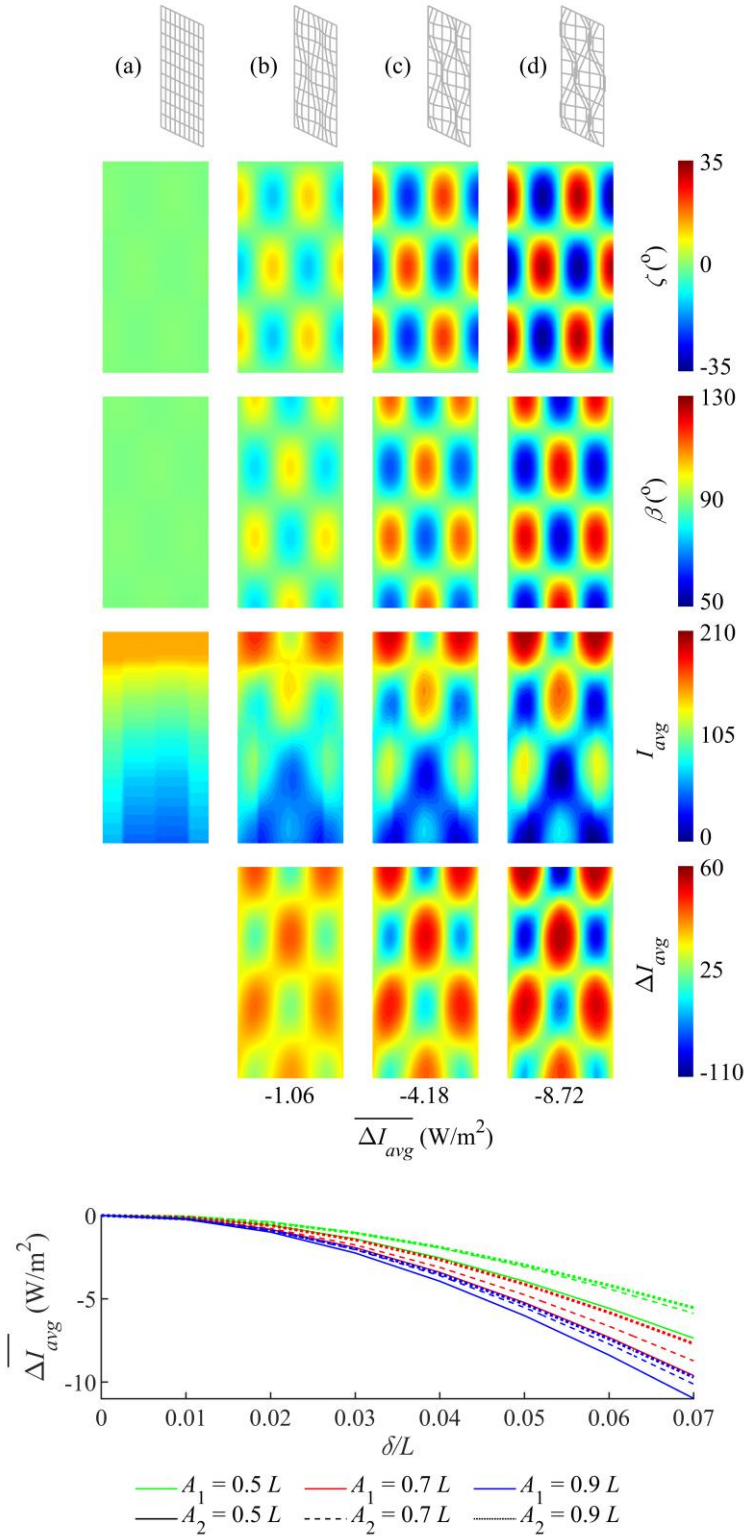


Figure 6.15. Top, impact of δ/L on surface azimuth angle (ζ), tilt angle (β), irradiation (I_{avg}), and irradiation difference (ΔI_{avg}) for free-form façades. a) δ = 0.00 L, b) δ = 0.02 L, c) δ = 0.05 L, and d) δ = 0.07 L. Bottom, variation of façade irradiation difference ($\overline{\Delta I_{avg}}$) for different street and surroundings width.

6.3.3 Chemical model equivalent efficiency

The model was then applied on an hourly basis throughout the year to calculate the cumulative bioenergy generation. The results were compared to utilizing a conversion efficiency of 9% as applied by [14,15]. For this conversion efficiency, the cumulative bioenergy harvest was 54.6 kWh/m^2. This was 63.6% higher than the cumulative bioenergy harvest estimated by the chemical kinetics model, 33.3 kWh/m^2. The same harvest of 33.3 kWh/m^2 was then achieved by reducing the conversion efficiency to 5.5%. This resulted in a Root Mean Square Error of 1.04 kWh/m^2 for the monthly cumulative bioenergy yield. Such an error was 12.3 kWh/m^2 when employing a conversion efficiency of 9%. Hence, to align with the chemical kinetics model, a conversion efficiency of 5.5% was adopted in the study to ensure a more accurate analysis.

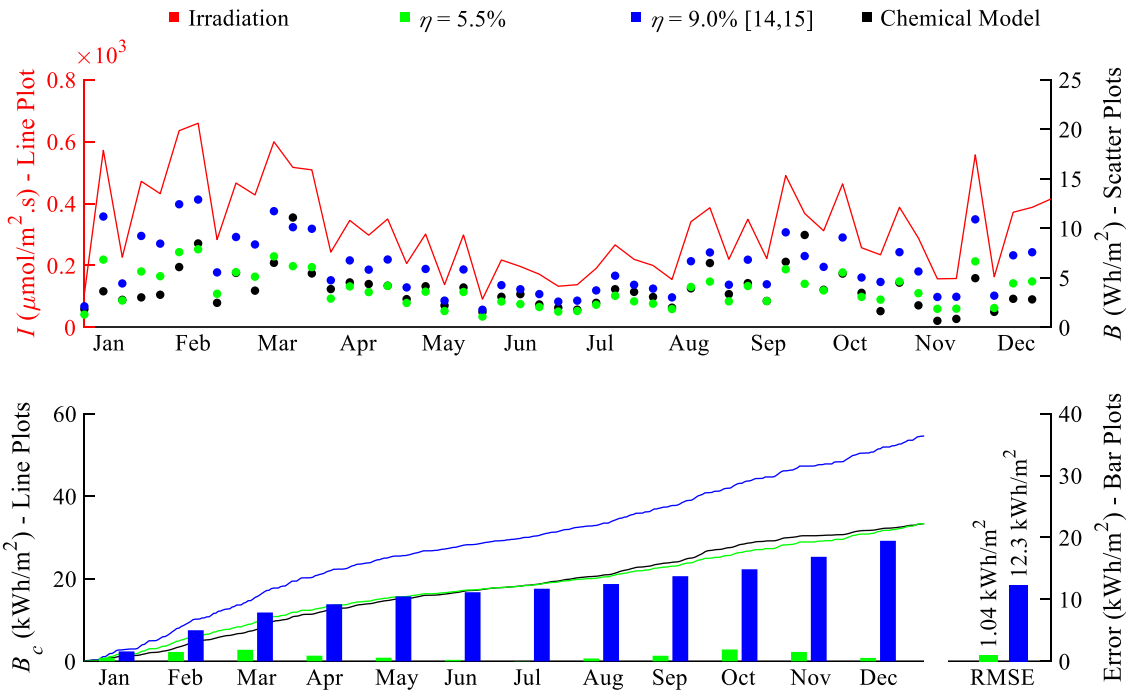


Figure 6.16. Top, verification of the developed model against literature. Middle, weekly average irradiation (I) and bioenergy Generation (B). Bottom, cumulative bioenergy generation (B_c) and the corresponding Error.

6.3.4 Bioenergy façades performance

The HJ algorithm was employed to optimize the folded façades. Numerical values of the optimal solutions (x_{opt}, y_{opt}) are presented in Table 6.1. PBRs tilt angle (β) increased at higher latitudes (φ)

to compensate for lower solar elevation angles. Optimal façades were thus flatter at higher latitudes to increase the tilt angle of PBRs. As the latitude angle increased from 35° to 55°, the optimal tilt angle increased from 26.4° to 79.1°. This range included the optimal tilt of 47.4° concluded by [14] for a latitude angle of 43.5°. Optimized façades at higher latitudes generated higher bioenergy by 66.3%, 4.49 W/m^2 compared to 2.70 W/m^2. This was justified by the excessive shading imposed on the PBRs at a latitude angle of 35° due to the higher solar elevation angle. Varying the façade orientation caused a reduction in solar harvest and associated energy generation. This was interpreted by the incidence factor impact represented by cos θ shown in Equation 14. Maximum bioenergy generation corresponded to façades with surface azimuth angles (ζ) of ±61◦ and ±48◦ for latitudes of 25◦ and 35◦, respectively. Otherwise, the optimal façade orientation was due south for locations with latitudes greater than 35◦ (see Figure 6.17). That was mainly because locations near the equator were subjected to higher solar irradiation from the east and west directions compared to the south direction. Associated bioenergy harvest ranged from 2.32 W/m^2, for façades with a surface azimuth angle of ±61◦ and latitude of 25◦, to 5.94 W/m^2, for façades with surface azimuth angle of 0◦ and latitudes of 65◦. This was again interpreted by the considerable shading at lower latitudes and higher solar elevation angles. Free-form façades had a narrower range of maximum bioenergy generation from 1.87 W/m^2 to 2.5 W/m^2 as the latitude angle increased from 25° to 65° for south-facing façades. This was attributed to their reduced curvature compared to folded façades.

Table 6.1. Optimal solution with associated tilt angles.

Latitude angle, φ (°)	Optimum design, (x_{opt}, y_{opt})		Maximum bioenergy, B_{max} (W/m^2)	Optimal tilt angle, $\beta_{opt,\,1}$ (°)
35	(-2.40, 1.19)	(2.40, 2.81)	2.70	26.4
45	(-1.63, 1.44)	(1.63, 2.56)	3.46	41.5
55	(-0.62, 3.22)	(0.62, 0.78)	4.49	79.1

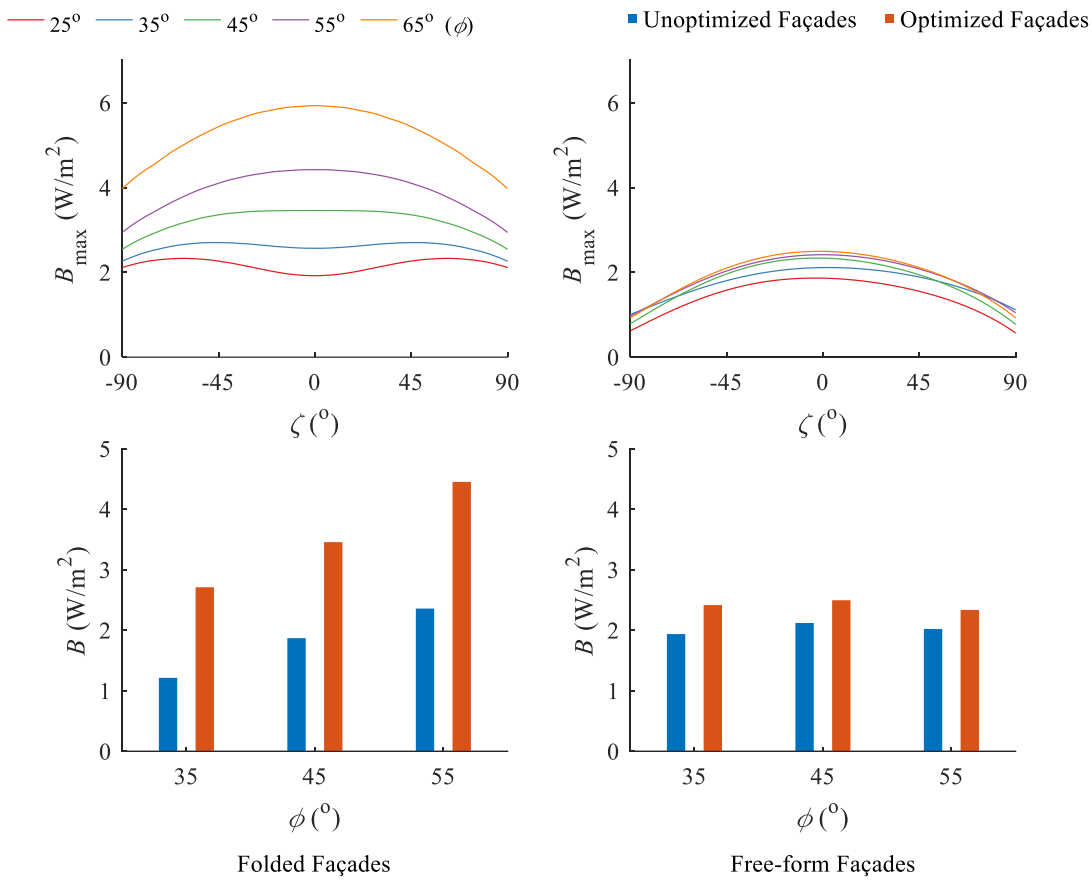


Figure 6.17. Top, variation of maximum bioenergy generation (B_{max}) with different locations (latitude angles, φ) and façade orientations (surface azimuth angles, ζ). Bottom, comparison between optimized and unoptimized façades.

6.3.5 Optimization methods performance

The HJ algorithm was initiated with six different points for three different locations. Initial points and solution paths are shown in Figure 6.18. Two optimum points achieving the same maximum bioenergy generation were concluded for latitude angles (φ) of 35°, 45°, and 55°. However, the algorithm occasionally produced inaccurate points, which were classified as misleading outcomes due to their lower bioenergy generation. This necessitated trying various initial points while applying the HJ algorithm to avoid imprecise solutions. The obtained results were further verified by applying the graphical optimization shown in Figure 6.18. At a latitude angle of 45°, flat façades (represented by $x = 0$) generated 2.7 W/m^2 of bioenergy while optimized folded façades generated 3.5 W/m^2, 29.6% higher.

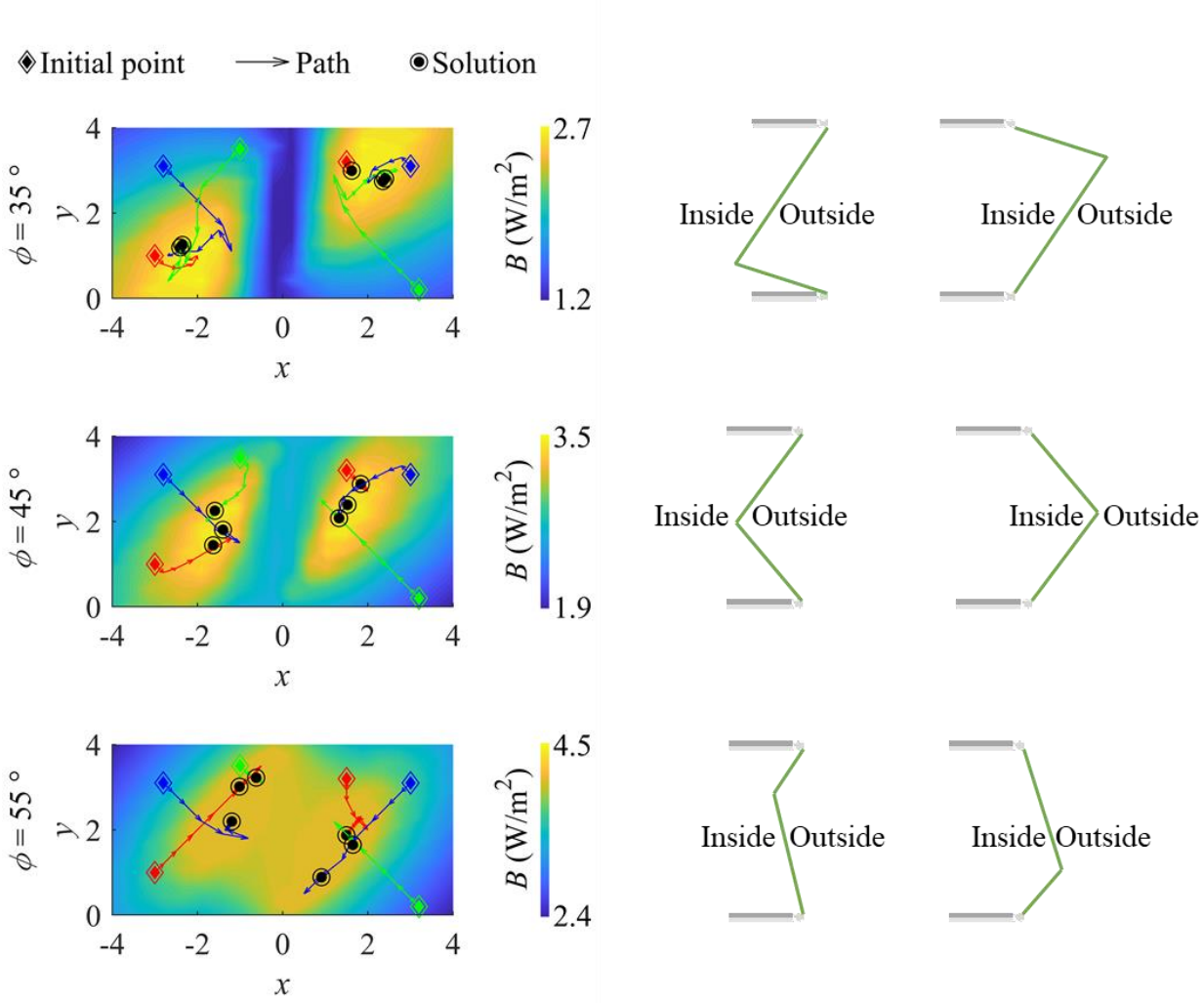


Figure 6.18. Folded façades optimum points, solution paths, and section views.

GA was applied to optimize the inclusion of PBRs into free-form façades. The population sizes (*p*) varied from 10 to 50 points. PBRs were distributed to maintain the average window-wall ratio of 0.5 for each floor. Figure 6.19 shows the bioenergy generation evolution for different population sizes along with the associated distribution of PBRs over the free-form façades. The transformation of the optimized façade is presented with different iterations. PBRs were placed in locations with lower tilt angle (<90°). The remaining locations with higher tilt angles (>90°) were more convenient to host vision glass panels. This tilt decreased the solar gain in summer and increased it in winter for occupied spaces. Such a passive design can improve building energy consumption by up to 45% [237]. The algorithm was almost stable with no significant improvements after the 500^{th} iteration for population sizes greater than 20. For population sizes of 10, the algorithm required around 1000 iterations to achieve comparable stability. GA increased bioenergy generation by 14.3%, from 2.1 W/m^2 to 2.4 W/m^2. This was achieved by locating the PBRs on the façade panels with higher solar harvest while leaving the remaining spots for vision glass panels. All GA populations showed a tolerance of 0.3%, between 2.36 W/m^2 and 2.37 W/m^2, after 3000 iterations. Façades oriented due south generated the highest energy harvest of 2.4 W/m^2. This value decreased by 20%, from 2.4 W/m^2 to 2.0 W/m^2, for southwest and southeast oriented façades. The minimum bioenergy generation was 0.8 W/m^2 for façades oriented due west or east.

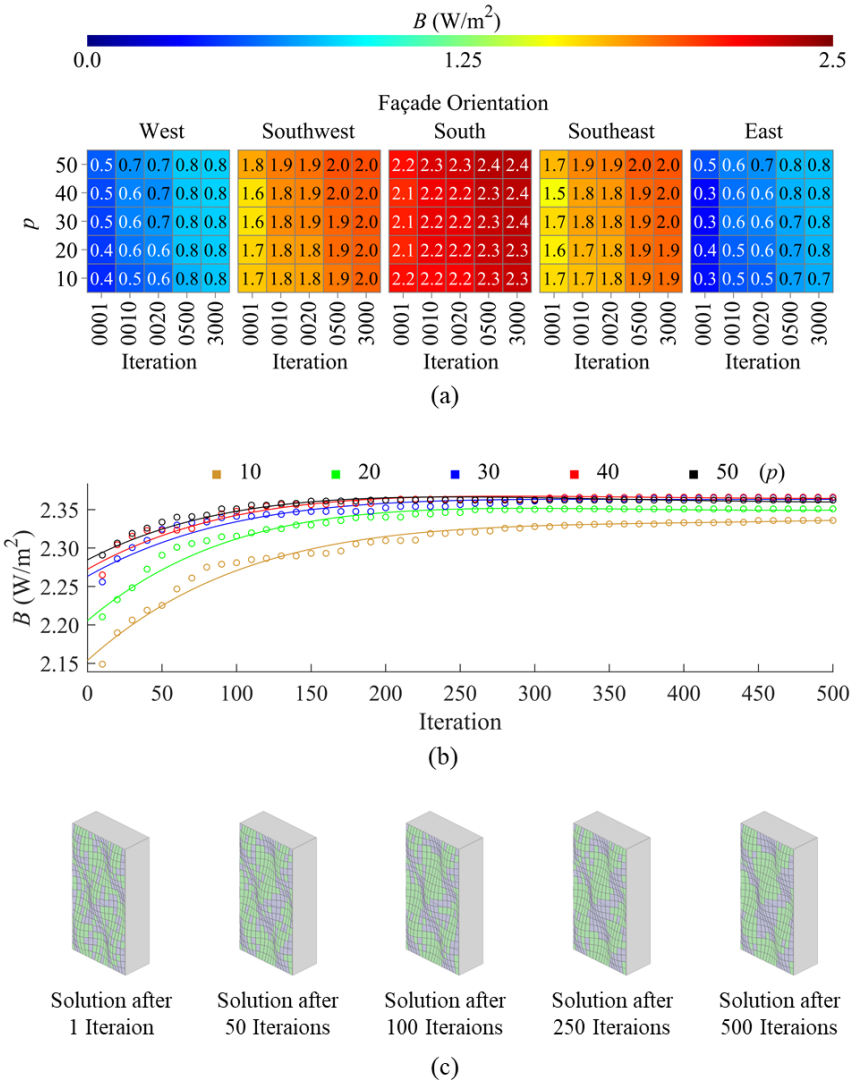


Figure 6.19. (a) Performance of GA for different façade orientations. (b) Bioenergy generation (*B*) evolution with iterations for south-oriented façades. (c) Façade transformation at different iterations.

The performance evaluation of Hooke-Jeeves (HJ) and Genetic Algorithms (GA) was conducted based on three key criteria: accuracy, stability, and computational efficiency. Accuracy was monitored by assessing each algorithm's ability to converge to the maximum solution. Stability was evaluated using a stability index, which measured the deviation of the algorithm's function values from a polynomial fit passing through the same data points. Computational efficiency was determined by the number of function evaluations required to reach the maximum function value. Figure 6.20 illustrates a comparative analysis of the performance of HJ and GA in optimizing both folded and free-form façades. For folded façades, the HJ algorithm demonstrated remarkable computational efficiency, achieving the optimal bioenergy generation with only 88 function evaluations. In contrast, GA required significantly more evaluations, nearly five times as many with function evaluations of 420. This level of efficiency for the HJ was further notable when compared to alternative gradient-free methods like Powell's Conjugate Direction method, which required 168 evaluations to reach an optimal solution in a similar design optimization study [12]. Both algorithms exhibited satisfactory accuracy as they converged to the same optimal solution for the folded façades. HJ and GA also displayed adequate stability, with stability index values remaining below 2% for both. However, HJ exhibited some limitations for free-form façades. It reported an optimal value approximately 40% lower than that achieved by GA. HJ also demonstrated high instability with a stability index exceeding 27%, whereas GA maintained a lower stability index below 0.3% during the final iterations. This performance comparison supported the initial hypothesis outlined in this study by utilizing the HJ algorithm for folded façades optimization and applying GA for free-form façades optimization.

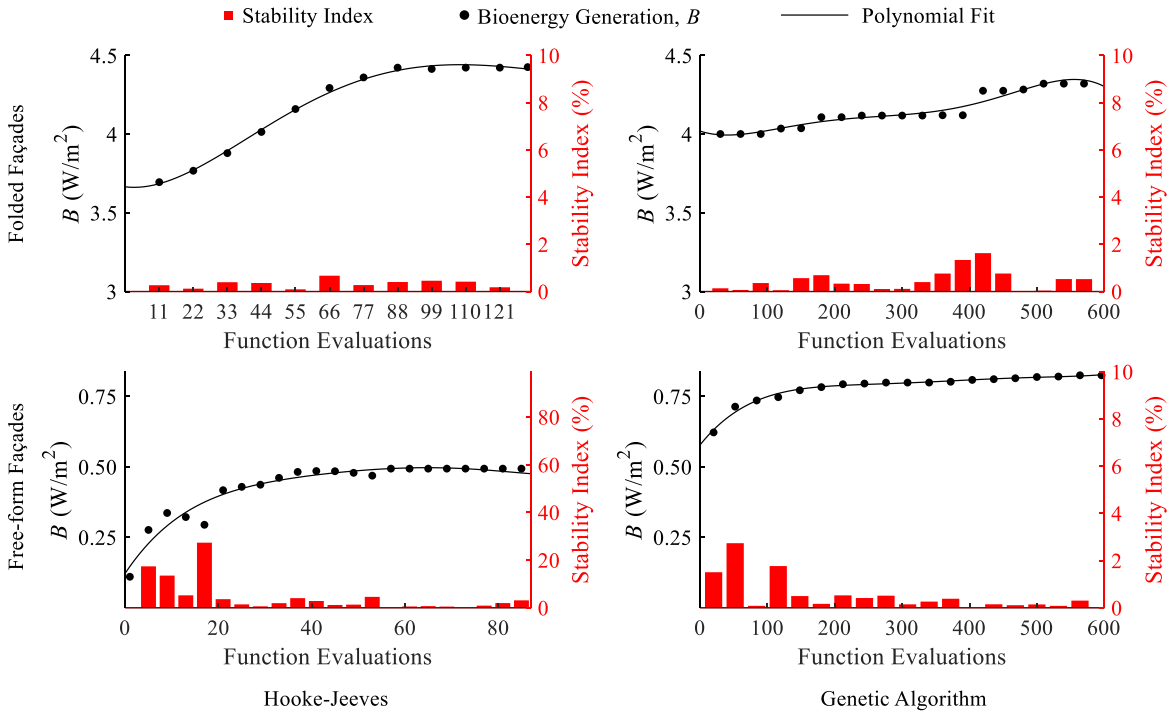


Figure 6.20. Performance comparison between HJ and GA for optimizing folded façades at a latitude of 55°, and free-form façades oriented east/west.

6.4 Summary of Chapter

In this chapter, a novel operational strategy for PBRs by varying the microalgae residence time on an hourly basis. The model employed the fixed residence times of 1.2, 1.3, 1.4, and 2 days as recommended by [1,22,226,227]. Hourly residence times were optimized by employing GA with three different selection techniques. PBRs were then integrated into various façade geometries, including folded and free-form façades. Both façade geometries were expressed by the coordinates (x, y) and polynomial equations, respectively. HJ algorithm was applied to optimize folded façades due to the limited number of decision variables. For free-form façades, GA were applied to find the optimal distribution of PBRs. The algorithm showed high potential in optimizing objective functions with a large number of variables. Findings related to hourly residence times highlight:

- **GA Techniques Evolution:** Technique III was the most efficient with an evolution rate of 1.2 mg/m^2·day per iteration. This technique applied the tournament scheme, addition of new points, and evolution. Other techniques were achieving either insignificant or no improvements.
- **Residence Optimization:** Optimized hourly residence times varied between 0.91 days and 1.97 days to increase both biomass generation and CO_2 extraction by 28.8% and 10.8%,

respectively. On average, the associated biomass production and CO_2 absorption were 13.9 g/m^2 and 31.4 g/m^2, respectively.

Findings related to façade geometry optimization highlight:

- **Population Size:** Solution convergence of the developed GA was adequately fast for population sizes greater than 10 points.
- **Solution Stability:** GA showed a fluctuation of 0.3% even after 3000 iterations for all population sizes.
- **HJ Performance:** HJ algorithm concluded an optimal value approximately 40% lower than GA when applied to free-form façades. The HJ algorithm occasionally concluded inaccurate points that were classified as misleading outcomes by comparing them to graphical optimization. This necessitated trying various initial points while applying the HJ algorithm to avoid imprecise solutions.
- **Free-Form Façades Optimization:** Free-form façades received lower solar irradiation by 8.72 W/m^2 on average, compared to flat façades. However, free-form façades had specific points with higher local irradiation of up to 210 W/m^2 compared to 180 W/m^2. Optimal placement of PBRs on free-form façade points with lower tilt angles increased bioenergy generation by 14.3%. This also allocated points with higher tilt angles for vision glass panels to reduce summer heat gain and enhance the energy demand by up to 45%.
- **Folded Façades Optimization:** For locations with a latitude angle of 45°, optimized folded façades generated higher bioenergy by 29.6%, compared to flat façades. Folded façades had two optimum designs that achieved the same maximum bioenergy generation for each latitude angle. The façade geometry for folded façades was flatter at higher latitude locations to compensate for the lower solar elevation.

These findings indicate higher efficiency for PBRs with variable residence time in relation to enhancing biomass generation and CO_2 extraction rates. Façade geometry optimization demonstrates the GA's effectiveness in achieving stable solutions, while the HJ algorithm has shown higher computational efficiency for optimizing free-form façades despite occasional inaccuracies. Future research should consider optimizing air pump control for efficient microalgae mixing and conducting a detailed cost analysis of building integrated PBR systems. It’s also

recommended to develop continuous microalgae harvesting mechanisms to enhance productivity and reduce operational downtime in cultivation setups.

Chapter 7: Conclusions

This chapter summarizes the key contributions and conclusions of the thesis and suggests potential directions for future research.

7.1 Summary

As the demand for sustainable energy in buildings rises, incorporating microalgae PBRs into façades offers great promise but also significant challenges. Among these, DSFs stand out as a potential solution for colder climates, tackling issues like low temperatures and snow buildup. However, the emergence of building integrated PBRs underscores the necessity for advancements in optimizing façade geometry, considering chemical kinetics, developing non-invasive microalgae monitoring techniques, reducing heat accumulation in hot weather, and reinforcing thermal insulation during cold spells.

This thesis aimed to address important gaps in the study of renewable façade systems, with a particular focus on DSFs integrating PBRs. Chapters 1 and 2 reviewed existing literature by highlighting gaps in research on the optimal design of DSFs with PVs/PBRs in cold climates. No studies were found on using constrained local optimization for building-integrated PBRs to maximize heat and biomass while accounting for space heat gain. The impact of façade geometry on the PBRs performance is still unknown. Additionally, limiting the residence time to a constant value over long periods can reduce the overall system productivity. In response, this thesis aimed to bridge these gaps and propose solutions through the comprehensive design and optimization of DSFs integrating PBRs.

Chapter 3 accomplished the thesis first objective by investigating a novel DSF system integrating PBRs to mitigate low temperatures and snow accumulation for façade-based energy generation. Through hourly heat transfer analysis, the chapter compared the energy production, panels efficiency, and heat gain of PV and PBR modules within the DSF cavity and occupied spaces. Shading analysis determined solar irradiation exposure on the modules. A numerical model was developed to assess airflow effects on panel temperature and performance under various

ventilation schemes. The chapter highlighted the necessity of a mixed ventilation approach with adjustable external vents, adjusted according to ambient temperature and cavity occupancy, particularly in wide cavities. In narrow cavities, where inhabitation is constrained, vents should remain fully open when ambient temperature is lower than that of the panels.

Chapter 4 achieved the second objective of the thesis by applying the developed model to two façade systems: 1) A cellular DSF with PBRs integrated at the floor plenum, and 2) A multistory DSF with PBRs alternating with the inner glass layer of the façade. Graphical optimization identified the optimal design parameters for these systems, followed by formulating a multi-objective problem to minimize heating and cooling loads while maximizing bioenergy generation from the PBRs. This was approached using both a pattern search algorithm and a controlled elitist GA. The chapter highlighted the significance of coupling shading and thermal models to ensure overall efficient performance, as higher solar exposure didn't always mean higher energy generation. The chapter also highlighted that even suboptimal DSFs designs proved to be energy-efficient, achieving significant energy savings in cold regions and maintaining a slight advantage over SSFs in hot climates.

Chapter 5 achieved the third objective of the thesis by developing a detailed chemical kinetics model for building-integrated PBRs. This model accounted for light attenuation, oxygen production, and day-night cycles affecting microalgae growth. Two innovative methods for predicting biomass were introduced: one utilizing RGB image processing and the other employing neural networks (FNNs and CNNs). An experimental setup was constructed to monitor microalgae growth through RGB imaging. The accuracy of the developed chemical model was confirmed using collected experimental data. Various optimization techniques were assessed for both accuracy and computational efficiency. The computational time of exhaustive methods was compared with those incorporating neural networks. The chapter emphasized the significance of non-invasive microalgae monitoring techniques like ML and RGB image-based monitoring. It also underscored the potential of neural networks in reducing the computational burden of exhaustive optimization problems.

Chapter 6 achieved the third objective of the thesis by applying the detailed chemical kinetics model for assessing a novel PBR with a variable flow rate of fresh medium. It assessed the system's performance in reducing carbon footprints for buildings of varying heights and optimized PBR integration into different façade designs. Solar energy conversion to bioenergy was estimated using the chemical kinetics model. TgMs were developed and refined to analyze the shading effects caused by surrounding buildings. Solar angle variations were assessed to determine their impact on irradiation and bioenergy yield. Various building orientations were explored to identify optimal façade azimuth angles, employing the HJ algorithm for folded façades and the GA for free-form designs due to their respective advantages. The chapter highlighted the impact of optimized hourly residence time on increasing both biomass generation and CO_2. Additionally, it demonstrated a notable increase in bioenergy generation when PBRs were incorporated into free-form or folded façades, compared to flat façades explored in prior literature.

Overall, this thesis has filled significant research gaps and offered valuable insights and methodologies for designing and optimizing building integrated PBRs. These contributions offer advancements in thermal and bioenergy generation, benefiting engineers and researchers enhancing PBRs efficiency in building façades.

7.2 Conclusions on Heat Transfer Modeling for DSF Systems Integrating PBR Panels

- DSF systems with internal and mixed ventilation provide superior heat insulation, particularly in cold climates. Internally ventilated wide cavities maintained warmer temperatures, while mixed ventilation improved insulation by directing warm air over the inner glass layer. This suggests optimized ventilation strategies for thermal comfort and energy efficiency.
- PBRs outperform PVs in terms of space heating efficiency, delivering 8.1% more energy (91.7 W/m² compared to 84.8 W/m²). PBRs maintained efficiency even under high temperatures due to the cooling effect of fluid circulation, whereas PVs experienced efficiency drops and increased temperatures due to shading and electrical load issues.
- The integration of PVs/PBRs in DSF systems significantly reduced heat loss in winter, achieving an annual average gain of 35.7 W/m² against a loss of 82.1 W/m² from conventional façades. The chapter also highlighted seasonal insulation benefits, with mixed

ventilated cavities providing optimal thermal shields in winter and effective cooling in summer, emphasizing the need for adaptable ventilation strategies year-round.

7.3 Conclusions on Optimization to Maximize Thermal and Bioenergy Generation

- PBRs in the cellular design had no shade all time when the tilt angle was 90º and the cavity width was below 1.1 m. In the multistory design, 1.5 m wide PBRs tilted at 75º offered the highest possible solar exposure percent where the shaded area percent was always below 26.2, and 23.4% in summer, and winter, respectively.
- Optimum parameters (cavity width, plates' width, tilt angle) were chosen based on overall performance, not just solar exposure, by integrating shading and thermal models. For example, vertical plates in 0.6 m wide cavities minimized shading, but 45° tilted plates in 1.2 m wide cavities produced the highest thermal and biological energy (119.4 and 11.8 W/m², respectively).
- On average, the cellular design generated 31.9 W/m^2 thermal energy and 3.9 W/m^2 biological energy. However, the multistory design thermal and biological energy generation was higher by 20.4% (38.4 W/m^2) and 79.5% (7.0 W/m^2), respectively.
- DSFs demonstrated energy savings in both hot and cold climates compared to SSFs. Optimal DSF designs yielded energy savings of 10.1 W/m² in hot regions and 40.2 W/m² in cold regions. Even suboptimal DSFs maintained energy efficiency, achieving 31.1 W/m² savings in cold regions and 1.1 W/m² in hot climates, highlighting DSFs' ability to block solar irradiation and act as thermal buffers.

7.4 Conclusions on Chemical Kinetics and Experimental Analysis for PBRs in DSFs

- In relation to ML Image-Based Techniques, the Adam algorithm with SGDF = 0.9 achieved the highest R values of 0.98 among all CNN algorithms. However, it did not reach the perfect linear relationship (R = 1) achieved by FNNs.
- The optimal microalgae residence time (τ_d), PBR's thickness (δ), DSF cavity width (W_c), and PBR's tilt angle (β) were [1.043 days; 0.199 m; 1.24 m; 48.6°] that achieved an aerial biomass generation of 2.3 kg/m^2. δ approached both lower (1 cm) and upper (20 cm) constraints for volumetric and aerial production objectives. However, smaller δ indicated a more efficient design by reducing structural and environmental impacts caused by heavier

and thicker PBRs. The proposed system was optimized in different provinces across Canada. The maximum biomass generation was 3.0 kg/m^2 for both Calgary and Vancouver.

- The HJ algorithm outperformed the PCD method in computational time, reaching optimal solutions in 65.6% fewer function evaluations. However, the PCD method's line searches enhanced result accuracy compared to the fixed step size of the HJ algorithm. NN-Aided algorithms significantly reduced computational time compared to their original counterparts. Neural Network-Aided GA achieved system optimization in just 6.0 minutes, a substantial improvement over the original's 24.4 hours. Similarly, Neural Network-Aided Particle Swarm Optimization and Simulated Annealing took 5.9 and 7.6 minutes respectively, compared to 7.4 and 19.9 hours for the originals. This highlights the efficiency gains and optimization setup improvements achievable through Neural Network integration in simulation software.

7.5 Conclusions on Variable Flow of Fresh Medium and Façade Geometry Impact

- The optimized hourly residence times ranged from 0.91 to 1.97 days, resulting in a 28.8% increase in biomass generation and a 10.8% increase in CO_2 extraction. On average, this led to 13.9 g/m^2 of biomass production and 31.4 g/m^2 of CO2 absorption. Genetec Algorithms using Technique III demonstrated the highest efficiency by evolving at a rate of 1.2 mg/m^2·day per iteration. Such a technique utilized the tournament scheme, addition of new points, and evolution.
- Free-form façades, on average, received 8.72 W/m^2 less solar irradiation compared to flat façades. However, specific points on free-form façades received higher local irradiation, reaching up to 210 W/m^2 compared to 180 W/m^2. Strategic placement of PBRs on points with lower tilt angles on free-form façades increased bioenergy generation by 14.3%. Points with higher tilt angles were allocated for vision glass panels to mitigate summer heat gain, potentially reducing energy demand by up to 45%.
- For locations with a latitude angle of 45°, optimized folded façades generated higher bioenergy by 29.6%, compared to flat façades. Folded façades had two optimum designs that achieved the same maximum bioenergy generation for each latitude angle. The façade geometry for folded façades was flatter at higher latitude locations to compensate for the lower solar elevation.

7.6 Contributions

The research undertaken in this thesis offers comprehensive understanding of the integration of microalgae PBRs into building façades, particularly focusing on DSFs. Through detailed analysis and experimentation, the thesis fills critical gaps in research, providing methodologies for designing and optimizing building integrated PBRs. Main contributions of the thesis can be summarized as follows:

- **Building Thermal Energy Preservation:** PVs/PBRs managed to preserve the occupied space thermal energy. Heat loss from common façades in winter had an annual average of 82.1 W/m^2. This was countered by 35.7 W/m^2 heat gain with the proposed DSF.
- **PVs/PBRs Performance Comparison:** PBRs outweighed PVs by 8.1% for space heating purposes (91.7 W/m^2 compared to 84.8 W/m^2).
- **DSFs Performance Comparison:** Cellular design generated 31.9 W/m^2 thermal energy and 3.9 W/m^2 biological energy. However, the multistory design thermal and biological energy generation was higher by 20.4% (38.4 W/m^2) and 79.5% (7.0 W/m^2), respectively.
- **Climate Adaptation:** Optimal DSFs in hot and cold regions yielded energy savings of 10.1 W/m² and 40.2 W/m², respectively, compared to SSFs. Surprisingly, even suboptimal DSFs designs proved to be energy-efficient, achieving energy savings of 31.1 W/m² in cold regions and maintaining a slight advantage over SSFs in hot climates with energy savings of 1.1 W/m².
- **ML Image-Based Techniques:** The Adam algorithm with SGDF = 0.9 achieved the highest R values of 0.98 among all CNN algorithms. However, it did not reach the perfect linear relationship (R = 1) achieved by FNNs.
- **NN – Aided algorithms:** NN – Aided algorithms achieved a substantial reduction in computational time, compared to the original algorithms. For instance, Neural Network – Aided GA accomplished system optimization in just 6.0 minutes, a significant improvement over the 24.4 hours required by the original algorithm. Efficiency improved with Neural Network – Aided Particle Swarm Optimization, which took 5.9 minutes compared to 7.4 hours for the original method. Similarly, Neural Network – Aided Simulated Annealing took 7.6 minutes compared to the original's 19.9 hours.

- **Optimal PBR Variables:** The objective function considered the decision variables to be the microalgae residence time (τ_d), PBR's thickness (δ), DSF cavity width (W_c), and PBR's tilt angle (β). The optimal decision variables $[\tau_d; \delta; W_c; \beta]_{opt}$ were [1.043 days; 0.199 m; 1.24 m; 48.6°] that achieved an aerial biomass generation of 2.3 kg/m^2.
- **Location Impact:** The proposed system was optimized in different provinces across Canada. The maximum biomass generation was 3.0 kg/m^2 for both Calgary and Vancouver.
- **Residence Optimization:** Optimized hourly residence times varied between 0.91 days and 1.97 days to increase both biomass generation and CO_2 extraction by 28.8% and 10.8%, respectively. On average, the associated biomass production and CO_2 absorption were 13.9 g/m^2 and 31.4 g/m^2, respectively.
- **Free-Form Façades Optimization:** Free-form façades received lower solar irradiation by 8.72 W/m^2 on average, compared to flat façades. However, free-form façades had specific points with higher local irradiation of up to 210 W/m^2 compared to 180 W/m^2. Optimal placement of PBRs on free-form façade points with lower tilt angles increased bioenergy generation by 14.3%.
- **Folded Façades Optimization:** For locations with a latitude angle of 45°, optimized folded façades generated higher bioenergy by 29.6%, compared to flat façades.

Overall, this research significantly advances the understanding and implementation of building integrated PBRs, offering practical strategies for achieving sustainable energy solutions in the built environment.

7.7 Future Works

Further investigation is recommended into the following domains to expand upon the research outlined in this doctoral thesis.

Development of Advanced Monitoring Techniques: More sophisticated and non-invasive monitoring techniques should be developed for microalgae growth within PBRs through the integration of advanced imaging technologies, such as hyperspectral imaging or infrared thermography, to provide real-time data on microalgae health and biomass production.

Integration of Renewable Energy Sources: Multiple renewable energy sources within DSFs should be explored, such as combining PBRs with solar PV panels to create hybrid energy generation systems. Such systems could optimize energy transfer by utilizing excess heat from the PV panels to reduce their temperature, thereby enhancing their efficiency. This excess heat could be directed towards the PBRs to maintain their optimal operating temperature for microalgae growth and bioenergy production.

Air pump control for efficient microalgae mixing: It is recommended to implement a control system with the air pump to generate discrete bursts of air bubbles rather than a continuous airflow. This transition promises a reduction in the operational expenses associated with the air pump. However, it is essential to optimize the intensity and duration of these bursts to ensure minimal disruption to the efficient mixing and agitation of the microalgae medium.

Cost analysis and economic feasibility: A detailed cost analysis should be conducted to assess the economic feasibility of building integrated PBR systems and DSFs compared to traditional building envelopes and renewable energy alternatives. Specifically, investigations should evaluate the long-term maintenance needs of PBR systems, including cleaning, algae health monitoring, and system repairs, as these factors can significantly impact overall cost and performance. This would also involve comparing the initial installation and maintenance costs of DSFs with PBRs to understand the payback period and overall economic feasibility. This will help researchers assess if PBRs' environmental advantages justify their use in building façades.

Continuous microalgae harvesting mechanisms: It is advised to investigate the integration of a continuous separation system into the microalgae cultivation setup to enable the continuous harvesting of microalgae biomass. This will optimize the harvesting process by increasing the overall productivity and reducing downtime without interrupting ongoing growth cycles. Additionally, automated monitoring and control mechanisms should be explored to ensure optimal separation efficiency while minimizing energy consumption and operational costs.

Enhancing microalgae biomass value through processing: It is recommended to explore innovative post-processing techniques for solid microalgae biomass after harvesting to maximize its usability and value. This involves investigating methods such as drying, cell disruption, extraction of valuable compounds (e.g., lipids, proteins, pigments), and conversion into various bio-based products (e.g., biofuels, bioplastics, nutraceuticals). The economic viability of different post-processing approaches should be assessed by considering factors such as energy consumption, waste generation, and product purity.

References

[1] J. Pruvost, B. Le Gouic, O. Lepine, J. Legrand, F. Le Borgne, Microalgae culture in building-integrated photobioreactors: Biomass production modelling and energetic analysis, Chemical Engineering Journal 284 (2016) 850–861. https://doi.org/10.1016/j.cej.2015.08.118.

[2] A. Trombadore, B. Paludi, M. D'Ostuni, Adaptive Design of Green Facades and Vertical Farm: Examples of Technological Integration of Microalgae for Energy Production in Resilient Architecture, in: 2022: pp. 273–294. https://doi.org/10.1007/978-3-030-68556-0_10.

[3] R.N. Singh, S. Sharma, Development of suitable photobioreactor for algae production - A review, Renewable and Sustainable Energy Reviews 16 (2012) 2347–2353. https://doi.org/10.1016/j.rser.2012.01.026.

[4] C.U. Ugwu, H. Aoyagi, H. Uchiyama, Photobioreactors for mass cultivation of algae, Bioresour Technol 99 (2008) 4021–4028. https://doi.org/https://doi.org/10.1016/j.biortech.2007.01.046.

[5] S.W. Lee, J.S. Park, Evaluating thermal performance of double-skin facade using response factor, Energy Build 209 (2020). https://doi.org/10.1016/j.enbuild.2019.109657.

[6] S. Zeyninejad Movassag, K. Zamzamian, Numerical investigation on the thermal performance of double glazing air flow window with integrated blinds, Renew Energy 148 (2020) 852–863. https://doi.org/10.1016/j.renene.2019.10.170.

[7] E. Gratia, A. De Herde, Optimal operation of a south double-skin facade, Energy Build 36 (2004) 41–60. https://doi.org/10.1016/j.enbuild.2003.06.001.

[8] J. Zhou, Y. Chen, A review on applying ventilated double-skin facade to buildings in hot-summer and cold-winter zone in China, Renewable and Sustainable Energy Reviews 14 (2010) 1321–1328. https://doi.org/10.1016/j.rser.2009.11.017.

[9] N. Pourshab, M.D. Tehrani, D. Toghraie, S. Rostami, Application of double glazed façades with horizontal and vertical louvers to increase natural air flow in office buildings, Energy 200 (2020) 117486. https://doi.org/10.1016/j.energy.2020.117486.

[10] N. Izadyar, W. Miller, B. Rismanchi, V. Garcia-Hansen, Impacts of façade openings' geometry on natural ventilation and occupants' perception: A review, Build Environ 170 (2020) 106613. https://doi.org/10.1016/j.buildenv.2019.106613.

[11] C. Şirin, J. Goggins, M. Hajdukiewicz, A review on building-integrated photovoltaic/thermal systems for green buildings, Appl Therm Eng 229 (2023) 120607. https://doi.org/10.1016/j.applthermaleng.2023.120607.

[12] A.M. Elmalky, M.T. Araji, Optimization of Cooled Building-Integrated Photovoltaics Using Powell's Conjugate Direction Method in Canada, in: 2022 International Conference on Electrical, Computer and Energy Technologies (ICECET), IEEE, 2022: pp. 1–6. https://doi.org/10.1109/ICECET55527.2022.9872898.

[13] J. Pruvost, B.L. Gouic, J. Legrand, Symbiotic integration of photobioreactors in a factory building façade for mutual benefit between Buildings and Microalgae Needs, in: 21st International Congress of Chemical and Process Engineering CHISA 2014 Prague 17th Conference on Process Integration, Modelling and Optimisation for Energy Saving and Pollution Reduction PRES 2014, Praha, Czech Republik, 2014.

[14] A.M. Elmalky, M.T. Araji, Multi-objective problem of optimizing heat transfer and energy production in algal bioreactive façades, Energy 268 (2023) 126650. https://doi.org/10.1016/j.energy.2023.126650.

[15] A.M. Elmalky, M.T. Araji, Computational fluid dynamics using finite volume method: A numerical model for Double Skin Façades with renewable energy source in cold climates, Journal of Building Engineering 60 (2022) 105231. https://doi.org/10.1016/j.jobe.2022.105231.

[16] S. Preet, M.K. Sharma, J. Mathur, A. Chowdhury, S. Mathur, Performance evaluation of photovoltaic double-skin facade with forced ventilation in the composite climate, Journal of Building Engineering 32 (2020) 101733. https://doi.org/10.1016/j.jobe.2020.101733.

[17] Z. Ioannidis, E.-D. Rounis, A. Athienitis, T. Stathopoulos, Double skin façade integrating semi-transparent photovoltaics: Experimental study on forced convection and heat recovery, Appl Energy 278 (2020) 115647. https://doi.org/10.1016/j.apenergy.2020.115647.

[18] J. Peng, D.C. Curcija, L. Lu, S.E. Selkowitz, H. Yang, R. Mitchell, Developing a method and simulation model for evaluating the overall energy performance of a ventilated semi-

transparent photovoltaic double-skin facade, Progress in Photovoltaics: Research and Applications 24 (2016) 781–799. https://doi.org/10.1002/pip.2727.

[19] M.T. Araji, I. Shahid, Symbiosis optimization of building envelopes and micro-algae photobioreactors, Journal of Building Engineering 18 (2018) 58–65. https://doi.org/10.1016/j.jobe.2018.02.008.

[20] R. Sirohi, A. Kumar Pandey, P. Ranganathan, S. Singh, A. Udayan, M. Kumar Awasthi, A.T. Hoang, C.R. Chilakamarry, S.H. Kim, S.J. Sim, Design and applications of photobioreactors- a review, Bioresour Technol 349 (2022) 126858. https://doi.org/10.1016/j.biortech.2022.126858.

[21] H. Takache, J. Pruvost, J.-F. Cornet, Kinetic modeling of the photosynthetic growth of Chlamydomonas reinhardtii in a photobioreactor, Biotechnol Prog 28 (2012) 681–692. https://doi.org/10.1002/btpr.1545.

[22] J. Pruvost, J.F. Cornet, F. Le Borgne, V. Goetz, J. Legrand, Theoretical investigation of microalgae culture in the light changing conditions of solar photobioreactor production and comparison with cyanobacteria, Algal Res 10 (2015) 87–99. https://doi.org/10.1016/j.algal.2015.04.005.

[23] J.-F. Cornet, Calculation of optimal design and ideal productivities of volumetrically lightened photobioreactors using the constructal approach, Chem Eng Sci 65 (2010) 985–998. https://doi.org/10.1016/j.ces.2009.09.052.

[24] Z. Csőgör, M. Herrenbauer, K. Schmidt, C. Posten, Light distribution in a novel photobioreactor – modelling for optimization, J Appl Phycol 13 (2001) 325–333. https://doi.org/10.1023/A:1017974232510.

[25] B. Farges, C. Laroche, J.-F. Cornet, C.-G. Dussap, Spectral kinetic modeling and long-term behavior assessment of *Arthrospira platensis* growth in photobioreactor under red (620 nm) light illumination, Biotechnol Prog 25 (2009) 151–162. https://doi.org/10.1002/btpr.95.

[26] J. Pruvost, G. Van Vooren, B. Le Gouic, A. Couzinet-Mossion, J. Legrand, Systematic investigation of biomass and lipid productivity by microalgae in photobioreactors for biodiesel application, Bioresour Technol 102 (2011) 150–158. https://doi.org/10.1016/j.biortech.2010.06.153.

[27] S. Freitas, C. Catita, P. Redweik, M.C. Brito, Modelling solar potential in the urban environment: State-of-the-art review, Renewable and Sustainable Energy Reviews 41 (2015) 915–931. https://doi.org/10.1016/j.rser.2014.08.060.

[28] G. Desthieux, C. Carneiro, R. Camponovo, P. Ineichen, E. Morello, A. Boulmier, N. Abdennadher, S. Dervey, C. Ellert, Solar Energy Potential Assessment on Rooftops and Facades in Large Built Environments Based on LiDAR Data, Image Processing, and Cloud Computing. Methodological Background, Application, and Validation in Geneva (Solar Cadaster), Front Built Environ 4 (2018). https://doi.org/10.3389/fbuil.2018.00014.

[29] A.M. Elmalky, M.T. Araji, A new trigonometric model for solar radiation and shading factor: Varying profiles of building façades and urban eccentricities, Energy Build 282 (2023) 112803. https://doi.org/10.1016/j.enbuild.2023.112803.

[30] J. Esclapés, I. Ferreiro, J. Piera, J. Teller, A method to evaluate the adaptability of photovoltaic energy on urban façades, Solar Energy 105 (2014) 414–427. https://doi.org/10.1016/j.solener.2014.03.012.

[31] J. Jia, F. Gao, Y. Cheng, P. Wang, H.H. EI-Ghetany, J. Han, A comparative study on thermoelectric performances and energy savings of double-skin photovoltaic windows in cold regions of China, Solar Energy 206 (2020) 464–472. https://doi.org/10.1016/j.solener.2020.05.094.

[32] J. Peng, L. Lu, H. Yang, An experimental study of the thermal performance of a novel photovoltaic double-skin facade in Hong Kong, Solar Energy 97 (2013) 293–304. https://doi.org/10.1016/j.solener.2013.08.031.

[33] M. Shakouri, H. Ghadamian, A. Noorpoor, Quasi-dynamic energy performance analysis of building integrated photovoltaic thermal double skin façade for middle eastern climate case, Appl Therm Eng 179 (2020) 115724. https://doi.org/10.1016/j.applthermaleng.2020.115724.

[34] A. Ghosh, Potential of building integrated and attached/applied photovoltaic (BIPV/BAPV) for adaptive less energy-hungry building's skin: A comprehensive Review, J Clean Prod (2020) 123343. https://doi.org/10.1016/j.jclepro.2020.123343.

[35] X. Zhang, S.K. Lau, S.S.Y. Lau, Y. Zhao, Photovoltaic integrated shading devices (PVSDs): A review, Solar Energy 170 (2018) 947–968. https://doi.org/10.1016/j.solener.2018.05.067.

[36] A.A. Hegazy, Effect of dust accumulation on solar transmittance through glass covers of plate-type collectors, Renew Energy 22 (2001) 525–540. https://doi.org/10.1016/S0960-1481(00)00093-8.

[37] S. Heibati, W. Maref, H.H. Saber, Developing a model for predicting optimum daily tilt angle of a PV solar system at different geometric, physical and dynamic parameters, Advances in Building Energy Research 15 (2021) 179–198. https://doi.org/10.1080/17512549.2019.1684366.

[38] A. Ullah, H. Imran, Z. Maqsood, N.Z. Butt, Investigation of optimal tilt angles and effects of soiling on PV energy production in Pakistan, Renew Energy 139 (2019) 830–843. https://doi.org/10.1016/j.renene.2019.02.114.

[39] Natural Resourses Canada, "Solar resource maps of Canada," (n.d.). https://solargis.com/maps-and-gis-data/download/canada (accessed June 28, 2024).

[40] F. Biljecki, J. Stoter, H. Ledoux, S. Zlatanova, A. Çöltekin, Applications of 3D city models: State of the art review, ISPRS Int J Geoinf 4 (2015) 2842–2889. https://doi.org/10.3390/ijgi4042842.

[41] E. Sorooshnia, M. Rashidi, P. Rahnamayiezekavat, F. Rezaei, B. Samali, Optimum external shading system for counterbalancing glare probability and daylight illuminance in Sydney's residential buildings, Engineering, Construction and Architectural Management 30 (2023) 296–320. https://doi.org/10.1108/ECAM-03-2021-0191.

[42] E. Nault, G. Peronato, E. Rey, M. Andersen, Review and critical analysis of early-design phase evaluation metrics for the solar potential of neighborhood designs, Build Environ 92 (2015) 679–691. https://doi.org/10.1016/j.buildenv.2015.05.012.

[43] A.R. Adi, J.A. Suryabrata, E. Pradipto, Optimizing Shading Devices Through the Shading Effect of Surrounding Buildings, DIMENSI (Journal of Architecture and Built Environment) 46 (2020) 79–86. https://doi.org/10.9744/dimensi.46.2.79-86.

[44] E. Simá, M.A. Chagolla-Aranda, G. Huelsz, R. Tovar, G. Alvarez, Tree and neighboring buildings shading effects on the thermal performance of a house in a warm sub-humid climate, Build Simul 8 (2015) 711–723. https://doi.org/10.1007/s12273-015-0247-2.

[45] Y. Ye, P. Xu, H. Sha, P. Yue, H. Zhang, ShadingPlus—a fast simulation tool for building shading analysis, Energy Effic 9 (2016) 239–248. https://doi.org/10.1007/s12053-015-9360-4.

[46] A. Boccalatte, M. Fossa, C. Ménézo, Best arrangement of BIPV surfaces for future NZEB districts while considering urban heat island effects and the reduction of reflected radiation from solar façades, Renew Energy 160 (2020) 686–697. https://doi.org/10.1016/j.renene.2020.07.057.

[47] M. Heidarinejad, S. Gracik, M. Sadeghipour Roudsari, S. Khoshdel Nikkho, J. Liu, K. Liu, G. Pitchorov, J. Srebric, Influence of building surface solar irradiance on environmental temperatures in urban neighborhoods, Sustain Cities Soc 26 (2016) 186–202. https://doi.org/10.1016/j.scs.2016.06.011.

[48] G. Lobaccaro, F. Fiorito, G. Masera, T. Poli, District geometry simulation: A study for the optimization of solar façades in urban canopy layers, Energy Procedia 30 (2012) 1163–1172. https://doi.org/10.1016/j.egypro.2012.11.129.

[49] H. Lakenbrink, C. Roedel, J.P. Petersen, Smart Material House BIQ, 2013.

[50] J. Wurm, Photobioreactors on facades for energy generation Alternative technologies in the building envelope, International Rosenheim Window & Facade Conference 2013 (2013) 83–87.

[51] J. Masojídek, M. Sergejevová, K. Rottnerová, V. Jirka, J. Korečko, J. Kopecký, I. Zaťková, G. Torzillo, D. Štys, A two-stage solar photobioreactor for cultivation of microalgae based on solar concentrators, J Appl Phycol 21 (2009) 55–63. https://doi.org/10.1007/s10811-008-9324-6.

[52] C. Wu, G. Herbst, A. Lujan, K.H. Kim, A Stochastic Approach To Simulate And Optimize The Coating Uniformity Of Rotational Molding For Microalgae Facades, in: 2022 Annual Modeling and Simulation Conference (ANNSIM), IEEE, 2022: pp. 569–580. https://doi.org/10.23919/ANNSIM55834.2022.9859444.

[53] K. Warren, J. Milovanovic, K.H. Kim, Effect of a Microalgae Facade on Design Behaviors: A Pilot Study with Architecture Students, Buildings 13 (2023) 611. https://doi.org/10.3390/buildings13030611.

[54] M. Marani, This algae facade curtain naturally filters polluted air, (2018). https://www.archpaper.com/2018/12/this-algae-facade-curtain-naturally-filters-polluted-air/#gallery-0-slide-0 (accessed August 4, 2022).

[55] S. Pawar, Effectiveness mapping of open raceway pond and tubular photobioreactors for sustainable production of microalgae biofuel, Renewable and Sustainable Energy Reviews 62 (2016) 640–653. https://doi.org/10.1016/j.rser.2016.04.074.

[56] O. Kalyanova, Double-skin facade: modelling and experimental investigations of thermal performance, 2008.

[57] A. GhaffarianHoseini, A. GhaffarianHoseini, U. Berardi, J. Tookey, D.H.W. Li, S. Kariminia, Exploring the advantages and challenges of double-skin facądes (DSFs), Renewable and Sustainable Energy Reviews 60 (2016) 1052–1065. https://doi.org/10.1016/j.rser.2016.01.130.

[58] A. Lloret, J. Andreu, J. Merten, J. Puigdollers, O. Aceves, L. Sabata, M. Chantant, U. Eicker, Large grid-connected hybrid PV system integrated in a public building, Progress in Photovoltaics: Research and Applications 6 (1998) 453–464.

[59] T.T. Chow, G. Pei, L.S. Chan, Z. Lin, K.F. Fong, A Comparative Study of PV Glazing Performance in Warm Climate, Indoor and Built Environment 18 (2009) 32–40. https://doi.org/10.1177/1420326X08100323.

[60] T.T. Chow, K.F. Fong, W. He, Z. Lin, A.L.S. Chan, Performance evaluation of a PV ventilated window applying to office building of Hong Kong, Energy Build 39 (2007) 643–650. https://doi.org/10.1016/j.enbuild.2006.09.014.

[61] J. Peng, D.C. Curcija, L. Lu, S.E. Selkowitz, H. Yang, W. Zhang, Numerical investigation of the energy saving potential of a semi-transparent photovoltaic double-skin facade in a cool-summer Mediterranean climate, Appl Energy 165 (2016) 345–356. https://doi.org/10.1016/j.apenergy.2015.12.074.

[62] S. Yang, A. Cannavale, D. Prasad, A. Sproul, F. Fiorito, Numerical simulation study of BIPV/T double-skin facade for various climate zones in Australia: Effects on indoor thermal comfort, Build Simul 12 (2019) 51–67. https://doi.org/10.1007/s12273-018-0489-x.

[63] W. Ke, J. Ji, C. Wang, C. Zhang, H. Xie, Y. Tang, Y. Lin, Comparative analysis on the electrical and thermal performance of two CdTe multi-layer ventilated windows with and without a middle PCM layer: A preliminary numerical study, Renew Energy 189 (2022) 1306–1323. https://doi.org/10.1016/j.renene.2022.03.090.

[64] J. Peng, L. Lu, H. Yang, T. Ma, Comparative study of the thermal and power performances of a semi-transparent photovoltaic façade under different ventilation modes, Appl Energy 138 (2015) 572–583. https://doi.org/10.1016/j.apenergy.2014.10.003.

[65] C. Wang, J. Ji, B. Yu, C. Zhang, W. Ke, J. Wang, Comprehensive investigation on the luminous and energy-saving performance of the double-skin ventilated window integrated with CdTe cells, Energy 238 (2022) 121757. https://doi.org/10.1016/j.energy.2021.121757.

[66] M.K. Sharma, S. Preet, J. Mathur, A. Chowdhury, S. Mathur, Parametric analysis of factors affecting thermal performance of photovoltaic triple skin façade system (PV-TSF), Journal of Building Engineering 40 (2021) 102344. https://doi.org/10.1016/j.jobe.2021.102344.

[67] C. Wang, M.M. Uddin, J. Ji, B. Yu, J. Wang, The performance analysis of a double-skin ventilated window integrated with CdTe cells in typical climate regions, Energy Build 241 (2021) 110922. https://doi.org/10.1016/j.enbuild.2021.110922.

[68] A.L.S. Chan, T.T. Chow, K.F. Fong, Z. Lin, Investigation on energy performance of double skin façade in Hong Kong, Energy Build 41 (2009) 1135–1142. https://doi.org/https://doi.org/10.1016/j.enbuild.2009.05.012.

[69] X. Liu, C. Shen, J. Wang, C. Zhang, Y. Shuai, Static and dynamic regulations of photovoltaic double skin facades towards building sustainability: A review, Renewable and Sustainable Energy Reviews 183 (2023) 113458. https://doi.org/10.1016/j.rser.2023.113458.

[70] A.M. Elmalky, M.T. Araji., Integral Model with Machine Learning for Balancing Heat Transfer and Energy Generation in Algal Bio-reactive Façades, in: Proceedings of USim Conference 2022: 3rd USim Conference of IBPSA-Scotland, IBPSA-Scotland, Glasgow, Scotland, 2022. https://publications.ibpsa.org/conference/paper/?id=usim2022_p114.

[71] A.M. Elmalky, M.T. Araji, Pareto Optimization for Enhanced Building Energy Efficiency and Bioenergy Generation, in: 2024 4th International Conference on Smart Grid and Renewable Energy (SGRE), IEEE, 2024: pp. 1–6. https://doi.org/10.1109/SGRE59715.2024.10458419.

[72] A.M. Elmalky, M.T. Araji, Chemical Kinetics Model with Experimental Validation for Optimal Microalgae Generation in Double Skin Façades, Energy - Under Review (2024).

[73] A.M. Elmalky, M.T. Araji, Efficient Conversion of Solar Energy to Algal Biomass in Buildings Using Neural Network-Aided Optimization, Renewable Energy - Under Review (2024).

[74] A.M. Elmalky, M.T. Araji, Neural Networks for Monitoring Microalgae Biomass in Building Façades, Technology|Architecture + Design 8 (2024) 60–69. https://doi.org/10.1080/24751448.2024.2313441.

[75] A.M. Elmalky, M.T. Araji, Optimization models for photosynthetic bioenergy generation in building façades, Renew Energy 228 (2024) 120607. https://doi.org/10.1016/j.renene.2024.120607.

[76] A.M. Elmalky, M.T. Araji, Computational procedure of solar irradiation: A new approach for high performance façades with experimental validation, Energy Build 298 (2023) 113491. https://doi.org/10.1016/j.enbuild.2023.113491.

[77] A.M. Elmalky, M.T. Araji, A Novel Genetic Algorithm for Optimizing Microalgae Residence Time in Flat Panel Photobioreactors, in: ICMAME 2023 Conference Proceedings, ECER, Aksaray, 2023. https://doi.org/10.53375/icmame.2023.264.

[78] A. Prokop, R.K. Bajpai, M.E. Zappi, Algal Biorefineries Volume 2: Products and Refinery Design, Springer, 2015. https://doi.org/10.1007/978-3-319-20200-6.

[79] M. Talaei, M. Mahdavinejad, R. Azari, Thermal and energy performance of algae bioreactive façades: A review, Journal of Building Engineering 28 (2020). https://doi.org/10.1016/j.jobe.2019.101011.

[80] J. Ruiz, G. Olivieri, J. De Vree, R. Bosma, P. Willems, J.H. Reith, M.H.M. Eppink, D.M.M. Kleinegris, R.H. Wijffels, M.J. Barbosa, Towards industrial products from microalgae, Energy Environ Sci 9 (2016) 3036–3043. https://doi.org/10.1039/c6ee01493c.

[81] P. Feng, K. Yang, Z. Xu, Z. Wang, L. Fan, L. Qin, S. Zhu, C. Shang, P. Chai, Z. Yuan, L. Hu, Growth and lipid accumulation characteristics of Scenedesmus obliquus in semi-continuous cultivation outdoors for biodiesel feedstock production, Bioresour Technol 173 (2014) 406–414. https://doi.org/10.1016/j.biortech.2014.09.123.

[82] P. Feng, Z. Xu, L. Qin, M. Asraful Alam, Z. Wang, S. Zhu, Effects of different nitrogen sources and light paths of flat plate photobioreactors on the growth and lipid accumulation of Chlorella sp. GN1 outdoors, Bioresour Technol 301 (2020) 122762. https://doi.org/10.1016/j.biortech.2020.122762.

[83] J.O.H.T.C. Ugwu, Improvement of mass transfer characteristics and productivities of inclined tubular photobioreactors by installation of internal static mixers, Appl Microbiol Biotechnol 58 (2002) 600–607. https://doi.org/10.1007/s00253-002-0940-9.

[84] J. Degen, A. Uebele, A. Retze, U. Schmid-Staiger, W. Trösch, A novel airlift photobioreactor with baffles for improved light utilization through the flashing light effect, J Biotechnol 92 (2001) 89–94. https://doi.org/10.1016/S0168-1656(01)00350-9.

[85] J. Huang, S. Kang, M. Wan, Y. Li, X. Qu, F. Feng, J. Wang, W. Wang, G. Shen, W. Li, Numerical and experimental study on the performance of flat-plate photobioreactors with different inner structures for microalgae cultivation, J Appl Phycol 27 (2015) 49–58. https://doi.org/10.1007/s10811-014-0281-y.

[86] X. Guo, L. Yao, Q. Huang, Aeration and mass transfer optimization in a rectangular airlift loop photobioreactor for the production of microalgae, Bioresour Technol 190 (2015) 189–195. https://doi.org/10.1016/j.biortech.2015.04.077.

[87] A. Massart, A. Mirisola, D. Lupant, D. Thomas, A.-L. Hantson, Experimental characterization and numerical simulation of the hydrodynamics in an airlift photobioreactor for microalgae cultures, Algal Res 6 (2014) 210–217. https://doi.org/10.1016/j.algal.2014.07.003.

[88] Z. Yang, M. del Ninno, Z. Wen, H. Hu, An experimental investigation on the multiphase flows and turbulent mixing in a flat-panel photobioreactor for algae cultivation, J Appl Phycol 26 (2014) 2097–2107. https://doi.org/10.1007/s10811-014-0239-0.

[89] L. Meier, P. Barros, A. Torres, C. Vilchez, D. Jeison, Photosynthetic biogas upgrading using microalgae: Effect of light/dark photoperiod, Renew Energy 106 (2017) 17–23. https://doi.org/10.1016/j.renene.2017.01.009.

[90] A. Juneja, R.M. Ceballos, G.S. Murthy, Effects of environmental factors and nutrient availability on the biochemical composition of algae for biofuels production: A review, Energies (Basel) 6 (2013) 4607–4638. https://doi.org/10.3390/en6094607.

[91] Q. Béchet, M. Laviale, N. Arsapin, H. Bonnefond, O. Bernard, Modeling the impact of high temperatures on microalgal viability and photosynthetic activity, Biotechnol Biofuels 10 (2017) 1–11. https://doi.org/10.1186/s13068-017-0823-z.

[92] S.E. Jorgensen, Handbook of environmental data and ecological parameters, Pergamon, 1979.

[93] C. Sorokin, R.W. Krauss, The Effects of Light Intensity on the Growth Rates of Green Algae, Plant Physiol 33 (1958) 109–113.

[94] A. Dauta, J. Devaux, F. Piquemal, L. Boumnich, Growth rate of four freshwater algae in relation to light and temperature, Hydrobiologia 207 (1990) 221–226. https://doi.org/10.1007/BF00041459.

[95] I. Havlik, P. Lindner, T. Scheper, K.F. Reardon, On-line monitoring of large cultivations of microalgae and cyanobacteria, Trends Biotechnol 31 (2013) 406–414. https://doi.org/10.1016/j.tibtech.2013.04.005.

[96] S. Wilkinson, P. Stoller, P. Ralph, B. Hamdorf, L.N. Catana, G.S. Kuzava, Exploring the Feasibility of Algae Building Technology in NSW, Procedia Eng 180 (2017) 1121–1130. https://doi.org/10.1016/j.proeng.2017.04.272.

[97] E.G. Nwoba, D.A. Parlevliet, D.W. Laird, K. Alameh, N.R. Moheimani, Sustainable phycocyanin production from Arthrospira platensis using solar-control thin film coated photobioreactor, Biochem Eng J 141 (2019) 232–238. https://doi.org/10.1016/j.bej.2018.10.024.

[98] B. Gris, T. Morosinotto, G.M. Giacometti, A. Bertucco, E. Sforza, Cultivation of Scenedesmus obliquus in photobioreactors: Effects of light intensities and light-dark cycles on growth, productivity, and biochemical composition, Appl Biochem Biotechnol 172 (2014) 2377–2389. https://doi.org/10.1007/s12010-013-0679-z.

[99] M. Decker, G. Hahn, L.M. Harris, Bio-Enabled Façade Systems Managing Complexity of Life through Emergent Technologies, in: Proceedings of the 34th ECAADe Conference on Complexity & Simplicity, Oulu, Finland: University of Oulu, 2016: pp. 603–612. http://papers.cumincad.org/cgi-bin/works/paper/ecaade2016_102.

[100] M. Castrillo, R. Díez-Montero, I. Tejero, Model-based feasibility assessment of a deep solar photobioreactor for microalgae culturing, Algal Res 29 (2018) 304–318. https://doi.org/10.1016/j.algal.2017.12.004.

[101] M. Raeisossadati, N.R. Moheimani, D. Parlevliet, Luminescent solar concentrator panels for increasing the efficiency of mass microalgal production, Renewable and Sustainable Energy Reviews 101 (2019) 47–59. https://doi.org/10.1016/j.rser.2018.10.029.

[102] A.P. Peter, A.K. Koyande, K.W. Chew, S.-H. Ho, W.-H. Chen, J.-S. Chang, R. Krishnamoorthy, F. Banat, P.L. Show, Continuous cultivation of microalgae in

photobioreactors as a source of renewable energy: Current status and future challenges, Renewable and Sustainable Energy Reviews 154 (2022) 111852. https://doi.org/10.1016/j.rser.2021.111852.

[103] P.M. Slegers, P.J.M. van Beveren, R.H. Wijffels, G. van Straten, A.J.B. van Boxtel, Scenario analysis of large scale algae production in tubular photobioreactors, Appl Energy 105 (2013) 395–406. https://doi.org/10.1016/j.apenergy.2012.12.068.

[104] S. Fon Sing, A. Isdepsky, M.A. Borowitzka, D.M. Lewis, Pilot-scale continuous recycling of growth medium for the mass culture of a halotolerant Tetraselmis sp. in raceway ponds under increasing salinity: A novel protocol for commercial microalgal biomass production, Bioresour Technol 161 (2014) 47–54. https://doi.org/10.1016/j.biortech.2014.03.010.

[105] M. Torres, P. Alavedra, A. Guzmán, E. Cuerva, C. Planas, R. Clemente, V. Escalona, Double skin facades—cavity and exterior openings dimensions for saving energy on Mediterranean climate., (2007).

[106] B. Rahmani, M. Kandar, P. Rahmani, How Double Skin Façade's Air-Gap Sizes Effect on Lowering Solar Heat Gain in Tropical Climate?, World Appl Sci J 18 (2012). https://doi.org/10.5829/idosi.wasj.2012.18.06.3184.

[107] C.A. Rundle, M.F. Lightstone, P. Oosthuizen, P. Karava, E. Mouriki, Validation of computational fluid dynamics simulations for atria geometries, Build Environ 46 (2011) 1343–1353. https://doi.org/https://doi.org/10.1016/j.buildenv.2010.12.019.

[108] H. Radhi, S. Sharples, F. Fikiry, Will multi-facade systems reduce cooling energy in fully glazed buildings? A scoping study of UAE buildings, Energy Build 56 (2013) 179–188. https://doi.org/https://doi.org/10.1016/j.enbuild.2012.08.030.

[109] T. Zhang, H. Yang, Flow and heat transfer characteristics of natural convection in vertical air channels of double-skin solar façades, Appl Energy 242 (2019) 107–120. https://doi.org/https://doi.org/10.1016/j.apenergy.2019.03.072.

[110] S. Barbosa, K. Ip, Perspectives of double skin façades for naturally ventilated buildings: A review, Renewable and Sustainable Energy Reviews 40 (2014) 1019–1029. https://doi.org/10.1016/j.rser.2014.07.192.

[111] K. Hou, S. Li, H. Wang, Simulation and experimental verification of energy saving effect of passive preheating natural ventilation double skin façade, Energy Exploration & Exploitation 39 (2021) 464–487. https://doi.org/10.1177/0144598720956288.

[112] A. Jankovic, F. Goia, Impact of double skin facade constructional features on heat transfer and fluid dynamic behaviour, Build Environ 196 (2021). https://doi.org/10.1016/j.buildenv.2021.107796.

[113] O.A. Tkachenko, V. Timchenko, S. Giroux-Julien, C. Ménézo, G.H. Yeoh, J.A. Reizes, E. Sanvicente, M. Fossa, Numerical and experimental investigation of unsteady natural convection in a non-uniformly heated vertical open-ended channel, International Journal of Thermal Sciences 99 (2016) 9–25. https://doi.org/https://doi.org/10.1016/j.ijthermalsci.2015.07.029.

[114] Y. Tao, H. Zhang, L. Zhang, G. Zhang, J. Tu, L. Shi, Ventilation performance of a naturally ventilated double-skin façade in buildings, Renew Energy 167 (2021) 184–198. https://doi.org/10.1016/j.renene.2020.11.073.

[115] Z. Yılmaz, F. Çetintaş, Double skin façade's effects on heat losses of office buildings in Istanbul, Energy Build 37 (2005) 691–697. https://doi.org/https://doi.org/10.1016/j.enbuild.2004.07.010.

[116] A. Fallahi, F. Haghighat, H. Elsadi, Energy performance assessment of double-skin façade with thermal mass, Energy Build 42 (2010) 1499–1509. https://doi.org/https://doi.org/10.1016/j.enbuild.2010.03.020.

[117] A. Guardo, M. Coussirat, E. Egusquiza, P. Alavedra, R. Castilla, A CFD approach to evaluate the influence of construction and operation parameters on the performance of Active Transparent Façades in Mediterranean climates, Energy Build 41 (2009) 534–542. https://doi.org/https://doi.org/10.1016/j.enbuild.2008.11.019.

[118] N. Mingotti, T. Chenvidyakarn, A.W. Woods, Combined impacts of climate and wall insulation on the energy benefit of an extra layer of glazing in the facade, Energy Build 58 (2013) 237–249. https://doi.org/https://doi.org/10.1016/j.enbuild.2012.11.033.

[119] A. de Gracia, L. Navarro, A. Castell, L.F. Cabeza, Energy performance of a ventilated double skin facade with PCM under different climates, Energy Build 91 (2015) 37–42. https://doi.org/10.1016/j.enbuild.2015.01.011.

[120] E. Sanchez, A. Rolando, R. Sant, L. Ayuso, Influence of natural ventilation due to buoyancy and heat transfer in the energy efficiency of a double skin facade building, Energy for Sustainable Development 33 (2016) 139–148. https://doi.org/10.1016/j.esd.2016.02.002.

[121] Z. Su, X. Li, F. Xue, Double-skin façade optimization design for different climate zones in China, Solar Energy 155 (2017) 281–290. https://doi.org/10.1016/j.solener.2017.06.042.

[122] F. Xue, X. Li, A fast assessment method for thermal performance of naturally ventilated double-skin façades during cooling season, Solar Energy 114 (2015) 303–313. https://doi.org/10.1016/j.solener.2015.01.040.

[123] T. Srisamranrungruang, K. Hiyama, Balancing of natural ventilation, daylight, thermal effect for a building with double-skin perforated facade (DSPF), Energy Build 210 (2020). https://doi.org/10.1016/j.enbuild.2020.109765.

[124] A. Dama, D. Angeli, O.K. Larsen, Naturally ventilated double-skin façade in modeling and experiments, Energy Build 144 (2017) 17–29. https://doi.org/10.1016/j.enbuild.2017.03.038.

[125] G. Pomaranzi, N. Daniotti, P. Schito, L. Rosa, A. Zasso, Experimental assessment of the effects of a porous double skin façade system on cladding loads, Journal of Wind Engineering and Industrial Aerodynamics 196 (2020) 104019. https://doi.org/10.1016/j.jweia.2019.104019.

[126] A. Morrison, D. Walshe, Products and Texhnology: Double Skin Façades, (2022). https://archiglass.nethouse.ru/static/doc/0000/0000/0211/211321.khhwenr6g5.pdf (accessed November 12, 2022).

[127] Single vs. Double vs. Triple Glazing: Heat Loss and U-Values, (2022). https://abbeyglass.co.uk/news/single-vs-double-vs-triple-glazing/#:~:text=Generally%2C%20the%20U%2Dvalues%20are,Triple%20glazing%3A%200.8%20%E2%80%93%201.6 (accessed November 12, 2022).

[128] R. Sinclair, D. Phillips, V. Mezhibovski, Ventilating façades, ASHRAE J 51 (2009) 16–27.

[129] L. Zhu, J. Zhang, Q. Li, Z. Shao, M. Chen, Y. Yang, Y. Sun, Comprehensive analysis of heat transfer of double-skin facades integrated high concentration photovoltaic (CPV-DSF), Renew Energy 161 (2020) 635–649. https://doi.org/10.1016/j.renene.2020.07.045.

[130] H. Li, K. Zhong, Z. (John) Zhai, A new double-skin façade system integrated with TiO2 plates for decomposing BTEX, Build Environ 180 (2020). https://doi.org/10.1016/j.buildenv.2020.107037.

[131] A.P. de A. Rocha, R.C.L.F. Oliveira, N. Mendes, Experimental validation and comparison of direct solar shading calculations within building energy simulation tools: Polygon

clipping and pixel counting techniques, Solar Energy 158 (2017) 462–473. https://doi.org/10.1016/j.solener.2017.10.011.

[132] A. Márquez-García, M. Varo-Martínez, R. López-Luque, New model for the estimation of solar radiation on façades in urban environments, Renewable Energy and Power Quality Journal 1 (2014) 729–734. https://doi.org/10.24084/repqj12.468.

[133] M. Tripathy, S. Yadav, P.K. Sadhu, S.K. Panda, Determination of optimum tilt angle and accurate insolation of BIPV panel influenced by adverse effect of shadow, Renew Energy 104 (2017) 211–223. https://doi.org/10.1016/j.renene.2016.12.034.

[134] Y. Cascone, V. Corrado, V. Serra, Calculation procedure of the shading factor under complex boundary conditions, Solar Energy 85 (2011) 2524–2539. https://doi.org/10.1016/j.solener.2011.07.011.

[135] B.R. Vatti, A generic solution to polygon clipping, Commun ACM 35 (1992) 56–63. https://doi.org/10.1145/129902.129906.

[136] EnergyPlus, EnergyPlus Engineering Reference: the reference to EnergyPlus calculations, (2013).

[137] I. Maestre, L. Pérez-Lombard, J. Foncubierta, P. Cubillas, Improving direct solar shading calculations within building energy simulation tools, J Build Perform Simul 6 (2013) 437–448. https://doi.org/10.1080/19401493.2012.745609.

[138] A.P. de A. Rocha, A. Rodler, R.C.L.F. Oliveira, J. Virgone, N. Mendes, A pixel counting technique for sun patch assessment within building enclosures, Solar Energy 184 (2019) 173–186. https://doi.org/10.1016/j.solener.2019.03.081.

[139] N.L. Jones, D.P. Greenberg, K.B. Pratt, Fast computer graphics techniques for calculating direct solar radiation on complex building surfaces, J Build Perform Simul 5 (2012) 300–312. https://doi.org/10.1080/19401493.2011.582154.

[140] A.P. de A. Rocha, N. Mendes, R.C.L.F. Oliveira, Domus method for predicting sunlit areas on interior surfaces, Ambiente Construído 18 (2018) 83–95. https://doi.org/10.1590/s1678-86212018000300269.

[141] C. Chatzipoulka, R. Compagnon, M. Nikolopoulou, Urban geometry and solar availability on façades and ground of real urban forms: using London as a case study, Solar Energy 138 (2016) 53–66. https://doi.org/10.1016/j.solener.2016.09.005.

[142] H. Takebayashi, E. Ishii, M. Moriyama, A. Sakaki, S. Nakajima, H. Ueda, Study to examine the potential for solar energy utilization based on the relationship between urban morphology and solar radiation gain on building rooftops and wall surfaces, Solar Energy 119 (2015) 362–369. https://doi.org/10.1016/j.solener.2015.05.039.

[143] L. Romero Rodríguez, R. Nouvel, E. Duminil, U. Eicker, Setting intelligent city tiling strategies for urban shading simulations, Solar Energy 157 (2017) 880–894. https://doi.org/10.1016/j.solener.2017.09.017.

[144] R. Blaise, D. Gilles, Adapted strategy for large-scale assessment of solar potential on facades in urban areas focusing on the reflection component, Solar Energy Advances 2 (2022) 100030. https://doi.org/10.1016/j.seja.2022.100030.

[145] P. Redweik, C. Catita, M. Brito, Solar energy potential on roofs and facades in an urban landscape, Solar Energy 97 (2013) 332–341. https://doi.org/10.1016/j.solener.2013.08.036.

[146] X. Zhang, Y. Lei, R. Li, A. Ackerman, N. Guo, Y. Li, Q. Yang, Y. Liu, Research on Thermal Comfort of Underside of Street Tree Based on LiDAR Point Cloud Model, Forests 13 (2022) 1086. https://doi.org/10.3390/f13071086.

[147] D. Lingfors, S. Killinger, N.A. Engerer, J. Widén, J.M. Bright, Identification of PV system shading using a LiDAR-based solar resource assessment model: An evaluation and cross-validation, Solar Energy 159 (2018) 157–172. https://doi.org/10.1016/j.solener.2017.10.061.

[148] P. Littlefair, J. Ortiz, C. Das Bhaumik, A simulation of solar shading control on UK office energy use, Building Research & Information 38 (2010) 638–646. https://doi.org/10.1080/09613218.2010.496556.

[149] H. Sghiouri, A. Mezrhab, M. Karkri, H. Naji, Shading devices optimization to enhance thermal comfort and energy performance of a residential building in Morocco, Journal of Building Engineering 18 (2018) 292–302. https://doi.org/10.1016/j.jobe.2018.03.018.

[150] Y. Wang, Y. Chen, C. Li, Energy performance and applicability of naturally ventilated double skin façade with Venetian blinds in Yangtze River Area, Sustain Cities Soc 61 (2020) 102348. https://doi.org/10.1016/j.scs.2020.102348.

[151] D. Iyi, R. Hasan, R. Penlington, C. Underwood, Double skin façade: Modelling technique and influence of venetian blinds on the airflow and heat transfer, Appl Therm Eng 71 (2014) 219–229. https://doi.org/10.1016/j.applthermaleng.2014.06.024.

[152] C. Popa, D. Ospir, S. Fohanno, C. Chereches, Numerical simulation of dynamical aspects of natural convection flow in a double-skin façade, Energy Build 50 (2012) 229–233. https://doi.org/10.1016/j.enbuild.2012.03.042.

[153] A. Pappas, Z. Zhai, Numerical investigation on thermal performance and correlations of double skin façade with buoyancy-driven airflow, Energy Build 40 (2008) 466–475. https://doi.org/10.1016/j.enbuild.2007.04.002.

[154] M. Talaei, M. Mahdavinejad, R. Azari, Thermal and energy performance of algae bioreactive façades: A review, Journal of Building Engineering 28 (2020) 101011. https://doi.org/10.1016/j.jobe.2019.101011.

[155] J.N. Young, K. Schmidt, It's what's inside that matters: physiological adaptations of high-latitude marine microalgae to environmental change, New Phytologist 227 (2020) 1307–1318. https://doi.org/10.1111/nph.16648.

[156] M. Shakouri, H. Ghadamian, S. Hoseinzadeh, A. Sohani, Multi-objective 4E analysis for a building integrated photovoltaic thermal double skin Façade system, Solar Energy 233 (2022) 408–420. https://doi.org/10.1016/j.solener.2022.01.036.

[157] S. Barbosa, K. Ip, Perspectives of double skin façades for naturally ventilated buildings: A review, Renewable and Sustainable Energy Reviews 40 (2014) 1019–1029. https://doi.org/https://doi.org/10.1016/j.rser.2014.07.192.

[158] Y.B. Yoon, B. Seo, B.B. Koh, S. Cho, Heating energy savings potential from retrofitting old apartments with an advanced double-skin façade system in cold climate, Frontiers in Energy 14 (2020) 224–240. https://doi.org/10.1007/s11708-020-0801-1.

[159] S.L. Adrienne, F. Incropera, T. Bergman, D.P. Dewitt, Fundamentals of Heat and Mass Transfer, 7th ed., John Wiley & Sons, Inc., Jefferson City , USA, 2011.

[160] G. Năstase, A. Şerban, G. Dragomir, S. Bolocan, A.I. Brezeanu, Box window double skin façade. Steady state heat transfer model proposal for energetic audits, Energy Build 112 (2016) 12–20. https://doi.org/10.1016/j.enbuild.2015.11.058.

[161] X. Wang, B. Lei, H. Bi, T. Yu, Study on the Thermal Performance of a Hybrid Heat Collecting Facade Used for Passive Solar Buildings in Cold Region, Energies (Basel) 12 (2019) 1038. https://doi.org/10.3390/en12061038.

[162] G. Ren, X. Zhao, C. Zhan, H. Jin, A. Zhou, Investigation of the Energy Performance of a Novel Modular Solar Building Envelope, Energies (Basel) 10 (2017) 880. https://doi.org/10.3390/en10070880.

[163] C. Shen, X. Li, Potential of Utilizing Different Natural Cooling Sources to Reduce the Building Cooling Load and Cooling Energy Consumption: A Case Study in Urumqi, Energies (Basel) 10 (2017) 366. https://doi.org/10.3390/en10030366.

[164] C. Shen, X. Li, Solar heat gain reduction of double glazing window with cooling pipes embedded in venetian blinds by utilizing natural cooling, Energy Build 112 (2016) 173–183. https://doi.org/10.1016/j.enbuild.2015.11.073.

[165] W. Pasut, M. De Carli, Evaluation of various CFD modelling strategies in predicting airflow and temperature in a naturally ventilated double skin façade, Appl Therm Eng 37 (2012) 267–274. https://doi.org/10.1016/j.applthermaleng.2011.11.028.

[166] C. Moler, MATLAB, (2019).

[167] F.A. Tiano, G. Rizzo, M. Marino, A. Monetti, Evaluation of the potential of solar photovoltaic panels installed on vehicle body including temperature effect on efficiency, ETransportation 5 (2020) 100067. https://doi.org/10.1016/j.etran.2020.100067.

[168] ANSYS Fluent, (2018).

[169] F.R. Menter, Two-equation eddy-viscosity turbulence models for engineering applications, AIAA Journal 32 (1994) 1598–1605. https://doi.org/10.2514/3.12149.

[170] B. Lotfi, M. Zeng, B. Sundén, Q. Wang, 3D numerical investigation of flow and heat transfer characteristics in smooth wavy fin-and-elliptical tube heat exchangers using new type vortex generators, Energy 73 (2014) 233–257. https://doi.org/10.1016/j.energy.2014.06.016.

[171] Transport Equations for the Standard k-omega Model, (2009). https://www.afs.enea.it/project/neptunius/docs/fluent/html/th/node66.htm (accessed August 2, 2022).

[172] Heating, ventilating, and air-conditioning applications, ASHRAE, Atlanta, 2015.

[173] S. P., R. Ballal, L. Sagar, G. Kumar, Effect of Shading on the Performance of Solar PV Panel, Energy and Power 5 (2015) 1–4. https://doi.org/10.5923/c.ep.201501.01.

[174] A.S. Anđelković, I. Mujan, S. Dakić, Experimental validation of a EnergyPlus model: Application of a multi-storey naturally ventilated double skin façade, Energy Build 118 (2016) 27–36. https://doi.org/10.1016/j.enbuild.2016.02.045.

[175] H.A. Zondag, D.W. de Vries, W.G.J. van Helden, R.J.C. van Zolingen, A.A. van Steenhoven, The thermal and electrical yield of a PV-thermal collector, Solar Energy 72 (2002) 113–128. https://doi.org/10.1016/S0038-092X(01)00094-9.

[176] A. Fouad, A. Galal, K. Dessoki, M.H. Eldakamawy, M.A. Hassan, M.T. Araji, Influence of geometric design variables on the performance of a novel V-shaped cavity receiver, Renew Energy 230 (2024) 120790. https://doi.org/10.1016/j.renene.2024.120790.

[177] M.A. Hassan, M.T. Araji, Hierarchical optimization of district heating plants by integrating evolutionary and non-linear programming algorithms, Appl Energy 373 (2024) 123935. https://doi.org/10.1016/j.apenergy.2024.123935.

[178] M.T. Araji, A. Waqas, R. Ali, Utilizing deep learning towards real-time snow cover detection and energy loss estimation for solar modules, Appl Energy 375 (2024) 124201. https://doi.org/10.1016/j.apenergy.2024.124201.

[179] E.A. Pina, M.A. Lozano, L.M. Serra, A multiperiod multiobjective framework for the synthesis of trigeneration systems in tertiary sector buildings, Int J Energy Res 44 (2020) 1140–1166. https://doi.org/10.1002/er.5006.

[180] M. Martell, F. Rodríguez, M. Castilla, M. Berenguel, Multiobjective control architecture to estimate optimal set points for user comfort and energy saving in buildings, ISA Trans 99 (2020) 454–464. https://doi.org/10.1016/j.isatra.2019.10.006.

[181] B. Chen, Q. Liu, H. Chen, L. Wang, T. Deng, L. Zhang, X. Wu, Multiobjective optimization of building energy consumption based on BIM-DB and LSSVM-NSGA-II, J Clean Prod 294 (2021) 126153. https://doi.org/10.1016/j.jclepro.2021.126153.

[182] N. Chakraborty, A. Mondal, S. Mondal, Multiobjective Optimal Scheduling Framework for HVAC Devices in Energy-Efficient Buildings, IEEE Syst J 13 (2019) 4398–4409. https://doi.org/10.1109/JSYST.2019.2933308.

[183] M. Fleischer, The Measure of Pareto Optima: Applications to Multi-Objective Metaheuristics, in: Proceedings of the Second International Conference on Evolutionary Multi-Criterion Optimization (EMO), Springer-Verlag, Faro, Portugal, 2003: pp. 519–533.

[184] Bratley, P., B.L. Fox, Algorithm 659: Implementing Sobol's quasirandom sequence generator, ACM Transactions on Mathematical Software 14 (1988) 88–100.

[185] Custòdio, A. L., J.F.A. Madeira, A.I.F. Vaz, L.N. Vicente, Direct Multisearch for Multiobjective Optimization, SIAM Journal on Optimization 21 (2011) 1109–1140.

[186] D. Kalyanmoy, Multi-Objective Optimization Using Evolutionary Algorithms, in: Multi-Objective Evolutionary Optimisation for Product Design and Manufacturing, Springer London, London, 2011: pp. 3–34.

[187] S. Kasiri, S. Abdulsalam, A. Ulrich, V. Prasad, Optimization of CO2 fixation by Chlorella kessleri using response surface methodology, Chem Eng Sci 127 (2015) 31–39. https://doi.org/10.1016/j.ces.2015.01.008.

[188] H.-L. Tran, J.-S. Kwon, Z.-H. Kim, Y. Oh, C.-G. Lee, Statistical optimization of culture media for growth and lipid production of Botryococcus braunii LB572, Biotechnology and Bioprocess Engineering 15 (2010) 277–284. https://doi.org/10.1007/s12257-009-0127-7.

[189] B. Wang, C.Q. Lan, Optimising the lipid production of the green alga Neochloris oleoabundans using box-behnken experimental design, Can J Chem Eng 89 (2011) 932–939. https://doi.org/10.1002/cjce.20513.

[190] H. Tebassi, M.A. Yallese, I. Meddour, F. Girardin, T. Mabrouki, On the Modeling of Surface Roughness and Cutting Force when Turning of Inconel 718 Using Artificial Neural Network and Response Surface Methodology: Accuracy and Benefit, Periodica Polytechnica Mechanical Engineering 61 (2017) 1–11. https://doi.org/10.3311/PPme.8742.

[191] A. Shakya, M. Mishra, D. Maity, G. Santarsiero, Structural health monitoring based on the hybrid ant colony algorithm by using Hooke–Jeeves pattern search, SN Appl Sci 1 (2019). https://doi.org/10.1007/s42452-019-0808-6.

[192] E. Günerken, E. D'Hondt, M. Eppink, K. Elst, R. Wijffels, Flow cytometry to estimate the cell disruption yield and biomass release of Chlorella sp. during bead milling, Algal Res 25 (2017) 25–31. https://doi.org/10.1016/j.algal.2017.04.033.

[193] G. Aminti, A. Cinotti, C. Lombardini, R. Spinelli, G. Picchi, Industrial stress-test of a magnetic resonance moisture meter for woody biomass in southern European conditions, Fuel Processing Technology 178 (2018) 189–196. https://doi.org/10.1016/j.fuproc.2018.05.032.

[194] D.K. Seo, S.S. Park, J. Hwang, T.-U. Yu, Study of the pyrolysis of biomass using thermo-gravimetric analysis (TGA) and concentration measurements of the evolved species, J Anal Appl Pyrolysis 89 (2010) 66–73. https://doi.org/10.1016/j.jaap.2010.05.008.

[195] Liu, Junker, Murakami, Hu, Automated Counting of Cancer Cells by Ensembling Deep Features, Cells 8 (2019) 1019. https://doi.org/10.3390/cells8091019.

[196] E. Gottardini, F. Cristofolini, A. Cristofori, A. Vannini, M. Ferretti, Sampling bias and sampling errors in pollen counting in aerobiological monitoring in Italy, Journal of Environmental Monitoring 11 (2009) 751. https://doi.org/10.1039/b818162b.

[197] A. Waqas, M.T. Araji, Machine learning-aided thermography for autonomous heat loss detection in buildings, Energy Convers Manag 304 (2024) 118243. https://doi.org/10.1016/j.enconman.2024.118243.

[198] A. Izadi, M. Shahafve, P. Ahmadi, Neural network genetic algorithm optimization of a transient hybrid renewable energy system with solar/wind and hydrogen storage system for zero energy buildings at various climate conditions, Energy Convers Manag 260 (2022) 115593. https://doi.org/10.1016/j.enconman.2022.115593.

[199] M. Sim, D. Suh, M.-O. Otto, Multi-Objective Particle Swarm Optimization-Based Decision Support Model for Integrating Renewable Energy Systems in a Korean Campus Building, Sustainability 13 (2021) 8660. https://doi.org/10.3390/su13158660.

[200] B. Garlík, M. Křivan, Renewable energy unit commitment, with different acceptance of balanced power, solved by simulated annealing, Energy Build 67 (2013) 392–402. https://doi.org/10.1016/j.enbuild.2013.07.062.

[201] C. Yang, H. Li, Y. Rezgui, I. Petri, B. Yuce, B. Chen, B. Jayan, High throughput computing based distributed genetic algorithm for building energy consumption optimization, Energy Build 76 (2014) 92–101. https://doi.org/10.1016/j.enbuild.2014.02.053.

[202] Z. Hu, L. Xu, J. Li, Q. Gan, X. Xu, Z. Song, Y. Shao, M. Ouyang, A novel diagnostic methodology for fuel cell stack health: Performance, consistency and uniformity, Energy Convers Manag 185 (2019) 611–621. https://doi.org/10.1016/j.enconman.2019.02.031.

[203] Z. Hu, L. Xu, Y. Huang, J. Li, M. Ouyang, X. Du, H. Jiang, Comprehensive analysis of galvanostatic charge method for fuel cell degradation diagnosis, Appl Energy 212 (2018) 1321–1332. https://doi.org/10.1016/j.apenergy.2018.01.005.

[204] R.E. Silva, R. Gouriveau, S. Jemeï, D. Hissel, L. Boulon, K. Agbossou, N. Yousfi Steiner, Proton exchange membrane fuel cell degradation prediction based on Adaptive Neuro-Fuzzy Inference Systems, Int J Hydrogen Energy 39 (2014) 11128–11144. https://doi.org/10.1016/j.ijhydene.2014.05.005.

[205] J. Li, Z. Hu, L. Xu, M. Ouyang, C. Fang, J. Hu, S. Cheng, H. Po, W. Zhang, H. Jiang, Fuel cell system degradation analysis of a Chinese plug-in hybrid fuel cell city bus, Int J Hydrogen Energy 41 (2016) 15295–15310. https://doi.org/10.1016/j.ijhydene.2016.06.136.

[206] Z. Hu, L. Xu, J. Li, M. Ouyang, Z. Song, H. Huang, A reconstructed fuel cell life-prediction model for a fuel cell hybrid city bus, Energy Convers Manag 156 (2018) 723–732. https://doi.org/10.1016/j.enconman.2017.11.069.

[207] O. Kramer, Genetic Algorithm Essentials, Springer, Cham, Switzerland, 2017.

[208] A. Shukla, H.M. Pandey, D. Mehrotra, Comparative review of selection techniques in genetic algorithm, in: 2015 International Conference on Futuristic Trends on Computational Analysis and Knowledge Management (ABLAZE), IEEE, 2015: pp. 515–519. https://doi.org/10.1109/ABLAZE.2015.7154916.

[209] N. Delgarm, B. Sajadi, F. Kowsary, S. Delgarm, Multi-objective optimization of the building energy performance: A simulation-based approach by means of particle swarm optimization (PSO), Appl Energy 170 (2016) 293–303. https://doi.org/10.1016/j.apenergy.2016.02.141.

[210] H. Molavi, M.M. Ardehali, Utility demand response operation considering day-of-use tariff and optimal operation of thermal energy storage system for an industrial building based on particle swarm optimization algorithm, Energy Build 127 (2016) 920–929. https://doi.org/10.1016/j.enbuild.2016.06.056.

[211] R. Velik, P. Nicolay, Energy management in storage-augmented, grid-connected prosumer buildings and neighborhoods using a modified simulated annealing optimization, Comput Oper Res 66 (2016) 248–257. https://doi.org/10.1016/j.cor.2015.03.002.

[212] R. Arjomandnia, M. Ilbeigi, M. Kazemidemneh, A.N. Hashemi, Renovating buildings by modelling energy–CO_2 emissions using particle swarm optimization and artificial neural network (case study: Iran), Indoor and Built Environment 32 (2023) 1621–1637. https://doi.org/10.1177/1420326X231151244.

[213] T.G. Kolda, R.M. Lewis, V. Torczon, Optimization by Direct Search: New Perspectives on Some Classical and Modern Methods, SIAM Review 45 (2003) 385–482. https://doi.org/10.1137/S003614450242889.

[214] X. Yang, J. Li, Chaos DNA Hooke-Jeeves Evolutionary Algorithm and Its Application in River Pollution Control, in: 2010 International Conference on Mechanic Automation and Control Engineering, IEEE, 2010. https://doi.org/10.1109/MACE.2010.5536472.

[215] B. Gao, C. Wang, Y. Hu, C.K. Tan, P.A. Roach, L. Varga, Function value-based multi-objective optimisation of reheating furnace operations using hooke-jeeves algorithm, Energies (Basel) 11 (2018). https://doi.org/10.3390/en11092324.

[216] M. Farhan Tabassum, M. Saeed, N. Ahmad Chaudhry, J. Ali, M. Farman, S. Akram, Evolutionary simplex adaptive Hooke-Jeeves algorithm for economic load dispatch problem considering valve point loading effects, Ain Shams Engineering Journal 12 (2021) 1001–1015. https://doi.org/10.1016/j.asej.2020.04.006.

[217] S. BABU, T.S. KUMAR, V. BALASUBRAMANIAN, Optimizing pulsed current gas tungsten arc welding parameters of AA6061 aluminium alloy using Hooke and Jeeves algorithm, Transactions of Nonferrous Metals Society of China (English Edition) 18 (2008) 1028–1036. https://doi.org/10.1016/S1003-6326(08)60176-4.

[218] A.-T. Nguyen, S. Reiter, P. Rigo, A review on simulation-based optimization methods applied to building performance analysis, Appl Energy 113 (2014) 1043–1058. https://doi.org/10.1016/j.apenergy.2013.08.061.

[219] C. Kao, C.-C. Li, S.-P. Chen, Simulation response optimization via direct conjugate direction method, Comput Oper Res 30 (2003) 541–552. https://doi.org/10.1016/S0305-0548(02)00023-0.

[220] C.H. Endres, A. Roth, T.B. Brück, Thermal Reactor Model for Large-Scale Algae Cultivation in Vertical Flat Panel Photobioreactors, Environ Sci Technol 50 (2016) 3920–3927. https://doi.org/10.1021/acs.est.5b05414.

[221] V. Belohlav, T. Zakova, T. Jirout, L. Kratky, Effect of hydrodynamics on the formation and removal of microalgal biofilm in photobioreactors, Biosyst Eng 200 (2020) 315–327. https://doi.org/10.1016/j.biosystemseng.2020.10.014.

[222] H. Qiang, A. Richmond, Productivity and photosynthetic efficiency ofSpirulina platensis as affected by light intensity, algal density and rate of mixing in a flat plate photobioreactor, J Appl Phycol 8 (1996) 139–145. https://doi.org/10.1007/BF02186317.

[223] A.M.J. Kliphuis, L. de Winter, C. Vejrazka, D.E. Martens, M. Janssen, R.H. Wijffels, Photosynthetic efficiency of Chlorella sorokiniana in a turbulently mixed short light-path photobioreactor, Biotechnol Prog 26 (2010) 687–696. https://doi.org/10.1002/btpr.379.

[224] W. Jiang, W. Levasseur, J. Casalinho, T. Martin, F. Puel, P. Perré, V. Pozzobon, Shear stress computation in a millimeter thin flat panel photobioreactor: Numerical design validated by experiments, Biotechnol Appl Biochem 68 (2021) 60–70. https://doi.org/10.1002/bab.1894.

[225] J. Pruvost, J.F. Cornet, V. Goetz, J. Legrand, Theoretical investigation of biomass productivities achievable in solar rectangular photobioreactors for the cyanobacterium Arthrospira platensis, Biotechnol Prog 28 (2012) 699–714. https://doi.org/10.1002/btpr.1540.

[226] P. Westerhoff, Q. Hu, M. Esparza-Soto, W. Vermaas, Growth parameters of microalgae tolerant to high levels of carbon dioxide in batch and continuous-flow photobioreactors, Environ Technol 31 (2010) 523–532. https://doi.org/10.1080/09593330903552078.

[227] L. Borella, D. Diotto, E. Barbera, D. Fiorimonte, E. Sforza, N. Trivellin, Application of flashing blue-red LED to boost microalgae biomass productivity and energy efficiency in continuous photobioreactors, Energy 259 (2022) 125087. https://doi.org/10.1016/j.energy.2022.125087.

[228] D.S. Wágner, B. Valverde-Pérez, B.G. Plósz, Light attenuation in photobioreactors and algal pigmentation under different growth conditions – Model identification and complexity assessment, Algal Res 35 (2018) 488–499. https://doi.org/10.1016/j.algal.2018.08.019.

[229] R.R. Rhinehart, Engineering optimization: applications, methods and analysis, The American Society of Mechanical Engineers, New York, N.Y, 2018.

[230] A. Antoniou, W. Lu, Practical Optimization: Algorithms and Engineering Applications, Springer, New York, NY, 2021.

[231] A. El Jery, A. Noreen, M. Isam, J.L. Arias-Gonzáles, T. Younas, N. Al-Ansari, S.Sh. Sammen, A novel experimental and machine learning model to remove COD in a batch reactor equipped with microalgae, Appl Water Sci 13 (2023) 153. https://doi.org/10.1007/s13201-023-01957-8.

[232] L. Borella, E. Sforza, A. Bertucco, Effect of residence time in continuous photobioreactor on mass and energy balance of microalgal protein production, N Biotechnol 64 (2021) 46–53. https://doi.org/10.1016/j.nbt.2021.05.006.

[233] J.M. Adánez, B.M. Al-Hadithi, A. Jiménez, Multidimensional membership functions in T–S fuzzy models for modelling and identification of nonlinear multivariable systems using genetic algorithms, Appl Soft Comput 75 (2019) 607–615. https://doi.org/10.1016/j.asoc.2018.11.034.

[234] W.F. Siahaan, O.S. Sitompul, Z. Situmorang, The Accuracies of ANFIS and Genetic Algorithm with Tournament Selection on Classifying Hepatitis Data, J Phys Conf Ser 1566 (2020) 012121. https://doi.org/10.1088/1742-6596/1566/1/012121.

[235] G. Mashina, M. Gadi, Intensity of solar radiation on convex walls using a new computerized tool, in: International Conference on Computer Civil and Building Engineering, 2010.

[236] Y.-W. Lim, M.Z. Kandar, M.H. Ahmad, D.R. Ossen, A.M. Abdullah, Building façade design for daylighting quality in typical government office building, Build Environ 57 (2012) 194–204. https://doi.org/10.1016/j.buildenv.2012.04.015.

[237] M.M. Saad, M.T. Araji, Optimization of double skin façades with integrated renewable energy source in cold climates, ASHRAE Topical Conference Proceedings (2020) 366–373.

[238] M.M. Saad, M.T. Araji, Co-model for urban density permutations and building form optimization with high-performance energy criteria, Journal of Building Engineering 43 (2021) 103109. https://doi.org/10.1016/j.jobe.2021.103109.

[239] J. Ferdyn-Grygierek, K. Grygierek, Multi-Variable Optimization of Building Thermal Design Using Genetic Algorithms, Energies (Basel) 10 (2017) 1570. https://doi.org/10.3390/en10101570.

[240] S. Herrería-Alonso, A. Suárez-González, M. Rodríguez-Pérez, R.F. Rodríguez-Rubio, C. López-García, A Solar Altitude Angle Model for Efficient Solar Energy Predictions, Sensors 20 (2020) 1391. https://doi.org/10.3390/s20051391.

[241] R.A. Memon, D.Y.C. Leung, C.H. Liu, Effects of building aspect ratio and wind speed on air temperatures in urban-like street canyons, Build Environ 45 (2010) 176–188. https://doi.org/10.1016/j.buildenv.2009.05.015.

[242] A.M.R. Aminuddin, S.P. Rao, H.W. Thing, Thermal comfort field studies in two certified energy efficient office buildings in a tropical climate, International Journal of Sustainable

Building Technology and Urban Development 3 (2012) 129–136. https://doi.org/10.1080/2093761X.2012.696324.